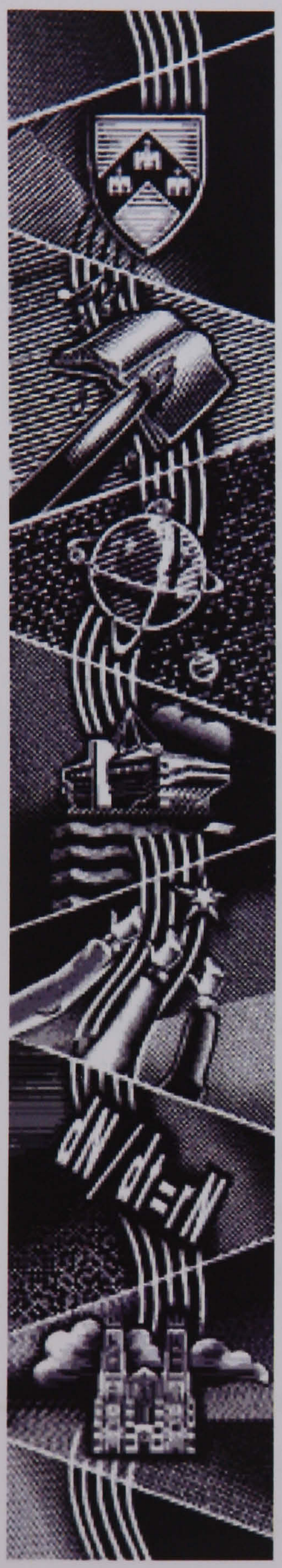

Formation and Reactivity of High Valent Metal-Oxo Species

Anna Eleni Anastasi

A thesis submitted for the degree of
Doctor of Philosophy

University of York
Department of Chemistry

July 2006

Table of Contents

List of Tables

List of Figures

Chapter 5

Chapter 6

Appendix

Acknowledgements

This thesis would not have been written without the help of many many people, and I am eternally grateful for their help and support through the past 3 and a half years.

First I have to thank my supervisor, **John** (or Professor McGrady, as he is now deservedly called) for letting me work for him in the first place, and believing in me when I needed someone to. I would also like to thank **Achim Lienke** from Unilever for his many suggestions, advice, and the occasional kick when needed, and **Simon Duckett** for answering my many random questions when he didn't have to, and sometimes didn't have time to!

My boyfriend, **Dave Fildes** has been an unwavering support for me throughout my PhD. Without him I wouldn't have got this far, and even if I had I wouldn't be anywhere near as happy.

I would never even have started a PhD without the support and encouragement (or, more accurately, under the orders of) **Sushilla Knottenbelt**. So thanks for telling me what I want – any suggestions of what to do next?

Huge thanks also go to all the people who have worked in the McGrady group during my time there: **Sushi**, **Dimi** (who has been more fantastic than there are words for),**Katerina** (who isn't strictly a member of the group, but feels like it, and is a fab cook too! **Charlotte** (thanks to whom I can now whistle a little bit), **Thomas**, **Julia**, **Pete**, **Ainara**, **Maria**, **Ekaterina**, and **Marianna**. I hope our paths cross again.

I also have to thank the many other people from C-block who have been there when I needed to moan, boast, or just drink tea (or, if we made the effort to go further than the coffee room, beer). Thanks **Nick**, **Nicola**, **Kirsten**, **Vicky**, **Tracy**, **Joaquin**, **Paul** and everyone else who I haven't forgotten but don't have time to mention.

I also owe a massive thanks to my family: **Mum**, **Dad, Pete**, **Maro**, **Paul**, **Charlotte**, **Philip**, **George**, **Katriona** and **Ellie** – you had the hardest job of keeping me cheerful and happy, and failing that, keeping me topped up with wine and tea., and to **Dave's family** for doing the same, just because they are great people.

Thanks also to the **EPSRC** and **Unilever** for funding, and to **NSCCS** (and particularly **Sarah Wilsey**) for extra computational time.

Authors Declaration

The work presented in this thesis is the original work of the author, except where references have been made to other sources. No part of this work has previously been submitted for any other degree.

Anna Anastasi

Chapter 1 – General Introduction

1.1 Introduction

This thesis describes a computational study of transition metal complexes and, in particular, their role in oxidation. This is a large subject area and we consider only a small portion of it – specifically the reactivity of transition metal species that react with H_2O_2 or O_2 to form an active oxidant that can initiate oxidation and/or oxygenation reactions. This general introduction section discusses metal-catalysed oxidation in a very general context - the introductions to each of the results chapters cover literature that is of specific importance to each topic.

This thesis focuses on two classes of complex – one containing iron, the other manganese. Both types of complex, shown in Figure 1-1, have applications in the textile and wood pulp bleaching industries, and both utilise H_2O_2 for oxidation catalysis.

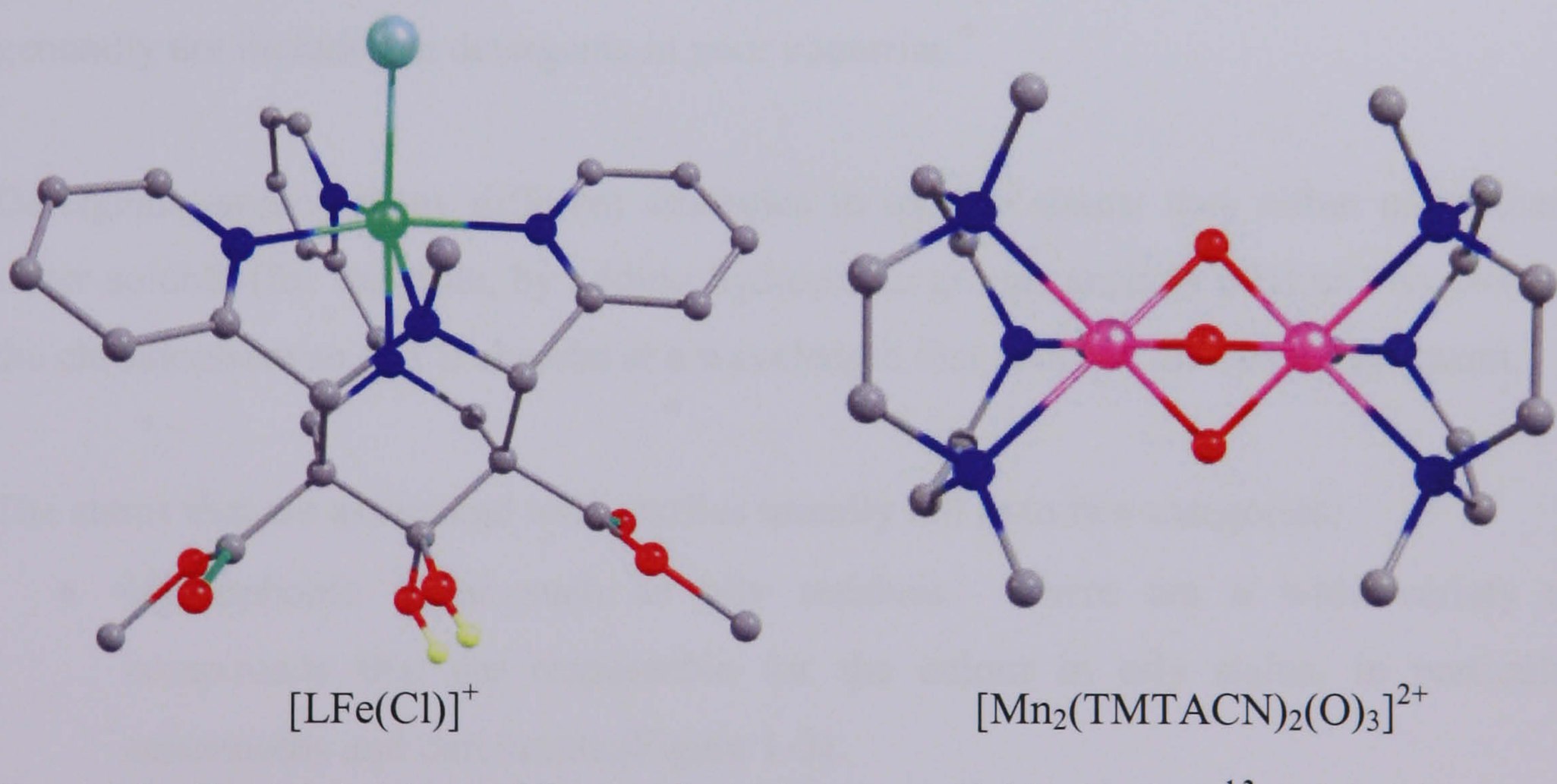

$[LFe(Cl)]^+$ $[Mn_2(TMTACN)_2(O)_3]^{2+}$

Figure 1-1 – Crystal structures of the complexes that are studied in this thesis[1,2] {original in colour}

The wood pulp bleaching industry consumes half of the worldwide production of H_2O_2 and the laundry and textile bleaching industry consumes another 10% of it. However, H_2O_2 in isolation requires washing at temperatures of around 90°C for prolonged amounts of time (around 3 hours to bleach wood pulp) to afford complete oxidation.[3]

Consumers do not usually wash laundry at such high temperatures, and many people worldwide wash at temperatures as low as 5°C. For this reason catalysts are required that reduce the temperature for oxidation, and consequently reduce the amount of energy required.

For these reasons, washing powders do not currently use H_2O_2 for stain bleaching. However it is desirable as a bleaching agent as it is environmentally benign, giving water as a by-product from oxidation, and water and O_2 as by-products from the catalase reaction which is decomposition of H_2O_2 without oxidation of the substrate.[4] An even more desirable bleaching agent is atmospheric oxygen which, in addition to being environmentally benign, is affordable, as only a catalyst to utilise this molecule would be required.

Bleaching agents such as sodium hypochlorite, in contrast, give halogenated waste products, while peracid precursors generate organic waste. Hydrogen peroxide is traditionally included in washing powders in the form of either sodium perborate or percarbonate, which releases a carbonate buffer in addition to H_2O_2 when it dissolves in water. The relatively high cost of these bleaching agents, however, means that they are generally not included in detergents in poor countries.[4]

Detergents employ many different strategies to oxidise stains: they either make them water soluble (for example, by adding hydrophilic groups such as OH) or they oxidise the chromophore so that it absorbs at a wavelength that is not in the visible spectrum.[4]

The stains that are associated with textiles broadly fall in to two categories:

- Hydrophobic stains such as oily residues. There are a wide variety of compounds that are responsible for the colour in oily stains, in particular carotenoids and curcumins (Figure 1-2).
- Hydrophilic stains such as tea, fruit juice and wine, whose colour is caused by polyphenolic compounds (Figure 1-2).

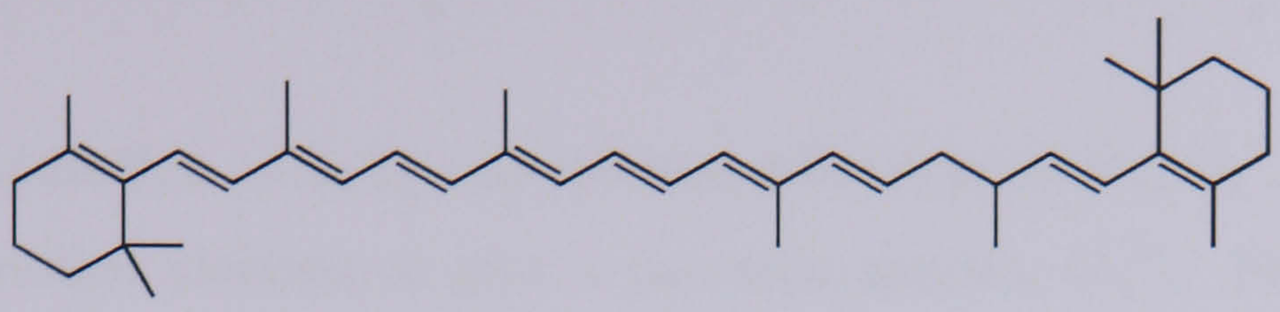

β-Carotene

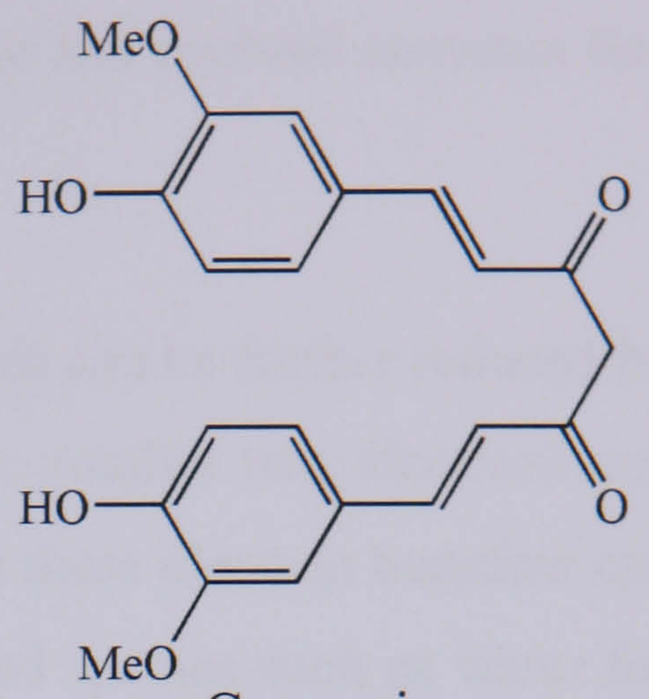

Curcumin

Both examples of chromophores abundant in hydrophobic stains

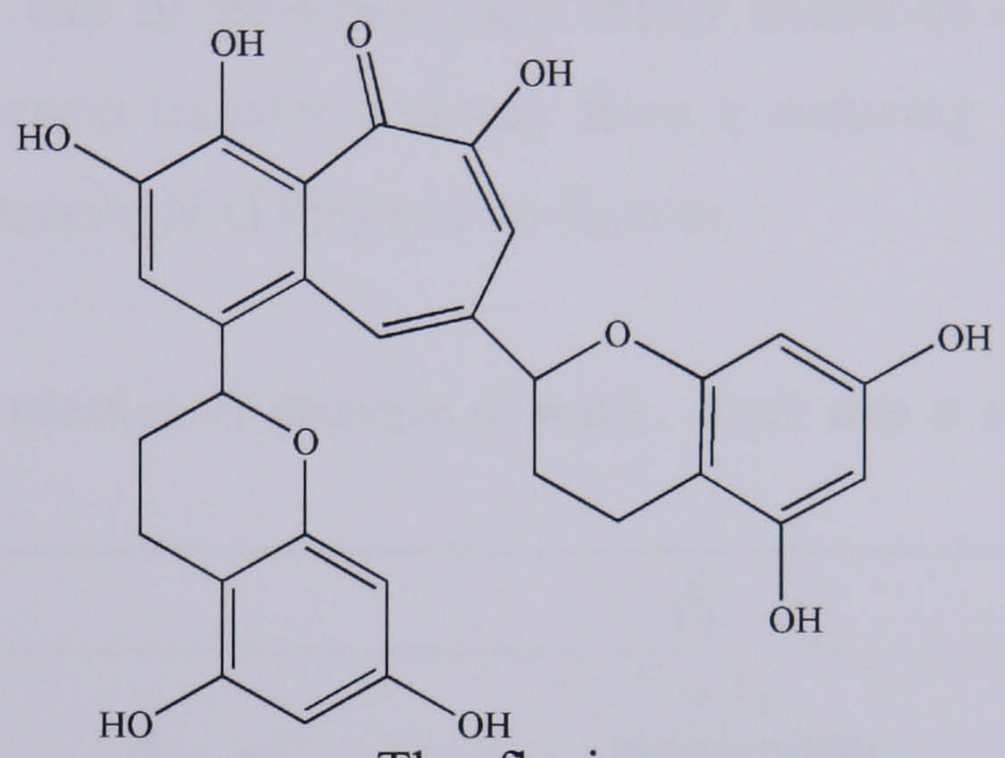

Theaflavin

A polyphenolic chromophore found in tea stains

Figure 1-2 – Examples of the chromophores in hydrophobic and hydrophilic stains

Although effective oxidation is desirable in a bleaching agent, selectivity is also an important factor. Oxygen based radicals, promoted by transition metals, such as iron, that are found in tap water, can indiscriminately attack fabrics and dyes causing damage. For this reason sequesterants such as EDTA are added to washing powders.[4] One of the complexes studied in this thesis, $[Mn_2(TMTACN)_2(O)_3]^{2+}$, provides a good example of the importance of selectivity. It shows high bleaching activity at 40°C, but under certain circumstances also causes dye and fabric damage and so its use within the detergents industry has been limited to use as a component of dishwasher tablets.[5]

1.2 Oxygen and its Different Forms

Dioxygen has a triplet ground state and as a result is unreactive with other compounds that have singlet ground states at room temperature. Were it not for this, we and everything around us, would spontaneously combust. The reaction of organic species

with O_2 therefore involves a change in spin state, and nature has evolved enzymes that facilitate such processes by reduction of the oxygen moiety.

Reduction of O_2 by one electron gives superoxide, O_2^-, which can be further reduced by another electron to give a peroxide species, O_2^{2-}. Finally, another two electrons can reduce peroxide to two oxo species, O^{2-}. In aqueous media these electron transfers can be followed by proton transfers giving the related protonated species such as water for an oxo group. This is depicted in Table 1-1. In enzymes, the four electrons that facilitate this reduction can be provided from either oxidation of one or more metal centre(s), or via an electron transfer pathway from a reducing species or part of the enzyme such as Fe-S clusters, NAD(H) and co-factors.

Table 1-1 – Overview of reduction of dioxygen to water. Each step is accompanied by a proton transfer.

Dioxygen		$\dot{O}—\dot{O}$	
Superoxide	$\dot{O}—O^-$	$\overset{+H^+}{\underset{-H^+}{\rightleftharpoons}}$	$\dot{O}—OH$
Peroxide	$^-O—OH$	$\overset{+H^+}{\underset{-H^+}{\rightleftharpoons}}$	$HO—OH$
Hydroxyl radical	$^\bullet OH + {}^-OH$	$\overset{+H^+}{\underset{-H^+}{\rightleftharpoons}}$	$^\bullet OH + H_2O$
Water	$^-OH + H_2O$	$\overset{+H^+}{\underset{-H^+}{\rightleftharpoons}}$	$H_2O + H_2O$

1.3 Types of Enzyme: Oxidases and Oxygenases

To utilise O_2 nature has evolved a variety of chemical processes that involve weakening or cleaving the O=O double bond by reduction and inserting one of the oxygen atoms in a CH bond to give an alcohol.[6] These processes involve enzymes with transition metals in their active site to bind the substrate and products. Iron – an abundant and non-toxic transition metal – is particularly common in many oxygen activating enzymes.

There are two broad classes of enzymes that react with O_2[7]:

- Oxidases afford O_2 reduction to hydroxide or water by one. two, or four electrons.
- Oxygenases activate O_2 for insertion into organic substrates. Oxygenases can be further divided in to subcategories, as summarised in Table 1-2 and explained below.

Table 1-2 – Oxidases and Oxygenases

Type of enzyme	Number of electrons	Reaction
Oxidase	2 electron	$2RH + O_2 \rightarrow 2R + H_2O_2$
	2 electron	$RH_2 + O_2 \rightarrow R + H_2O_2$
	4 electron	$4RH + O_2 \rightarrow 4R + 2H_2O$
	4 electron	$2RH_2 + O_2 \rightarrow 2R + H_2O$
	4 electron	$RH_4 + O_2 \rightarrow R + 2H_2O$
Monooxygenase	External	$S + RH_2 + O_2 \rightarrow SO + R + H_2O$
	External (uncoupled)	$S' + RH_2 + O_2 \rightarrow S' + R' + H_2O_2$
	Internal	$SH_2 + O_2 \rightarrow SO + H_2O$
Dioxygenase	Intramolecular	$S + O_2 \rightarrow SO_2$
	Intermolecular	$S + C_o + O_2 \rightarrow SO + C_oO$

RH_n = reductant, S = substrate, S' = poor substrate, C_o = cofactor

Monooxygenases incorporate one oxygen atom into the substrate, and the other into water by using either:

- An additional two-electron reductant (external monooxygenases). Poor substrates still lead to the reductant being oxidised, but rather than the oxygen atom being incorporated in to the substrate, H_2O_2 is produced.
- The substrate (internal or mixed function).

Dioxygenases either incorporate both atoms into the substrate (intramolecular), or one atom is incorporated into the substrate and the other incorporated into an additional organic cofactor. Some enzymes exhibit both oxidase and oxygenase activity depending on the substrates and conditions of the reaction.

1.4 Examples of Different Enzymes

There have been many studies done on enzymes to elucidate their mechanisms and these have been aided by the synthesis and study of small model complexes which mimic in some way – be it the structure or mechanism – the enzymes.[8-11] This information may also provide insight into the mechanism of the complexes studied in this thesis. This survey deals largely with iron based enzymes as this metal is found in a huge number of oxygen transporting and activating enzymes.

Non-heme iron containing enzymes responsible for oxidation and oxygenation reactions are often found to utilise ferrous iron (Fe^{2+}) and O_2. Many studies have been carried out to understand the active site of these enzymes, and there are a wealth of model complexes that can be found in recent literature. Some of these are discussed in more detail in section 3.1. Comparison of the spectroscopy of the enzymes and model complexes has, on one hand, led to a greater knowledge of the active sites of the enzymes, and on the other hand, inspired the synthesis of catalytically active model complexes.

In general, there are three types of iron enzymes and bioinspired model species that have been considered. These are:

- Mononuclear heme enzymes such as Cytochrome P450.
- Non heme mononuclear iron enzymes such as bleomycin.
- Dinuclear iron enzymes such as methane monooxygenase.

Alkane oxidation and oxygenation catalysts share a number of mechanistic features: they cleave C-H bonds and aid C-O bond formation. This can either be done in two distinct steps, as a concerted mechanism or anywhere in the spectrum inbetween.[12]

1.4.1 Cytochrome P450 – an Example of a Mononuclear Heme Enzyme

One of the most widely studied enzymes for oxygenation is the heme enzyme cytochrome P450 (CYP), so called because a Soret band appears in the UV/vis spectrum at 450 nm upon binding of CO.[10] It uses O_2 and two reducing equivalents to

catalyse many different regio- and stereospecific oxygen insertion reactions into the C=C and C-H bonds of organic compounds. The two key classes of reactions that it carries out are the synthesis of steroids and the oxidation of xenobiotic compounds to facilitate their excretion. The ability to activate inert C-H bonds is a "holy grail" of chemistry, and there has been a great deal of research into the mechanistic details of the reaction including many attempts to mimic this chemistry.[13]

Although there are a wide variety of CYP enzymes, the structure of their active site is conserved. They have an iron ion ligated to a protoporphyrin IX macrocycle and are two additional coordination sites. The proximal site has the thiolate group of a cysteine moiety coordinated to the iron centre and the distal site has (in the ferric (Fe^{3+}) resting state) either a water or hydroxide ligand which is displaced upon binding of the substrate to leave a vacant coordination site where O_2 eventually binds.[14] This is depicted in Figure 1-3.

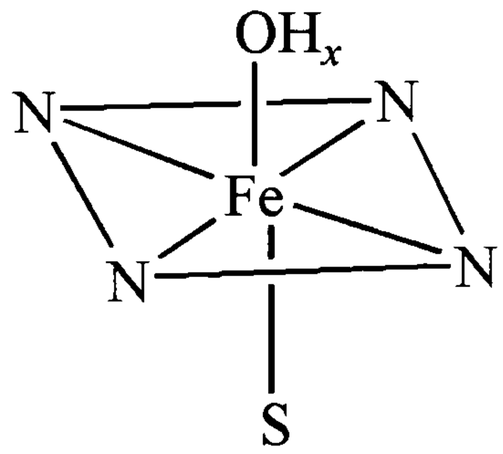

Figure 1-3 – Schematic diagram of the structure of the resting state of cytochrome P450 (*x*=1 or 2)

In the resting state of the enzyme, the iron centre is in a +3 oxidation state and is low spin. When the substrate binds the spin state changes to high spin due to the displacement of the water ligand. This makes the Fe a better electron acceptor than in the resting state, and it is then reduced to Fe^{2+} by an external reductant (usually NADPH or NADH) to give a high spin Fe^{2+} complex. O_2 then binds to the iron centre giving a low spin Fe^{2+}-O_2 state. This accepts a second electron to reduce the O_2 to O_2^-. There has been some discussion in the literature as to whether this complex corresponds to a ferrous superoxo species, or whether the oxygen species oxidises the iron centre to give a ferric peroxo species. Regardless, this species accepts a proton to give a ferric hydroperoxide species, also known as **compound 0,** which then accepts another proton, and loses a water molecule to form **compound I**. **Compound I** is believed to be the species that is responsible for oxygen atom transfer, and is now generally accepted as an

oxoiron(IV) species with the porphyrin ring bearing a radical cation. After the transfer of this oxygen atom the resting state of the enzyme is once again regenerated. The entire catalytic cycle is shown in Figure 1-4.[15]

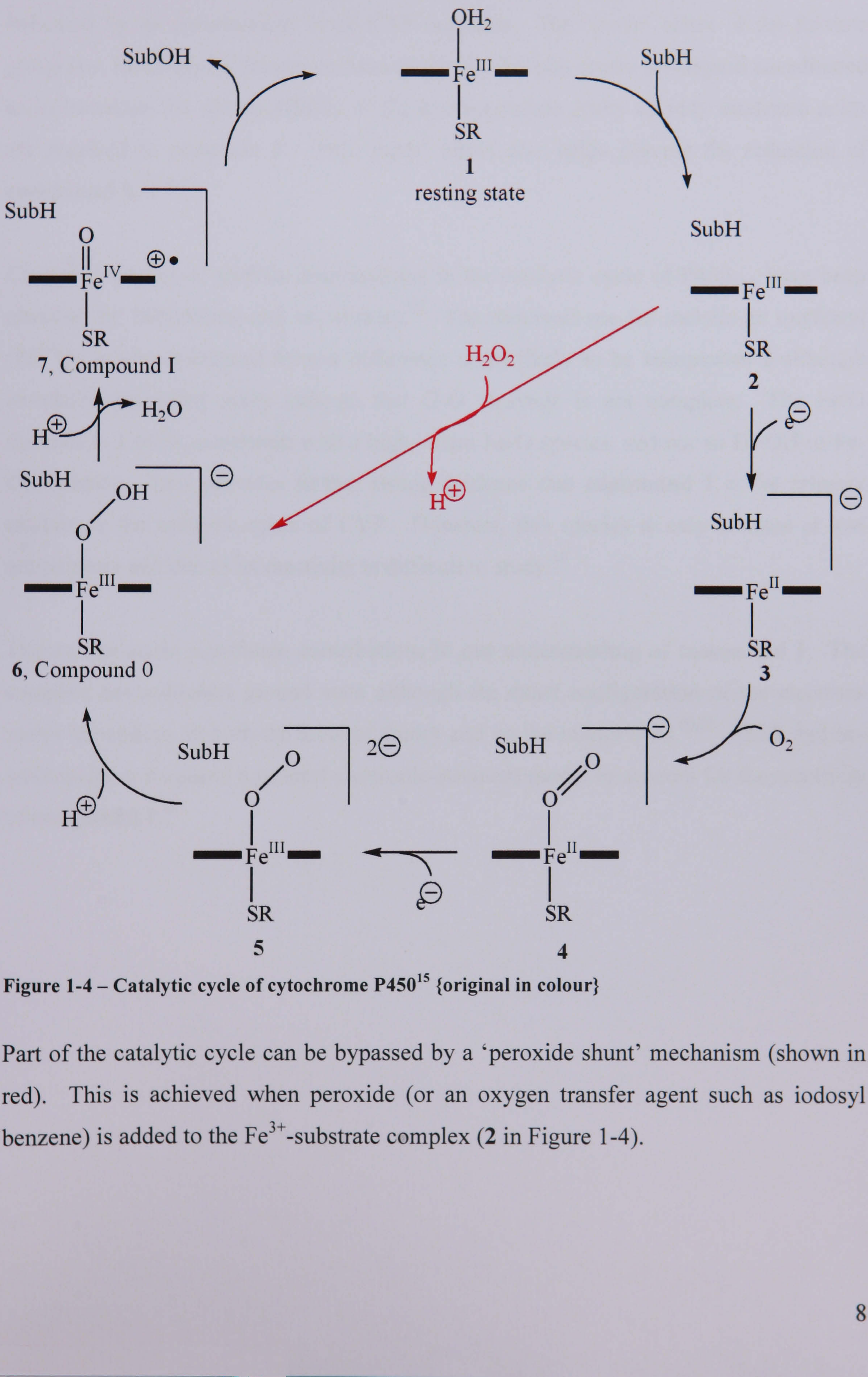

Figure 1-4 – Catalytic cycle of cytochrome P450[15] {original in colour}

Part of the catalytic cycle can be bypassed by a 'peroxide shunt' mechanism (shown in red). This is achieved when peroxide (or an oxygen transfer agent such as iodosyl benzene) is added to the Fe^{3+}-substrate complex (**2** in Figure 1-4).

As mentioned above, **compound I** is the species that is actually responsible for C-H activation, and because of this it has been studied extensively by both theory and experiment. **Compound I** is formed by heterolysis of the O-O bond, promoted by protonation of the distal O, and the proximal cysteine ligand plays a key role, as indicated by its conservation in all CYP enzymes. The "push" effect of the thiolate group (i.e. its ability to donate electron density to the iron centre and ligand coordinated to it) increases the proton affinity of the hydroperoxide group so only moderate acids are required to protonate it. The "push" effect also helps prevent the reduction of **compound 0**.[13,16,17]

Crystal structures of various intermediates in the catalytic cycle of $P450_{cam}$ have been obtained by Schlichting and co-workers.[18] The observed species include an oxyferryl ($Fe^{5+}O$) species (obtained from a difference map) likely to be **compound I** although simulated annealing maps indicate that O-O cleavage is not complete. The Fe-O distance is 1.65 Å, consistent with a high valent Fe-O species, and not an Fe-OH or Fe-OO species. This provides further strong evidence that **compound I** is the primary oxidant in the catalytic cycle of CYP. However, this species is only isolated at low temperature and due to its reactivity is difficult to study.[19]

Theory has made significant contributions to our understanding of **compound I**. The complex has a doublet ground state although the exact configuration of the electrons varies depending on both the level of theory and on the model used.[20,21] Shaik and co-workers have proposed a general electronic-structure model to account for the reactivity of **compound I**.[22]

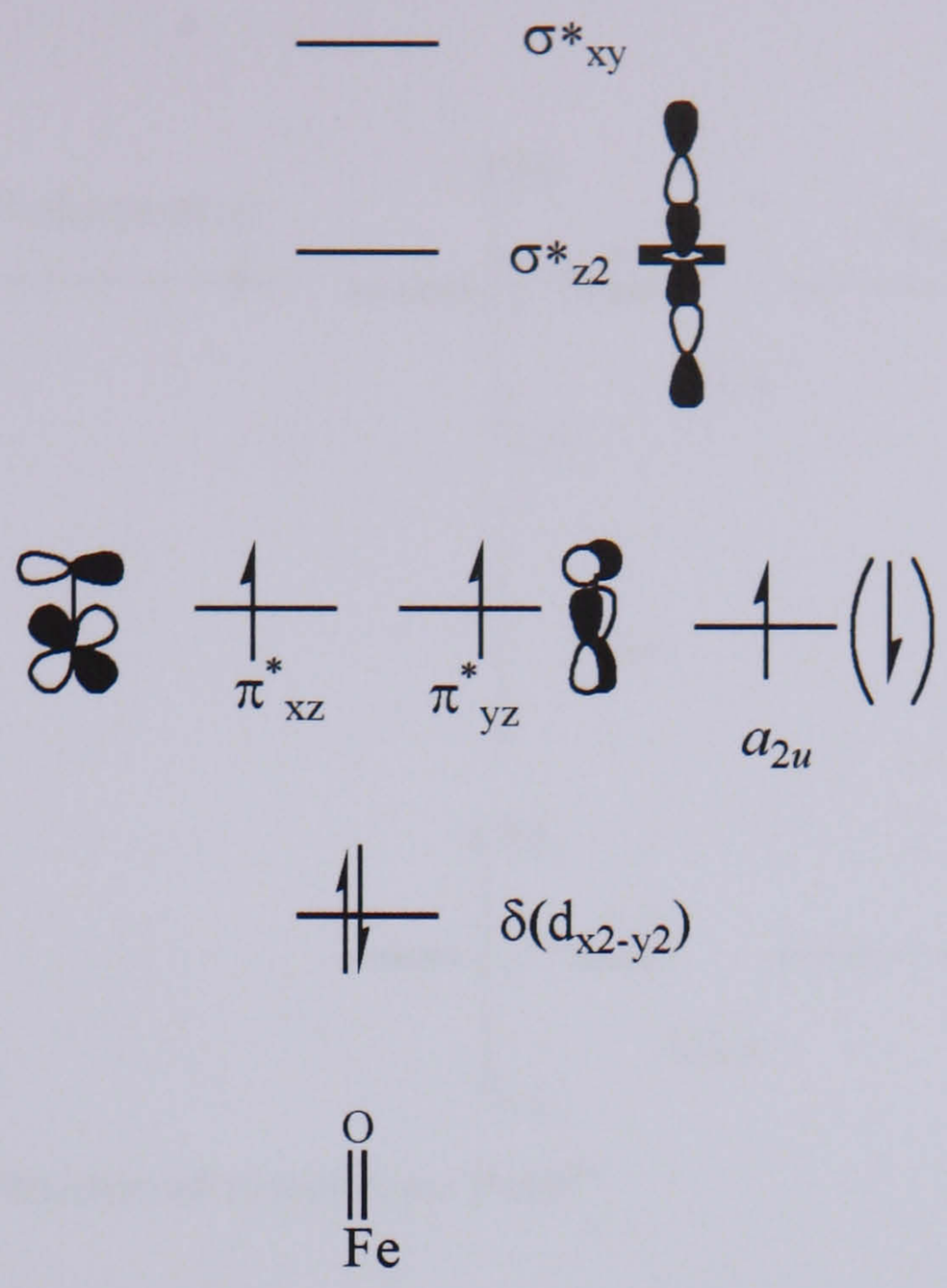

Figure 1-5 – Schematic molecular orbital diagram of compound I of cytochrome P450

In Shaik's model, **compound I** is proposed to have a $^2A_{2u}$ ground state, and a closely lying $^4A_{2u}$ state, (Figure 1-5). The π^*_{xz} and π^*_{yz} orbitals, located on the metal are singly occupied and the electrons in them are anti-ferromagnetically coupled to the one in the singly occupied a_{2u} orbital on the porphyrin, confirming that **compound I** contains an oxoiron(IV) unit coordinated to a radical cation porphyrin. Due to the large number of closely lying orbitals in CYP there is potential for more than one spin state to be involved in the oxygenation of organic species and this will have a significant effect on the product distribution.

1.4.1.1 Mechanism of Reaction of Compound I

The rebound mechanism by which CYP inserts an oxygen atom into a CH bond is shown in Figure 1-6. The oxo group abstracts the hydrogen atom from a CH bond leaving an $Fe^{3+}OH$ complex and an alkyl radical. The Alk• radical can then "rebound" to attack the coordinated hydroxo ligand to give an alcohol. However, depending on the stability of the radical it can first rearrange leading a mixture of products. The alcohol then leaves the enzyme and is replaced by a water ligand, returning the active site to its resting state.

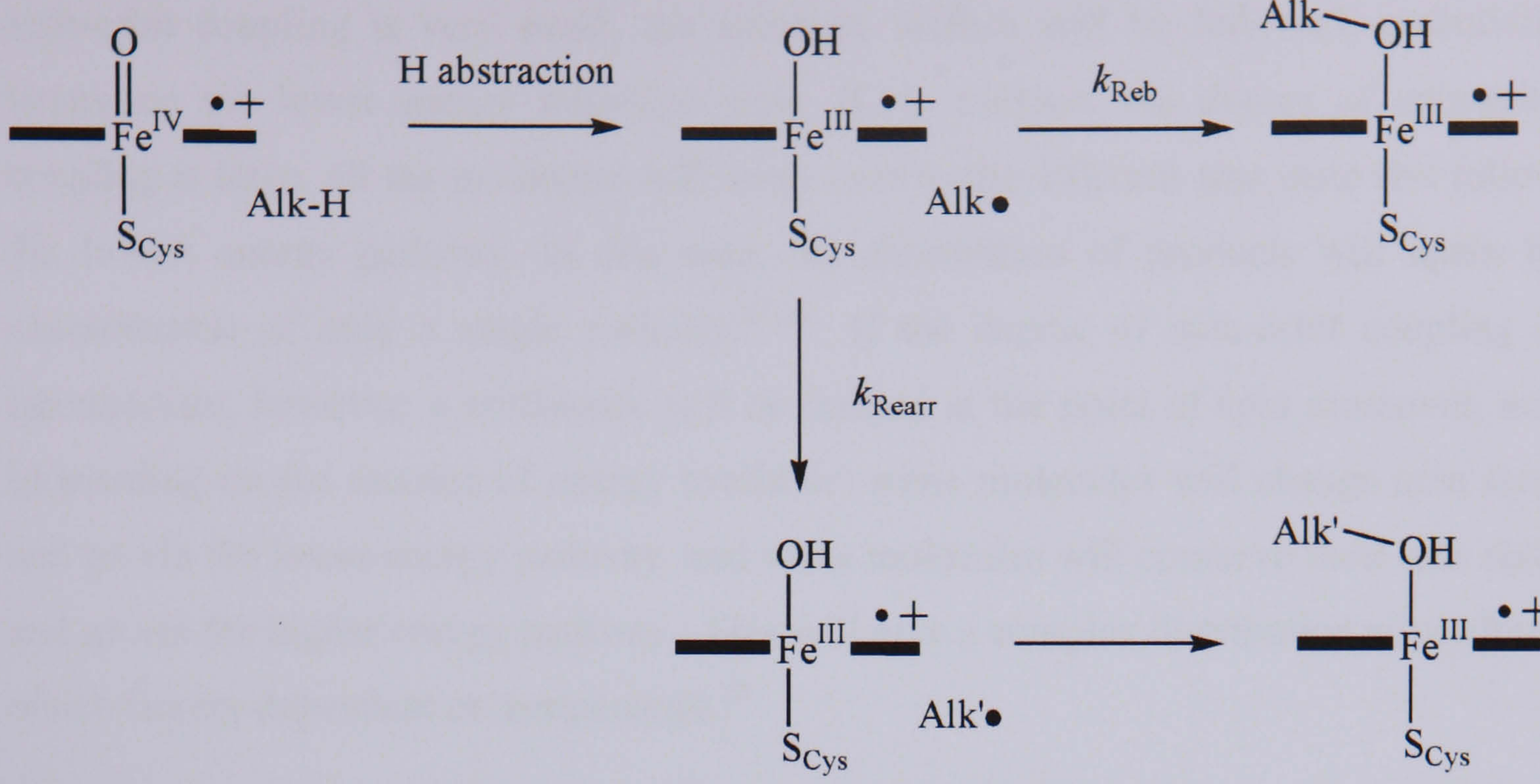

Figure 1-6 – Rebound mechanism of cytochrome P450[21]

The rebound mechanism proposed by Groves *et al.*[23] (Figure 1-6) is supported by findings such as rearranged alcohol products,[24] and more recently, kinetic isotope effect studies.[25] Additionally the products of hydroxylation indicate that there are radical intermediates involved. However, doubt has been cast on this mechanism by ultrafast radical clocks that suggest the lifetime of radicals is much shorter than the product rearrangement allows (τ = 80-200 fs).[26] This has led to the suggestion of two different oxidants being responsible for the reactivity of CYP. However, no second oxidant has been observed. An alternative explanation has been proposed for the observed product distribution, the so-called two-state reactivity (TSR) hypothesis that has been developed by Shaik and co-workers.

1.4.2 Two-State Reactivity

In a typical reaction pathway, the system moves along a single potential energy surface without a change in multiplicity. However, in organometallic and inorganic chemistry, where 3d and 4d transition metal ions are present, there is often sufficient spin-orbit coupling to allow rapid transitions between surfaces of different spin. In these cases a reaction can occur where more than one spin surface connects reactants and products, and in some cases changing to a different spin surface leads to a lower transition state. The products of the reaction can arise from either single-state or two-state pathways or a

combination of both depending on the extent of spin-orbit coupling. If the degree of spin-orbit coupling is very small, the adiabatic surface will be followed, potentially bypassing the lower energy transition state. If, in contrast, the degree of spin-orbit coupling is large, all the molecules will cross over to the different spin state and follow the lowest energy pathway. In this case, the distribution of products will again be characteristic of only a single pathway.[27,28] If the degree of spin-orbit coupling is intermediate, however, a bottleneck will be formed at the point of spin crossover, and (depending on the amount of energy available) some molecules will change spin state and go via the lower energy pathway, and some molecules will conserve their spin state and go via the higher energy pathway. This will give a complex distribution of products which is very dependent on temperature.[28]

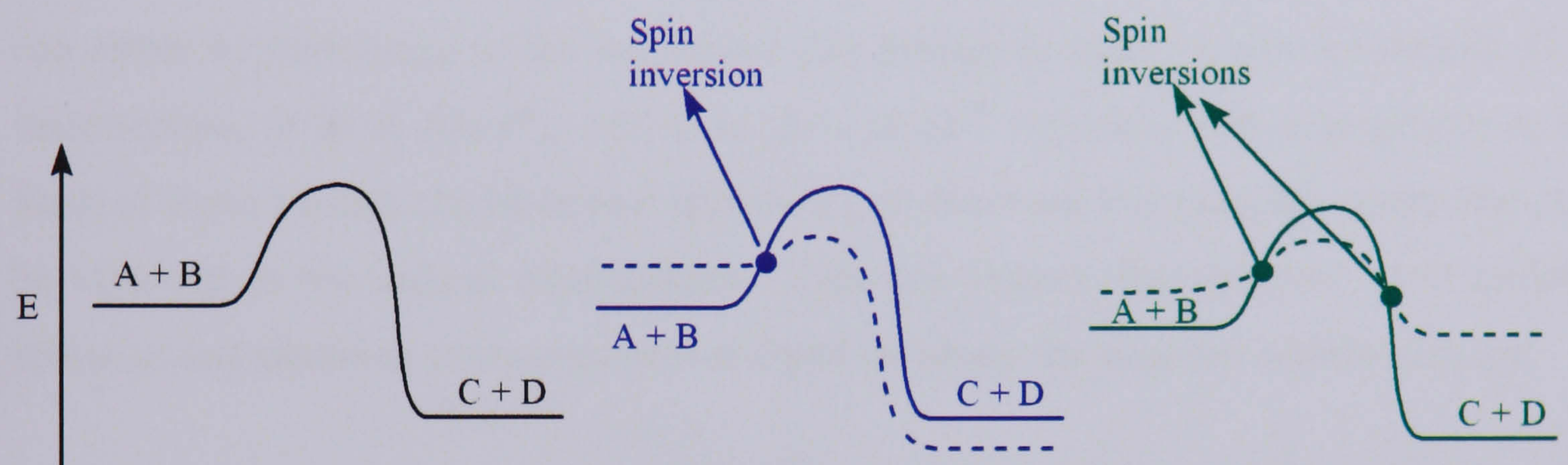

Figure 1-7 – Diagram showing TSR and SSR {original in colour}

1.4.2.1 Examples of Two-State Reactivity

TSR has been shown to be important in a number of simple reactions such as the oxidation of H_2 by FeO^+:

$$FeO^+ + H_2 \rightarrow Fe^+ + H_2O \qquad (1)$$

In this reaction, both the reactants and the products have a septet ground state. The H-H bond cleavage step is not rate determining and the rate of reaction is inversely proportional to the temperature. In addition to this, if the temperature is elevated, a competing endothermic product ($FeOH^+$) is formed. These observations are not consistent with a single potential energy surface, but can be explained by a spin-

crossover to the quartet surface before the first transition state, followed by another spin crossover back to the sextet surface before the products are formed, as shown schematically in Figure 1-7c.[28] Unambiguous examples of TSR are confined to the gas-phase reactions of coordinatively unsaturated compounds in the gas phase, but it has been proposed as a fundamental concept in oxidation catalysis, such as in the mechanism of cytochrome P450.[29]

1.4.3 Two State Reactivity and Cytochrome P450

The origin of TSR in CYP is the presence of close lying Fe^{3+} and porphyrin radicals, which means that the $^2A_{2u}$ and $^4A_{2u}$ states lie close in energy. Moreover, when the H• atom is abstracted, the Fe-Porphyrin species is reduced by one electron and this electron can either be transferred to the a_{2u} orbital (the porphyrin hole) to give a formally Fe^{4+} intermediate, or in to the π^*_{xz} orbital to give an Fe^{3+} complex with a porphyrin hole. Each of these species can be in two spin states, so there are four possible states that can be involved in the radical intermediate. TSR can explain the observed short radical lifetimes and observed rearrangements without invoking the need for another oxidant.

A DFT study by Ogliaro *et al.*[30] on the oxidation of methane by a model of **compound I** considers the role of TSR on the observed products. For the first step (hydrogen atom abstraction), the doublet and quartet transition states are similar in energy and geometry, and this leads to intermediates where a methyl radical is coordinated to the hydroxyl group of the ferryl-hydroxo species. However, in the second step, the doublet pathway is (approximately) concerted, leading to a short lifetime of the intermediate and consequently giving no rearrangement of products. In contrast, the quartet pathway must overcome a large energy barrier, giving the intermediate time to rearrange and leading to a mixture of products. Therefore, TSR is consistent with the anomalies in the product distribution highlighted earlier.

Very recently, Shaik and co-workers have shown that the kinetic isotope effect (KIE) can be used as a probe for TSR so it can be observed experimentally, as well as postulated and demonstrated theoretically. By comparing semi-classical values for kinetic isotope effects along with Wigner corrected values which indicate how much

tunnelling is occurring, they showed that comparing KIE_{HS} and KIE_{LS} can serve as a probe of the reactive spin state.[31]

1.5 Other Iron Containing Enzymes

Although porphyrin based oxidants have been most studied, it has become apparent in recent years that a heme based ligand environment is not an essential element of iron-containing metalloenzymes.

1.5.1 Bleomycin – an Example of a Mononuclear Non-Heme Iron Enzyme

Bleomycin (BLM) (Figure 1-8) is a glycopeptide antibiotic found in the fungus *Streptomyces verticillus*, and is used as a chemotherapeutic agent to treat a variety of cancers. It was first studied by Burger who noted its resemblance, in terms of reactivity, to the heme oxygenases.[32,33] In the presence of a reduced redox active metal (usually iron), O_2, and a source of electrons, it forms an active species, activated bleomycin (ABLM) that is able to cleave both single (ss) and double (ds) stranded DNA by H atom abstraction at the C4′ position of ribose. This is done selectively at certain DNA sequences: $^{5'}GC^{3'}$ and $^{5'}CT^{3'}$. BLM is also able to attack all types of RNA, cell walls and small organic molecules resulting in olefin epoxidation and aromatic ring hydroxylation. It is the ability to cleave ds DNA that gives BLM its cytotoxicity. BLM and a metal co-factor are also able to initiate DNA cleavage in the presence of hydroperoxo and superoxo oxygen species.

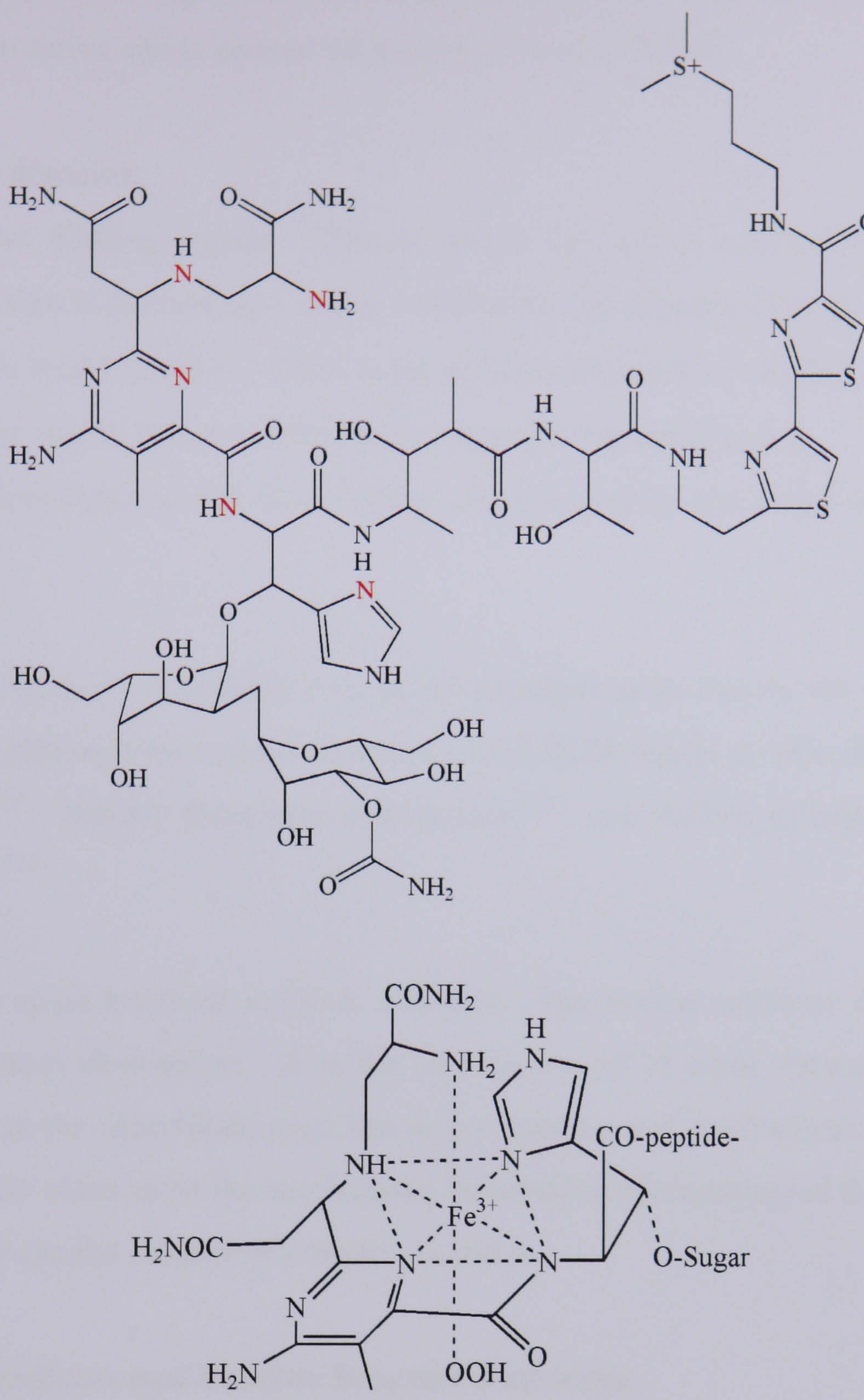

Figure 1-8 – (top) Structure of bleomycin[33] - atoms that coordinate to Fe are shown in red, and (bottom) iron coordination sphere in ABLM[34] {original in colour}

Following H-atom abstraction a radical is formed at the C4′ position of deoxyribose. This reacts with molecular oxygen to give a peroxyl radical that, upon addition of one electron, forms a peroxide intermediate which can then decompose to give a ketone and other products.

The activity of BLM is highest when the metal co-factor is Fe^{2+}, although bleomycins containing other metals, such as cobalt, are also known. The overall structure of

different bleomycins is largely conserved, differing only at the C-terminus; therefore the structure of the active site is conserved within a series of BLMs.

BLM has four domains:

- A metal binding region. This is where the active species that mediates H abstraction is formed, and is also responsible for strand selectivity.
- A DNA binding region. BLM binds to the minor groove of DNA.
- A linker region that connects the two regions discussed above.
- A carbohydrate moiety that enables cell recognition and helps regulate cellular uptake.

Bleomycin is believed to provide five or six nitrogen atom donors for coordination to the Fe centre although no crystal structure of Fe-BLM exists so this data is based on spectroscopy[35-37], density functional calculations[38,39] and studies of copper, cobalt and other metals.[40-46]

There are two steps involved in DNA cleavage. The first is substrate binding and the second is H atom abstraction. It is the mechanism of H atom abstraction that is of interest to us as the identification of the active species and mechanism responsible for this can provide clues as to the mechanism involved in the activity of the Fe-bispidone complexes that are the subject of Chapters 3 and 4.

1.5.1.1 Intermediates and Possible Reaction Pathways

Activated bleomycin (ABLM) is the last observed intermediate before DNA cleavage , and has been identified as a hexacoordinate low spin $Fe^{3+}OOH$ species by ES-MS[47], EPR[32] and X-ray absorption spectroscopy.[49] There has been some debate as to whether it is actually the species responsible for H atom abstraction, or whether it is a precursor to a more reactive species (c.f. CYP). Three possible pathways are proposed for the reaction of ABLM:

- The $Fe^{3+}OOH$ species directly abstracts a hydrogen atom, and the O-O bond is broken at the same time.

- O-O bond homolysis occurs to give $Fe^{4+}O$ and an OH radical which then reacts with DNA to abstract a hydrogen atom.
- O-O bond heterolysis occurs to give an oxoiron(V) species which then reacts with DNA.

Early studies of ABLM supported the idea (postulated by Burger[49]) that the active species responsible for C-H bond cleavage was $Fe^{5+}O$, largely because titrations with I^- showed that ABLM had two oxidising equivalents above Fe^{3+}. This was supported by a molecular mechanics study on the model complex, PMAH[50], (Figure 1-9) by Wu, who showed that there is a hydrogen bond between an N-H group on the PMAH (and therefore BLM) ligand and the HOO^- ligand coordinated to Fe^{3+} that facilitates O-O heterolytic cleavage. The presence of this N-H bond has since been shown not to be essential to the activity of the Fe-PMA species as a related complex with the N-H group replaced by an N-Methyl group shows the same activity.[51] However, the $Fe^{5+}O$ mechanism was not favoured by everyone, and Natrajan and co-workers showed that it did not give the expected products from the oxidation of 10-hydroperoxy-8,12-octadecadienoic acid (2-octenol), and therefore could not be the active species.[52]

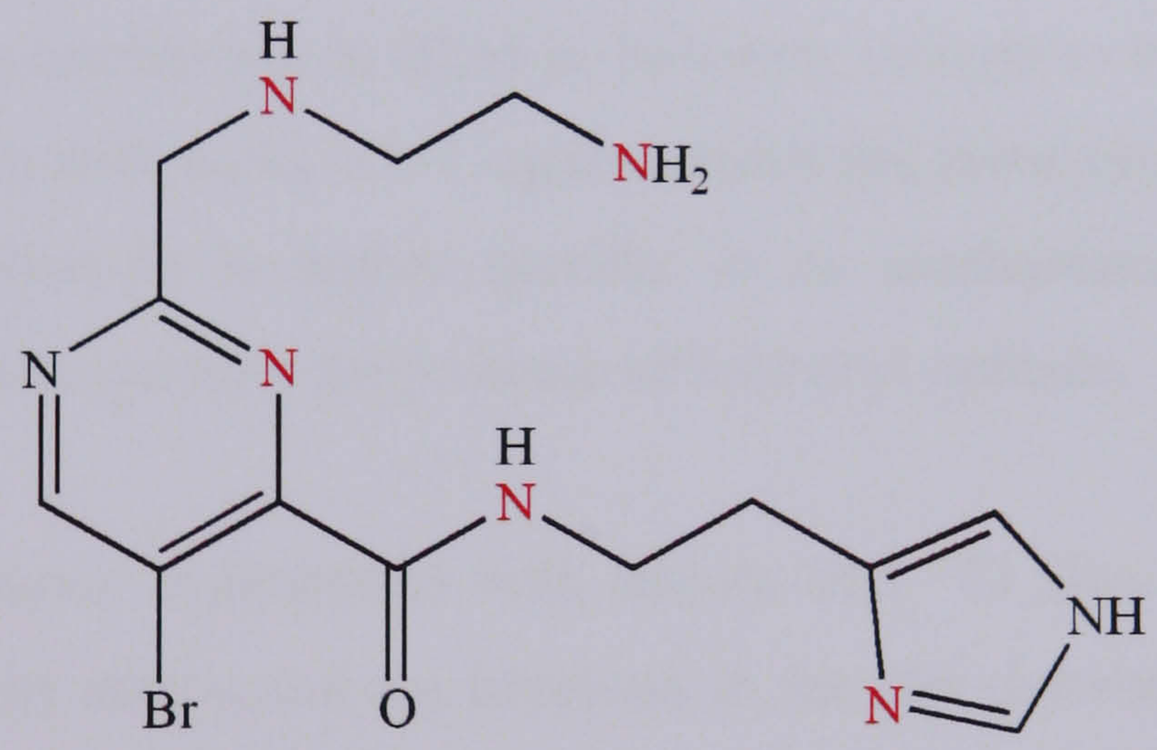

Figure 1-9 – PMAH ligand[50] (atoms that coordinate to Fe shown in red) {original in colour}

More recently the general consensus has become that O-O heterolysis is highly unlikely as the BLM ligand is unable to stabilise a Fe^{5+} oxidation state, and unlike CYP can not delocalise the charge around the ligand.[53-55] Theoretical calculations show that the formally Fe^{5+}BLM species actually corresponds to Fe^{4+} with the amide functionality of the ligand oxidised, and the radical centred on it rather than delocalised.[55] Energetically the heterolytic cleavage of the O-O bond has been calculated to be uphill in the region

of 80 kcal mol^{-1}. Therefore the literature has focussed on whether homolytic cleavage of the O-O bond occurs before H atom abstraction, or whether a concerted mechanism is in operation. These arguments and their conclusions are discussed below.

Evidence both in support of and against a mechanism involving O-O homolysis has been presented, in part by the study of model complexes. A study of the reactivity of $[Fe(N4Py)(OOH)]^{2+}$, which is a model for bleomycin, by Que and co-workers has shown that in the oxidation of cyclohexane a kinetic isotope effect (k_H/k_D) of 2 is observed. This is relatively small and implies an indiscriminate and highly reactive oxidant such as hydroxyl radicals. Oxidation of adamantane also shows selectivity for C3/C2 of approximately 3, consistent with what is observed for radical oxidations, and a much lower selectivity for the tertiary positions than that observed for 2 electron oxidants such as $Fe^{5+}O$.[56] Further investigation, such as the use of radical traps shows that the reactivity is not fully quenched and therefore another oxidant is also present. Therefore the authors conclude that the $[Fe(N4Py)(OOH)]^{2+}$ must react by homolytic cleavage of the O-O bond to give an OH radical and an oxoiron(IV) species, both of which act as oxidants.

The O-O homolysis mechanism in BLM is, however, thought to be unlikely as a strong kinetic isotope effect with k_H/k_D = 2-7 argues against the involvement of highly reactive OH radicals. Bleomycin is highly specific in its mechanism of action, and this observation is inconsistent with the presence of hydroxyl radicals.

Evidence from separate experiments with tritium and ^{18}O also show that both O-O cleavage and H atom abstraction are involved in the rate determining step. Together these results suggest that the direct mechanism is more likely.[53] The protonation of the $Fe^{3+}(OO)$ species lowers the energy of the σ* orbital of the peroxide group, activating it for electrophilic attack on the substrate.[57] Electron density is transferred from the σ orbital of a C-H group to the σ* orbital of the peroxo group weakening both the O-O and C-H bonds, and promoting H atom transfer. Therefore ABLM is already activated for H atom abstraction. DFT calculations indicate that this reaction is thermoneutral.

Thermodynamically, the direct mechanism is indistinguishable from the homolytic cleavage pathway, but the mechanism is different, leading to different kinetic properties.

DFT studies by Solomon and co-workers show that O-O homolysis has an energy barrier of 13 kcal mol^{-1} without any additional kinetic barrier along the reaction surface. The potential energy surface of the direct mechanism has been modelled using DFT and a transition state linking ABLM and deoxyribose to the products has been located with a change in energy of −7 kcal mol^{-1}. The transition state has a long O-O bond (2.73 Å) and a shorter C-H bond (1.17 Å) showing that the O-O bond is almost broken, but H atom transfer has not yet occurred.[53]

Although the DFT and experimental study by Solomon *et al.* is in favour of the direct mechanism, low spin $Fe^{3+}OOH$ complexes do have weak O-O and strong Fe-O bonds that make O-O homolysis conceivable.[53] For the DFT study the full bleomycin protein was not used, but the structure of the metal binding domain, with the pyrimidine, deprotonated amide and imidazole moieties was completely retained. The primary and secondary amines in the first coordination sphere were replaced with ammonias. Although this is a simplification of the real system it has been shown to only slightly affect the structure of BLM.[58]

1.5.1.2 Model Complexes and Relevance to Our Work

Model complexes have also provided insight in to the structure of the active site. These fall into two categories: Complexes with amidate based ligands such as PMAH and $PaPy_3$; and those with neutral N-donor ligands (such as N4Py and RTPEN discussed further in chapter 3). Mascharak *et al.* have synthesised a ligand, PMAH (Figure 1-9), that mimics the metal-binding domain of BLM, and when deprotonated, coordinated to Fe, and reacted with H_2O_2, it exhibits an EPR spectrum identical to ABLM.[59] The reaction of $[Fe(PMA)(OOH)]^+$ and cyclohexane in acetonitrile leads to a 1:1 mixture of alcohol and ketone, indicative of a Russell termination mechanism,[60,61] shown in Figure 8. This type of mechanism is commonly associated with the formation of alkyl radicals that react with dioxygen to give a peroxyl radical. Two of these species react together to release a molecule of O_2 and give one alcohol product, and one ketone. Dioxygen has been identified as the source of O atoms for oxidation in the presence of the bispidone catalysts discussed in chapters 3 and 4, and the distribution of products is also indicative of the Russell mechanism. For this reason, the reactivity of BLM may be able to provide insight in to the reactivity of the bispidone species.

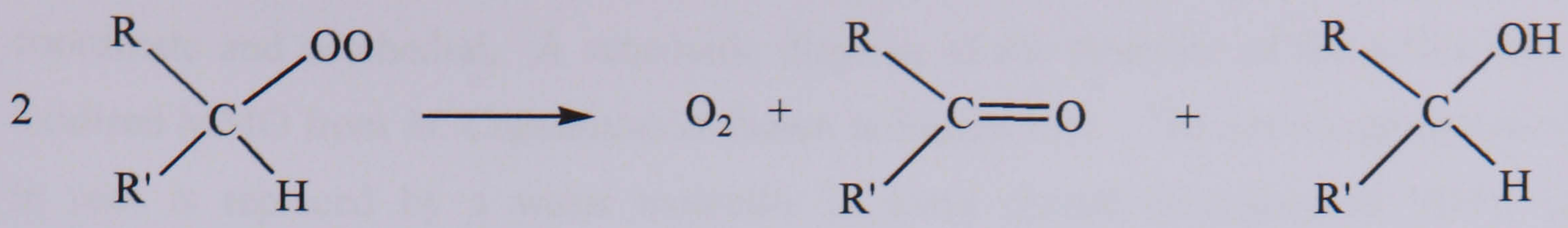

Figure 1-10 – Russell termination mechanism

1.5.2 Methane Monooxygenase – an Example of a Dinuclear Non-Heme Iron Enzyme

Attempts to oxidise methane to methanol by activation of the C-H bond is a commercially desirable reaction as the latter (and therefore also methane) can be used as a chemical feedstock. However, the C-H bond in methane is extremely unreactive and for this reason there has been much interest in enzymes that are able to effect its activation.[62] In particular, methane monooxygenase (MMO) has been studied as it is able to activate methane for oxidation – a reaction that even CYP can not catalyse.[63] MMO is found in two forms: particulate MMO (pMMO) contains a copper centre and is found bound to membranes in all methanotrophs[64,65] but it is not discussed here. Soluble MMO (sMMO) contains a diiron active site, reacts with dioxygen and methane to give methanol and is also able to effect the epoxidation of olefins. The remaining oxygen atom is converted to water.[9] sMMO is found in fewer methanotrophs than pMMO, and in addition to the oxidation of methane, it is also able to oxidise carbohydrates to alcohols, and eventually to CO_2. A great deal of investigation into the geometry of the active site and mechanism of sMMO has been done,[62,63,66-70] and selected examples of this are summarised here.

The MMO enzyme has three components: a reductase (MMOR), a protein coupling component (MMOB) that is responsible for electron transfer[71] and a hydroxylase component (MMOH) in which the active site containing the iron centres responsible for the oxygenase properties of the enzyme is found. Crystal structures of sMMO from two types of bacteria (*Methylococcus capsulatus* (Bath), and *Methylosinus trichosporium* (OB3b)) have been obtained for the reduced ($Fe^{2+}Fe^{2+}$) and oxidised ($Fe^{3+}Fe^{3+}$) forms of the enzyme and these have provided valuable insight into the mechanism and geometry of sMMO.[57,72-73]

Crystal structures of the hydroxylase components show that each iron centre is 6-coordinate and octahedral. A schematic diagram of the structure of the active site of oxidised MMO from *M. Capsulatus* is shown in Figure 1-11. The acetate group (shown in red) is replaced by a water molecule in some crystal structures of MMO (*M. Capsulatus*, oxidised form, −160°C, and *M. Trichosporium*, oxidised form, −18°C), or can be replaced by one of the glutamate acids bridging both Fe atoms (*M. Capsulatus*, reduced form, −160°C). The presence of many carboxylate ligands from the amino acids may play a role in stabilising high oxidation states on the iron atoms during the catalytic cycle, and one of the carboxylate ligands has also been shown to change from mono-dentate and bound to one iron centre, to bridging both the iron centres depending on the oxidation state of iron.[62]

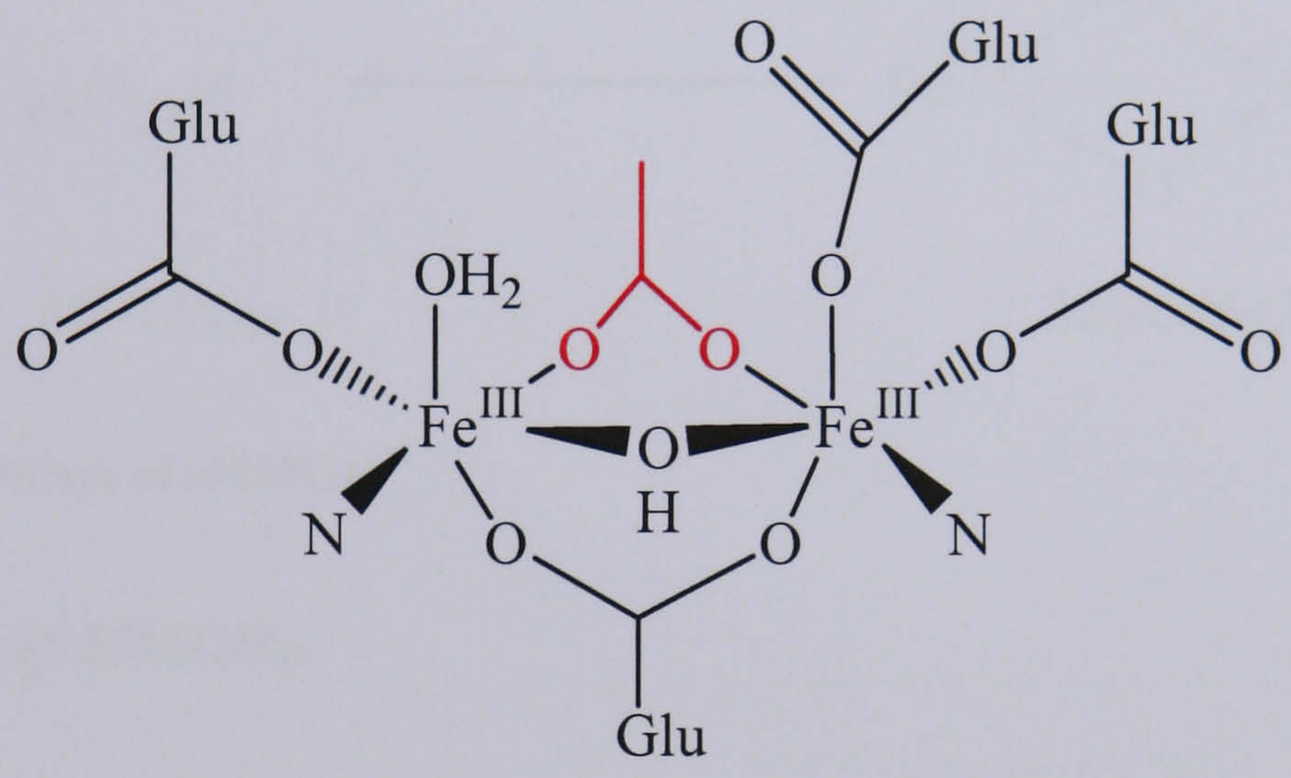

Figure 1-11 – Crystal structure of MMO (*Bath*)[74] at 4°C {original in colour}

1.5.2.1 Reaction Cycle

The generally accepted reaction cycle of MMO is shown in Figure 1-12. The reduced form of MMO (with both iron centres in the +2 oxidation state) rapidly reacts with O_2 to give an intermediate species, P, that has been identified by resonance Raman spectroscopy as a symmetrically bound $Fe^{3+}Fe^{3+}$ peroxide.[75] Mössbauer spectroscopy further identifies P as having a μ-η^1:η^1 or, more likely, a μ-η^2:η^2 structure. This decomposes to a species with a high valent diiron centre called intermediate Q, the species that is kinetically competent to oxidise methane to methanol. Intermediate Q has been studied by Mössbauer and EXAFS spectroscopy[63] and the experimental data has been interpreted as a diiron $Fe^{4+}Fe^{4+}$ *bis*(μ-oxo) "diamond core" with one short (1.77 Å) and one long (2.05 Å) Fe-O bond to each oxygen centre and an Fe-Fe distance

of 2.46 Å determined by EXAFS. The iron centres are high spin and anti-ferromagnetically coupled,[63,75] and EXAFS indicates that the iron centres are highly distorted with coordination numbers of no more than 5.[75]

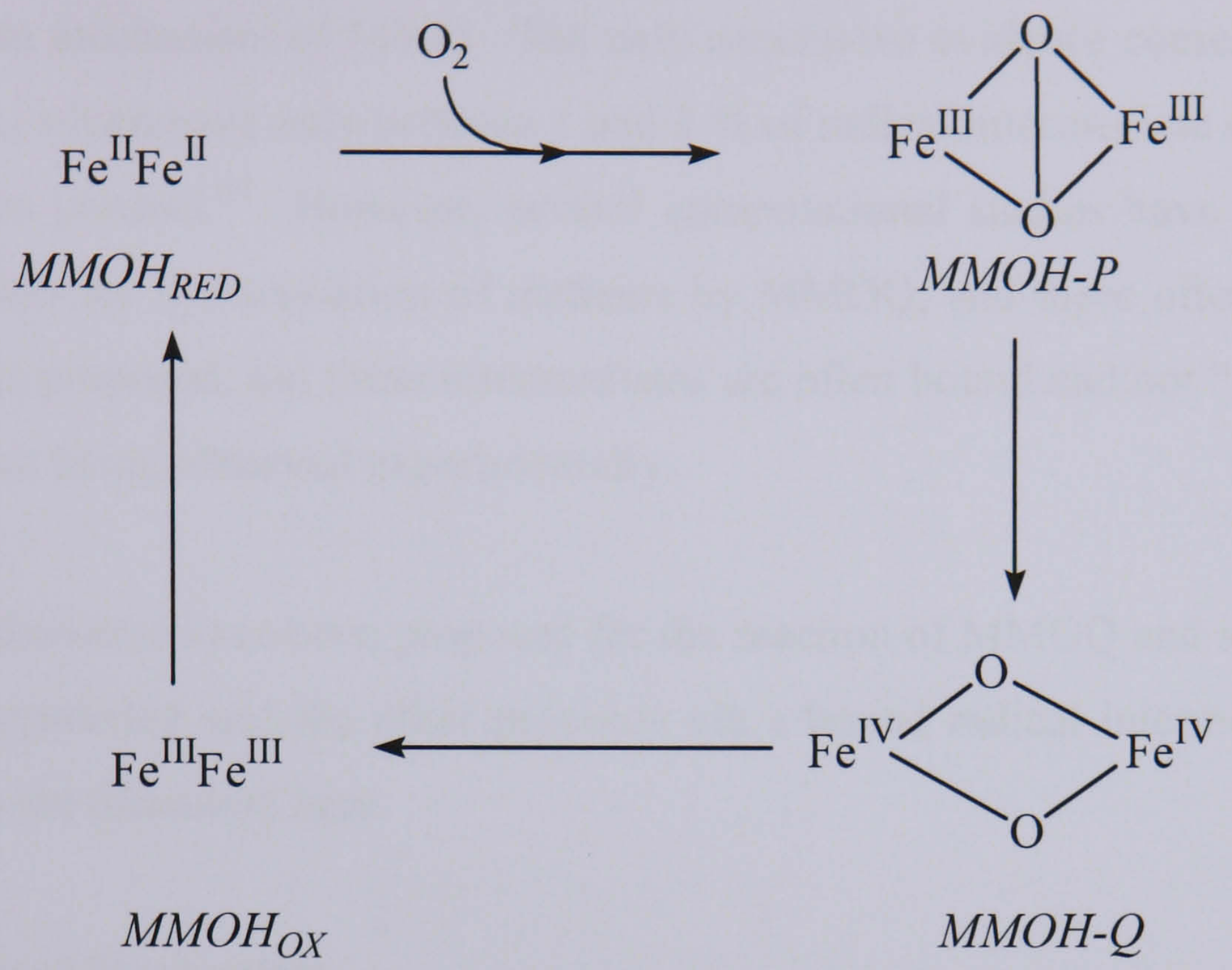

Figure 1-12 – Mechanism of sMMOH[34]

1.5.3 Reactivity of $MMOH_Q$

The mechanism of reaction of MMOH is clearly pertinent to our study of hydrogen peroxide activation. It has already been established that intermediate Q is responsible for the oxidation of methane but its structure has not been unequivocally determined, although it is known to contain a (μ-oxo)diiron(IV) core which has been the basis of many studies.[8,76-78] In addition to the experimental work that has been carried out, the structure of intermediate Q and the reaction mechanism by which methane (and other substrates) are oxidised have been studied using DFT.

There has been much discussion in the literature over the mechanism by which MMO effects hydroxylation. Some mechanistic probes indicate that a cationic, rather than radical, intermediate is present.[62,72] Oxidation of dimethylcyclopropane gives a product ratio that corresponds to an unrearranged product : cationic : radical ratio of 81:13:6.[80] Oxidation of methyl cubane also gives a radical derived product. Therefore there is little dispute that cationic intermediates exist in the reaction of MMO and alkyl

substrates, but there is not a consensus as to how this should be interpreted in terms of mechanism, and it is not considered further here.

There is scant evidence for the presence of a free radical intermediate in the hydroxylation mechanism of MMO. The only conclusive evidence comes from the use of norcarane, which gave only between 1 and 3 % of radical intermediate out of the total hydroxylation product.[62] However, several computational studies have been done on the mechanism for hydroxylation of methane by MMOQ, and these often have radical intermediates proposed, but these intermediates are often bound and not "free" resulting in radicals not being observed experimentally.

Several mechanisms have been proposed for the reaction of MMOQ and substrate. One of these is concerted and the other proceeds via a bound radical intermediate. These mechanisms are discussed here.

1.5.3.1 Radical Mechanism

Siegbahn has proposed a H abstraction mechanism that is shown in Figure 1-13.[63,80] Initially intermediate Q rearranges via intramolecular electron transfer to a new active species, Q′, that is 2.3 kcal mol^{-1} higher in energy. A linear C-H-O transition state then occurs for H abstraction, following which the methyl radical binds to a vacant coordination site on the active iron centre. The methyl and hydroxyl radicals then combine to release methanol. This mechanism is supported by DFT calculations that give good agreement with experiment for the free energy of activation from the bound starting complex.

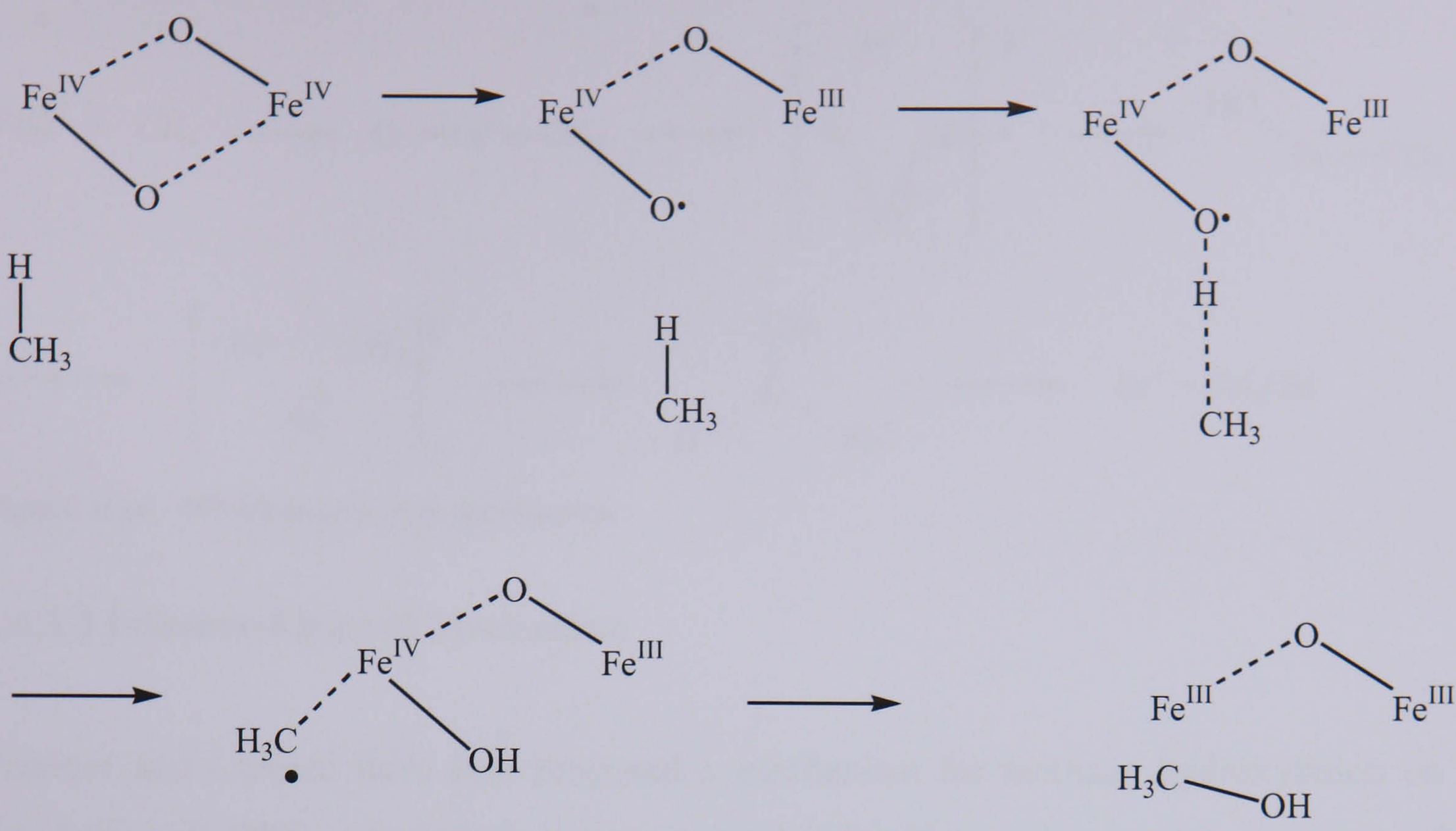

Figure 1-13 – Mechanism for MMO oxidation of methane proposed by Siegbahn – The majority of the ligands have been omitted for clarity

The mechanism occurs by sequential electron transfer from the σ orbital of the C-H bond, and the first electron transfer, which is proton coupled and corresponds to H atom transfer, is the rate determining step with the transition state 13.8 kcal mol^{-1} higher in energy than Q.[80]

1.5.3.2 Concerted Mechanism

An alternative mechanism has been proposed by Yoshizawa and co-workers.[66,81] Density functional calculations indicate that (assuming intermediate Q has a vacant coordination site on one Fe centre) a "non-synchronous concerted mechanism" occurs (Figure 1-14). In this mechanism, a four centre transition state is negotiated which leads to an intermediate where both a hydroxo group and a methyl group are coordinated to Fe. These then recombine via a second transition state to give the methane product. Only one iron centre is actually involved, and radical species are not formed. Furthermore, the authors show that this can occur on an open shell singlet surface using broken symmetry calculations, consistent with experimental data that shows that in intermediate Q the two iron centres are anti-ferromagnetically coupled.

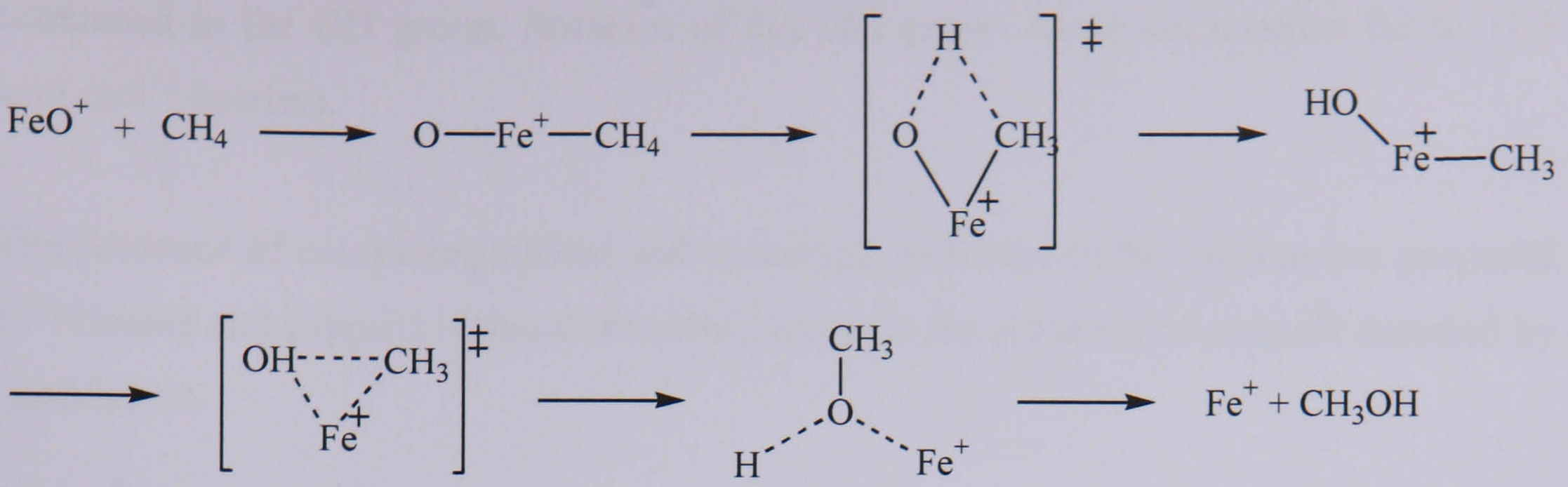

Figure 1-14 - MMO four centre mechanism

1.5.3.3 Friesner-Lippard Mechanism

Friesner and Lippard have also proposed a mechanism for methane hydroxylation on the basis of DFT calculations using a model based on the crystal structure of $MMOH_{Red}$.[82] Unlike Yoshizawa and Siegbahn, they have focussed on reproducing the structural features of MMO as well as locating a viable mechanism.[83]

The first step proposed is attack of the methane substrate on the bridging oxo moiety. This is a proton coupled electron transfer with an activation energy of 17.9 kcal mol^{-1}, and is identified as the rate determining step.[83] Molecular orbital analysis shows that this electron transfer is strongly coupled to structural distortion of the μ-oxo diiron core, and accompanied by transfer of an electron from the bridging oxo group to an iron centre. After the rate determining step the reaction pathway diverges and there are two potential mechanisms: one involving a bound radical, the other a non-synchronous concerted pathway.

In the bound radical mechanism, the first transition state leads to an intermediate in which the methyl radical is found with an O-H…C distance of 1.97 Å, so effectively the methyl radical is bound leading to only a small amount of inversion of configuration, as observed in studies of epoxidation of chiral ethane.[84] This intermediate then rearranges via rotation of the OH group and the C-O bond is formed by transfer of the second electron. From the intermediate this has a barrier of only 3.9 kcal mol^{-1}.

In the non-synchronous concerted mechanism an intermediate is located 8.3 kcal mol^{-1} higher in energy than the bound radical intermediate, where the methyl group is tightly

connected to the OH group. Rotation of this OH group, however, remains facile. (1.3 kcal mol^{-1} barrier).

The presence of competing radical and concerted pathways in the mechanism proposed by Friesner and Lippard is therefore consistent with the presence of radicals detected by experiment.

We have not exhausted all the possible mechanisms for MMO to oxygenate methane, nor have we considered all the studies. However, those we have described all have in common a bound radical species that then recombines to give methanol. Without the presence of the iron centres, the hydroxyl and methyl radicals would be free and able to damage the enzyme and lead to a lack of specificity of the product. Therefore MMO indicates how the metal centre can play a role in trapping radicals, hence preventing them from becoming "free". In the iron catalyst studied here, this is important because if it produces free radicals, their indiscriminate nature will make it unsuitable for its role as bleaching agent in a detergent. MMO teaches us that the presence of a metal centre can allow such species to be formed in an attenuated from, or prevent their formation altogether.

1.6 Concluding Remarks

The reaction mechanisms of some important iron enzymes have been summarised. From them we can take inspiration for the possible active species and mechanisms that are at play in the complexes studied here. As some of the discussion demonstrates, even after careful spectroscopic and experimental study supported by theoretical calculations the mechanisms of the different enzymes are not necessarily clear cut, and in many cases remain a topic of debate. In subsequent chapters, we attempt to shed light on the mechanism of oxidation catalysis by a specific class of iron complexes, the bispidones, that are currently being tested as potential bleaching catalysts.

1.7 References

1) H. Börzel, P. Comba, K. S. Hagen, Y. D. Lampeka, A. Lienke, G. Linti, M. Merz, H. Pritzkow, L. V. Tsymbal, *Inorg. Chim. Acta*, **2002**, *337*, 407
2) K. Wieghardt, U. Bossek, B. Nuber, J. Weiss, J. Bonvoisin, M. Corbella, S. E. Vitols, J. J. Girerd, *J. Am. Chem. Soc.*, **1988**, *110*, 7398
3) R. Hage, A. Lienke, *J. Mol. Catal. A*, **2006**, *251*, 150
4) R. Hage, A. Lienke, *Angew. Chem. Int. Ed.*, **2006**, *45*, 206-222
5) R. Hage, J. E. Iburg, J. Kerschner, J. H. Koek, E. L M. Lempers, R. J. Martens, U. S. Racherla, S. W. Russell, T. Swarthoff, M. R. P. van Vilet, J. B. Warnaar, L. van der Wolf, B. Krijnen, *Nature*, **1994**, *369*, 637-639
6) V. Guallar, B. F. Gherman, S. J. Lippard, R. A. Friesner, *Curr. Op. Chem. Biol.*, **2002**, *6*, 236
7) R. H. Holm, P. Kennepohl, E. I. Solomon, *Chem. Rev.*, **1996**, *96*, 2239
8) E. Y. Tshuva, S. J. Lippard, *Chem. Rev.*, **2004**, *104*, 987
9) L. Westerheide, M. Pascaly, B. Krebs, *Curr. Op. Chem. Biol.*, **2000**, *4*, 235
10) M. C. Feiters, A. E. Rowan, R. J. M. Nolte, *Chem. Soc. Rev.*, **2000**, *29*, 375
11) C. R. Goldsmith, R. T. Jonas, T. D. P. Stack, *J. Am. Chem. Soc.*, **2002**, *124*, 83
12) M. Costas, K. Chem, L. Que, *Coord. Chem. Rev.*, **2000**, *200*, 517
13) J. A. Labinger, J. E. Bercaw, *Nature*, **2002**, *417*, 507
14) M. Sono, M. P. Roach, E. D. Coulter, J. H. Dawson, *Chem. Rev.*, **1996**, *96*, 2841
15) Adapted from 'Biochemistry', 4th edition, L. Stryer, New York, W. H. Freeman and company, **1995**
16) F. Ogliaro, S. P. de Visser, S. Shaik, *J. Inorg. Biochem.*, **2002**, *91*, 554
17) J. H. Dawson, M. Sono, *Chem. Rev.*, **1987**, *87*, 1255
18) I. Schlichting, J. Berendzen, K. Chu, A. M. Stock, S. A. Maves, D. E. Benson, R. M. Sweet, D. Ringe, G. A. Petsko, S. G. Sligar, *Science*, **2000**, *287*, 1615
19) M. Newcomb, R. Zhang, R. E. P. Chandrasena, J. A. Halgrimson, J. H. Homer, T. M. Markis, S. G. Sligar, *J. Am. Chem. Soc.*, **2006**, *128*, 4580
20) D. L. Harris, G. H. Loew, *J. Am. Chem. Soc.*, **1998**, *120*, 8941
21) S. Shaik, S. Cohen, S. P. de Visser, P. K. Sharma, D. Kumar, S. Kozuch, F. Ogliaro, D. Danovich, *Eur. J. Inorg. Chem.*, **2004**, 207
22) S. P. de Visser, F. Ogliaro, P. K. Sharma, S. Shaik, *J. Am. Chem. Soc.*, **2002**, *124*, 11809

23) J. T. Groves, *J. Chem. Ed.*, **1985**, *62*, 928

24) V. W. Bowry, K. U. Ingold, *J. Am. Chem. Soc.*, **1991**, *113*, 5699

25) J. I. Manchester, J. P. Dinnocenzo, L. A. Higgins, J. P. Jones, *J. Am. Chem. Soc.*, **1997**, *119*, 5069

26) P. H. Toy, M. Newcomb, P. F. Hollenberg, *J. Am. Chem. Soc.*, **1998**, *120*, 7719

27) J, N. Harvey, R. Poli, K. M. Smith, *Coord. Chem. Rev.*, **2003**, *238*, 347

28) D. Schroder, S. Shaik, H. Schwarz, *Acc. Chem. Res.*, **2000**, *33*, 129

29) S. Shaik, S. P. de Visser, D. Kumar, *J. Biol. Inorg. Chem.*, **2004**, *9*, 661

30) F. Ogliaro, N. Harris, S. Cohen, M. Filatov, S. P. de Visser, S. Shaik, *J. Am. Chem. Soc.*, **2000**, *122*, 8977

31) C. S. Li, W. Wu, D. Kumar, S. Shaik, *J. Am. Chem. Soc.*, **2006**, *128*, 394

32) R. M. Burger, J. Peisach, S. B. Horwitz, *J. Biol. Inorg. Chem.*, **1981**, *256*, 1636

33) R. M. Burger, *Struct. Bond.*, **2000**, *97*, 287

34) S. V. Kryatov, E. V. Rybak-Akimova, *Chem. Rev.*, **2005**, *105*, 2175, and references therein.

35) G. Smolentsev, A. V. Soldatov, E. C. Wasinger, E. I. Solomon, *Inorg. Chem.*, **2004**, *43*, 1825

36) K. E. Loeb, J. M. Zaleski, C. D. Hass, S. M. Hecht, E. I. Solomon, *J. Am. Chem. Soc.*, **1998**, *120*, 1249

37) K. E. Loeb, J. M. Zaleski, T. E. Westre, R. J. Guajardo, P. K. Mascharak, B. Hedman, K. O. Hodgson, E. I. Solomon, *J. Am. Chem. Soc.*, **1995**, *117*, 4545

38) M. Freindorf, P. M. Kozlowski, *J. Phys. Chem. A*, **2001**, *105*, 7267

39) A. Karawajczyk, F. Buda, *J. Biol. Inorg. Chem.*, **2005**, *10*, 33

40) S. M. Lui, D. E. Vanderwall, W. Wu, X.-J. Tang, C. J. Turner, J. W. Kozarich, J. Stubbe, *J. Am. Chem. Soc.*, **1997**, *119*, 9603

41) F. Fedeles, M. Zimmer, *Inorg. Chem.*, **2001**, *40*, 1557

42) T. E. Lehmann, M. L. Serrano, L. Que, *Biochemistry*, **2000**, *39*, 3886

43) P. Fulmer, C. Zhao, W. Li, E. DeRose, W. E. Antholine, D. H. Petering, *Biochemistry*, **1997**, *36*, 4367

44) R. X. Xu, D. Nettesheim, J. D. Otvos, D. H. Petering, *Biochemistry*, **1994**, *33*, 907

45) M. Sugiyama, T. Kumagai, M. Hayashida, M. Maruyama, Y. Matoba, *J. Biol. Chem.*, **2002**, *277*, 2311

46) T. E. Lehmann, *J. Biol. Inorg. Chem.*, **2004**, *9*, 323

47) J. W. Sam, X. J. Tang, J. Peisach, *J. Am. Chem. Soc.*, **1994**, *116*, 5250

48) T. E. Westre, K. E. Leob, J. M. Zakeski, B. Hedman, K. O. Hodgson, E. I. Solomon, *J. Am. Chem. Soc.*, **1995**, *117*, 1309

49) R. M. Burger, J. S. Blanchard, S. B. Horwitz, J. Peisach, *J. Biol. Chem.*, **1985**, *260*, 5406

50) Y. D. We, K. N. Houk, J. S. Valentine, W. Nam, *Inorg. Chem.*, **1992**, *31*, 718

51) R. J. Guajardo, J. D. Tan, P. K. Mascharak, *Inorg. Chem.*, **1994**, *33*, 2838

52) A. Natrajan, S. M. Hecht, *J. Org. Chem.*, **1991**, *56*, 5239

53) A. Decker, M. S. Chow, J. N. Kemsley, N. Lehnert, E. I. Solomon, *J. Am. Chem. Soc.*, **2006**, *128*, 4719, and references therein

54) A. Decker, E. I. Solomon, *Curr. Op. Chem. Biol.*, **2005**, *9*, 152

55) F. Neese, J. M. Zaleski, K. L. Zaleski, E. I. Solomon, *J. Am. Chem. Soc.*, **2000**, *122*, 11703

56) G. Roelfes, M. Lubben, R. Hage, L. Que, *Chem. Eur. J.*, **2000**, *6*, 2152

57) N. Elango, R. Radhakrishnan, W. A. Froland, B. J. Wallar, C. A. Earhart, J. D. Lipscomb, D. H. Ohlendorf, *Protein Sci.*, **1997**, *6*, 556

58) N. Lehnert, R. Y. N. Ho, F. Neese, L. Que, E. I. Solomon, *J. Am. Chem. Soc.*, **2002**, *124*, 10810

59) C. Nguyen, R. J. Guajardo, P. K. Mascharak, *Inorg. Chem.*, **1996**, *35*, 6273

60) G. A. Russell, *J. Am. Chem. Soc.*, **1956**, *78*, 1047

61) G. A. Russell, *J. Am. Chem. Soc.*, **1957**, *79*, 3871

62) M-H. Baik, M. Newcomb, R. A. Friesner, S. J. Lippard, *Chem. Rev.*, **2003**, *103*, 2385

63) B. J. Waller, J. D. Lipscomb, *Chem. Rev.*, **1996**, *96*, 2625

64) J. C. Murrell, B. Gilbert, I. R. McDonals, *Arch. Microbiol.*, **2000**, *173*, 325

65) J. C. Murrell, *Biodegradation*, **1994**, *5*, 145

66) K. Yoshizawa, T. Yumara, *Chem. Eur. J.*, **2003**, *9*, 2347

67) E. C. Carson, S. J. lippard, *Inorg. Chem.*, **2006**, *45*, 837

68) T. Lovell, J. Li, L. Noodleman, *Inorg. Chem.*, **2001**, *40*, 5251

69) M. Merkx, D. A. Kopp, M. H. Sazinsky, J. L. Blazyk, J. Muller, S. J. Lippard, *Angew. Chem., Int. Ed.*, **2001**, *40*, 2782

70) L. Westerheide, M. Pascaly, B. Krebs, *Curr. Op. Chem. Biol.*, **2000**, *4*, 235

71) B. G. Fox, W. A. Froland, J. E. Dege, J. D. Lipscomb, *J. Biol. Chem.*, **1989**, *264*, 10023

72) S. Y. Choi, P. E. Eaton, D. A. Kopp, S. J. Lippard, M. Newcomb, R. N. Shen, *J. Am. Chem. Soc.*, **1999**, *121*, 12198

73) A. C. Rosenzweig, P. Nordlund, P. M. Takahara, C. A. Frederick, S J. Lippard, *Chem. Biol.*, **1995**, *2*, 409

74) K. E. Liu, A. M. Valentine, D. Qin, D. E. Edmonson, E. H. Appelmna, T. G. Spiro, S. J. Lippard, *J. Am. Chem. Soc.*, **1995**, *117*, 4997

75) L. Shu, J. C. Nesheim, K. Kauffmann, E. Münck, J. D. Lipscomb, L. Que., *Science*, **1997**, *275*, 515

76) A. Ghosh, F. T. de Oliveira, T. Yano, T. Nishioka, E. S. Beach, I. Kinoshita. E. Munck, A. D. Ryabov, C. P. Horwitz, T. J. Collins, *J. Am. Chem. Soc.*, **2005**, *127*, 2505

77) K. Yoshizawa, T. Ohta, T. Yamabe, *Bull. Chem. Soc. Japan*, **1998**, *71*, 1899

78) D. A. Kopp, S. J. Lippard, *Curr. Op. Chem. Biol.*, **2002**, *6*, 568

79) F. Ruzicka, D-S. Huang, M. I. Donnelly, P. A. Frey, *Biochemistry*, **1990**, *29*, 1696

80) P. E. M. Siegbahn, *J. Biol. Inorg. Chem.*, **2001**, *6*, 27

81) K. Yoshizawa, *Acc. Chem. Res.*, ASAP, published 14/04/2006

82) D. A. Whittington, S. J. Lippard, *J. Am. Chem. Soc.*, **2001**, *123*, 827

83) B. D. Dunietz, M. D. Beachy, Y. X. Cao, D. A Whittington, S. J. Lippard, R. A. Friesner, *J. Am. Chem. Soc.*, **2000**, *122*, 2828

84) A. M. Valentine, B. Wilkinson, K. E. Liu, S. Komar-Panicucci, N. D. Priestly, P. D. Williams, H. Morimoto, H. G. Floss, S. J. Lippard, *J. Am. Chem. Soc.*, **1997**, *119*, 1818

2 Theory Chapter

2.1 Introduction

This chapter aims to serve as an introduction to the theory on which the computational methods used in this thesis are based. It is not intended to give lengthy mathematical proofs and derivations of the methods used, but just to give a general introduction to them. A more comprehensive introduction to the mathematical concepts can be found in most quantum mechanical textbooks,[1] and there are several textbooks dedicated to density functional theory (DFT) that give more details of the methods used.[2,3]

2.2 General Concepts

2.2.1 The Schrödinger Equation

The Schrödinger equation is the foundation of all quantum chemistry.[1] The time dependent version is expressed in short form as:

$$i\hbar\frac{\partial\psi}{\partial t} = -\hat{H}\psi$$

where $\hat{H}$ is the Hamiltonian operator corresponding to the total energy of the system and ψ is the wavefunction. The Schrödinger equation is an eigenvalue equation which, when solved leads to a set of mutually orthogonal eigenfunctions, ψ_i, with corresponding eigenvalues, E. The ground state of the system is described by the eigenfunction that gives the lowest energy, and in addition to this it also gives all other possible information about the system.

ψ is a probability amplitude and has no direct physical meaning, but the Born interpretation states that *the probability that a particle will be found in the volume*

element $d\tau$ at the point $\mathbf{r}$ *is proportional to* $|\psi(\mathbf{r})|^2\, d\tau$. $|\psi(\mathbf{r})|^2$ is, therefore, a probability density.

2.2.2 The Time-independent Schrödinger Equation

The Schrödinger equation ~~has a~~ time-dependent form ~~which~~ can be separated into time and space components by a separation of variables method to give a time-independent form, and the derivation is not shown here. This is only possible when the potential energy is independent of time. The time-independent Schrödinger equation (in one dimension) takes the form:

$$\frac{-\hbar^2}{2m}\frac{d^2\psi}{dx^2} + V(x)\psi = E\psi$$

The Hamiltonian operator therefore has both a kinetic energy and a potential energy component. These can be further separated into the kinetic (T_e and T_n) and potential energy (V_{en}, V_{ee}, V_{nn}) operators for electrons and nuclei, which are described by position vectors r_i and R_A respectively. In a simple form this is:

$$\hat{H} = \hat{T}_e + \hat{T}_n + \hat{V}_{en} + \hat{V}_{ee} + \hat{V}_{nn}$$

Or, in a more analytic form, with the operators described:

$$H = -\sum_{i=1}^{N}\frac{1}{2}\nabla_i^2 - \sum_{A=1}^{M}\frac{1}{2M_A}\nabla_A^2 - \sum_{i=1}^{N}\sum_{A=[1}^{M}\frac{Z_A}{r_{iA}} + \sum_{i=1}^{N}\sum_{j>i}^{N}\frac{1}{r_{ij}} + \sum_{A=1}^{M}\sum_{B>A}^{M}\frac{Z_A Z_B}{R_{AB}}$$

Where: $r_{iA} = |\mathbf{r}_i - \mathbf{R}_A|$ (i.e. the distance between nucleus A and electron *i*. The term involving this describes the attraction between nuclei and electrons);

$r_{ij} = |\mathbf{r}_i - \mathbf{r}_j|$ (i.e. the distance between electron *i* and electron *j*. The term that involves this describes the electron-electron repulsion);

$R_{AB} = |\mathbf{R}_A - \mathbf{R}_B|$ (i.e. The distance between nucleus A and nucleus B. This term describes nuclei-nuclei repulsion which is constant for a given geometry)

M_A, Z_A are the mass and atomic number of nucleus A.

Therefore, there are pairs of attractive and repulsive terms in the Hamiltonian, and this means that the motion of one particle is dependent on the motion of *all* the other particles in the system. For this reason, it is impossible to solve the Schrödinger equation for systems with more than two particles.

analytically

What about H_2^+?

2.2.3 The Born-Oppenheimer Approximation

The Born-Oppenheimer approximation provides an important simplification of the Hamiltonian operator. It postulates that due to the greater mass of the nuclei than the electrons, they move much more slowly. The electrons are able to rapidly (almost instantaneously) adjust to the changing positions of the nuclei, but the nuclei are much slower to respond to a change in the distribution of electrons. As a result of this the motions of the nuclei and electrons can be considered separately, and the electronic Schrödinger equation can be solved while the positions of the nuclei are fixed. Different arrangements of the nuclei can be adopted and the solution of the electronic Schrödinger equation calculated again to give a potential energy surface. Therefore we can solve just the electronic Schrödinger equation, which describes the movement of electrons in a field of fixed nuclei:

$$\hat{H}_e \psi_e(\mathbf{r},\mathbf{R}) = E_e(\mathbf{R})\psi_e(\mathbf{r},\mathbf{R})$$

In the electronic Schrödinger equation the nucleus-nucleus repulsion can be ignored and only added as a classical term once the electronic Schrödinger equation has been solved. The kinetic energy of the nuclei is zero by definition, thus simplifying the Hamiltonian significantly. The Hamiltonian is now simplified to:

$$H = -\frac{1}{2}\sum_i^n \nabla^2 - \sum_i^n \sum_I^N \frac{Z_I}{r_{Ii}} + \frac{1}{2}\sum_{i,j}^n \frac{1}{r_{ij}}$$

2.2.4 The Variation Theorem

The variation theorem states that the expectation value for the energy of a system that is calculated with a trial wavefunction, ψ' can not be lower than the true energy of the system. Therefore minimising the energy by improving the trial wavefunction establishes an upper bound to the energy.

2.2.5 Representation of the Wavefunction

The wavefunction must satisfy a variety of conditions. These are:

- $\psi^*\psi$ must be single valued
- It must not be infinite over a finite range
- It must be continuous
- It must have a continuous gradient (first derivative)

According to the Pauli principle which states *the total wavefunction must be antisymmetric under the interchange of any pair of identical fermions, and symmetrical under the interchange of any pair of identical bosons*, the wavefunction must be antisymmetric with respect to the exchange of two electrons (which are fermions). An appropriate way of describing the wavefunctions is using a Slater determinant.

$$\psi(1,2,\ldots,N) = \left(\frac{1}{N!}\right)^{1/2} \begin{vmatrix} \phi_a(1) & \phi_b(1) & \ldots & \phi_z(1) \\ \phi_a(2) & \phi_b(2) & \ldots & \phi_z(2) \\ \vdots & \vdots & \ddots & \vdots \\ \phi_a(N) & \phi_b(N) & \ldots & \phi_z(N) \end{vmatrix}$$

ϕ_a, ϕ_b are the spin orbitals, and N is the number of electrons. In a molecule, each one electron wavefunction, ϕ_i corresponds to a molecular spin orbital.

2.3 The Hartree-Fock Approximation

The Hartree-Fock approximation uses a single Slater determinant composed of a set of spin orbitals to represent the wavefunction. The electron-electron repulsions are treated in an average way and each electron is considered to be moving in a mean field of the nuclei and the other n-1 electrons. This assumes that the wavefunctions for all the electrons other than the one being optimised are known, but this is not the case so initially a trial wavefunction is used for the HF orbitals. The variation theorem is then applied to optimise the orbitals, ϕ_i, so that the determinant (and the overall wavefunction) gives the lowest energy. By doing this, the *N*-particle problem is reduced to a set of one electron eigenvalue problems that are known as the Hartree-Fock equations:

$$\hat{f}_i \phi_i = \varepsilon_i \phi_i$$

The Fock operator, $\hat{f}_i$ is a one particle Hamiltonian, and it gives a corresponding energy, ε_i, which can be interpreted as the orbital energy.

The Fock operator is defined as:

$$\hat{f}_i = -\frac{1}{2}\nabla_i^2 - \sum_{A=1}^{M} \frac{Z_A}{r_{iA}} + \hat{V}_i^{HF}$$

The final term in the expression describes the average potential experienced by electron *i* due to the presence of other electrons. It is defined as

$$\hat{V}_i^{HF} = \sum_j \left\{ \hat{J}_i(j) - K_i(j) \right\}$$

where $\hat{J}_i(j)$ is the Coulomb operator which describes the Coulombic interaction of electron *i* with the other electrons for orbital ϕ_j, and is defined as:

$$J_u(1)\phi_i(1) = \left\{ \int \phi_u^*(2) \left(\frac{e^2}{4\pi\varepsilon_0 r_{12}} \right) \phi_u(2) dx_2 \right\} \phi_i(1)$$

$\hat{K}_i$ is the exchange operator, and represents the modification of the potential energy due to the effects of spin correlation. It is defined as:

$$K_u(1)\phi_i(1) = \left\{ \int \phi_u^*(2) \left(\frac{e^2}{4\pi\varepsilon_0 r_{12}} \right) \phi_i(2) dx_2 \right\} \phi_u(1)$$

Although Hartree-Fock theory treats the average Coulombic potential felt by electrons, it does not take in to account the explicit electron-electron interactions. The negation of these interactions allows electrons to get closer to one another than if they were taken into account. Clearly the treatment of electrons in HF theory is inadequate – this is the main deficiency of HF theory. The difference between the exact energy of a system and the HF energy is called the correlation energy:

$$E_{correlation} = E_{exact} - E_{HF} < 0$$

The inclusion of correlation leads to better calculated energies and geometries. For transition metals it is often essential to include it to simply get a qualitatively accurate representation of the system. Correlation can be divided into two categories: dynamic and static. Dynamic correlation takes into account instantaneous electron-electron interactions. Static correlation needs to be included when the use of a single determinant results in an inadequate representation of nearly degenerate conformations.

2.3.1 The Self Consistent Field

The self consistent field (SCF) method, introduced by Hartree and improved (to include the effects of electron exchange) by Fock and Slater is a way of finding the best atomic orbitals by the numeric solution of the Schrödinger equation.

To solve a Fock equation for one electron, the solutions to the Fock equation for the other $N-1$ electrons must be known. However, this is not the case so we have to start

with an approximate wavefunction (this is often in the form of a Slater determinant, discussed in section 2.3.2.1). Using the initial guess for the orbitals (from the approximate wavefunction), the average potential is calculated, and the HF equations are solved to give a set of orbitals. From these a new, improved potential is obtained, and the process of solving the HF equations is repeated. This iterative procedure is repeated until the solution to the HF equations that is obtained at the end of a cycle is the same as the solution to the equations that was used at the start of the cycle (i.e. that self consistency is achieved).

2.4 Density Functional Theory

Density functional theory (DFT) takes a different approach to solving the electronic structure problem than HF and the post-HF methods. Rather than calculating the wavefunction, which depends on $3N$ coordinates, the electron density, ρ, is used. This only depends on three coordinates (x,y,z) simplifying the calculation significantly. In addition, as electron density is used, electron correlation is already taken into account.

The principle behind DFT is that the energy of an electronic system is fully determined by the electron density, $\rho(\mathbf{r})$. Therefore the energy, E, is a functional of the density, $E[\rho]$, and for a given electron density there is a single corresponding energy.[4]

2.4.1 Historical Development of DFT

Early forerunners to DFT include the Thomas-Fermi model (1920s), and the Xα (Hartree-Fock-Slater) method (1950s). Both these methods employed the idea that the density could be used as a basis for the energy.

2.4.1.1 The Hohenberg and Kohn Theorems

In 1964, a formal proof was given by Hohenberg and Kohn that the ground state energy and all other ground state properties are uniquely determined by the electron density.[4] Simply put, they showed that there is a one to one mapping of electron density and

PAGE NUMBERING AS ORIGINAL

$$E_{XC} = \int \rho(\mathbf{r}) \varepsilon_{XC}[\rho(\mathbf{r})] \mathrm{d}\mathbf{r}$$

where $\varepsilon_{XC}[\rho(\mathbf{r})]$ is the exchange correlation energy per electron in a homogeneous gas of constant density. In systems with unpaired spins, there will be different densities for alpha and beta electrons, so the version of LDA that deals with these densities separately is called LSDA.

The advantage of using LDA is that the expressions for exchange and correlation energies are known to a high accuracy – in fact the expression for the exchange energy is known exactly for a uniform electron gas. However, no analytical expression for the correlation energy is known, but due to the approximations imposed by the use of Kohn-Sham orbitals an expression for it does need to be included.

The use of LDA functionals generally gives good result with respect to calculated geometries and vibrational frequencies, with a similar accuracy to Hartree-Fock theory. However, LDA typically gives large errors in the calculated energies as the exchange energy is significantly underestimated and the correlation energy is grossly overestimated (by up to 100%), leading to "overbinding" where the bonds are estimated to be too strong.

2.4.3 Gradient Corrected Methods

Gradient corrected methods (also known as non-local methods or the generalised gradient approximation, GGA) are the next step up from LDA, and consider a non-uniform electron gas. A term involving a dependence of the exchange and correlation energies on the gradient of the density, $\Delta\rho$, as well as on just the density, ρ, is added to the overall functional to account for the inhomogeneity in the electron density. However, as DFT is not constructed as a Taylor expansion (as HF theory is) there is no standard way of constructing this term. In addition, the nomenclature is also non-standard although it is often based on the authors initials and the year (e.g. PW91 was developed by Perdew and Wang in 1991).

Gradient corrected functionals are corrected specifically for either exchange or correlation, and can be used in combination so that both an exchange and correlation term are added to the LDA. The most popular exchange functional was developed by Becke in 1988 and is simply known as 'B'.[7] It has a single empirical parameter that has been optimised by fitting to the exchange energy of six noble gas atoms.

Gradient-corrected correlation functionals have also been developed. These include P86, developed by Perdew in 1986, which has one empirical parameter fitted for Neon.[8] This functional was modified by Perdew and Wang to give the PW91 functional.[9] The most popular correlation functional is the LYP (Lee, Yang Parr) functional. This contains four empirical parameters which are fitted to helium. In particular, this functional is well suited to the efficient handling of the self-interaction error.

In general, GGAs perform better than LDAs, especially for the calculation of geometries and vibrational frequencies. However, they are not as good at predicting accurate reaction barriers as they are at predicting ground state geometries, and different energies for electronic states.

2.4.4 Hybrid Methods

Using the 'adiabatic connection formula' it is possible to calculate the exact Hartree-Fock exchange energy for a system. This can be combined with a correlation functional into a DFT method to give improved results. However, simply replacing the exchange functional with the exact HF exchange does not lead to an improvement in results over GGA methods because there is less cancellation of errors in comparison to when both approximate exchange and correlation functionals are used.

Combining a small amount of exchange energy into a density functional by expressing the exchange energy as a combination of LDA, GGA and HF terms does lead to significant improvements. The first successful hybrid functional developed was the B3PW91 functional which was developed in 1993.[10] Since then the B3LYP functional, which is a modification of B3PW91 by Stevens *et al*[11] but uses the LYP functional for correlation energy rather than the PW91 term, has been developed and has become ubiquitous in the DFT calculations of complexes that include first row transition metals

due to its ability to accurately predict the most stable spin state of open shell systems.[12] This is not necessarily to say that it is the best functional for this and modification of the proportion of exact exchange can lead to improved results. The form of the B3LYP functional is shown below:

$$0.2E_{HF} + 0.8E_X^{Slater} + 0.72E_X^{B88} + 0.81E_C^{LYP} + 0.19E_C^{VWN}$$

2.5 Basis Sets

Molecular DFT programs often use basis functions to expand the Kohn-Sham orbitals. Therefore we present here a discussion of some of the key facts regarding basis functions and the choice of basis sets. Although in principle any type of basis function could be used (for example, plane wave), generally Slater and Gaussian type orbitals centred on the nuclei are used.

When choosing the type of basis set to use, there are some key criteria to consider. Basis functions should exhibit behaviour which agrees with the physics of the problem. E.g. the electron density should tend to zero as the distance from the nucleus is large. This helps the calculation converge more rapidly. In addition the functions used should make it easy to compute the required integrals.

Two commonly proposed functions are Slater type orbitals (STOs), which have the form:

$$\chi_{\zeta,n,l,m}(r,\theta,\varphi) = NY_{l,m}(\theta,\varphi)r^{n-1}e^{-\zeta.r}$$

and Gaussian type orbitals (GTOs) which (in spherical polar coordinates) have the form:

$$\chi_{\zeta,n,l,m}(r,\theta,\varphi) = NY_{n,m}(\theta,\varphi)r^{(2n-2-l)}e^{-\zeta.r^2}$$

STOs give a better representation of the wavefunction than GTOs as they show a cusp (discontinuous derivative) at the nucleus, and tend to zero at a large distance from the nucleus. GTOs, on the other hand, have a gradient of zero at the nucleus and taper off too quickly at large distances from the nucleus. Therefore more GTOs are needed to get the same accuracy as STOs. However, GTOs are computationally much easier to handle than STOs and this more than compensates for the extra basis sets required to get the same accuracy. Individual STOs do not have radial nodes, but these are formed by linear combinations of the orbitals.

GTOs can also be written in Cartesian coordinates, and take the form:

$$\chi_{\zeta,l_x,l_y,l_z}(x,y,z) = Nx^{l_x} y^{l_y} z^{l_z} e^{-\zeta . r^2}$$

The sum of l_x, l_y and l_z determines the type of orbital (0=s, 1=p, 2=d etc). One of the key differences between the Cartesian and polar form of GTOs is that Cartesian form leads to six d-orbitals (xz, yz, xy, x^2, y^2, z^2) which equate to five spherical d-functions and one s-function, whereas the polar coordinates give the five expected orbitals. Similarly the Cartesian form leads to ten functions for the f orbital – seven f-orbitals and three p-orbitals.

Generally, basis functions are located on the nuclei, but this is by no means obligatory – addition of extra functions located, for example, along a bond, also lead to an improved description of the electronic structure of a molecule. In this thesis, only GTOs centred on the nuclei have been used.

2.5.1 Types of Basis Set

Choosing a suitable basis set is important to get a reasonable description of the electronic structure, energy and geometry of a molecule. Ideally, a very large basis set would be used, but in reality this is not computationally feasible for any but the smallest molecules, and so approximate basis sets are used. However, choosing a basis set is not an arbitrary procedure, and if better basis functions are chosen then not as many are needed to get the same quality electronic description.

The smallest possible basis set that can be used is a 'minimum basis set' and has only enough basis functions to contain all the electrons of the neutral atom. This allows no flexibility of the molecular orbitals and does not provide a good description of the molecule. A double zeta basis set has twice the number of basis functions of the minimum basis set. This allows a more flexible description of the electronic structure of the molecule. Triple zeta basis sets have three times the number of basis functions of the minimum basis set, and therefore even more flexibility.

Despite the core orbitals contributing a great deal to the energy of a molecule due to their proximity to the nucleus, they are usually constant, unlike the valence orbitals which contribute less to the energy, but vary much more. Therefore a good description of the core orbitals is initially needed, but does not need to be reoptimised in every SCF cycle. For this reason it is economical to use a single set of contracted basis functions for the core orbitals, but have many primitive Gaussian functions in this cGTO, therefore giving a good, but inflexible description of the core orbitals, and only have a double (or higher order) zeta basis set for the valence orbitals. This is known as a split valence basis set, such as valence double zeta (VDZ) when a double zeta basis set is used for the valence electrons.

Inclusion of polarisation functions allows higher angular momentum to be included into orbitals so they can adapt better to the molecular environment. P-functions are added to s-orbitals, d-functions to p-orbitals, etc. Diffuse basis functions can also be included in basis sets. These have a smaller exponent allowing the orbital to extend out further, and are important in the treatment of anions, excited states and other situations where electrons are only loosely bound. Inclusion of these extra basis functions to help augment the shape of the orbital is important for the valence orbitals, where the interaction of other nuclei and orbitals perturbs the shape of orbitals. However, the core orbitals, although energetically very important, are much less influenced by the external environment of the atom, and do not change as much. For this reason split valence basis sets can be used. As they so are important energetically, a good description of them is required, particularly at the cusp, but rather than being completely variable they are made into a fixed linear combination. These are known as contracted GTOs, and the functions that contribute to them are known as primitive GTOs.

2.5.2 Effective Core Potentials

Using an 'all electron basis set', where all the orbitals including the core orbitals are modelled using basis functions, can be very computationally demanding, especially for heavy atoms and transition metals. An alternative to this is the use of an effective core potential (ECP) (or pseudopotential) to represent the core electrons. The core electrons are modelled by a suitable function and only the valence electrons are treated explicitly. ECPs generally give good results, although care must be taken to choose a core so that electrons that are potentially involved in chemical bonding are not included in the core. For example, the valence space in first row transition metals includes the nd, (n+1)s and (n+1)p orbitals. However, the np orbitals often contribute significantly to the bonding, and should be included as well.

2.5.3 Basis Set Superposition Error

Basis set superposition error (BSSE) arises when a complete basis set is not used (i.e almost all the time), and is most significant when there is a very incomplete basis set. The basis functions at one nucleus may be used to describe the electron density at another nucleus. In a different geometry, these basis functions will be less available to the second nucleus and so one complex may be artificially lowered in energy. This is particularly true for weak interactions such as van der Waals forces and hydrogen bonds, where the nuclei may be quite separated in weakly bound species, and close in the strongly bound species, and therefore stabilisation of such complexes should be treated with caution.

The degree of BSSE can be evaluated by doing a "counterpoise correction" calculation.[13.14] Consider a dimer, AB, for which we want to calculate the BSSE. First the energy of complexation must be known. As the geometry of the isolated monomers and of the monomeric species in the dimer may be different, we have denoted the geometry of the species within the dimer with a *. The basis sets associated with monomer A are denoted $_a$. and for B are denoted $_b$.

$$\Delta E_{Complexation} = E(AB)^*_{ab} - E(A)_a - E(B)_b$$

The amount of this complexation energy that is due to BSSE can be estimated by working out the counterpoise correction. The energies of the fragments A and B with their geometries within the dimer must be calculated and are called $E(A)^*_a$ and $E(B)^*_b$ respectively. The energies of these same fragments must also be calculated using the full basis set from the dimer and are called $E(A)^*_{ab}$ and $E(B)^*_{ab}$. To do this, one must use ghost atoms. For $E(A)^*_{ab}$, real nuclei and basis functions are used for fragment A, and ghost atoms with *no* nuclear charge or electrons, but *with* basis functions are included for fragment B. The opposite situation is used for $E(B)^*_{ab}$ The counterpoise correction energy is defined as:

$$\Delta E_{CP} = E(A)^*_{ab} + E(B)^*_{ab} - E(A)^*_a - E(B)^*_b$$

And the counterpoise corrected complexation energy is given as $\Delta E_{Complexation} - \Delta E_{CP}$.

2.6 Transition State Searches

Transition states are stationary points on a potential energy surface that have one imaginary frequency (one negative eigenvalue in the Hessian matrix), and are therefore a minimum in all but one direction. There are several approaches to locating such stationary points, and they fall into two general categories; one method based on using local information, and the other based on interpolating between two minima. These are described in turn and their advantages/disadvantages discussed.

2.6.1 Methods Based on Local Information

One approach to locating transition states is to use information about the energy and its derivatives at the current point. No information about the reactant or product geometries is known. In the simplest form, the gradient of the energy is minimised (as

transition states, being stationary points, have an energy gradient of zero). However, as all stationary points have an energy gradient of zero, minima or higher order saddle points may also be located. In addition (and this applies to all methods based on local information), even if a transition state is located it may not connect the desired minima.

More advanced methods based on local information utilise Newton-Raphson methods. If the Hessian matrix is known and there is only one negative eigenvector, the transition state can be located relatively easily by maximising the energy in its direction, and minimising it in all other directions.

2.6.2 Methods Based on Interpolation Between Two Minima

If the reactant and product geometries are known, the transition state can usually be assumed to lie within these two structures. Several methods which locate transition states based on this observation have been developed, the most simple of which is linear synchronous transit (LST).[15] A geometry vector is formed between the reactant and product, and the highest energy structure along this line is located. However, this method has several weaknesses: it assumes that all the variables change at the same rate along the reaction pathway, which is a poor approximation for systems with more than a few atoms and a non-rigid structure and therefore poor approximations to the transition state are often obtained.

If this method is applied, care must be taken to use a sensible coordinate system (this is also true for methods discussed below). For example, in the rearrangement of the linear molecule HCN to CNH, in Cartesian coordinates, this would involve changing the position of the hydrogen atom along one axis. However, this would lead to the hydrogen atom being moved through the carbon and nitrogen atoms (Figure 2-1). If internal coordinates were used, the C-N-H angle could be changed from 0° to 180°, and a more reasonable estimate of the transition state would be formed.

Using Cartesian coordinates:

Using internal coordinates:

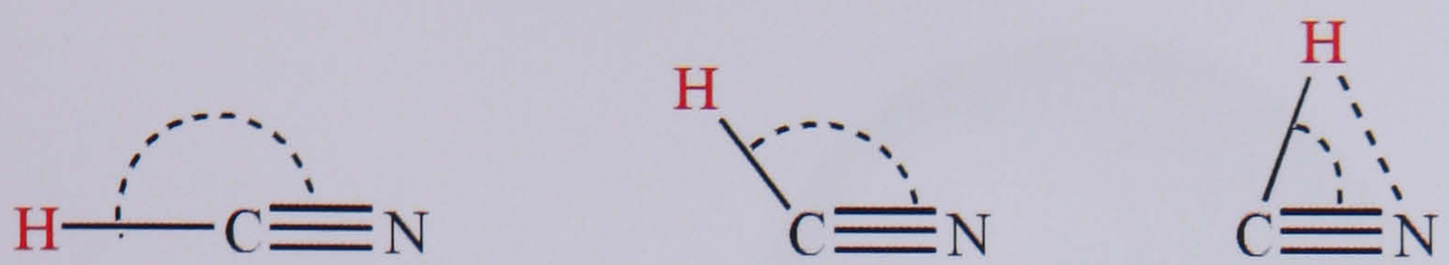

Figure 2-1 – Diagram showing how the choice of coordinates can influence a transition state search {original in colour}

A more sophisticated method to locate transition states is quadratic synchronous transit (QST). Again, a geometry vector between the reactant and product is formed, but instead of just locating a maximum along a straight line, a parabola is used. The energy is then maximised on the LST, and minimised in the directions perpendicular to this path. This method has been refined by Bell and Crighton[16] who perform the minimisation from the LST maximum in the directions conjugate to the LST rather than orthogonal to it.

A further development to the QST method uses a circle arc instead of a parabola for the interpolation, and the tangent to the circle for guiding the search towards the TS region.[17]. This is known as synchronous transit-guided quasi-newton (STQN), and switches to a quasi-Newton-Raphson method once the transition state region is located.

2.7 Modelling the External Environment – Inclusion of Solvent Effects

DFT (and other *ab initio methods*) calculate in the gas phase at 0 K. This is quite different to the environment in which the vast majority of experiments are conducted, and although DFT calculations generally give a reasonable qualitative description of the system studied, sometimes one may want to consider the effect of certain experimental conditions, for example, inclusion of solvent effects.

A common method used for modelling solvent effects is the "self consistent reaction field" (SCRF). This considers the solvent as a long range polarisable medium with a dielectric constant, ε, with a solute, M, placed in a suitable shaped cavity in the medium, as shown in Figure 2-2.[18]

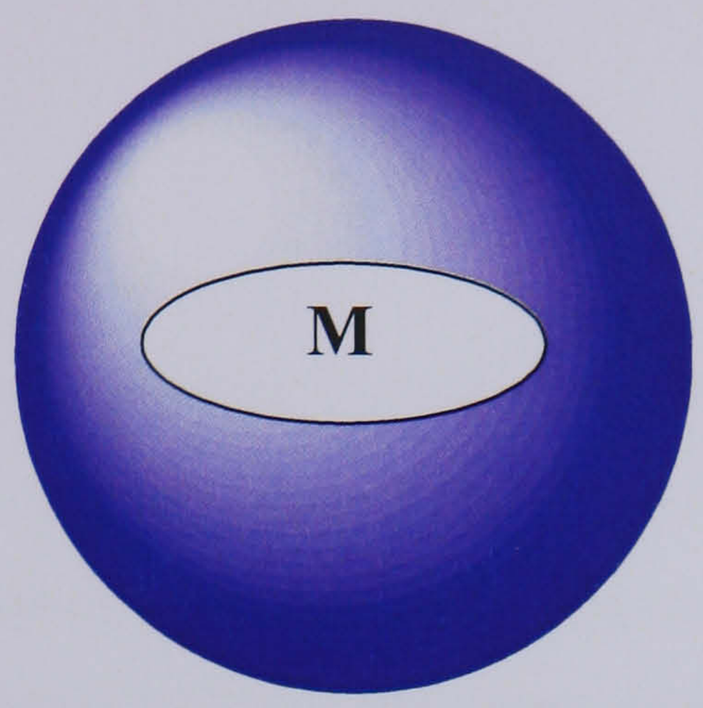

Figure 2-2 – Reaction field model {original in colour}

There are several things that contribute to the solvation energy. Creation of a cavity within the solvent is destabilising. However, there is an energy gain from the dispersion energy between the solvent and the solute. In addition the electronic charge distribution of the solute polarises the medium and leads to an electrostatic stabilisation of the solute by the solvent. Thus the free energy of solvation may be written as:

$$\Delta G_{Solvation} = \Delta G_{cavity} + \Delta G_{dispersion} + \Delta G_{electrostatic}$$

Reaction field models differ in several ways:

- How the size and shape of the cavity if defined.
- How the dispersion contributions are calculated.
- How the charge distribution of the solute is represented.
- How the solute is described.
- How the dielectric medium is described.

The simplest cavity is a sphere but more sophisticated models use a series of interconnecting spheres for the heavy atoms to give a molecular shaped cavity. Unless specifically requested, hydrogen atoms are not usually represented explicitly but incorporated into the heavier atoms.

Where solvent corrections have been used in this thesis, the conductor-like polarisable continuum model (CPCM)[18,19] has been used with a dielectric constant of 78.4 (which corresponds to water) for outside the cavity.

2.8 Software

Throughout this thesis the Gaussian suite of programs were used. Chapters 3 and 4 use Gaussian03 (revision C.01)[20], and chapters 4 and 5 use Gaussian98 (revision A.11).[21] Specific details about the methodology used are given in each chapter. The location of minimum energy crossing points (MECPs) was done using the code of Harvey and co-workers.[22]

2.9 References

1) P. W. Atkins R. S. Friedman, Molecular Quantum Mechanics, 3rd Ed., Oxford University Press, **1997**

2) F. Jensen, Introduction to Computational Chemistry, John Wiley & sons, **1999**

3) W. Koch, M. C. Holthausen, A Chemists Guide to DFT, 2nd Ed., Wiley-VCH, **2001**

4) P. Hohenberg, W. Kohn, *Phys. Rev.*, **1964**, *B136*, 864

5) M. Levy, *Proc. Natl. Acad. Sci. USA*, **1979**, *76*, 6062

6) W. Kohn, L. J. Sham, *Phys. Rev.*, **1965**, *A140*, 1133

7) A. D. Becke, *Phys. Rev. A.*, **1988**, *38*, 3098

8) J. P. Perdew, *Phys. Rev. B.*, **1986**, *33*, 3098

9) J. P. Perdew, Y. Wang, *Phys. Rev. B.*, **1992**, *45*, 13244

10) A. D. Becke, *J. Chem. Phys.*, **1993**, *98*, 5648

11) P. J. Stevens, J. F. Devlin, C. F. Chabalowski, M. J. Frisch, *J. Phys. Chem.*, **1994**, *98*, 11623

12) M. Swart, A. R. Groenhof, A. W. Ehlers, K. Lammertsma, *J. Phys. Chem. A.*, **2004**, *108*, 5479

13) F. B. van Duijneveldt, J. G. C. M. van Duijneveldt-van de Rijdt, J. H. van Lenthe, *Chem. Rev.*, **1994**, *94*, 1973

14) S. F. Boys, F. Bernardi, *Mol. Phys.*, **1970**, *19*, 553

15) T. A. Halgren, W. N. Lipscomb, *Chem. Phys. Lett.*, **1977**, *49*, 225

16) S. Bell, J. S. Crighton, *J. Chem. Phys.*, **1984**, *80*, 2464

17) C. Peng, H. B. Schlegel, *Isr. J. Chem.*, **1993**, *33*, 449

18) J. Thomasi, M. Persico, *Chem. Rev.*, **1994**, *94*, 2027

19) M. Cossi, N. Rega, G. Scalmani, V. Barone, *J. Comp. Chem.*, **2003**, *24*, 669

20) Gaussian 03, Revision C.01, M. J. Frisch, G. W. Trucks, H. B. Schlegel, G. E. Scuseria, M. A. Robb, J. R. Cheeseman, J. A. Montgomery, Jr., T. Vreven, K. N. Kudin, J. C. Burant, J. M. Millam, S. S. Iyengar, J. Tomasi, V. Barone, B. Mennucci, M. Cossi, G. Scalmani, N. Rega, G. A. Petersson, H. Nakatsuji, M. Hada, M. Ehara, K. Toyota, R. Fukuda, J. Hasegawa, M. Ishida, T. Nakajima, Y. Honda, O. Kitao, H. Nakai, M. Klene, X. Li, J. E. Knox, H. P. Hratchian, J. B. Cross, C. Adamo, J. Jaramillo, R. Gomperts, R. E. Stratmann, O. Yazyev, A. J. Austin, R. Cammi, C. Pomelli, J. W. Ochterski, P. Y. Ayala, K. Morokuma, G. A. Voth, P. Salvador, J. J. Dannenberg, V. G. Zakrzewski, S. Dapprich, A. D. Daniels, M. C. Strain, O. Farkas, D. K. Malick, A. D. Rabuck, K. Raghavachari, J. B. Foresman, J. V. Ortiz, Q. Cui, A. G. Baboul, S. Clifford, J. Cioslowski, B. B. Stefanov, G. Liu, A. Liashenko, P. Piskorz, I. Komaromi, R. L. Martin, D. J. Fox, T. Keith, M. A. Al-Laham, C. Y. Peng, A. Nanayakkara, M. Challacombe, P. M. W. Gill, B. Johnson, W. Chen, M. W. Wong, C. Gonzalez, J. A. Pople, Gaussian, Inc., Pittsburgh PA, **2003**

21) Gaussian 98, Revision A.11, M. J. Frisch, G. W. Trucks, H. B. Schlegel, G. E. Scuseria, M. A. Robb, J. R. Cheeseman, V. G. Zakrzewski, J. A. Montgomery. Jr., R. E. Stratmann, J. C. Burant, S. Dapprich, J. M. Millam, A. D. Daniels, K. N. Kudin, M. C. Strain, O. Farkas, J. Tomasi, V. Barone, M. Cossi, R. Cammi, B. Mennucci, C. Pomelli, C. Adamo, S. Clifford, J. Ochterski, G. A. Petersson, P. Y. Ayala, Q. Cui, K. Morokuma, P. Salvador, J. J. Dannenberg, D. K. Malick, A. D. Rabuck, K. Raghavachari, J. B. Foresman, J. Cioslowski, J. V. Ortiz, A. G. Baboul, B. B. Stefanov, G. Liu, A. Liashenko, P. Piskorz, I. Komaromi, R. Gomperts, R. L. Martin, D. J. Fox, T. Keith, M. A. Al-Laham, C. Y. Peng, A. Nanayakkara, M. Challacombe, P. M. W. Gill, B. Johnson, W. Chen, M. W. Wong, J. L. Andres, C. Gonzalez, M. Head-Gordon, E. S. Replogle, J. A. Pople, Gaussian Inc. Pittsburgh PA, USA

22) J. N. Harvey, M. Aschi, H. Schwarz, W. Koch, *Theor. Chim. Acc.*, **1998**, *99*, 95

Chapter 3 – Formation of an Oxoiron(IV) Intermediate

3.1 Introduction to Bispidone Complexes

The nitrogen-donor ligands known as bispidones, based on the structure shown in Figure 3-1 form a variety of complexes with transition metals. The rigid backbone shows very little structural variation in its metal complexes.[1] In particular, the N3-N7 distance is constant regardless of the identity of the metal ion.[2] However, despite the rigidity of the ligand, the coordination site of the metal is fairly elastic with a soft potential energy surface (PES) as the metal can move out of the plane of the equatorial nitrogen atoms, and consequently vary the M-N bond lengths.

A number of metal bispidone complexes have recently been shown to be effective catalysts for oxidation processes (including bleaching) in the presence of peroxides and/or O_2. It is possible that this catalytic efficiency is in some part due to the restrained coordination geometries that can stabilise unusual electronic states of transition metal ions.

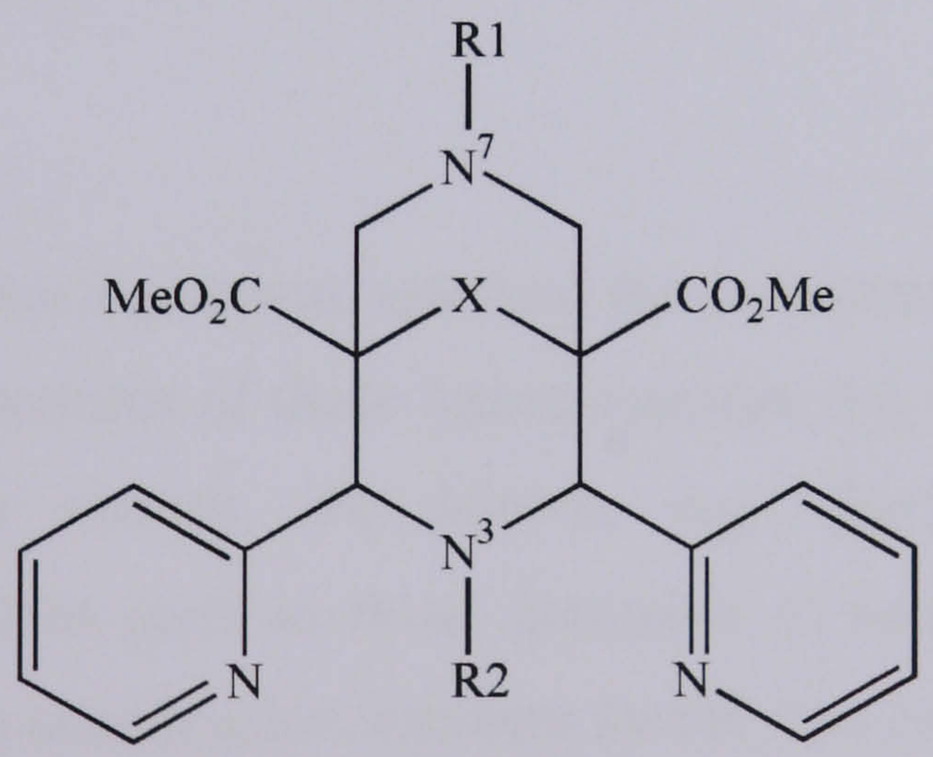

Figure 3-1 – Structure of the backbone of bispidone ligands discussed in this thesis (X = C=O or $C(OH)_2$)

3.2 Other Fe-N Based Complexes that Catalyse Oxidation of Organic Species by O_2 or H_2O_2

The iron bispidone complexes are only one member of the general class of non-heme iron species that are known to catalyse the oxidation of hydrocarbons in the presence of O_2 or H_2O_2. Complexes of both tetra- and pentadentate ligands are suited to this type of catalysis,[3] most notably the iron complexes of the tris(pyridylmethyl)amine (TPA) and *N,N*-bis(2-pyridylmethyl)-*N*-bis(2-pyridyl)-methylamine (N4Py) ligands reported by Que and co-workers, and discussed in more detail below.[4-14] A summary of the various iron-based oxidation catalysts that have been reported in the literature are presented here along with a discussion of their reactivity and the possible active species that have been proposed. All the species discussed share one common feature: they have polydentate nitrogen donor ligands that are able to enforce the coordination geometry around the iron centre. The non-heme iron complexes discussed here broadly fall into two categories: those with a tetradentate ligand with the two vacant coordination sites *cis* to one another (such as TPA) and those with a pentadentate ligand (such as N4Py), and only one vacant coordination site. It is worth emphasising at this early stage that the mechanisms by which complexes in these two categories react may be completely different as a consequence of the different number of labile sites for ligand binding to the metal.[15]

Although we have, in this discussion, assumed the iron centres to be hexacoordinate in line with the crystal structures of these ligand systems, this is not necessarily the case. Heptacoordinated iron centres are known, e.g. $[Fe(EDTA)(H_2O)]^-$,[16] as are pentacoordinate complexes such as those discussed in section 3.2.3. Therefore, we cannot exclude different coordination numbers for the iron centre, but in this thesis have generally assumed the iron centre to have a coordination number of six.

3.2.1 Tetradentate Ligands

The TPA ligand (Figure 3-2) has three pyridine and one amine nitrogen donor atoms, and these occupy four coordination sites of an octahedral geometry leaving two *cis* vacant sites (Figure 3-3). Fe^{3+} complexes of this ligand, in the presence of

hydroperoxide ligands, are able to oxidise alkanes and have been studied under a variety of conditions.

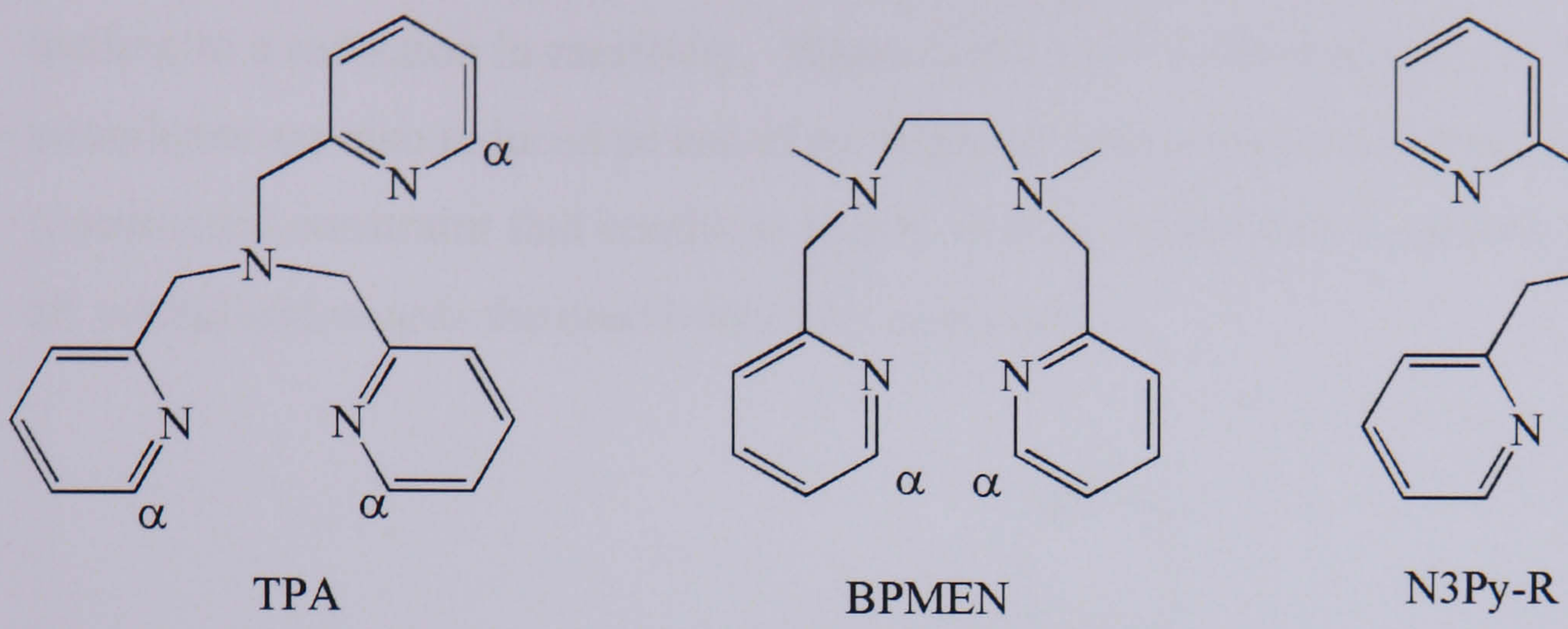

TPA BPMEN N3Py-R

Figure 3-2 – Tetradentate ligands with nitrogen donor atoms

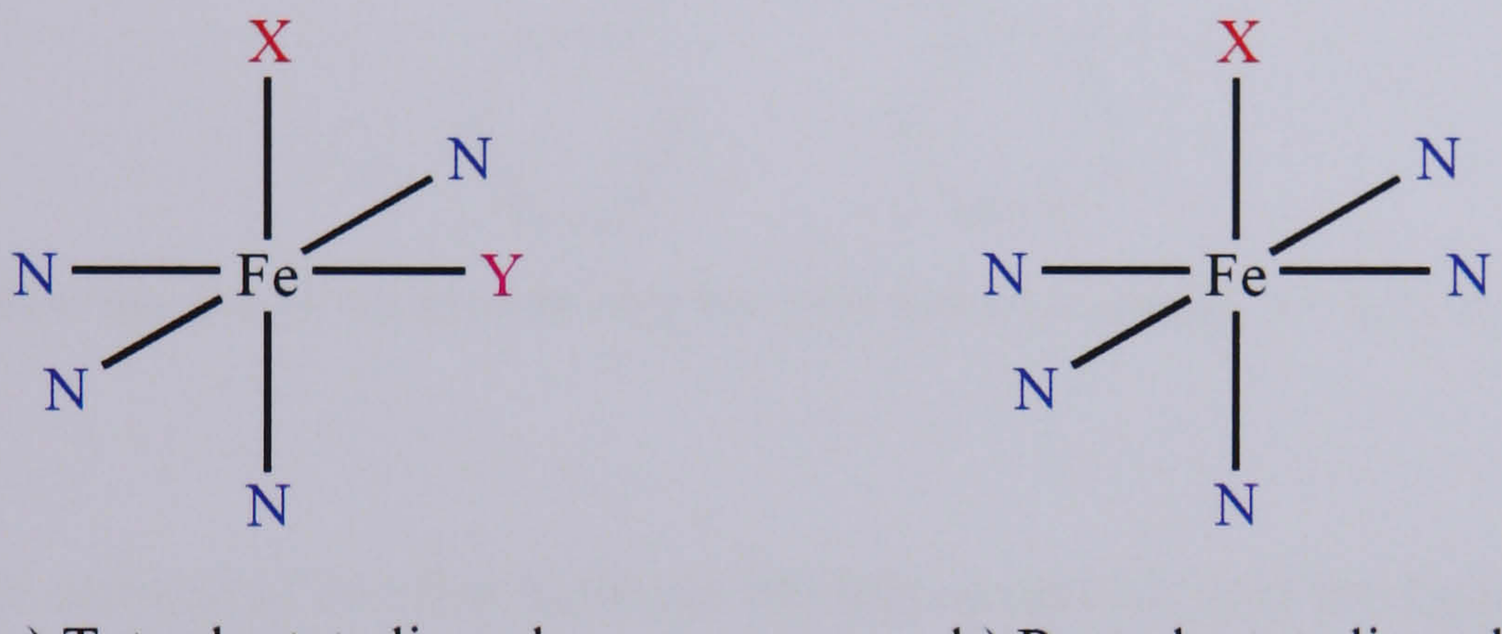

a) Tetradentate ligands b) Pentadentate ligands

Figure 3-3 – General coordination sphere of the tetra- and pentadentate ligands {original in colour}

The general structure of the TPA ligand has been modified by adding substituents to the pyridine rings. Of particular interest are the compounds where the hydrogen in the position α to the nitrogen atom is substituted by a methyl group (6-Me-TPA, 6-Me_2-TPA or 6-Me_3-TPA depending on the number of pyridine rings carrying a methyl substituent). The methyl groups are sterically bulky and so tend to elongate the Fe-N bonds, leading to a stronger preference for the Fe complex to be high spin in the more heavily substituted complexes. However, even with only one methyl group, the Fe^{2+} is high spin. This has allowed the effect of spin state on the reactivity of the complex to be studied as well as the effect of the ligand backbone.[17]

Further modifications have been made to the TPA ligand backbone, and their effect on the catechol cleaving ability of the Fe^{3+} complexes with O_2 in methanol solution has been studied. These include changing the size of the chelate ring by altering the length

of the alkyl chain connecting the tertiary amine to the pyridine rings[18] (Figure 3-4). This study showed that the TPA ligand (l=m=n=1) is the most reactive. Where l=1, m=0 and n=0 or 1, a low concentration of the monomeric Fe^{3+} complexes was observed, leading to a reduction in reactivity. Where l, m or n > 1, the reactivity of the catecholate complexes are also reduced as use of an ethylene, rather than methylene, spacer imposes a geometric constraint that results in poorer overlap of the iron d-orbitals and the ligand π^* orbital and retards the reactivity of the complex.

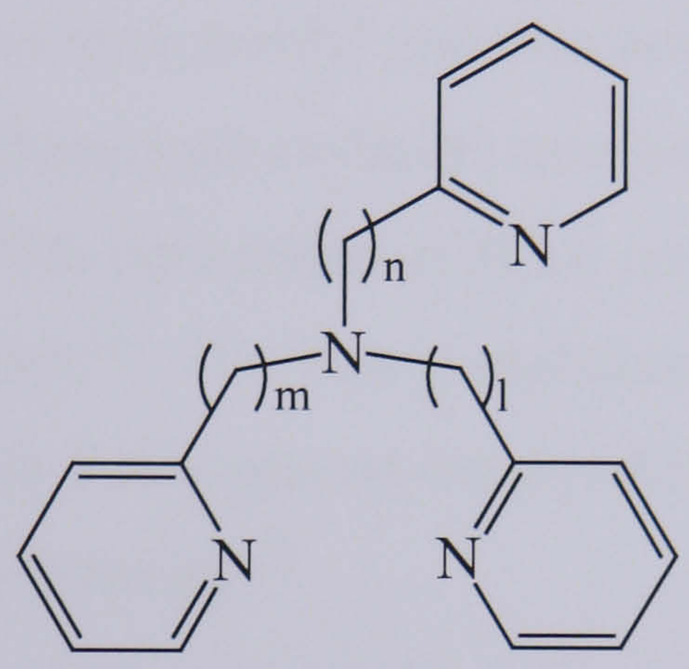

Figure 3-4 – How the size of the chelate ring for TPA can be changed. l = 0, 1, 2; m = 0, 1, 2; n = 0, 1, 2

Changing the amount of overlap between the iron d-orbitals and the ligand π^* orbitals is believed to affect the oxidative ability of the Fe^{3+} complexes. For this reason, Britovsek has investigated the effect of replacing the pyridine groups on the TPA ligand by tertiary amine groups on the oxidation of cyclohexane by H_2O_2 in acetonitrile solution. Substitution of one pyridylmethyl group in TPA by a dimethylaminoethyl group, with the two remaining coordination sites occupied by triflate anions, leads to exchange between the triflate groups indicating an equilibrium between a pentadentate and hexadentate species. Furthermore, this substitution also leads to the iron complex being high spin despite the lack of steric hindrance that occurs in the 6-Me_n-TPA species.[16] When all three pyridylmethyl groups are replaced by dimethylaminoethyl groups, the ^{19}F NMR spectrum in CH_2Cl_2 indicates that there is one coordinated triflate group, and one free in solution that do not exchange, and therefore the iron centre is pentacoordinate.

The oxidation of cyclohexane by the Fe-TPA based complexes is more efficient when there are more pyridine rings present, resulting in both a higher amount of H_2O_2

incorporation into the cyclohexane oxidation products, and a higher alcohol : ketone ratio indicating that free alkyl radicals are formed more readily when more methyl pyridyl groups are replaced by dimethylaminoethyl groups. The exception to this is the BPMEN ligand, discussed below, which has a slightly different ligand architecture to the TPA ligands, and the Fe^{3+} complex of which is the most effective oxidation catalyst of this general type known to date.[16]

A second, closely related ligand, *N,N'*-bis(2-pyridylmethyl)ethylene-1,2-diamine (BPMEN) (Figure 3-2) features two pyridyl and two amine donor atoms, and the iron complex is a more effective alkane hydroxylation catalyst than the TPA analogue under similar conditions, effecting 70% conversion of H_2O_2 into the products, compared with only 40% for the TPA analogue.[19] The iron complexes are again low spin unless the pyridine ring is substituted α to a nitrogen on the pyridine rings, when steric hindrance forces the high spin state to be favoured.[20]

The nature of the monodentate ligands occupying the two vacant coordination sites in the Fe-TPA and Fe-BPMEN complexes has a significant effect on reactivity. The reactivity of complexes (High catalytic efficiency (40-70% H_2O_2 converted to product), high alcohol : ketone ratios,[3,22-24] and a high kinetic isotope effect (>3), all of which indicate that the oxidant is more selective than a hydroxyl radical) with labile ligands such as solvent (e.g. CH_3CN) in the presence of H_2O_2 indicates a metal based oxidant. When the ligands are more strongly bound, in contrast, there is evidence that hydroxyl radicals are the active oxidant (KIE values > 2 with deuterated alkanes, alcohol : ketone ratio less than 2 and dependent on the concentration of O_2). The effect of strongly and weakly binding ligands is particularly emphasised by the comparison between the reactivity of $[Fe_2O(OAc)(BPMEN)_2]^{3+}$ and $[Fe(BPMEN)(CH_3CN)_2]^{2+}$, the former of which is coordinatively saturated and exhibits a reactivity pattern associated with hydroxyl radicals and the latter has labile solvent ligands and a reactivity pattern indicating a metal based oxidant. On this basis, Que and co-workers concluded that one labile coordination site is required to form $Fe^{3+}OOH$, and a second site is required to activate this species and generate a metal bound oxidant.[23]

Another general class of tetradentate ligands with amine and pyridine donors are the N3Py-R ligands, whose general structure is shown in Figure 3-2. Their catalytic

oxidative ability in both acetonitrile and acetone has been investigated, and with both R = Me and R = Ph, the iron complexes are able to oxygenate cyclohexene and other organic species. However, although in acetonitrile they show a similar reactivity pattern to the TPA or BPMEN complexes discussed above (i.e. stereoselective *cis*-dihydroxylation and epoxidation, incorporation of O from both H_2O and H_2O_2, as shown by labelling studies, and a high alcohol : ketone ratio) , their efficiency is much lower.[25]

The complexes of the ligands discussed above all share a common coordination geometry: the two vacant coordination sites must be mutually *cis*. In complexes of 1,4,8,11-tetramethyl-1,4,8,11-tetraazacyclotetradecane (TMC) (Figure 3-5), in contrast, the two vacant coordination sites are *trans* to one another. $[Fe(TMC)]^{2+}$ is a high spin complex which is able to effect the deformylation of aldehydes in the presence of O_2. Several other tetradentate cyclic ligands have been synthesised and show catalase activity, and therefore might also be able to effect alkane oxidation.[26]

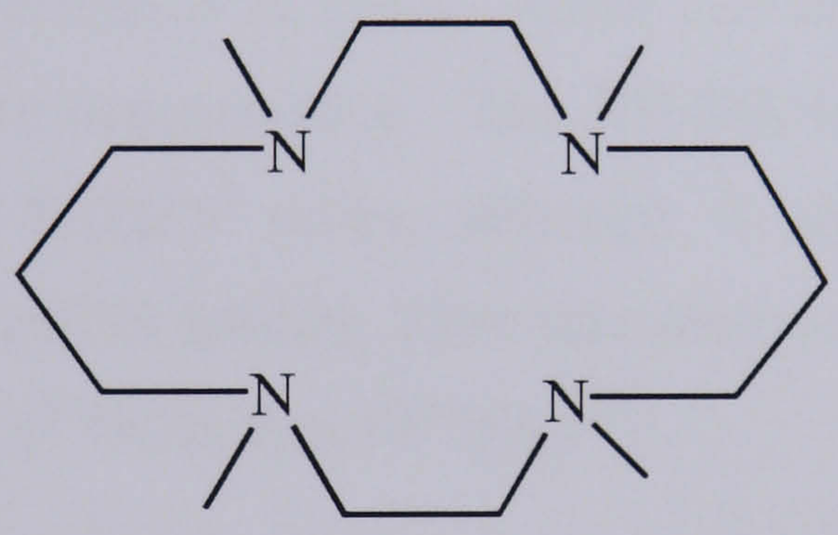

Figure 3-5 – Diagram of the TMC ligand

3.2.2 Pentadentate Ligands

The properties of the N3PyR ligand, where R = alkyl or aryl, were discussed in the previous section. Where R = CH_2Py, however, the ligand (abbreviated N4Py) is pentadentate, and its properties have been extensively studied. An $Fe^{3+}OOH$ intermediate of this ligand has been identified, and resonance Raman studies show that it has a weak O-O bond.[23,27] It is also able to effect alkane oxidation, but exhibits a different reactivity pattern to the TPA complex: a low kinetic isotope effect (1.5) and alcohol/ketone ratio (1.4, but dependent on O_2 concentration) along with the inability to afford stereospecific oxidation indicate that hydroxyl and long-lived alkyl radicals play a role in the mechanism of oxidation. Decomposition of $[Fe(N4Py)(OOH)]^{2+}$ is believed to occur via O-O bond homolysis.

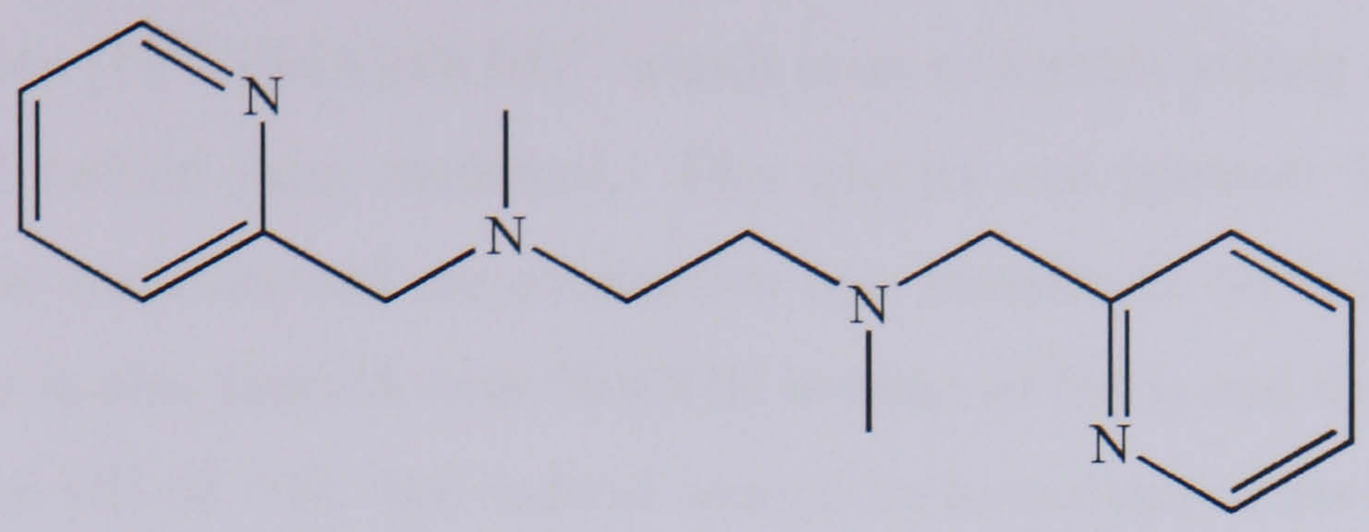

Figure 3-6 – Structure of the BPMEN ligand

A closely related pentadentate ligand based on the BPMEN architecture, *N*-benzyl-*N,N',N'*-tris(2-pyridylmethyl)ethane-1,2-diamine (Bn-TPEN), is also able to effect oxidation. Again it has a similar coordination sphere to the bispidine and N4Py ligands in that it has only nitrogen donors that come from amines and pyridines.

McKenzie and co-workers have synthesised and investigated a series of pentadentate ligands based on the RTPEN framework shown in Figure 3-7 below. These form purple $Fe^{3+}(OOH)$ species in the presence of H_2O_2, which can be deprotonated to give blue $Fe^{3+}(\eta^2\text{-}O_2)$ complexes upon deprotonation. The ESI-MS spectrum has peaks for both of these species for the RTPEN series, although it also has a prominent peak corresponding to the oxoiron(IV) species. They also observe that O-O bond cleavage is more likely to occur from $Fe^{3+}OOH$ than $Fe^{3+}(O_2)$.[28]

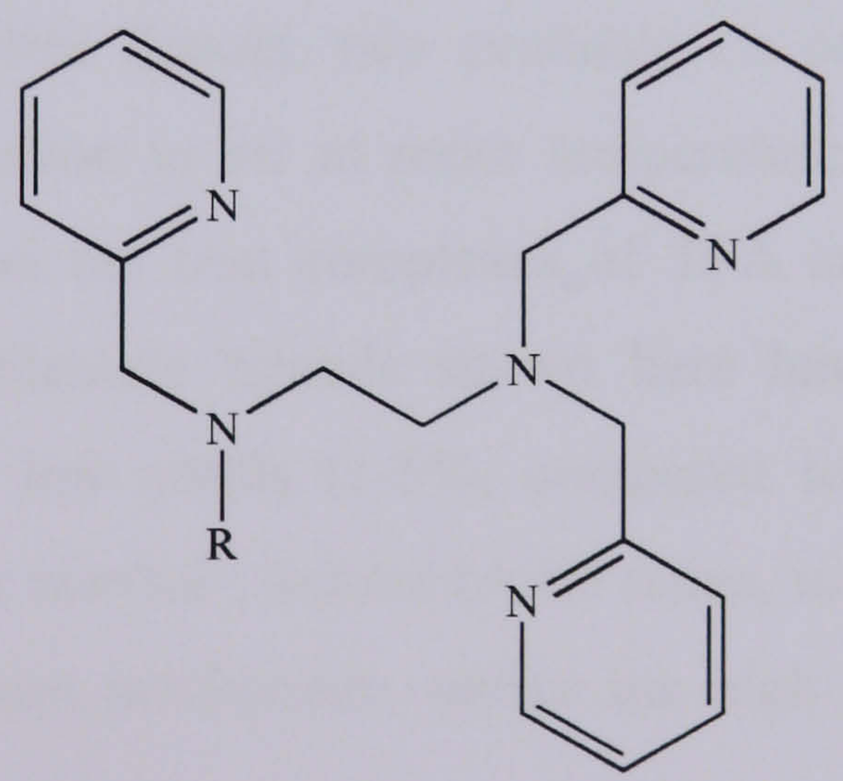

Figure 3-7 – RTPEN ligand framework

Another pentadentate ligand, PMAH, coordinates to Fe^{2+} and Fe^{3+} through four amine nitrogen donors, and one amide, to form $[Fe^{2+}(PMA)]^+$ and $[Fe^{3+}(PMA)]^{2+}$, as shown in Figure 3-8. The coordination sphere of PMA, and in particular the presence of an amide group, closely mimics that of the active site of bleomycin, and the reactivity shows

many similar features to this important enzyme. Oxygenation with H_2O_2 affords the low spin complex $[Fe^{3+}(PMA)(OOH)]^+$ which is an extremely strong oxidant capable of abstracting a H radical from methanol. This species can promote DNA cleavage via damage to sugar moieties and stereoselective oxo transfer to olefinic substrates. The reactive species is also formed with ^tBuOOH instead of H_2O_2 and the active oxidant is believed to be an OR (R = H, ^tBu) radical formed by homolysis of the O-O bond.[29]

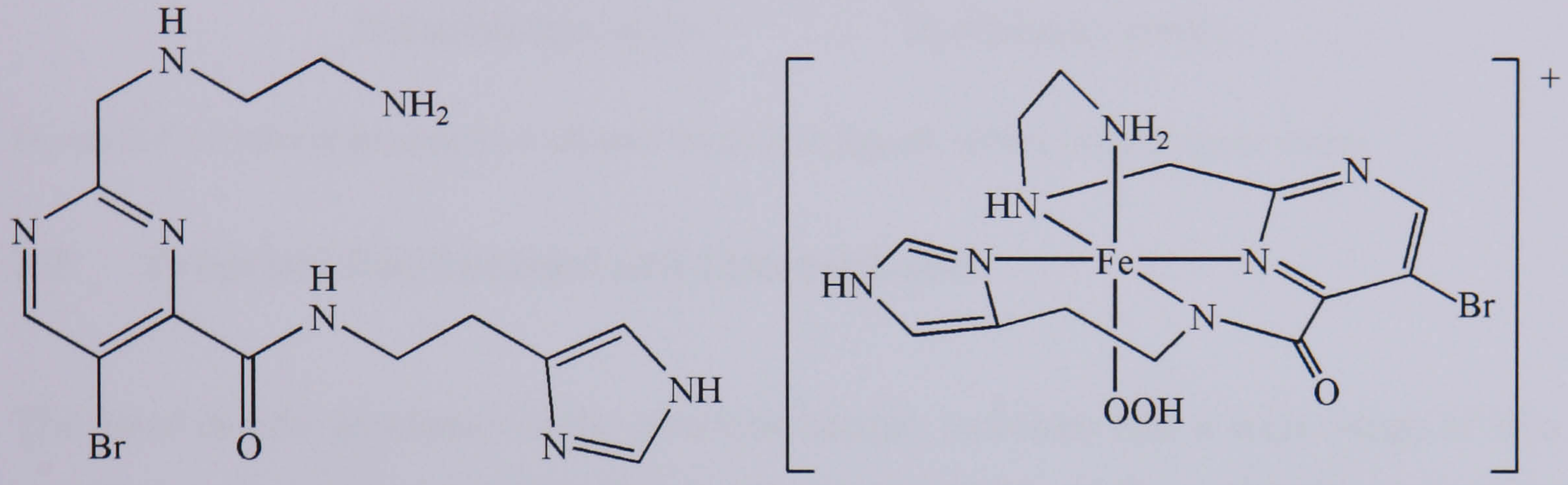

Figure 3-8 – Structure of the PMAH ligand, and its coordination geometry to Fe^{2+}

3.2.3 Tridentate Ligands

Tridentate ligands have received considerably less attention in the literature than their tetra- or pentadentate analogues, but a few examples of catalytic oxidation have been reported. As for the tetradentate ligands, the tridentate ligands (Figure 3-9) have nitrogen amine and pyridine donors, two available *cis* coordination sites, and effect oxidation in CH_3CN solution in air at room temperature with H_2O_2 solution added, albeit in lower yields than the iron complexes of TPA and BPMEN under the same conditions. The two tridentate ligands shown here have similar reactivity to one another, and both show low yields (1-5%, compared to 30-65% for the TPA and BPMEN ligands) and low alcohol : ketone (A:K) ratios, indicative of hydroxyl radicals and an auto-oxidation chain mechanism, unlike the high A:K ratios observed for the tetradentate ligands.[30]

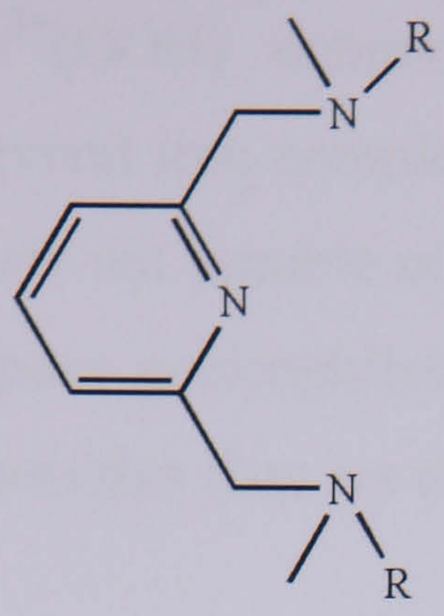

bis(amino)pyridine

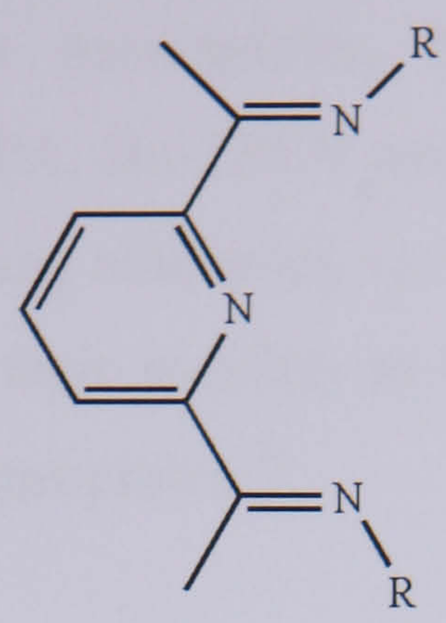

bis(imino)pyridine

Figure 3-9 – General structure of selected tridentate ligands with nitrogen donor atoms

3.3 Proposed Mechanisms and Intermediates

The brief review presented in the previous section indicates that a wide range of iron complexes are capable of catalysing oxidation employing H_2O_2 or ROOH as primary oxidant. The precise mechanism is, in many cases, unclear, and it remains possible that the catalytic pathway differs from system to system. We present here a brief overview of the various mechanisms that have been proposed in the literature.

Since the earliest days of Fenton chemistry, it has been known that iron together with hydrogen peroxide is a powerful oxidant, though the precise mechanism is still under debate. Both high valent metal species and oxygen centred radicals have been proposed. The same applies to the poly-nitrogen iron complexes discussed above.

In the presence of cyclooctene and 10 equivalents of H_2O_2, the [Fe(6-Me_3-TPA)] complex is able to afford oxidation of the cyclooctene to give the *cis* diol.[31] In the following sections, we discuss in turn each of the possible active species.

3.3.1 $Fe^{3+}OOH$

The iron(III) hydroperoxo species, $Fe^{3+}OOH$, has been proposed as an intermediate in many systems, including oxidation by cytochrome P450,[32] and by activated bleomycin.[33-35] However, whether the species is itself an oxidant, or whether it is a precursor to an undetected high valent active species has been disputed. It has been

proposed that $Fe^{3+}(OOH)$ complexes act as nucleophiles, but a study of this intermediate for several iron complexes with TPA, Bn-TPEN and N4Py ligands shows that these species are not capable of deformylating aldehydes via nucleophilic reaction, and are therefore poor nucleophiles. Equally, their inability to oxidise thioanisole or cyclohexene indicates that they are also poor electrophiles.[36]

This contradicts the evidence presented in section 1.5.1.2 that the low spin $Fe^{3+}OOH$ intermediate observed in bleomycin is the oxidising species.[37] Early studies of iron catalysts also proposed an $Fe^{3+}OOH$ intermediate as the active oxidant, in part due to the different reactivity some complexes displayed with hydroperoxide and alkylperoxide ligands.[38] Theoretical studies on the oxidants of cytochrome P450 also indicate that pathways involving an $Fe^{3+}OOH$ oxidant are high in energy and therefore this is not considered a possible oxidant.[39]

A study of the high spin Fe^{3+}-η^1-OOH complex $[Fe(H_2bppa)(OOH)]^{2+}$ showed that O_2 and free radicals did not participate in the reaction, and the complex did not show any oxidative abilities until the solution was warmed from −70°C to 20°C and began to show decomposition of the iron species. The authors propose that the catalyst undergoes homolysis of the O-O bond, and the resultant •OH radical and $Fe^{4+}O$ species simultaneously attack the substrate.

There is plenty of evidence for the participation of an $Fe^{3+}(OOH)$ intermediate in non-heme monomeric iron complexes, but it is not clear whether these are the oxidising species, or whether they are precursors to the active species, like it is believed for the enzyme bleomycin discussed in the introduction.[40] The low spin purple species $[Fe(N4Py)(OOH)]^{2+}$ has been observed using ESI-MS, UV-Vis and EPR spectroscopy, and is believed to be formed in a two step process by addition of H_2O_2 to $[Fe(N4Py)(NCCH_3)_2]^{2+}$. Resonance Raman spectroscopy shows a particularly weak O-O bond with a stretch at 790 cm^{-1}, and an Fe-O stretch at 632 cm^{-1}. This O-O stretch is significantly lower than the typical O-O stretches found for similar complexes at 806-900 cm^{-1} suggesting that the O-O bond is weaker, and the Fe-O stretch is at higher energy than usual (421-503 cm^{-1}).

3.3.2 $Fe^{3+}(\eta^1\text{-}O_2)$ and $Fe^{3+}(\eta^2\text{-}O_2)$

Deprotonation of the $Fe^{3+}OOH$ species leads to a peroxo species characterised by a shift in the UV/Vis spectrum to lower energy and a change in colour from purple to blue is observed. Nam and co-workers showed that such intermediates with N4Py, TMC and Bn-TPEN ligands are capable of deformylating aldehydes via an oxidative nucleophilic addition reaction.[36,41] However, the same reactant was unable to effect the electrophilic oxidation of thioanisole and cyclohexene.

3.3.3 Fe(IV)O intermediates

Oxoiron(IV) complexes been shown to be capable of oxygenating various organic substrates such as sulfides, olefins, alcohols and alkanes, with concomitant reduction to iron(II). Hammett plots for the oxidation of substituted thioanisoles have a negative ρ value indicating that the oxidant is electrophilic in nature.[36] A number of stable oxoiron(IV) species have been directly observed: for example, a pale green $[Fe(IV)(O)(cyclam\text{-}acetate)]^+$ complex formed from the reaction of the iron species and ozone at −80°C has been identified on the basis of its absorption and Mössbauer spectra.[5,42] A second oxoiron(IV) species with the TMC ligand, formed by reaction of the iron complex with either PhIO or H_2O_2, has also been identified by its pale green colour (λ_{max} = 820 nm).[43] Mössbauer spectroscopy indicates that this species has a triplet ground state[44] and ESI-MS indicates that it is a combination of $[Fe(IV)(O)(TMC)(NCCH_3)]^{2+}$ and $[Fe(IV)(O)(TMC)(OTf)]^+$. A crystal structure of the former has been obtained,[43] and the isolation of this species has allowed a detailed study of spectroscopic properties of the Fe(IV)=O unit to be conducted. Most significantly, an FT-IR band at 834 cm^{-1} has been identified as the Fe=O stretch. More recently, this species has also been generated by the reaction of the Fe^{2+} complex $[Fe(TMC)(CF_3SO_3)_2]$ and O_2, although oxoiron(IV) species with other ligands such as TPA and N4Py can not be generated directly from O_2.[45] This unequivocal identification of an oxoiron(IV) species demonstrates that it is a plausible intermediate as an oxidant in the Fenton, and related, reactions. The TPA ligand discussed above also forms an oxoiron(IV) complex (from the reaction of $[Fe(TPA)(CH_3CN)_2]^{2+}$ in acetonitrile solution under anaerobic conditions with 2-methyl-1-phenyl-2-propyl hydroperoxide added via syringe pump)[42,46] (λ_{max} = 720 nm) that has been shown to effect the 2-

electron oxidations of cyclooctene to its epoxide and of benzyl alcohol and cyclobutanol to their carbonyl derivatives.[47]

Oxoiron(IV) complexes with the pentadentate ligands N4Py and Bn-TPEN have also been characterised: both species are a green colour and their spectra feature λ_{max} = 695 and 739 nm respectively, with a lower energy shoulder in each case. The oxoiron(IV) complexes with pentadentate ligands are more thermally stable than the equivalent tetradentate complexes, although this stability may be pH dependent.[44] They do, however, react readily with hydrocarbons, and are able to hydroxylate alkanes with C-H bonds that are up to around 100 kcal mol^{-1} in strength. These reactions also show a large kinetic isotope effect that would not be observed if hydroxyl radicals were present due to their high reactivity.

Studies on $[Fe(N4Py)(CH_3CN)]^{2+}$ and H_2O_2 in the presence of radical traps (acetone and benzene) have provided strong evidence to support the proposal that these $Fe^{4+}O$ species are indeed active oxidants. The radical traps remove hydroxyl radicals from the reaction, thereby decreasing the overall turnover number. However, the alcohol : ketone ratio and the KIE are increased for the oxidation of cyclohexane upon increasing the proportion of benzene in the acetonitrile medium the reactions were carried out in. Although the alcohol : ketone ratio is increased when radical traps are added to the reaction mixture, in the presence of air it decreases back to 0.9 indicating that an alkyl radical is formed that can react with O_2, eventually resulting in a Russell termination mechanism. Because the trapping of hydroxyl radicals by benzene or acetone leads only to partial quenching of the reactivity of the solution, the authors conclude that there must be another oxidation mechanism occurring too.[13]

The reaction of $[Fe(N4Py)(CH_3CN)]^{2+}$ with H_2O_2 gives an $Fe^{3+}OOH$ intermediate. The •OH radicals formed during substrate oxidation are assumed to originate from the homolysis of the O-O bond leaving $[Fe(O)(N4Py)]^{2+}$ which could be responsible for the observed oxidation that can not be ascribed to hydroxyl radicals. Alternatively the hydroperoxide intermediate itself could be the second oxidant, but this is ruled out as the rate of disappearance of $[Fe(OOH)(N4Py)]^{2+}$ is not affected by the use of [d^{12}]-cyclohexane instead of undeuterated cyclohexane even though there is a KIE of 2.3. Therefore the authors conclude the second oxidant must be an oxoiron(IV) species.[13]

3.3.4 Fe(V)O Intermediates

Oxoiron(IV) species have been proposed as an active oxidant by Que and co-workers in their study of TPA complexes. The $[Fe(TPA)(OOH)]^{2+}$ complex is believed to be converted, via a water assisted mechanism, to a *cis* O=Fe-OH oxidant, and labelling experiments using ^{18}O indicate that one oxygen atom is derived from the hydroperoxide ligand and the other is from a water molecule. This mechanism is supported by DFT calculations.[4,48] Que has proposed that the relatively weak O-O bond in LS $Fe^{3+}OOH$ cleaves easily, leading to the facile formation of $Fe^{5+}O$.[6] A similar species has been proposed for the Fe-BPMEN catalyst, although the $Fe^{3+}OOH$ species is also invoked as an oxidant and is shown by DFT calculations to be favoured in the absence of water.[49]

In the presence of H_2O_2, the high spin Fe^{3+} complex $[Fe(CH_3CN)_2(6\text{-}Me_3\text{-}TPA)]^{3+}$ is believed to form an $Fe^{5+}(O)(OH)$ intermediate during the *cis*-dihydroxylation of cyclooctene. However, unlike in the unsubstituted TPA complex, labelling experiments show that both the oxygen atoms incorporated into the product from dihydroxylation are from H_2O_2.[15,31] The same pattern (incorporation of one oxygen atom of H_2O_2 for low spin Fe^{3+} and both oxygen atoms for high spin precursors) is observed for Fe^{3+} complexes with a BPMEN ligand. The incorporation of both oxygen atoms from H_2O_2 in the *cis*-dihydroxylation of alkenes is not observed unless the iron complex has two *cis* coordination sites occupied by labile ligands.[12] In addition, the high spin complexes give higher ratios of dihydroxide to epoxide than the low spin complexes

The active oxidant in the reaction of $[Fe(TPA)(CH_3CN)_2]^{2+}$ with H_2O_2 is also postulated to be an $Fe^{5+}O$ species, and this proposal is again supported by DFT calculations.[48] The H_2O_2 ligand binds to the Fe^{2+} centre, is deprotonated, and the Fe^{2+} centre is oxidised to Fe^{3+}. The O-O bond can then cleave homo- or heterolytically leading to an Fe^{4+} or Fe^{5+} intermediate, respectively. DFT calculations suggest that formation of the Fe^{5+} oxidant is lower in energy when H_2O_2 is the oxidant, but if an alkyl peroxide is used instead, the homolytic pathway is preferred due to the greater stability of the alkoxyl radical over the hydroxyl radical.

A second iron complex with a tetradentate ligand, *N,N'*-bis(2[-pyridylmethyl)ethylene-1,2-diamine (BPMEN), $[Fe(BPMEN)(CH_3CN)_2]^{2+}$, has been shown to have a high catalytic activity with H_2O_2. A similar alkane oxidation pattern to $[Fe(TPA)(CH_3CN)_2]^{2+}$ is observed[19]; both species have high alcohol : ketone ratios that are independent of O_2 concentration, indicating that long lived alkyl radicals are not formed, and both are more selective than a hydroxyl radical, catalysing the stereospecific oxidation of tertiary C-H bonds. This evidence points to a metal based oxidant that generates short lived alkyl radicals. Que states that this oxidant must be a high valent oxoiron(V) species formed by heterolytic cleavage of the O-O bond, resulting in the iron centre being oxidised by two electrons, and rules out homolytic cleavage due to the absence of evidence for hydroxyl radicals.[19]

3.4 Summary of Experimental Results on Iron-Bispidone Complexes

In the previous sections, we have surveyed iron-based catalytic oxidation in its most general context. In this and the next chapter of this thesis, we focus specifically on the iron-bispidone complex $[Fe(N2Py3o)]^{2+}$ (Figure 3-10). Comba, Hage, Lienke and co-workers have shown that this species is an effective catalyst for oxidation of alkenes and stain bleaching in the presence of H_2O_2, either in aqueous or acetonitrile solution. Unilever patented the use of this complex and derivatives as stain bleaching agent in the absence of any source of hydrogen peroxide.[50] The source of active oxygen is however thought to arise from hydroperoxides to be found in the unsaturated oil matrix of the stain. Later it was found that $[Fe(NPy3o)]^{2+}$ is a catalyst especially in the epoxidation of cyclooctene, albeit in organic solvents such as acetonitrile. Total turnover numbers (TON) of up to 8 were found, which is high as compared to other iron catalysts on this reaction, but low with respect to efficiency for catalysts in general.

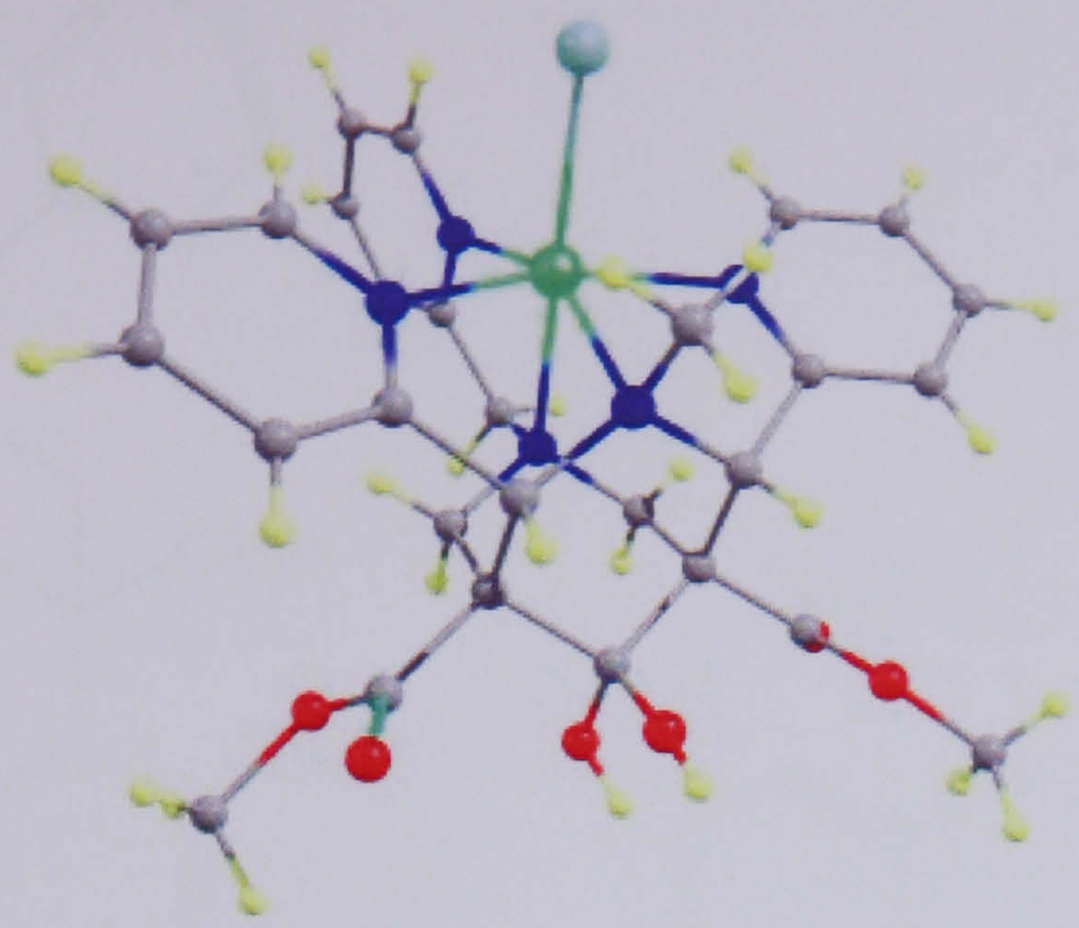

Figure 3-10 – N2Py3o bispidone ligand coordinated to Fe^{2+} with Cl^- in the 6th coordination site[51] {original in colour}

The active species in the reactions is unknown, but, on the basis of comparison with the literature precedents, it seems likely that an oxoiron(IV) species analogous to active intermediate in bleomycin and the Fe-O fragment of cytochrome P450 may play a role. Although there is very little data available on the mechanism of reaction of $[LFe(H_2O_2)]^{2+}$, where L = N2Py3o (Figure 3-11), the reactivity of a related bispidone complex, where L = N2Py3u (Figure 3-11), has been studied. This complex is able to stablise ligands in the sixth coordination site to a greater extent than the N2Py3o complex, and therefore more studies have been conducted on the intermediates in the reaction with the N2Py3u ligand. However, due to the similar coordination sphere of both complexes it is believed that they both oxidise substrates through the same mechanism and therefore conclusions from studies done on the $[Fe(N2Py3u)]^{2+}$ complex also apply to the $[Fe(N2Py3o)]^{2+}$ complex. In addition, resonance Raman studies indicate that the O-O bond is weaker in the N2Py3o complex than the N2Py3u complex, indicating that formation of the oxoiron(IV) intermediate will be easier.

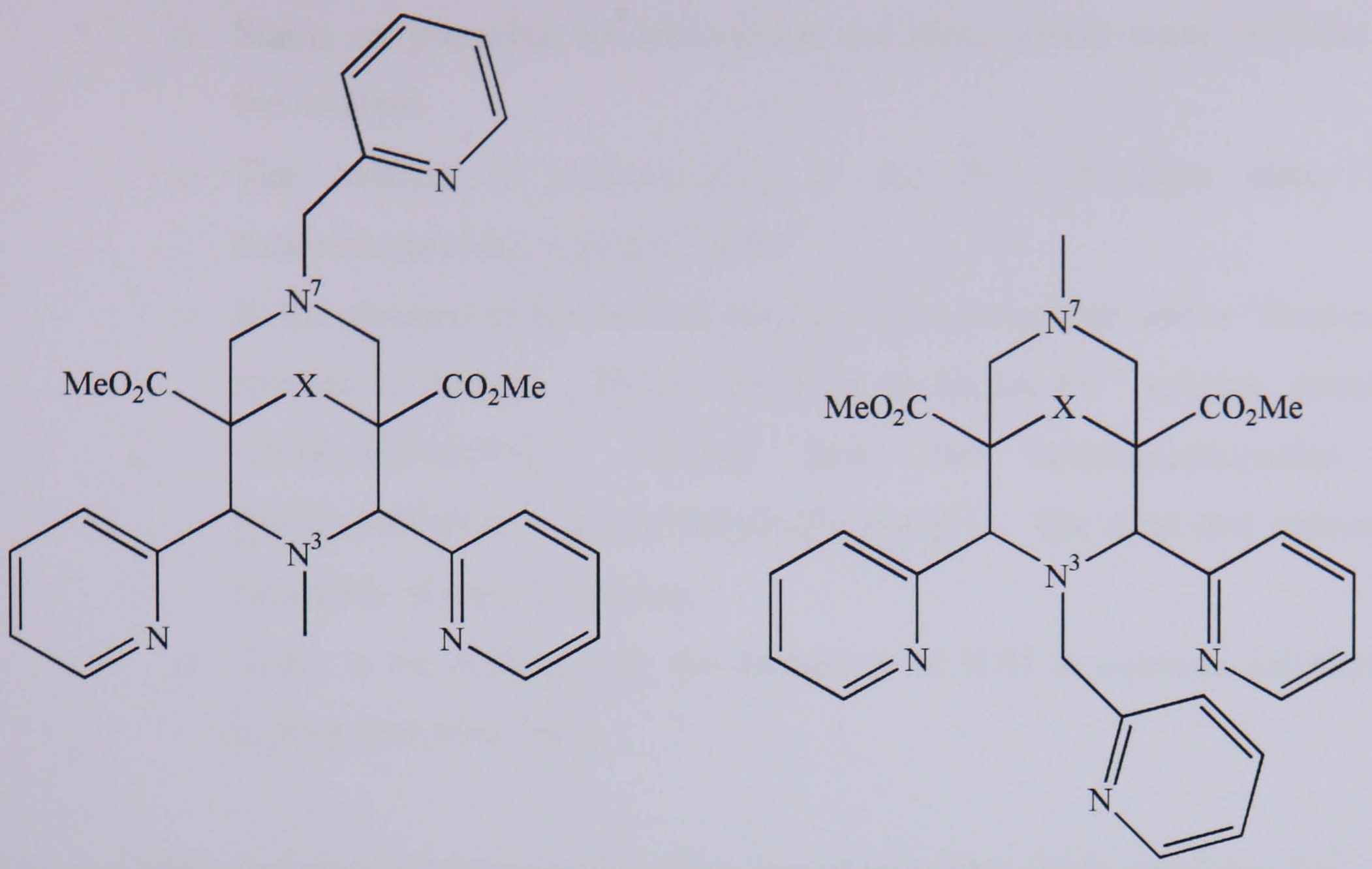

N2Py3o N2Py3u

Figure 3-11 – The pentadentate bispidone ligands

The key experimental data can be summarised as follows:

- Under "standard" conditions (the catalyst, H_2O_2 and a hydrocarbon substrate in acetonitrile solution) the active species are thought to be $Fe^{3+}OOH$, $Fe^{4+}O$ and possibly •OH.
    - H_2O_2 exchanges with the ligand in the 6th coordination site.
    - The process is not particularly efficient.
    - Turnover numbers do not exceed eight showing that true catalysis is not occurring, but rather amplification of the oxidation via a radical chain mechanism.
    - Carbon centred radicals are formed.
- In a stain, the catalyst is dissolved in aqueous solution as $[(N2Py3o)Fe(Cl)]^+$, but the chloride ligands undergo rapid exchange with water ligands. Surfactants are also present and the bleaching is carried out in an organic solvent.
    - The $[LFe(H_2O)]^{2+}$ species is adsorbed into the stain where is reacts with ROOH to initiate the reaction.
    - Turnover numbers exceed 100 indicating that the yield is due to true catalytic behaviour of $[(N2Py3o)Fe(H_2O)]^{2+}$ rather than amplification by a radical chain mechanism.

- Stains are protected by antioxidants and these are the main substrate for the catalyst.
- The catalyst is predominately in the Fe^{2+} oxidation state. The antioxidants reduce and Fe^{3+} to Fe^{2+}.
- In the absence of antioxidant catalysis does not occur, and a "dead-end" species is formed. This is believed to be an Fe^{3+} species, possibly $[(N2Py3o)Fe(OH)]^{2+}$, formed from the conproportionation of $[(N2Py3o)Fe(O)]^{2+}$ and $[(N2Py3o)Fe(H_2O)]^{2+}$. The dead-end species is incapable of stain bleaching.
- There is no evidence for the formation of •OH in aqueous solution or during stain bleaching.

The available experimental data are therefore consistent with a cycle involving Fe^{2+} and Fe^{4+}, the latter apparently being formed from Fe^{2+} + H_2O_2 without generation of intermediate radicals. A possible reaction cycle is shown in Figure 3-12. In the remainder of this chapter, we explore possible mechanisms for the direct formation of oxoiron(IV).

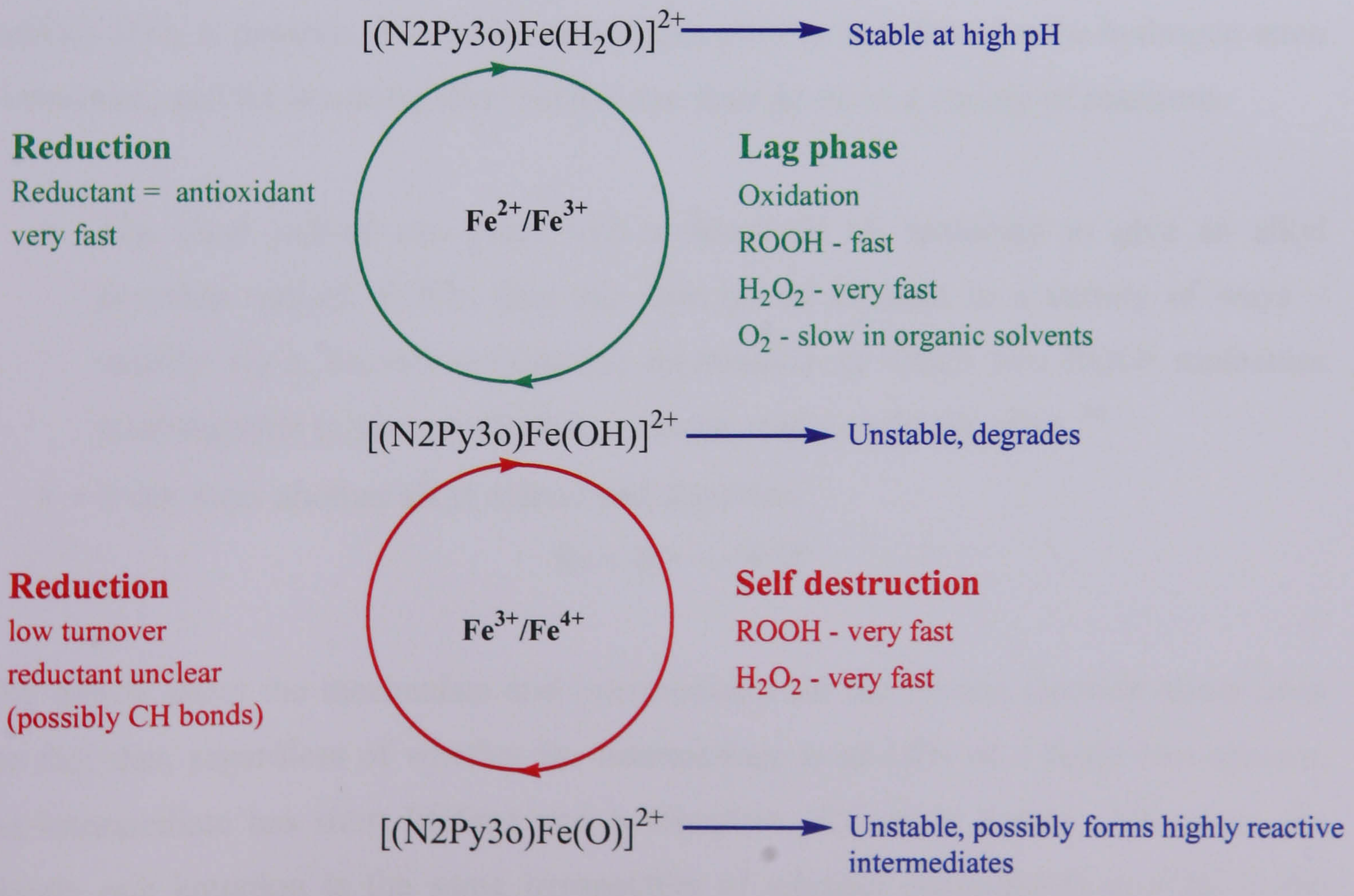

Figure 3-12 – Diagram showing the proposed reaction cycle of $[LFe(H_2O_2)]^{2+}$ {original in colour}

3.5 Fenton Chemistry

Fenton chemistry is the general name given to the transition-metal catalysed oxidation of organic substrates by H_2O_2. This type of reaction clearly has important industrial and biological applications. In the original reaction reported by Fenton in 1894,[52] Fe^{2+} (e.g. $FeCl_2$) in acidic aqueous solution (ca. pH 2) with an equimolar amount of H_2O_2, effected oxidation of tartaric acid. Remarkably, although the reaction is over a century old, the reactive species has still not been unequivocally identified. The intense discussion about its identity centres around two possible mechanisms, both proposed over 70 years ago. The Haber-Weiss mechanism (1934)[53] involves the formation of Fe^{3+} and an •OH radical by iron catalysed dissociation of H_2O_2. The Bray-Gorin mechanism (1932),[54] in contrast, postulates that an oxoiron(IV) species is the active oxidant. These mechanisms, and evidence for and against them, are discussed in sections 3.5.1 and 3.5.2.

Under Fenton conditions (Fe^{2+} salt, H_2O_2, acidic aerated queous solution), hydrocarbons (both aliphatic and aromatic) are oxidised and the products formed are mainly alcohols and ketones.[55] In addition to this, alkyl dimers can be formed, along with alkyl peroxyl radicals if O_2 is present. The initial step in this process is believed to be hydrogen atom abstraction, and the resulting alkyl radical can then go on to a variety of reactions:

- The alkyl radical can react with a dissolved O_2 molecule to give an alkyl peroxide radical, ROO•, that can then go on to react in a variety of ways – usually via a Russell termination mechanism in which two ROO• molecules react together to give an alcohol, a ketone, and a molecule of O_2.[56]
- It can meet another alkyl radical and dimerise:

$$R\bullet + R'\bullet \rightarrow R\text{-}R'$$

The debate about the mechanism and intermediates for the Fenton reaction stems from the fact that, regardless of whether the intermediate is an OH• or a ferryl oxo species, the intermediate has short lifetime and is therefore difficult to detect. Moreover, the kinetic rate equation is the same irrespective of whether oxoiron(IV) or •OH is the

active species. Therefore, the mechanism and key intermediates in this much studied subject area is still an open question.

3.5.1 Radical Mechanism - OH• as the Active Oxidant

The first mechanistic proposal for the Fenton reaction was presented by Haber and Weiss in 1934, and involved the formation of •OH radicals[53]:

1 $Fe^{2+} + H_2O_2 \rightarrow Fe^{3+} + OH^- + OH•$

Barb extended this proposal to generate a complete catalytic cycle[56] in which Fe^{2+} is regenerated:

2 $Fe^{2+} + OH• \rightarrow Fe^{3+} + OH^-$

3 $OH• + H_2O_2 \rightarrow OOH• + H_2O$

4 $HO_2• + Fe^{2+} \rightarrow HO_2^- + Fe^{3+}$

5 $HO_2• + Fe^{3+} \rightarrow H^+ + O_2 + Fe^{2+}$

OH radicals clearly play a key role in the Haber-Weiss model of Fenton chemistry, but evidence to confirm their presence in solution remains elusive. The radicals are short lived in solution, and therefore can not be detected by EPR, so their presence can only be implied from the presence of radical products and the use of radical traps. Walling[58] presented a substantial body of evidence supporting the production of OH• and RO• radicals, largely based on the similar distribution of oxidation products in the reaction of aromatic substrates by a) HO• produced by radiolysis of H_2O_2 in the absence of metal ions, and b) Fenton-type reagents. The EPR spectra of carbon centred radicals are also identical regardless of whether they are produced by route (a) or route (b).[59] The rates of reaction between a range of substrates with OH• in metal free systems are also very similar to those observed with Fenton reagents. It seems unlikely that another species, such as oxoiron(IV), will give the same relative rates of reaction. Moreover, the addition

of $NaClO_4$ to the reaction mixture rates has little impact on the rate, suggesting that ionic strength is not important, and hence that charged species are not involved.

Norman and co-workers have shown that carbon centred radicals are formed using Fentons reagent (2% H_2O_2 solution added to a suspension of $FeSO_4$ and (e.g.) benzene in water), shown by EPR studies. The radicals formed are identical to those formed when metal ions are absent, and irradiation of H_2O_2 is used to generate radicals.[60] This indicates that the same oxidant must be present in both situations, and as, in one case, the oxidant is known to be •OH, the active oxidant in the Fenton reaction must also be this.

Yamazaki and Piette have also proposed that •OH radicals are formed in the Fenton reaction, but they are bound to the metal centre rather than free in solution.[61] Using stopped flow EPR techniquies, Fe^{2+}EDTA (and other chelates), and nitroso spin trapping reagents (which give hydroxy radical adducts and are the most direct way of detecting hydroxyl radicals, see Figure 3-13) they noted that the concentration of this adduct was much lower than the initial concentration of Fe^{2+}, inconsistent with the idea that free •OH radicals were formed that were able to then react as shown in Figure 3-13. A 1:1 ratio of Fe^{2+} to adduct was only formed when there was a large excess of H_2O_2 relative to Fe^{2+}. However, when ethanol was also added to the reaction mixture, the hydroxyl adduct was replaced by an ethoxyl equivalent, the concentration of which is much higher than that of the original OH adduct. The increase in the amount of adduct suggests that a second species, quite distinct from the •OH radical, is active in the formation of the ethoxyl radicals. This led the authors to propose that the oxidant is a hydroxyl radical, but it is bound to the metal centre rather than free in solution.

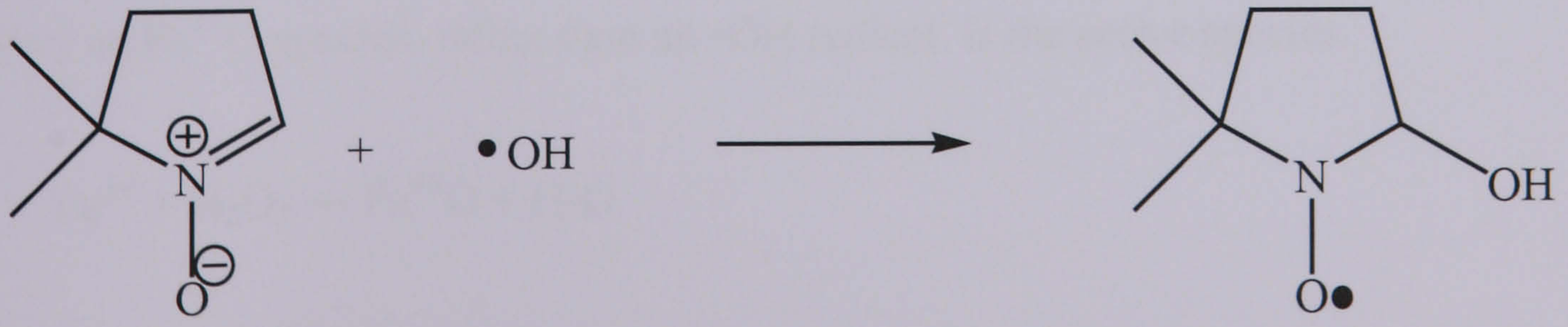

Figure 3-13 – DMPO (•OH spin trap)

Based on the kinetics of the reaction, Kremer has proposed a complex mechanism summarising the eventual fates of the active species produced from the reaction of

aqueous Fe^{2+} and H_2O_2 in acidic solution (pH 1-2.5).[62] This involves both monomeric and dimeric species, and a variety of intermediates, as shown in Figure 3-14.

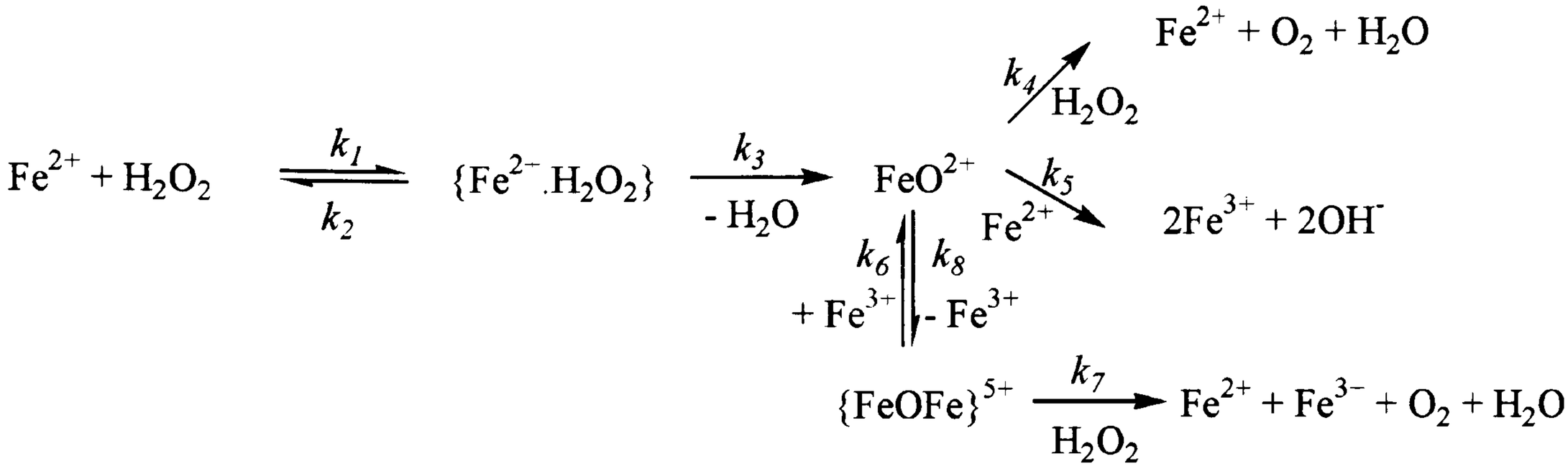

Figure 3-14 – Mechanism proposed by Kremer for the Fenton reaction in acidic solution[62]

Further evidence supporting the Haber-Weiss mechanism comes from work by Münck and co-workers,[63] who generated a complex identified as $[Fe(H_2O_2)_5O]^{2+}$ from a reaction of $[Fe(H_2O_2)_6]^{2+}$ and O_3 in acidic solution. However, when comparing the reactivities of this known complex and Fenton's reagent (in the absence of air) with dimethyl sulfoxide and (CH_3)-(*p*-tolyl)-SO, they found that $[Fe(H_2O)_5O]^{2+}$ gave the corresponding sulfones, while Fenton's reagent gives a mixture of ethane, methylsulfinic acid, and small amounts of methane and sulfone. The very different reactivities demonstrates that a ferryl oxo species can not be the main oxidant in the Fenton reaction in this case.

3.5.2 High Valent Oxo Species – Oxoiron(IV) as the Active Oxidant

Despite the evidence given in the previous paragraph, a number of groups have argued against the participation of •OH radicals in the Fenton reaction. Instead they argue that an alternative mechanism, originally proposed by Bray and Gorin in 1932,[54] which involves an $Fe^{4+}O$ species, rather than an •OH radical, is the active species.

6 $Fe^{2+} + H_2O_2 \rightarrow Fe^{4+}O + H_2O$

A key piece of evidence in favour of the Bray Gorin mechanism is that the reaction products when organic species are reacted with known •OH radicals (e.g. those formed from the photolysis of H_2O_2)[54,64] are different to when they are oxidised using Fenton's

reagent. For example, the product of cyclohexane and •OH is bicyclohexyl, whereas the product of cyclohexane and Fenton's reagent is an alcohol. Similar trends are seen with other aryl and alkyl species. Furthermore, unlike Fenton's reagent, •OH radicals are able to oxidise methane to methanol. Therefore other oxidants such as high valent oxoiron(IV) species, and an $Fe(H_2O_2)$ species must be involved.[65]

3.5.4 Theoretical Calculations by Baerends and Co-workers

Very recently, support for the Bray-Gorin mechanism has come from theory. Baerends and co-workers have performed several computational investigations into the Fenton Chemistry of $[Fe^{2+}(H_2O)_6]^{2+}$ and H_2O_2 with the aim of establishing the identity of the active species. In a study of the active intermediate Fentons reagent, Baerends and co-workers showed that formation of $[Fe(H_2O)_5O]^{2+}$ and water from $[Fe(H_2O)_6]^{2+}$ and H_2O_2 is energetically favourable, and proceeds without having to overcome high energy barriers.[66] In the first step of this reaction, they show that H_2O can easily dissociate from $[Fe(H_2O)_6]^{2+}$ and be replaced by H_2O_2. The H_2O_2 molecule is bound to the Fe^{2+} centre in an orientation that allows it to hydrogen bond to the H atom of a water molecule also coordinated to the iron centre, and *cis* to H_2O_2. (Figure 3-15, **A**) The O-O bond is stretched, and the water O-H bond also gets longer as the hydrogen bonding between the terminal O of the H_2O_2 molecule gets stronger (step **1**, leading to **B** which is a maximum along the O-O coordinate, and approximately 6 kcal mol^{-1} higher in energy than the starting species). Beyond this maximum, the O-O and O-H bonds break completely, leaving a water molecule in the second coordination sphere of a $[Fe(H_2O)_4(OH)_2]^{2+}$ complex (**C**) where the iron centre is now in a +4 oxidation state. Overall, this species is about 11 kcal mol^{-1} more stable than $[Fe(H_2O)_5(H_2O_2)]^{2+}$.

Next (step **3**), one of the OH groups coordinated to the iron centre rotates so that the H atom is able to hydrogen bond to the O of the water molecule in the outer coordination sphere. Another hydrogen bond is formed between the H of the water molecule and the O of the second OH group (**E**), and a proton shuttle mechanism (step **5**) the leads to formation of the product complex, $[Fe(H_2O)_5O]^{2+}$ (**F**), which is 9 kcal mol^{-1} more stable than the dihydroxy species with a barrier of only 3.5 kcal mol^{-1} when a water molecule is included in the second coordination sphere.

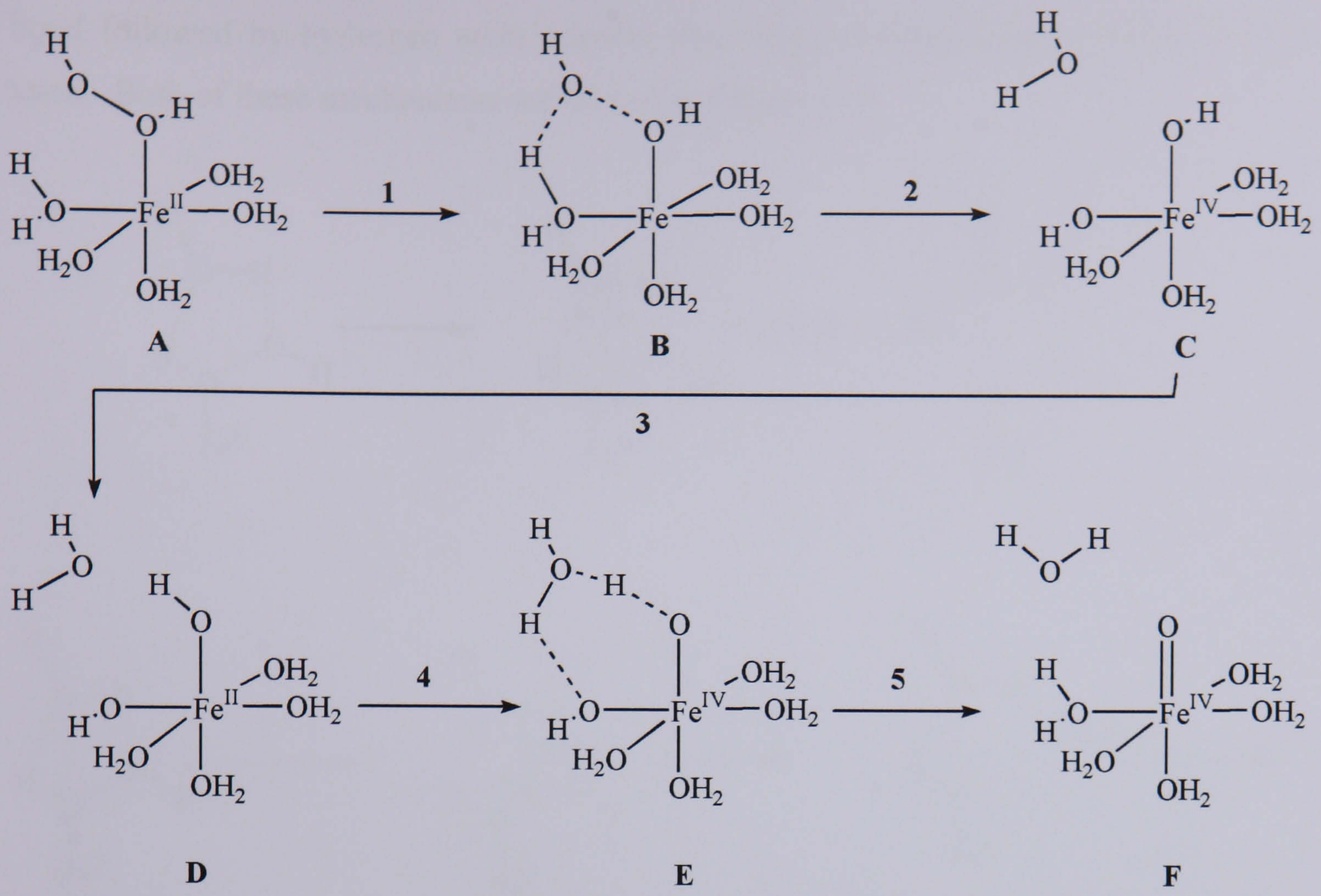

Figure 3-15 – Schematic representation of the mechanism of formation of $[Fe(H_2O)_5O]^{2+}$ from $[Fe(H_2O)_5(H_2O_2)]^{2+}$ as shown by Baerends and co-workers[66]

The results of this study were further corroborated by a Car-Parrinello study of the same system, starting from the $[Fe(H_2O)_5(H_2O_2)]^{2+}$ species in water at T=300K.[67] The authors wanted to see whether the presence of an aqueous environment affected the important conclusion that the •OH radical is trapped as it is being formed. They show that, although the solution is dynamic and several intermediates are formed, the $[Fe(H_2O)_5O]^{2+}$ is formed without the release of free •OH radicals.

In the bispidone complex we study in this thesis, the pentadentate ligand leaves only one available coordination site that is occupied by H_2O_2. Therefore there are no other H_2O molecules in the first coordination sphere, and a mechanism analogous to the one shown by Baerends can not be operative. However, it is possible that a solvent water molecule could play a similar role to the water co-ordinated to Fe. In this chapter, we investigate this possibility and see if it can assist in the formation of $Fe^{4+}O$ without the concomitant formation of •OH radicals. In particular, we assess two distinct mechanism that could lead to the formation of an $[LFe(O)]^{2+}$ species. The first is a one step mechanism involving proton transfer from the proximal to the terminal oxygen atom of coordinated H_2O_2. The second mechanism involves homolytic cleavage of the O-O

bond followed by hydrogen atom transfer from the proximal to the terminal oxygen atom. Both of these mechanisms are shown in Figure 3-16.

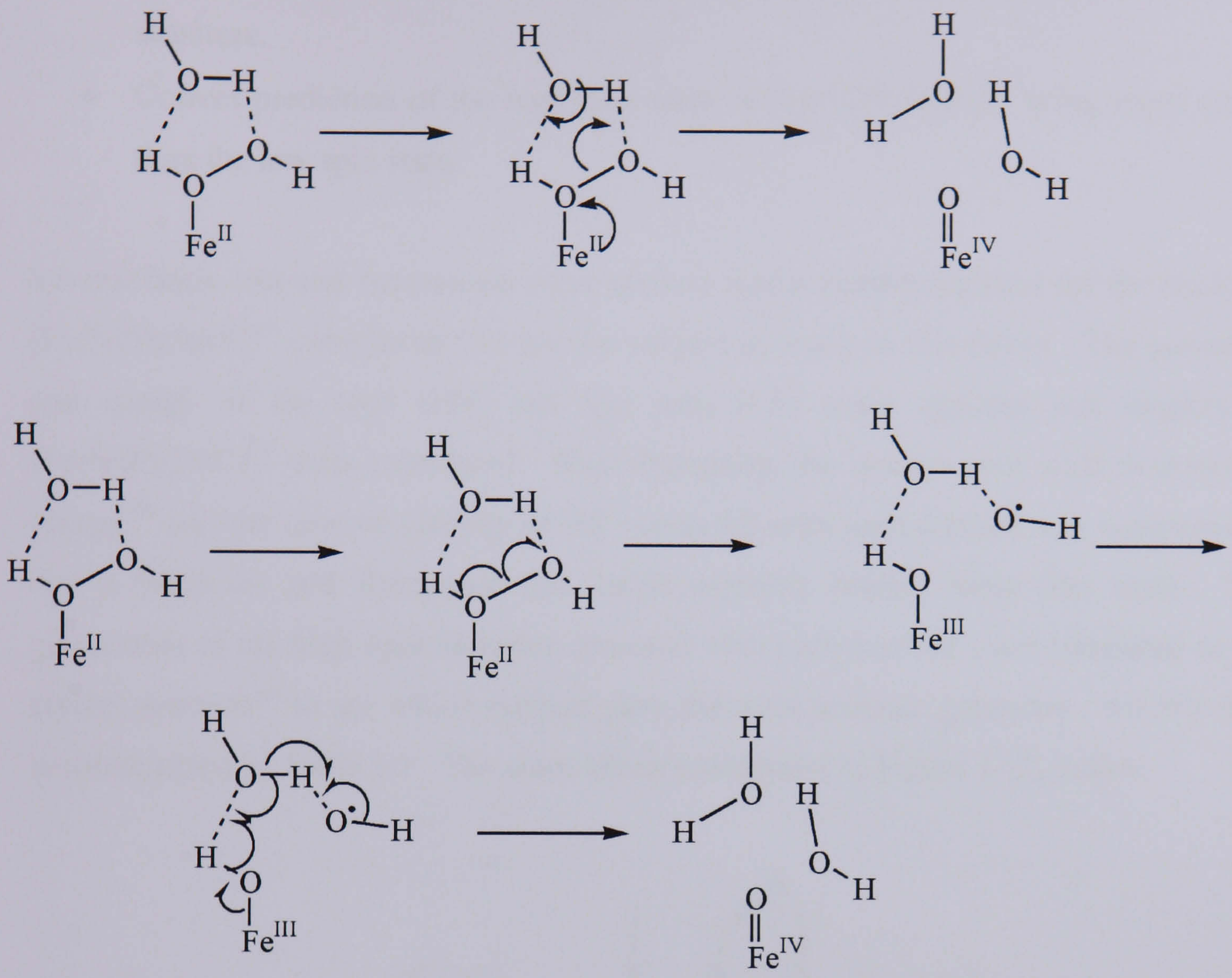

Figure 3-16 – Proposed mechanisms for water assisted $Fe^{IV}O$ formation: Comcerted (top) and radical (bottom)

3.6 Choice of Basis Set and Functional

All the calculations have been done using the Gaussian03 suite of programs (revision C.01) with the B3LYP functional and the 6-31G(d) basis set on all atoms. This combination of basis set and functional was chosen for several reasons outlined in this section. First, some of the work in this thesis relates closely to some work done by the Comba group in Heidelberg, Germany, and it would be useful to directly compare results. Therefore, we decided to use the same basis set and functional if appropriate.

Second, a brief survey of a selection of functionals and basis sets was carried out to evaluate which combination gave the best results without being unduly computationally

demanding. A summary of these results is shown in Table 3-1. The criteria considered for a good method are:

- Accurate description of the geometry of complex compared to the crystal structure.
- Correct prediction of the high spin state of $[Fe(N2Py3o)Cl]^+$ being more stable than the low spin state.

Several basis sets and functionals were used to find a suitable method for the study of $[Fe(N2Py3o)X]^{n+}$ complexes that are the subject of study in this thesis. The geometry and energy of the high (HS) and low spin (LS) states (quintet and singlet) of $[Fe(N2Py3o)Cl]^+$ were calculated. Experimentally, the quintet spin state is lower in energy,[68] and the relative stability of HS versus LS with each method was compared so that a basis set and functional that could correctly predict these was used. The geometries of the high spin complex obtained with each method were compared to the crystal structure[68] to see which method gave the most accurate geometry. All this data is summarised in Table 3-1. The atom labels correspond to Figure 3-17, below.

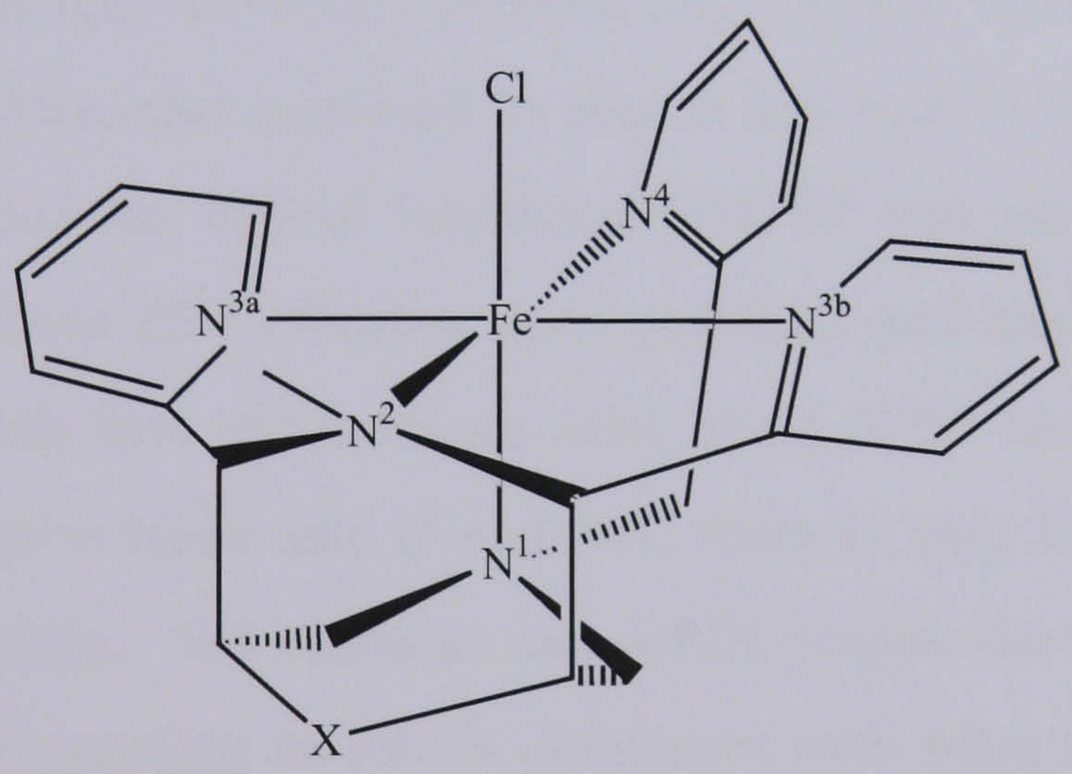

Figure 3-17 – Numbering scheme used in Table 3-1

Table 3-1 – Bond lengths (Å) and energies (kJ mol^{-1}) given by different functionals and basis sets for [LFe(Cl)]$^{+}$

Functional	Crystal Structure	BP86	BP86	B3LYP	B3LYP	B3LYP
Basis set		II	III	I	II	III
E(HS-LS)/ kJ mol^{-1}	HS more stable	−31	−42	+51	+51	+59
Fe-Cl	2.42	2.30	2.28	2.31	2.33	2.31
Fe-N^{1}	2.36	2.46	2.46	2.43	2.46	2.46
Fe-N^{2}	2.19	2.25	2.23	2.22	2.26	2.24
Fe-N^{3a}	2.14	2.20	2.15	2.22	2.25	2.22
Fe-N^{3b}	2.18	2.24	2.17	2.26	2.29	2.26
Fe-N^{5}	2.13	2.18	2.12	2.18	2.23	2.18

Key to the basis sets used in Table 3-1

I	II	III
Fe,Cl=6-31G* C,N=6-31G H,O=3-21G	Fe=LanL2DZ Other atoms=6-31G*	All 6-31G*

As Table 3-1 shows, calculations done with the BP86 functional are unable to correctly predict that the high spin state is more stable, consistent with the observation of other groups that hybrid functionals are better at predicting this gap than pure ones.[1] As spin state is related to reactivity, and expected to play a key role in the reaction pathways being studied, we decided the hybrid functional B3LYP was more appropriate. The calculations where the LanL2DZ effective core potential and basis set are used on Fe predict longer Fe-N bonds than the methods using the 6-31G* basis set on Fe. Of the large and small all-electron basis sets (I and III), there is very little difference in the geometry of the two species. We chose to use set III despite the fact that it is slightly more computationally demanding as this is consistent with what the Comba group are using, and allows us to directly compare results.

The model complex we have used for the calculations omits the ester chains that are coordinated to the ligand backbone, and replaces them with hydrogen atoms. This simplification was made to enhance computational efficiency by reducing the number of atoms, and therefore basis functions, in the calculation. In addition, inclusion of the ester groups would have posed addition questions about their orientation.

Further simplifications to the model were avoided. The most simple models possible, where nitrogen donors are replaced by ammonia for the amine donors, and imine for the pyridine rings, was avoided for several reasons, the most important of which is that the bispidone ligand backbone enforces the orientation of the pyridine rings. In the absence of the backbone, the pyridine rings (or imine groups) rotate by approximately 90° so they are in the same configuration as the N2Py3u ligand. Furthermore, the π-donor and acceptor abilities of double bonds and aromatic species are different, and it was felt that truncation of the ligand could potentially result in a qualitatively different potential energy surface being described, especially in terms of how strongly ligands are bound and which spin states are preferred.

Where solvent effects have been taken into consideration, the Conductor like Polarisable Continuum Model (C-PCM) has been used as implemented in Gaussian 03, revision B.03. Where hydrogen atoms are not part of the ligand backbone, but rather they are from solvent or the ligand in the sixth coordination site (e.g. H_2O_2, H_2O) they are explicitly included in the calculation. Otherwise the default treatment of the hydrogen atom being incorporated into a modified sphere of the heavy atom it is coordinated to is used.

3.7 Proposed Route for the Formation of $[LFe(O)]^{2+}$ from $[LFe(H_2O_2)]^{2+}$

In the subsequent sections, we examine the electronic structure of the $[LFe(H_2O_2)]^{2+}$ complex (where L = N2Py3o), and consider various possible routes for its decomposition to $[LFe(O)]^{2+}$. In particular, we will pay careful attention to the role of different spin states, and of water in the second coordination sphere. In the initial sections we describe the electronic structure of the two limits, $[LFe(H_2O_2)]^{2+}$ and $[LFe(O)]^{2+}$, and then consider different mechanisms for their interconversion.

3.7.1 Electronic Structure of the H_2O_2 Complex: $[LFe^{2+}(H_2O_2)]^{2+}$

The geometry, energy and electronic structure of $[LFe(H_2O_2)]^{2+}$ have been optimised for the singlet (S=0), triplet (S=1) and quintet (S=2) spin states. Structures and relative

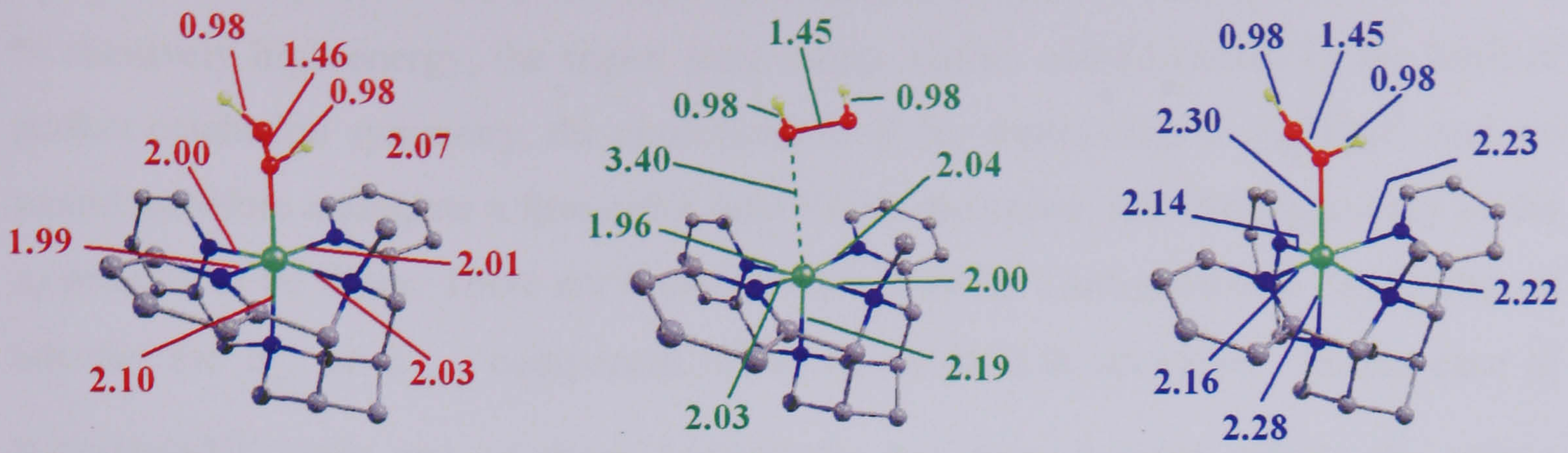

Singlet, S=0	Triplet, S=1	Quintet, S=2
E = +32.5 kJ mol^{-1}	E = +39.7 kJ mol^{-1}	E = 0.0 kJ mol^{-1}

Figure 3-18 – Geometries (bond lengths in Å) and relative energies of $[LFe(H_2O_2)]^{2+}$ {original in colour}

Of the three spin states, the quintet is clearly the most stable, lying 32.5 kJ mol^{-1} below the singlet and 39.7 kJ mol^{-1} below the triplet. The preference for the high spin state is consistent with the low-field nature of the donor set, which leads to a relatively small splitting between the t_{2g}- and e_g-type orbitals. A comparison of the structures of the singlet and quintet states reveals a significant lengthening of all Fe-N and Fe-O bonds in the latter, consistent with the occupation of the Fe-N and Fe-O antibonding ($d_{x^2-y^2}$ and d_{z^2}) orbitals (127a α and 129a α in Figure 3-19 (quintet)). In contrast, the bond lengths in the ligands are largely unaffected by the change in multiplicity. The O-O bond length of 1.46 Å in the singlet state is marginally longer than in the quintet (1.45 Å), due to the more effective back-donation into the O-O σ* orbital from the filled t_{2g} shell in the former. Solomon, Que and co-workers have observed similar trends in Fe^{3+}OOR (R=alkyl group, H) complexes, where the Fe-O bond is relatively strong, and the O-O bond relatively weak in the low-spin complexes compared to the high spin analogues.[69] In the present case, however, the mixing between t_{2g} and O-O σ * levels is very small (see 125a – 127a for the singlet), and the influence on the O-O bond length is minor. Instead, the O-O σ* orbital mixes with the higher energy, vacant d_{z^2} orbital which has no effect on O-O bond length.

Thus far we have focussed exclusively on the two lowest-energy spin states, the singlet and the quintet. The triplet state may, however, play an important role in the decomposition of $[LFe(H_2O_2)]^{2+}$ to $[LFe(O)]^{2+}$ because, as we show in the next section, the latter has a triplet ground state. Any concerted pathway must therefore involve a

switch to the triplet surface at some point along the reaction coordinate, and so, despite its relatively high energy, the triplet state merits further consideration. In the limit of perfect octahedral symmetry, the configuration of the triplet state is $(t_{2g})^5(e_g)^1$, and we would therefore anticipate a first-order Jahn-Teller distortion, and the degeneracy of the e_g orbitals to be lifted. There are therefore two possible configurations, depending on whether the d_{z^2} or $d_{x^2-y^2}$ component of the e_g manifold is occupied. In the case of $[LFe(H_2O_2)]^{2+}$ only one of these possibilities has been located, where the spin-α component of the d_{z^2} orbital is filled. The very long Fe-O distance of 3.40 Å indicates that the hydrogen peroxide is essentially unbound, and the iron coordination geometry can be described as a square based pyramid.

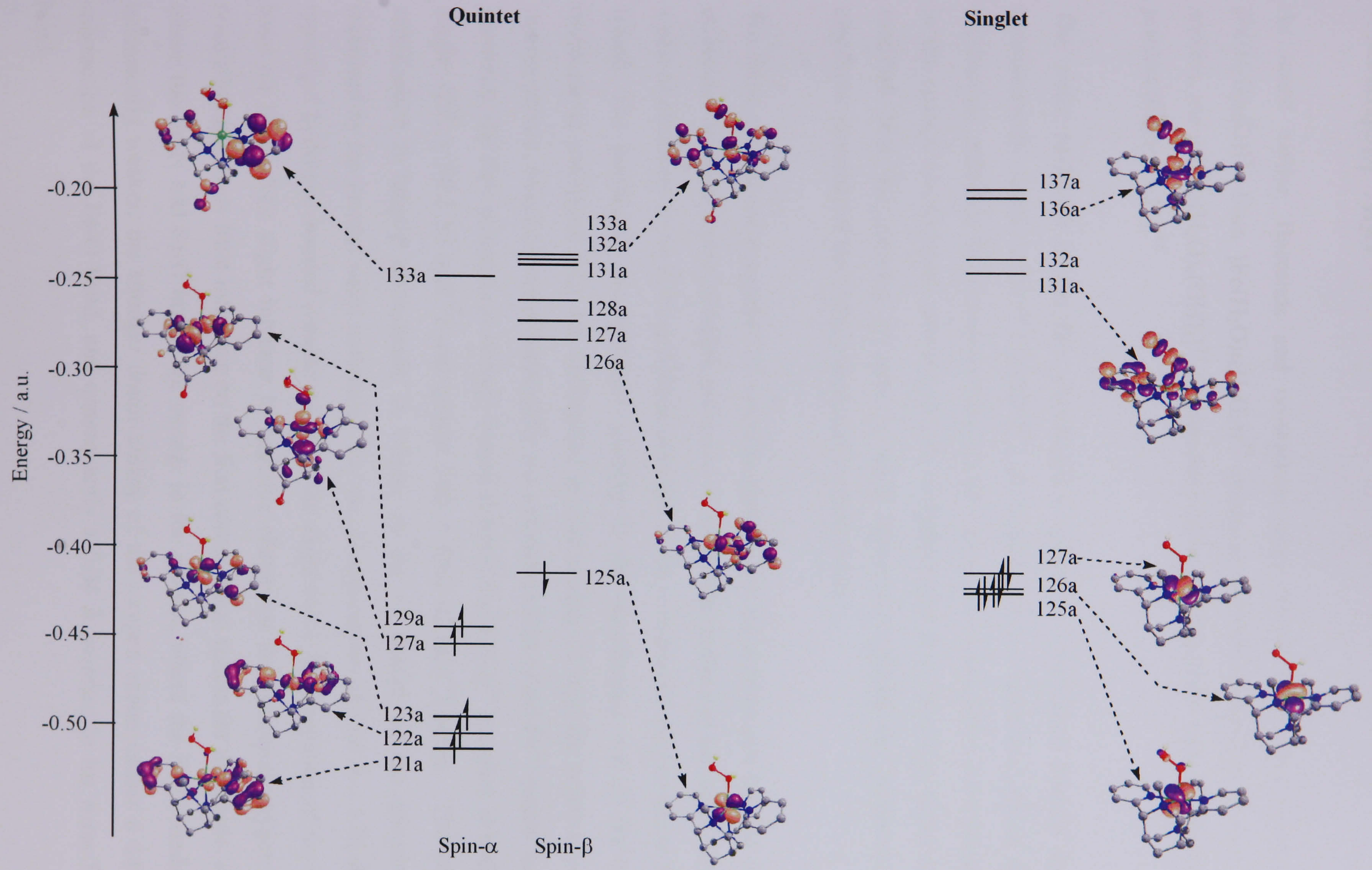

Figure 3-19 – Molecular orbital diagram showing selected orbitals for the singlet and quintet spin states of $[LFe(H_2O_2)]^{2+}$ {original in colour}

3.7.1.1 Influence of H_2O in the Second Coordination Sphere: Electronic Structure of $[LFe(H_2O_2)]^{2+}.H_2O$

As noted earlier, Baerends and co-workers have shown that the formation of $[Fe(H_2O)_5(O)]^{2+}$ from $[Fe(H_2O)_5(H_2O_2)]^{2+}$ proceeds without generation of a radical species, via an $[Fe(H_2O)_4(OH)_2]^{2+}$ intermediate which subsequently decomposes to the product (Figure 3-15).[66]

The water molecule in the first coordination sphere – a structural feature that is conspicuously absent in the $[LFe(H_2O_2)]^{2+}$ of interest here – is therefore critical to the mechanistic pathway. In subsequent sections we will examine whether a water molecule in the second coordination sphere can play a similar role. It is therefore important to establish how the presence of such a water molecule perturbs the geometry and electronic structure of the H_2O_2 complex described above.

We have considered a number of possible geometries for a hydrogen-bonded water molecule, the most stable of which proves to be where the oxygen of the water donates a pair of electrons to the hydrogen atom attached to the coordinated oxygen of the H_2O_2 ligand. The preference for hydrogen-bonding to the coordinated end of the H_2O_2 molecule is consistent with the anticipated greater acidity of this site relative to the remote proton, which is less influenced by the inductive effect of the Fe^{2+} centre. In this geometry, the H_2O molecule is strongly bound to the $[LFe(H_2O_2)]^{2+}$ complex in both the singlet (ΔE = 90.2 kJ mol^{-1}) and quintet (ΔE = 88.2 kJ mol^{-1}) states. The strong stabilisation is largely electrostatic in origin, as the +2 charge on the complex is stabilised by the neutral water molecule. The O…H separations of 1.66 Å – 1.72 Å are typical of hydrogen-bonded complexes, as is the slight (0.03 Å) elongation of the O-H bond on H_2O_2. The slight increase in negative charge on the proximal oxygen that results has relatively little influence on the first coordination sphere for the singlet state, where the Fe-N and Fe-O bonds are strong. In the quintet, where the Fe-L bonds are intrinsically weaker. the stronger donor ability of the oxygen centre causes a 0.08 Å contraction of the Fe-O bond, and consequently a 0.04 Å increase in the *trans* Fe-N bond.

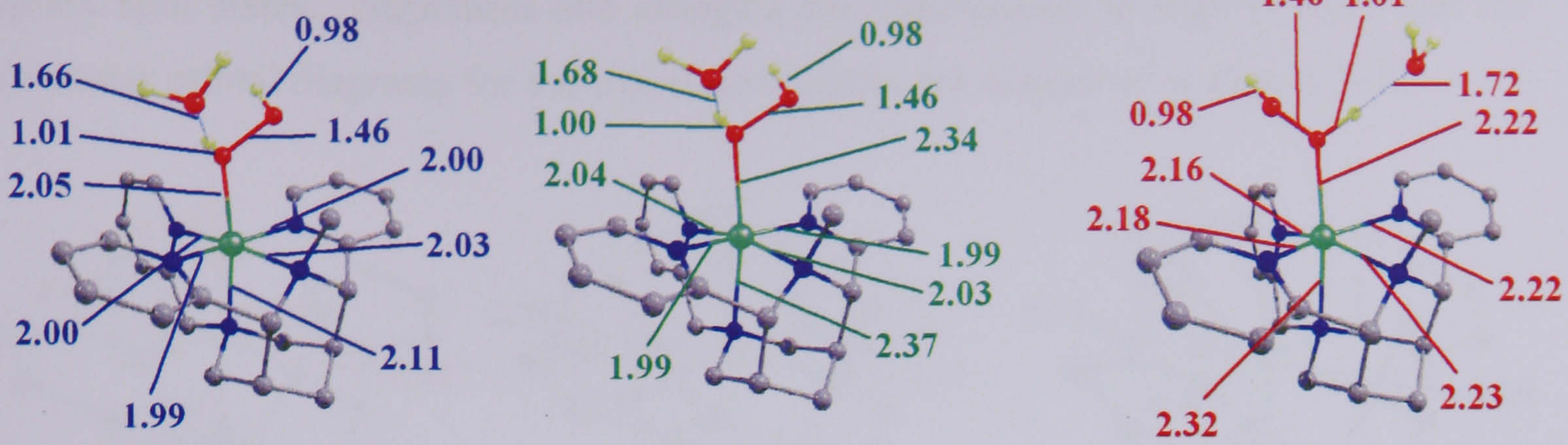

Singlet, S=0
$E = +30.5\ kJ\ mol^{-1}$

Triplet, S=1
$E = +50.7\ kJ\ mol^{-1}$

Quintet, S=2
$E = 0\ kJ\ mol^{-1}$

Figure 3-20 – Optimised geometries (bond lengths in Å) and relative energies of $[LFe(H_2O_2)]^{2+}.H_2O$. {original in colour}

The influence of the water molecule is most dramatic in the triplet state, where the Fe-O bond contracts significantly from 3.40 Å to 2.34 Å. The overall coordination geometry around the iron centre therefore changes from a square based pyramid with a loosely coordinated H_2O_2 molecule in the vacant coordination site, to an octahedral species with a Jahn-Teller distortion along the Fe-O axis. The Fe-N_{trans} bond length increases by 0.18 Å due to the increased *trans* effect as the Fe-O distance decreases and the oxygen is able to push more electron density into the d_{z^2} orbital.

The origin of the dramatic changes in the triplet state can be traced to the intrinsic weakness of the Fe-O bond: relatively small perturbations due to hydrogen bonding and electrostatic stabilisation can cause large changes in structure. The slight increase in electron density at the coordinated oxygen due to the hydrogen bond is clearly sufficient to enable the H_2O_2 ligand to compete more effectively with the *trans* amine ligand.

3.7.2 Geometry and Electronic Structure of $[LFe(O)]^{2+}$

In the previous section we have studied the geometries and relative energies of different spin states of the reactant species, $[LFe(H_2O_2)]^{2+}$. We now turn our attention to the product, $[LFe(O)]^{2+}$, before evaluating possible pathways for the interconversion of the two species. Our initial discussion again focuses on the isolated species before we consider the influence of second coordination sphere water molecules. As for the reactant, the structure of $[LFe(O)]^{2+}$ has been optimised for the singlet, triplet and

quintet spin states. Structures and energies are summarised in Figure 3-21, and the molecular orbital diagrams for the triplet and quintet are compared in Figure 3-22.

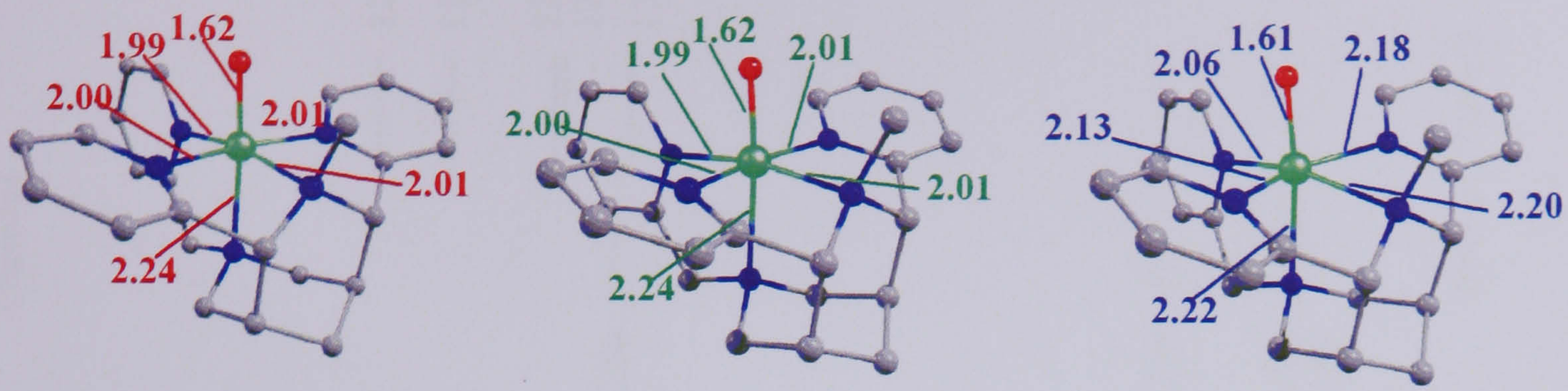

Singlet, S=0	Triplet, S=1	Quintet, S=2
E = +38.1 kJ mol^{-1}	E = 0 kJ mol^{-1}	E = 19.9 kJ mol^{-1}

Figure 3-21 – Geometries (bond lengths in Å) and Energies of $[LFe(O)]^{2+}$ for singlet, triplet and quintet spin states {original in colour}

Of the three states, the triplet is the most stable, followed by the quintet, and then the open shell singlet. A closed shell singlet has also been located but is much higher in energy (>120 kJ mol^{-1}) and therefore has not been considered here. For this reason we will mainly focus attention on the first two of these. In the triplet ground state there are two Fe-based electrons paired in the d_{xy} orbital (117a α and 120a β), which is orthogonal to the Fe-O bond, while the remaining two occupy the spin-α components of the Fe-O π* orbitals (d_{xz} and d_{yz}, 121a α and 122a α). The singlet complex has an almost identical electronic description to this, but the two electrons in the Fe-O π* orbitals are now anti-ferromagnetically coupled. In the quintet, in contrast, the spin-α component of the Fe-N antibonding $d_{x^2-y^2}$ orbital (123a) is occupied, leading to a significant elongation of the *cis* Fe–N bonds. The Fe-O bond, however, is almost entirely unaffected by the change in spin state as the d_{z^2} orbital (125a, α) remains unoccupied in both cases. In both the triplet and the quintet cases, the d_{xz} and d_{yz} orbitals are singly occupied so the amount of Fe-O π bonding remains fairly constant. In the singlet state two electrons are paired in one of the two Fe-O π* orbitals(d_{xz} or d_{yz}), giving rise to a structure that is very similar to the triplet, but at much higher energy. In the literature, there are several DFT studies on $Fe^{4+}O$ complexes, and these also suggest that the Fe-O bond length is unaffected by a switch from the triplet to quintet manifold.[70]

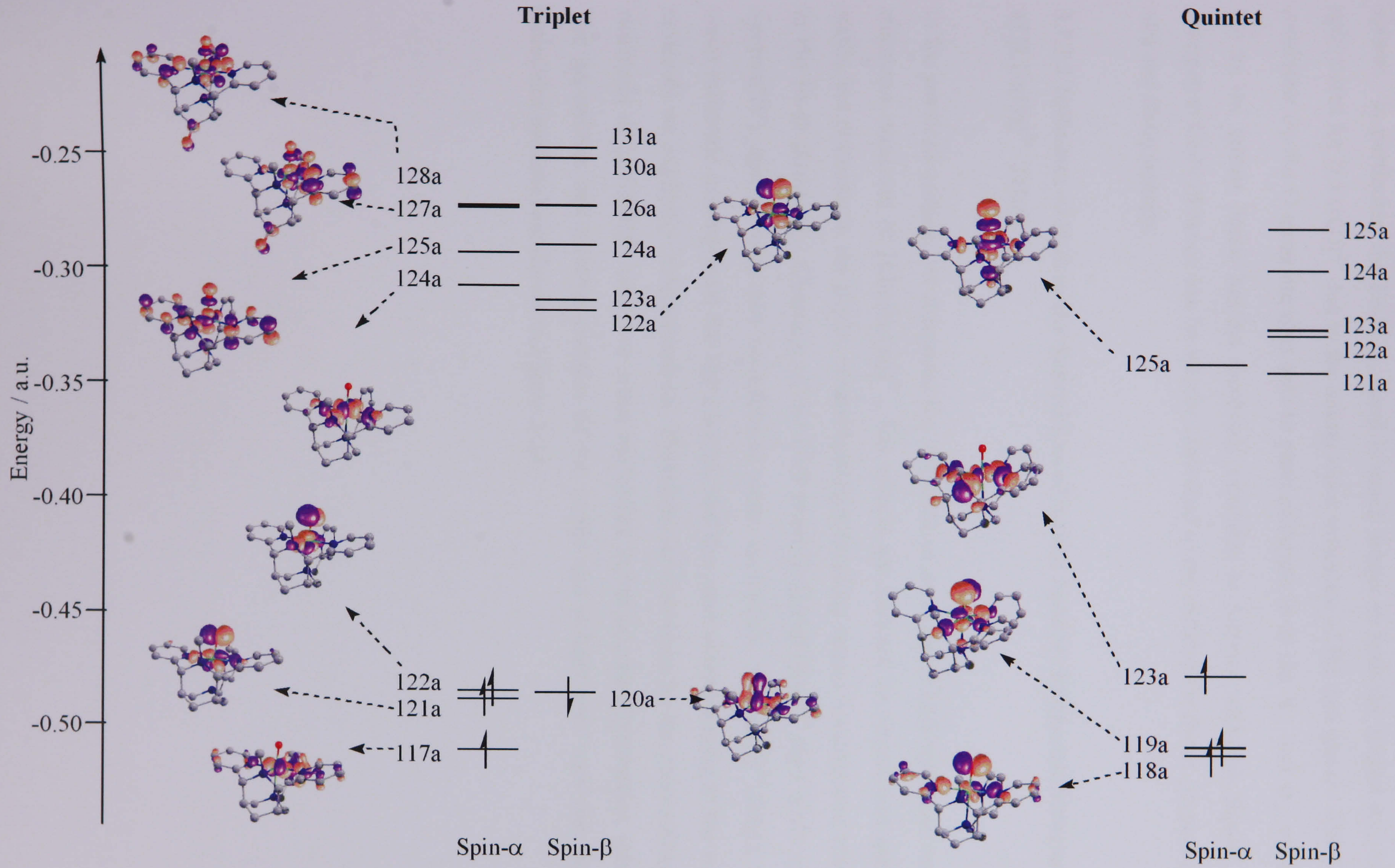

Figure 3-22 – MO diagram showing selected MOs of Triplet and Quintet spin states of $[LFeO]^{2+}$ {original in colour}

A comparison of $[FeL(H_2O_2)]^{2+}$ and $[FeL(O)]^{2+}$ complexes shows that the oxidation of the metal centre has a significant impact on the other ligands in the first coordination sphere. In particular, the Fe-N_{trans} bond is much longer in both the singlet and triplet spin states for $[LFe(O)]^{2+}$ due to the strong *trans* influence of the oxo group. The filled π-orbitals on the O atom are also able to push electrons in to the d_{xz} and d_{yz} orbitals, but as the amine donor has no π-orbitals available to interact with this ligand, the changes in Fe-N distance can be wholly attributed to the different σ-donor properties of oxo and H_2O_2 ligands.

3.7.2.1 Influence of H_2O in the Second Coordination Sphere: Electronic Structure of $[LFe(O)]^{2+}.\ 2H_2O$

In the previous section, we discussed the influence of an external H_2O molecule on the electronic structure of $[LFe(H_2O_2)]^{2+}$. The effects are minimal in singlet and quintet states, but dramatic in the triplet, where hydrogen bonding causes a substantial change in the Fe-O distances. Cleavage of the O-O bond in $[LFe(H_2O_2)]^{2+}.H_2O$ leads to an oxoiron(IV) species with two coordinated water molecules, $[LFe(O)]^{2+}.2H_2O$, one water molecule coming from the H_2O_2 ligand, and the other corresponding to the water molecule we explicitly included before. Therefore, we now consider the geometries and structures of $[LFe(O)]^{2+}$ with *two* water molecules in the second coordination sphere. The geometries and relative energies of the triplet and quintet spin with two water molecules included are shown in Figure 3-23.

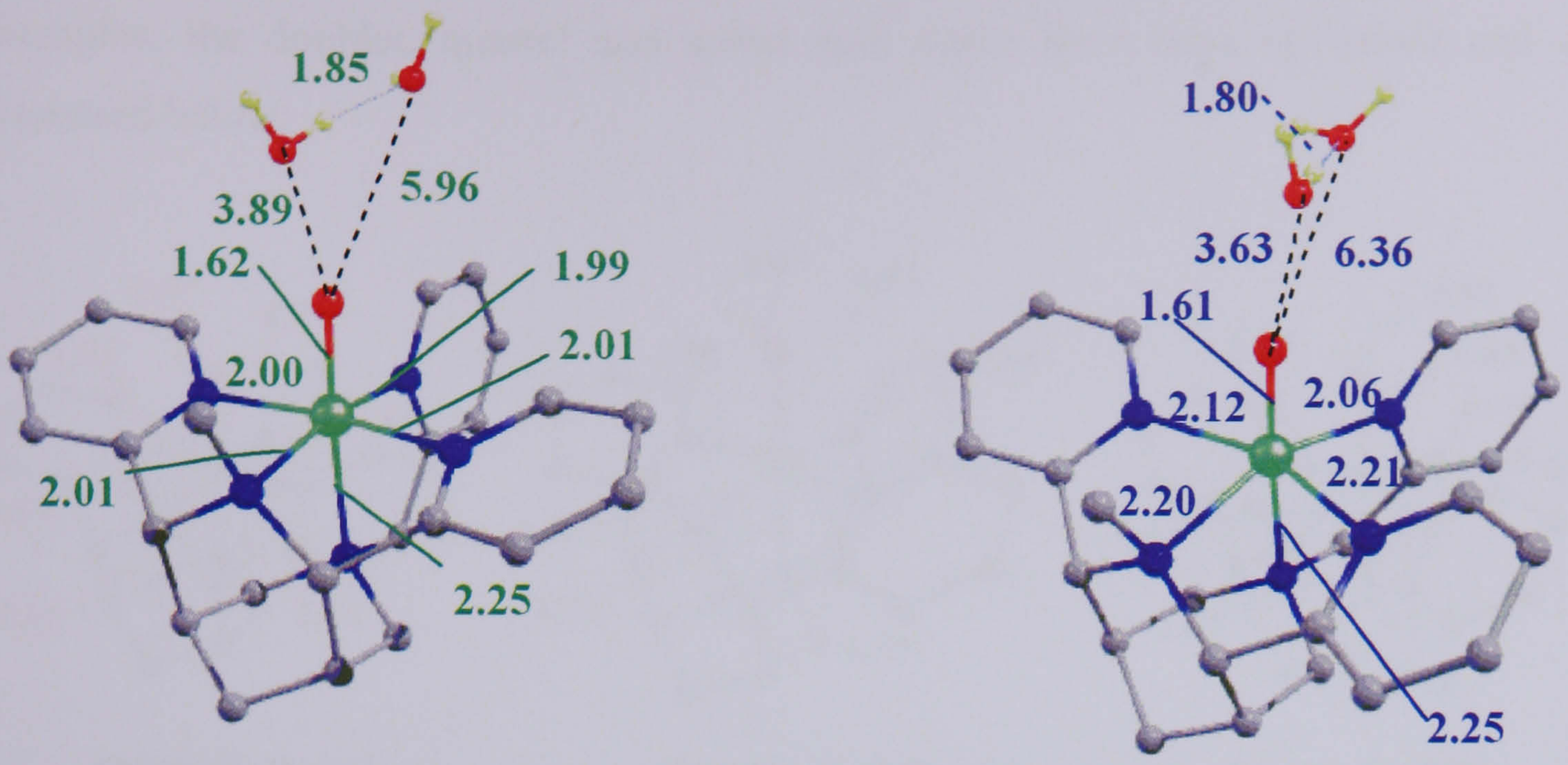

Triplet, S=1
$E = -98.9$ kJ mol^{-1}

Quintet, S=2
$E = -78.3$ kJ mol^{-1}

Figure 3-23 – Geometries (bond lengths in Å) and energies (reported with respect to quintet $[LFe(H_2O_2)]^{2+}.H_2O$) of the triplet and quintet spin states of $[LFe(O)]^{2+}.2H_2O$ {original in colour}

Inclusion of the two water molecules does not have much impact on the relative energies of the different spin states, with the quintet +20.6 kJ mol^{-1} higher in energy, and the singlet +38.9 kJ mol^{-1} higher in energy than the triplet respectively. In contrast to the H_2O_2 complexes, the presence of water molecules does not cause any significant changes in the first coordination sphere, with bond lengths only varying by up to 0.01 Å. The orientation of the water molecules is similar for all spin states, and they are aligned such that they are essentially a dimer of waters with one molecule much closer to the oxo group than the other. For this water molecule, the oxygen atom, rather than the hydrogen, interacts with the oxo group – a clear reflection of the electron deficiency of the latter. The interactions are, however, clearly weak (O…O separations of ~3.5 Å) and this, combined with the intrinsically strong Fe-N and Fe-O bonds, means that the structural impact of electrostatic stabilisation and hydrogen bonding is relatively minor in this case.

3.7.3 Possible Intermediates in the Formation of $[LFe(O)]^{2+}$: $[LFe(OH)]^{2+}$ and OH•

One of the possible intermediates in the formation of $[LFe(O)]^{2+}$ from $[LFe(H_2O_2)]^{2+}$ is a $[LFe(OH)]^{2+}$ species, which could be formed along with an •OH radical by the homolytic cleavage of the O-O bond. We now consider the geometry and electronic

structure of the Fe^{3+} species without the presence of the OH radical. As for the previous examples, the doublet, quartet and sextet spin states have been optimised and are discussed below.

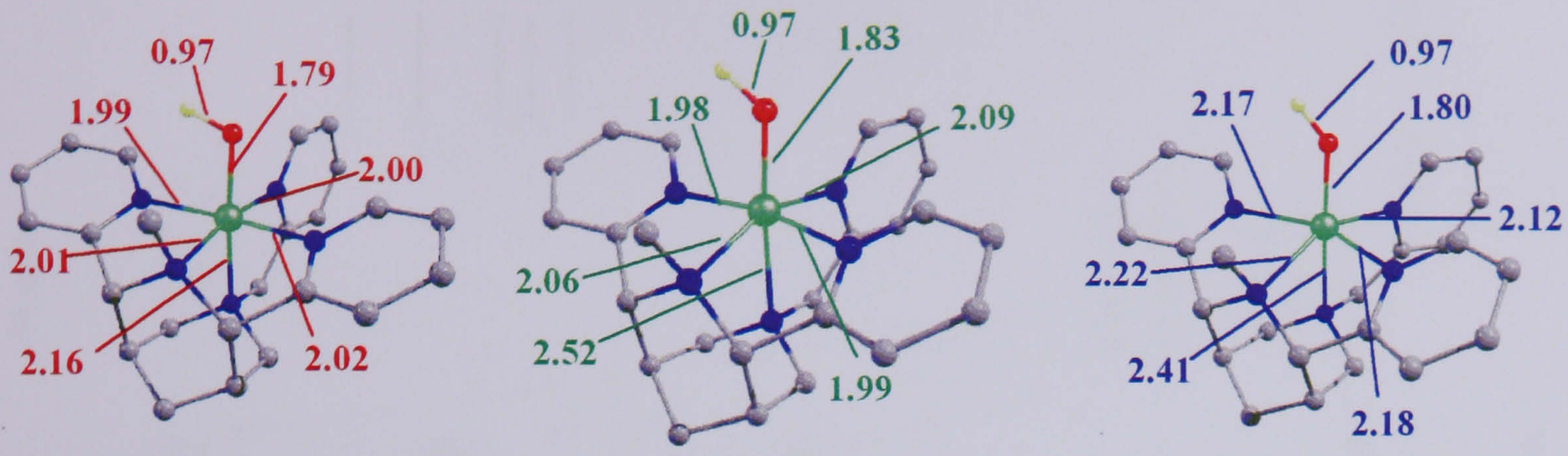

Doublet, S=1/2
E = +8 kJ mol^{-1}

Quartet, S=3/2
E = +55 kJ mol^{-1}

Sextet, S=5/2
E = 0 kJ mol^{-1}

Figure 3-24 – Geometries of the doublet, quartet and sextet minima (bond lengths in Å) {original in colour}

In the $[LFe(OH)]^{2+}$ intermediate, the Fe is in the +3 oxidation state. Therefore, the spin states accessible to the 5 d-electrons are a doublet (S=1/2), a quartet (S=3/2) and a sextet (5/2). The sextet ground state is marginally (8.3 kJ mol^{-1}) more stable than the doublet, while the quartet spin state, with only one of the e_g-like orbitals occupied, is high in energy and therefore it is not considered further. The similar energy of the doublet and sextet spin states means that small environmental effects may influence the ground state.

Molecular orbital diagrams for the doublet and sextet spin states are shown in Figure 3-25. In the sextet spin state, each of the spin-α d-orbitals is filled, and the equivalent MOs in the β manifold are all vacant. In contrast, in the doublet (low) spin state, there are 5 electrons that have to be shared between 3 spin-α and 3 spin-β t_{2g} like orbitals. Therefore, one of the spin-β orbitals is vacant, and as all three are of a similar energy, there are three different electronic configurations that are almost degenerate. Only one electronic configuration, shown in the MO diagram in Figure 3-25 has been located. The vacant spin-β orbital (123a), corresponding to d_{yz}, is destabilised by the strong π-donor effect of the OH ligand.

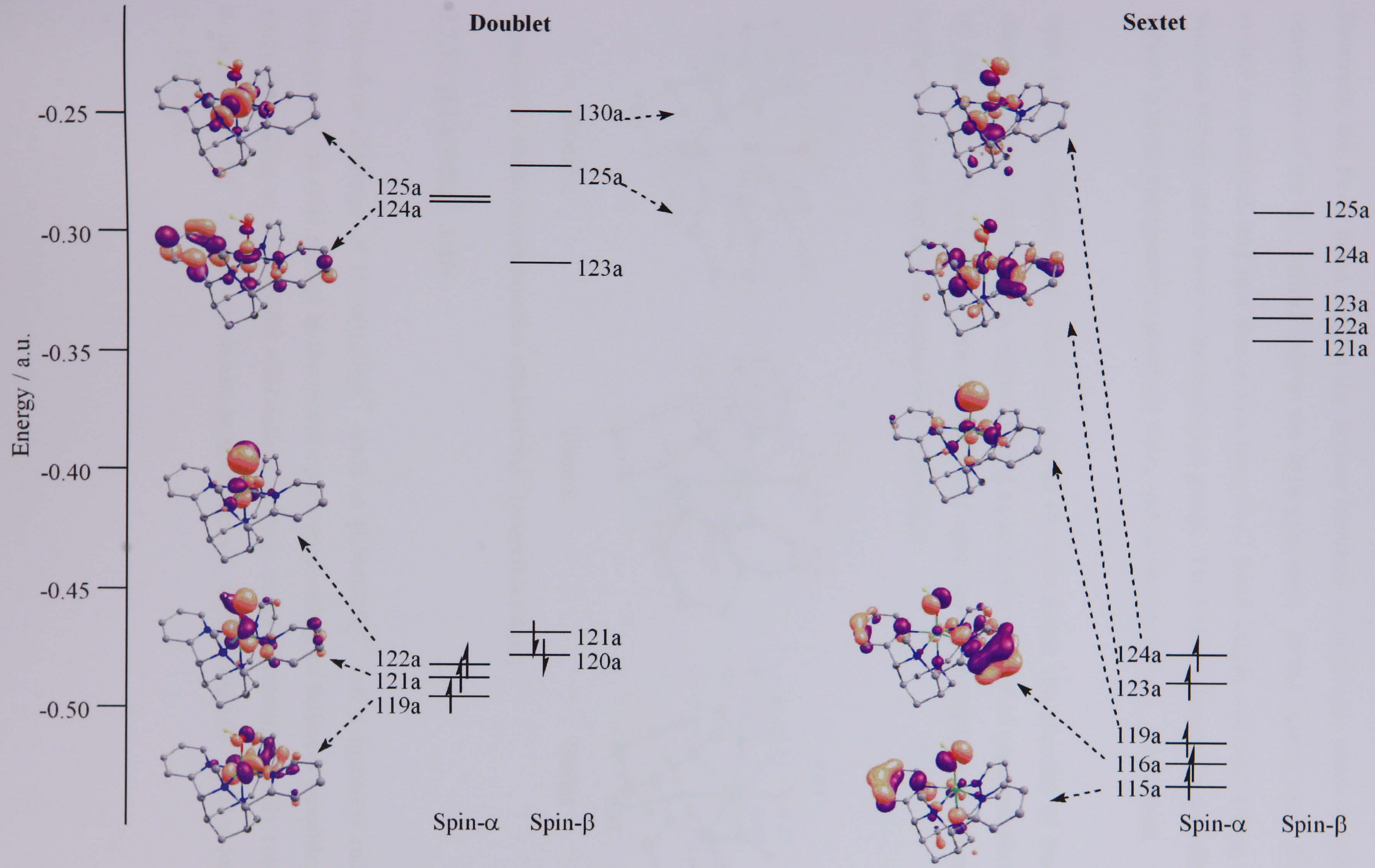

Figure 3-25 – MO diagrams (selected orbitals) of the doublet and sextet spin states of $[LFe(OH)]^{2+}$ {original in colour}

The relative geometries of the doublet and sextet spin states are consistent with the occupation of the e_g-like orbitals in the high spin state but not in the low spin state. The Fe-N bond lengths are significantly longer in the high spin state than the low spin state. However, the Fe-O bond lengths are almost identical in both spin states despite the occupation of the d_{z^2} orbital only in the high spin state. In the quartet state, the d_{z^2} orbital is occupied, and this results in a long Fe-O bond length, and also a long Fe-N distance for the amine *trans* to the hydroxyl group. The Fe-N distances for the nitrogen donors lying in the equatorial plane are short, indicating that the $d_{x^2-y^2}$ is vacant.

Spin densities (Figure 3-26) show that for all the spin states, the majority of the spin density is located on Fe, and is approximately equal to the number of unpaired electrons on this atom. In addition, there is significant spin density located on the O of the hydroxide ligand and this increases with multiplicity.

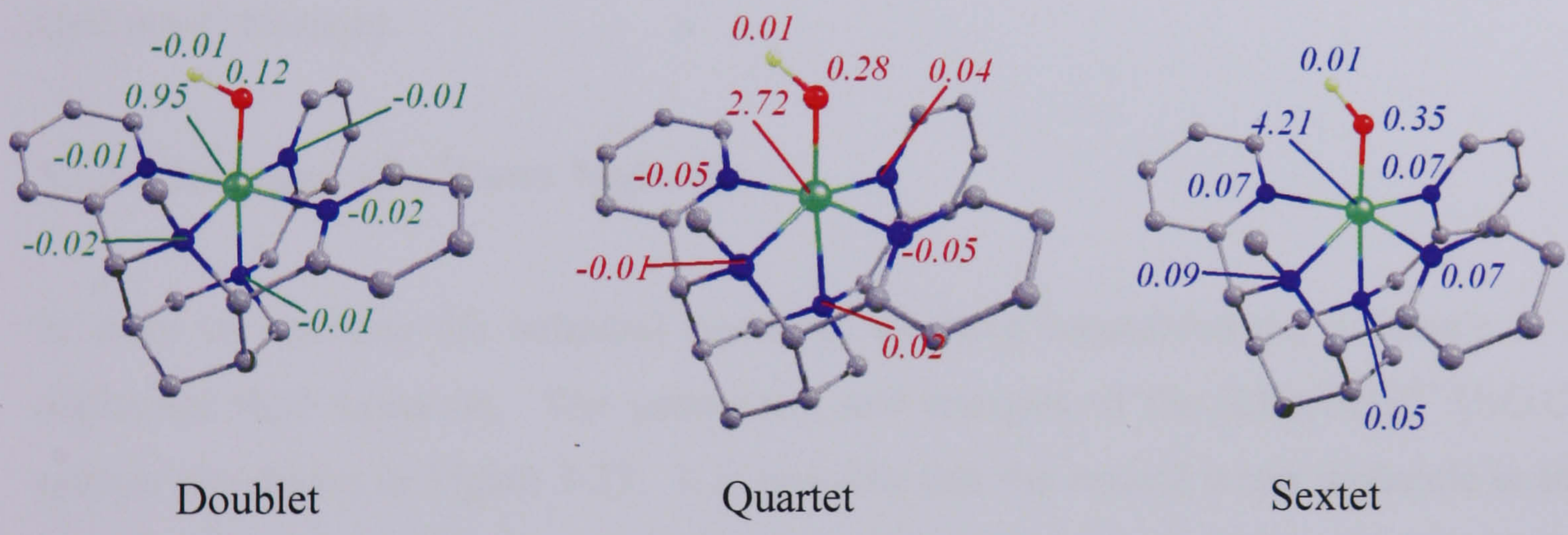

Doublet Quartet Sextet

Figure 3-26 – Mulliken spin densities of $[LFe(OH)]^{2+}$ {original in colour}

3.7.3.1 $[LFe(OH)]^{2+}$.OH•

Homolytic cleavage of $[LFe(H_2O_2)]^{2+}$ leads to $[LFe(OH)]^{2+}$ and a hydroxyl radical. Inclusion of the •OH radical in the model opens up a variety of different possible spin states depending on whether the •OH radical is ferro- or anti-ferromagnetically coupled to the $[LFe(OH)]^{2+}$ species which can, as noted above, itself be high (S = 1/2) or low (S = − 1/2) spin.

Table 3-2 – Possible spin states of $[LFe(OH)]^{2+}.H_2O.OH$

S ($[LFe(OH)]^{2+}$)	S (•OH)	Overall spin state
1/2	−1/2	0
1/2	+1/2	1
3/2	−1/2	1
3/2	+1/2	2
5/2	−1/2	2
5/2	+1/2	3

Therefore, there are potentially one open shell singlet, two triplets, two quintets and a septet spin state accessible. However, as we have already shown that the quartet spin state in isolation is high in energy, we do not expect it to participate, eliminating the need to consider one of the triplets and a quintet state. In the absence of a water molecule, attempts to locate these species failed as no minimum could be found and the O-O bond reformed.

3.7.3.2 Inclusion of a Water Molecule

In order to maintain the balanced equation, we have considered the influence of an additional H_2O molecule. The geometries and energies of the $[LFe(OH)]^{2+}:H_2O.OH$ species are shown in Figure 3-27. It is possible that the second water molecule is able to act as a hydrogen atom shuttle, linking the •OH radical to a hydrogen from the O that remains coordinated to the iron centre.

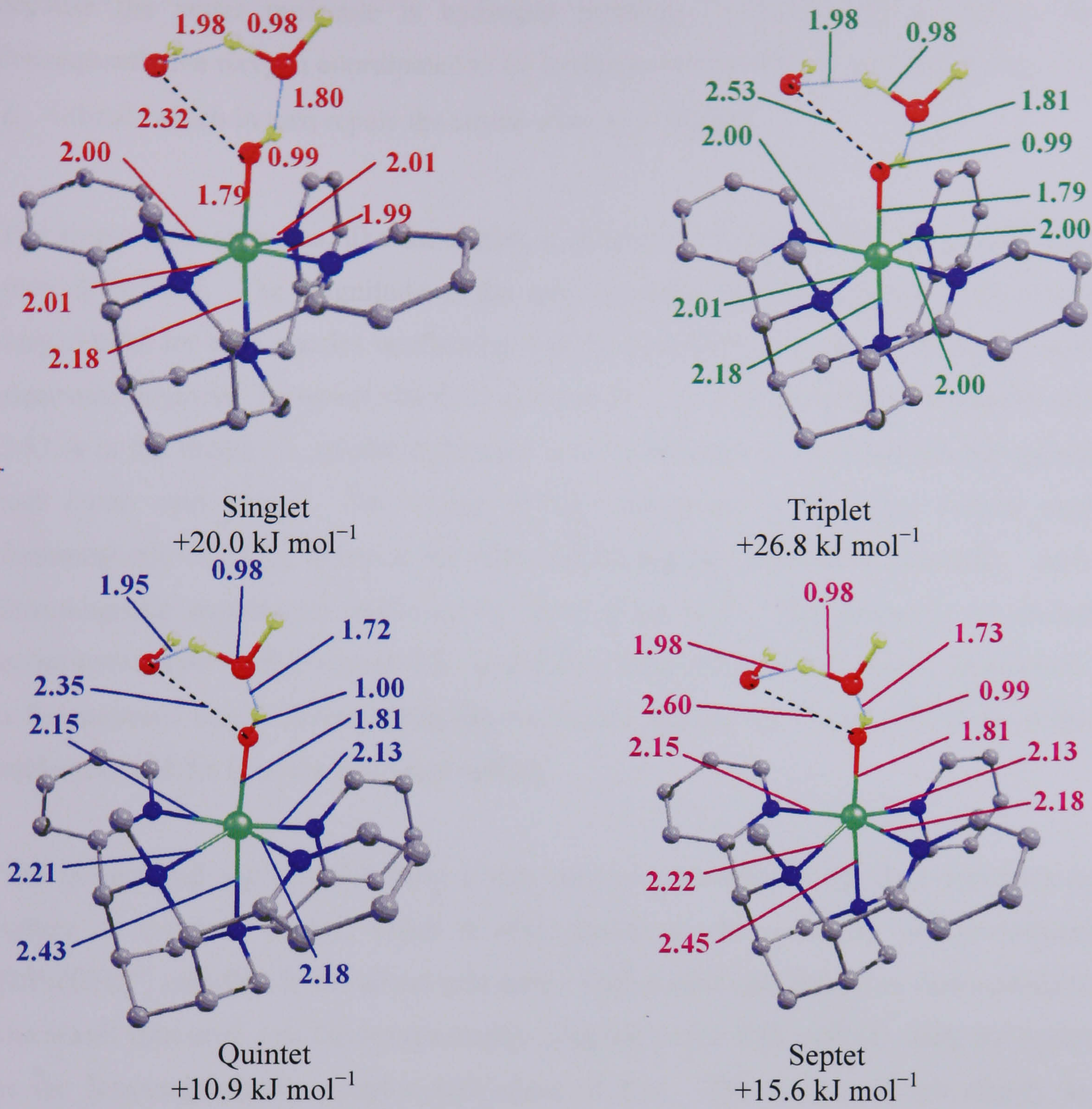

Figure 3-27 – Geometries (bond lengths in Å) and energies of the radical intermediates {original in colour}

3.7.3.3 Changes in Geometry when the Radical and Water Molecule are Included

When the water molecule and hydroxyl radical are included in the calculation, the geometry of the first coordination sphere of the iron centre does not change significantly. The triplet spin state (with a water molecule present) has a geometry consistent with the doublet spin state of $Fe^{3+}OH$, rather than the quartet, and is only 16 kJ mol^{-1} higher in energy than the quintet rather than being around 50 kJ mol^{-1} higher as would be expected if the iron centre was in the quartet spin state. In the triplet state, the Fe-O bond length is unchanged by the presence of the radical and a water molecule, although the Fe-N bond *trans* to this has increased very slightly in length. This is

because the water molecule is hydrogen bonding to the hydroxide ligand, and consequently the oxygen coordinated to Fe is able to donate more electron density to the d_{z^2} orbital, which in turn repels the amine *trans* to it slightly.

The singlet spin state has, like the triplet, a geometry consistent with the doublet spin state of $Fe^{3+}OH$. The magnitude of the spin densities, shown in Figure 3-28, is also very similar for both species confirming that the [LFe(OH)] fragments share the same electronic structure. However, the O-O distance is 2.32 Å in the singlet compared with 2.53 Å in the triplet. A similar difference in O-O distances is observed for the quintet and septet spin states. The origin of this difference is the ferro versus anti-ferromagnetic coupling between the •OH radical and the [LFe(OH)] fragment. Anti-ferromagnetic coupling is preferred by about 6 kJ mol^{-1}. The geometry of second coordination sphere of iron centre is similar for all the different spin states. In all cases, a 5-membered ring is formed from the hydroxide ligand, the O and a H of the water molecule, and the O of the hydroxyl radical.

The quintet and septet states have a very similar geometry of the first coordination sphere of the iron centre, which is also similar to the geometry of the isolated $[LFe(OH)]^{2+}$ complex in the sextet spin state. The quintet state therefore corresponds to the sextet spin state anti-ferromagnetically coupled to the •OH radical, while the septet is the ferromagnetically coupled equivalent of this. This is also shown clearly by examining the spin densities (Figure 3-28): in both the quintet and septet spin states the iron has net spin density of 4.2 units, almost identical to the value in the sextet spin state of isolated $[LFe(OH)]^{2+}$ (Figure 3-26). In the quintet spin state, the net spin density located on the hydroxyl radical is of the opposite spin to that on iron, while in the septet state it is the same spin as iron. However, the amount of spin density located on the O of the OH ligand is larger for the septet than for the quintet due to the partial formation of a covalent bond in the quintet spin state.

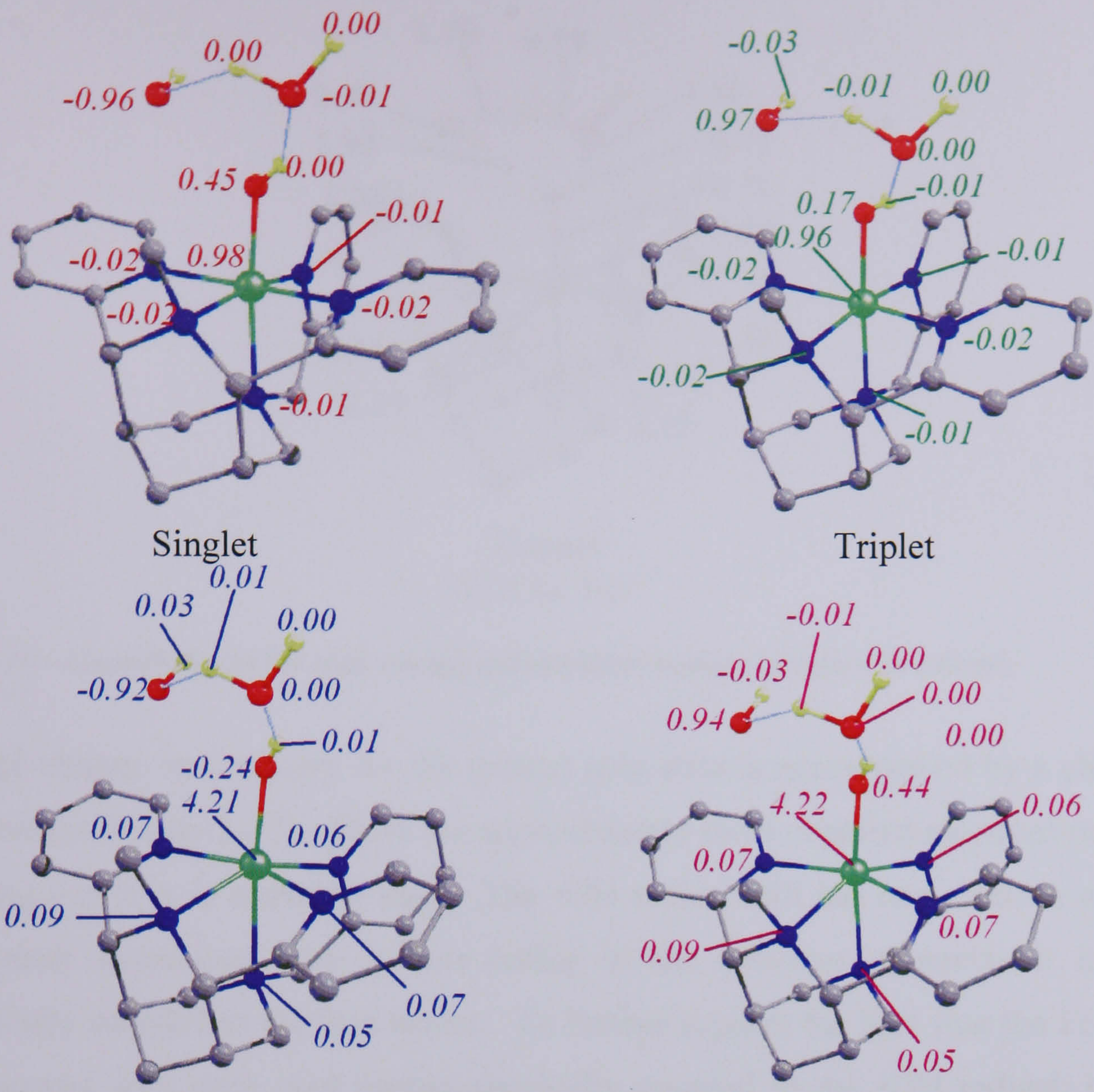

Figure 3-28 – Mulliken spin densities of $[LFe(OH)]^{2+}.OH.H_2O$ {original in colour}

A second minimum has been located for the quintet spin state, 43 kJ mol^{-1} higher in energy than the species discussed above. Upon rotation of the hydroxyl radical, a change in the geometry of the $[LFe(OH)]^{2+}$ fragment is trigged. The Fe-N_{trans} distance has decreased from 2.43 Å to 2.19 Å, and the Fe-O distance has decreased slightly from 1.81 Å to 1.79 Å. This change in geometry along the *z*-axis indicates that the occupation of the d_{z^2} orbital has decreased. The Fe-N bonds along the *x*-axis (connecting the two 'symmetry' related pyridine rings and the iron centre) have also decreased in length slightly.

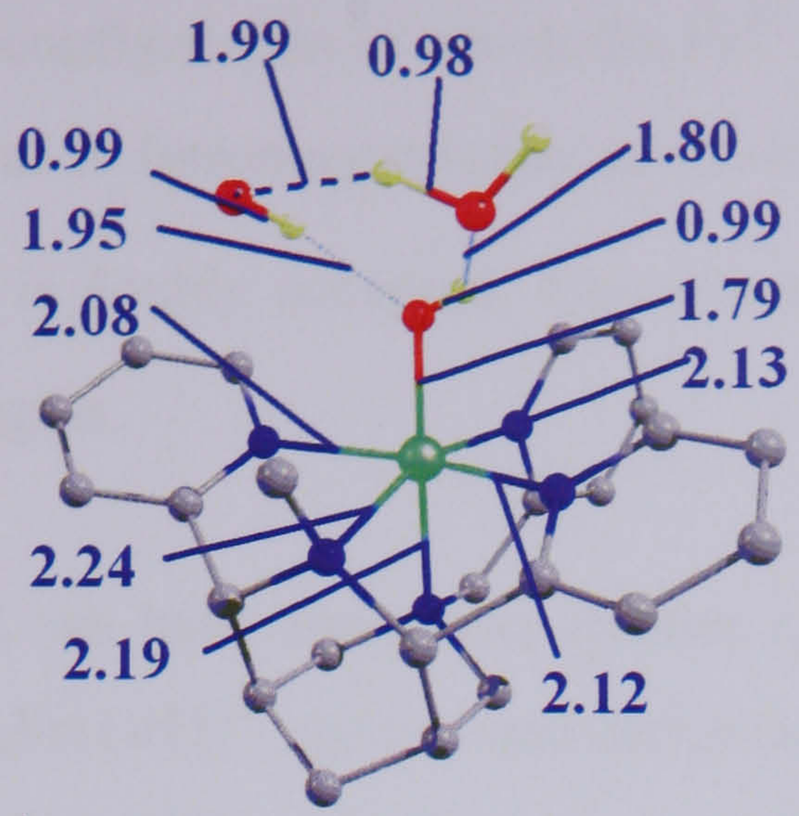

Quintet
+53.4 kJ mol^{-1}

Figure 3-29 – Geometries of the high energy quintet intermediate {original in colour}

The large change in geometry for the quintet spin state is accompanied by a change in spin densities (Figure 3-30). There are approximately three unpaired electrons on the Fe indicating that it is in a quartet state. The •OH radical still has one electron worth of spin density associated with it, but unlike in the previous geometry it is ferro-magnetically coupled to the iron centre. To further support the idea that the Fe is now in the quartet spin state, and ferromagnetically coupled to the •OH radical, the MO diagrams of the two quintet spin state geometries will be examined (Figure 3-31).

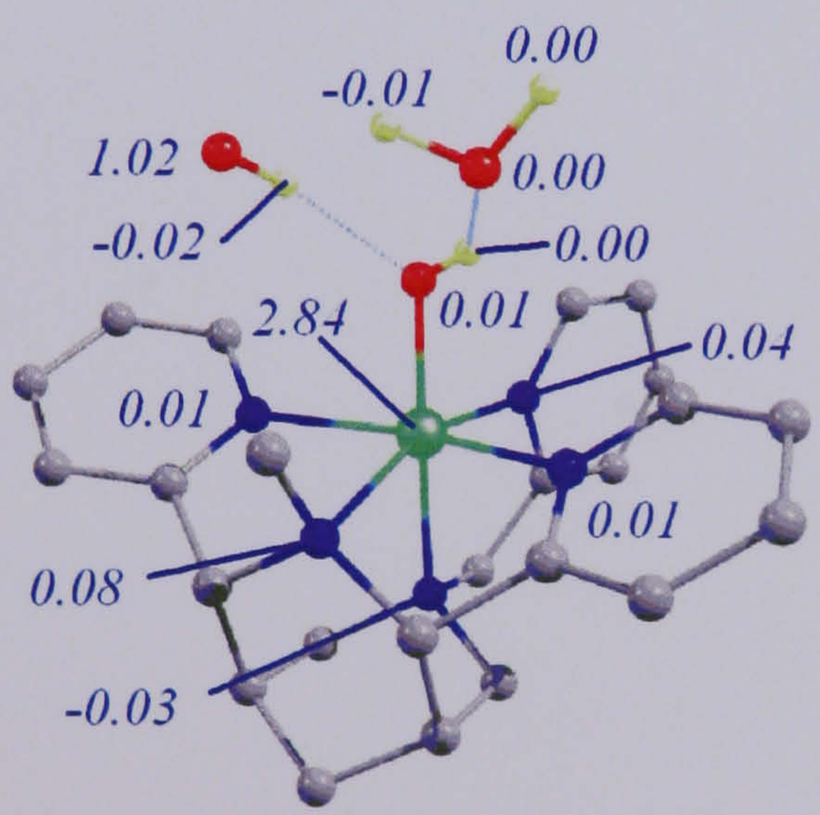

Figure 3-30 – Mulliken spin densities for the alternative geometry of quintet $[LFe(OH)]^{2+}.OH.H_2O$ {original in colour}

The more stable quintet geometry has all five spin-α d-orbitals occupied, and the spin-α OH radical is vacant. In the spin-β array, the d-orbitals are all vacant and the OH radical orbital is occupied. This configuration corresponds to Fe^{3+}, S = 5/2 anti-ferromagnetically coupling to the •OH radical. In contrast, the less stable

geometry has an electronic configuration in which the Fe^{3+} centre has an overall spin of S = 3/2, and the OH radical is ferromagnetically coupled to this. The d_{z^2} orbital is vacant, and the d_{xz} orbital is doubly occupied. This is consistent with the decrease in Fe-N_{trans} and Fe-O bond lengths.

As suggested in Table 3-2, we have found two quintet spin states – the more stable corresponding to a sextet $[LFe(OH)]^{2+}$ species anti-ferromagnetically coupled to the OH radical, and the higher energy species is quartet $[LFe(OH)]^{2+}$ fragment ferromagnetically coupling to the OH radical. For isolated $[LFe(OH)]^{2+}$, the energy difference between the sextet and quartet spin states is 55 kJ mol^{-1}. When coupled to an OH radical, this difference is reduced to 43 kJ mol^{-1} which is comparable to the difference in the isolated species. A similar change in electronic structure (from doublet $[LFe(OH)]^{2+}$ to quartet $[LFe(OH)]^{2+}$) was not observed on rotating the hydroxyl radical.

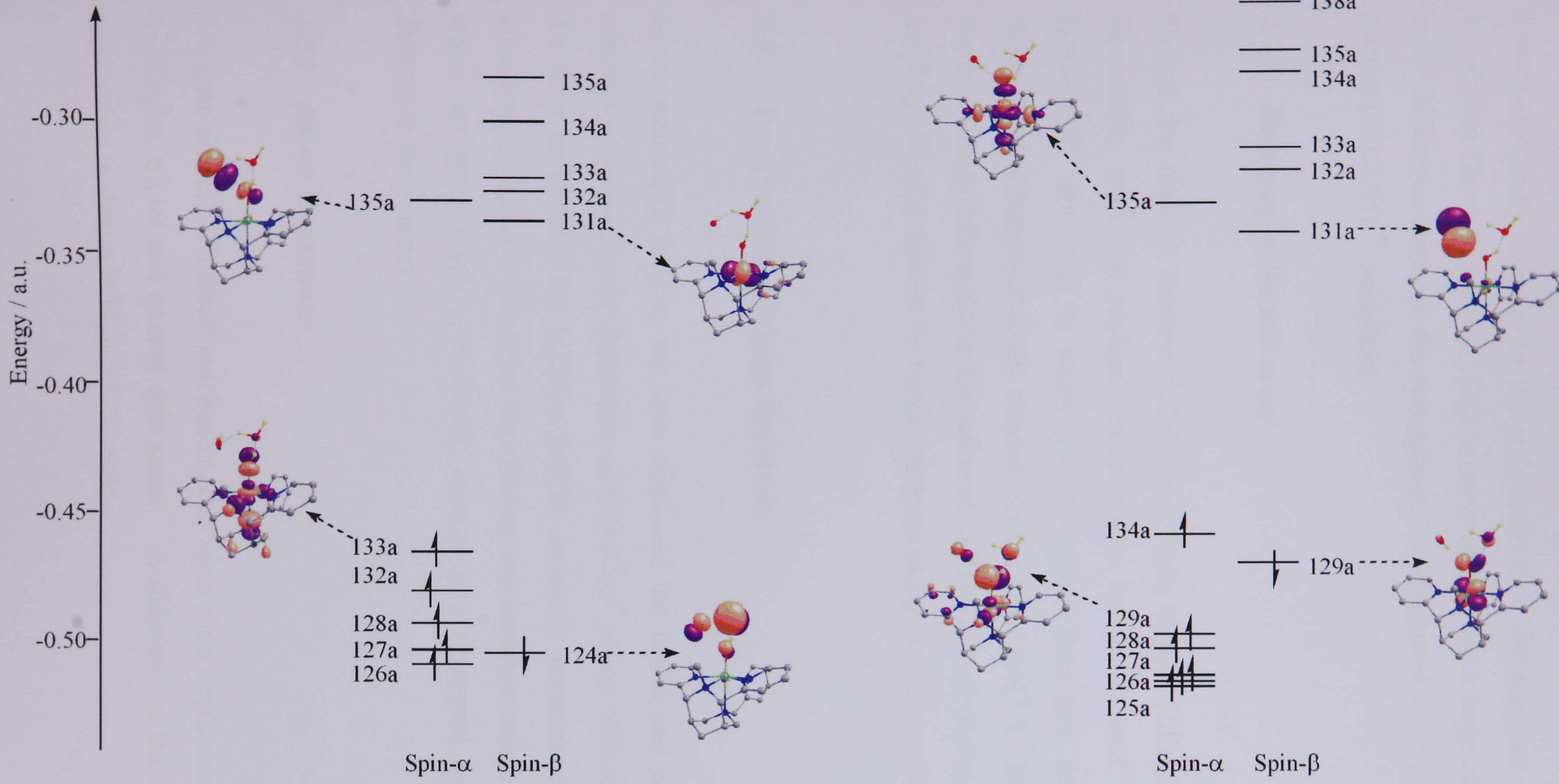

Figure 3-31 – MO diagram of the two different quintet geometries {original in colour}

The change in the orientation of the •OH radical in the quintet spin state leads to a change in the electronic configuration of the iron centre, from high spin anti-ferromagnetically coupled to the •OH radical, to intermediate spin ferromagnetically coupled to the •OH radical. This is accompanied by a large change in energy (43 kJ mol^{-1} difference between the two spin states, compared to 55 kJ mol^{-1} for the isolated quartet $[LFe(OH)]^{2+}$ complex).

3.7.4 Summary of Results so far

Overall the reaction between $[LFe]^{2+}$ and H_2O_2 to give $[LFe(O)]^{2+}$ and water is very favourable, with the products more stable by 99 kJ mol^{-1}. The formation of $[LFe(OH)]^{2+}$ and •OH is much less favourable than this, and only approximately thermoneutral compared to the reagents (ΔE = 11 kJ mol^{-1}). Therefore, irrespective of the mechanism followed, the formation of $Fe^{3+}OH$ and a hydroxyl radical is intrinsically unlikely. Should radicals be formed they are likely to further oxidise $[LFe(OH)]^{2+}$.

3.8 Possible Mechanisms Involved

In the preceding section, we have discussed the initial and final complexes on the reaction pathway for the formation of $[LFe(O)]^{2+}$ along with a possible intermediate. To fully understand the reaction profile, however, transition states also need to be considered. We have identified two distinct mechanisms: one is a two step mechanism where an intermediate is involved, another is a concerted mechanism which leads directly to the product.

3.8.1 Direct Mechanism

We have identified a direct mechanism that goes via a single transition state for each of the singlet, triplet and quintet spin states.* A summary of the energetics of the direct mechanism is shown in Figure 3-33, below.

In each spin state, the transition state geometry features an H_3O^+ molecule in close proximity to a coordinated OOH^-. The imaginary frequency involves the transfer of a proton from the H_3O^+ to the terminal O of OOH, after which H_2O is dissociated without barrier. The role of the second coordination sphere H_2O is therefore as a proton shuttle, transferring a proton from the proximal to the terminal oxygen. The role of the Fe centre in this mechanism is initially to act as a Lewis acid and make the hydrogen atom bound to the proximal oxygen more acidic, facilitating proton transfer. Only after the transition state does the iron centre play a role in electron transfer.

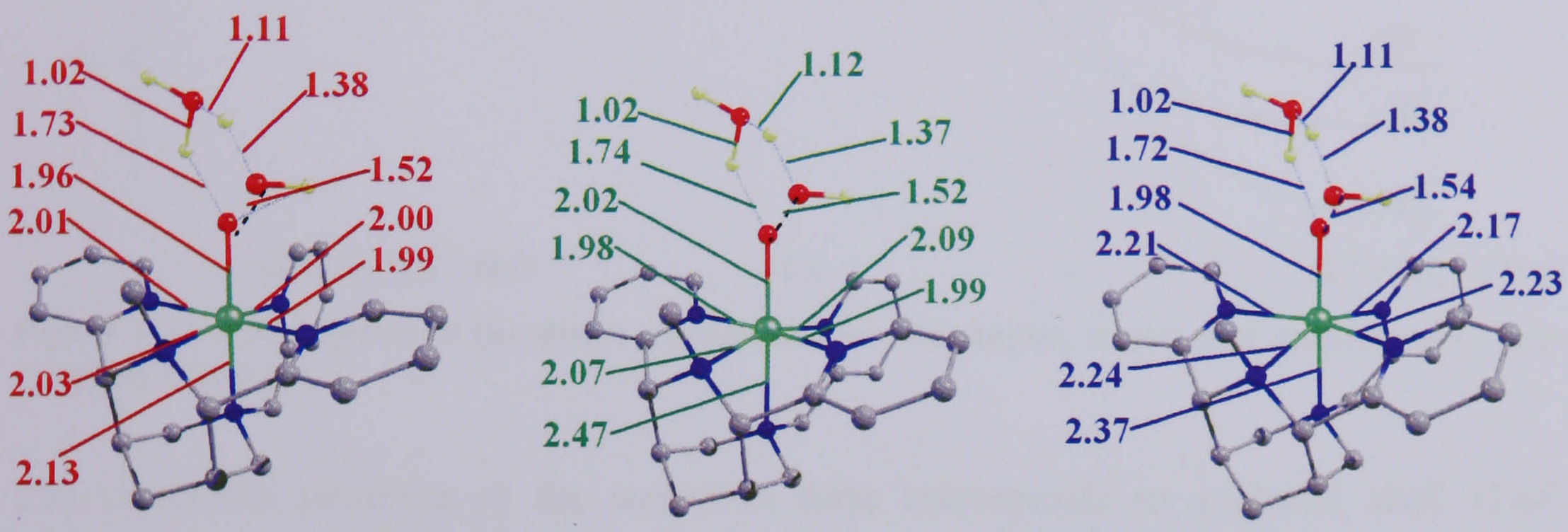

Singlet
$E = +130.1$ kJ mol^{-1}

Triplet
$E = +155.9$ kJ mol^{-1}

Quintet
$E = +101.3$ kJ mol^{-1}

Figure 3-32 – Geometries of the singlet, triplet and quintet transition state (bond lengths in Å) {original in colour}

The singlet spin state is never the lowest in energy on the PES, and so it is unlikely to play a role in this mechanism. Of the remaining spin states, the quintet TS is much lower in energy than the triplet TS, and so the reaction will follow the quintet surface until after the transition state, and will this spin state will therefore be rate-determining. The change in spin state from quintet to triplet does not occur until late in the reaction, and so it will not affect the kinetics or product distribution. To ascertain that the change in spin state does not require going via a high energy structure the minimum energy crossing point (MECP) for $[LFe(O)]^{2+}$ has been located, and is discussed later.

---

* The septet spin state is high in energy across the whole PES and there is no reason to believe that it may play a role in this reaction as both the septet starting complex and the product will be very high in energy.

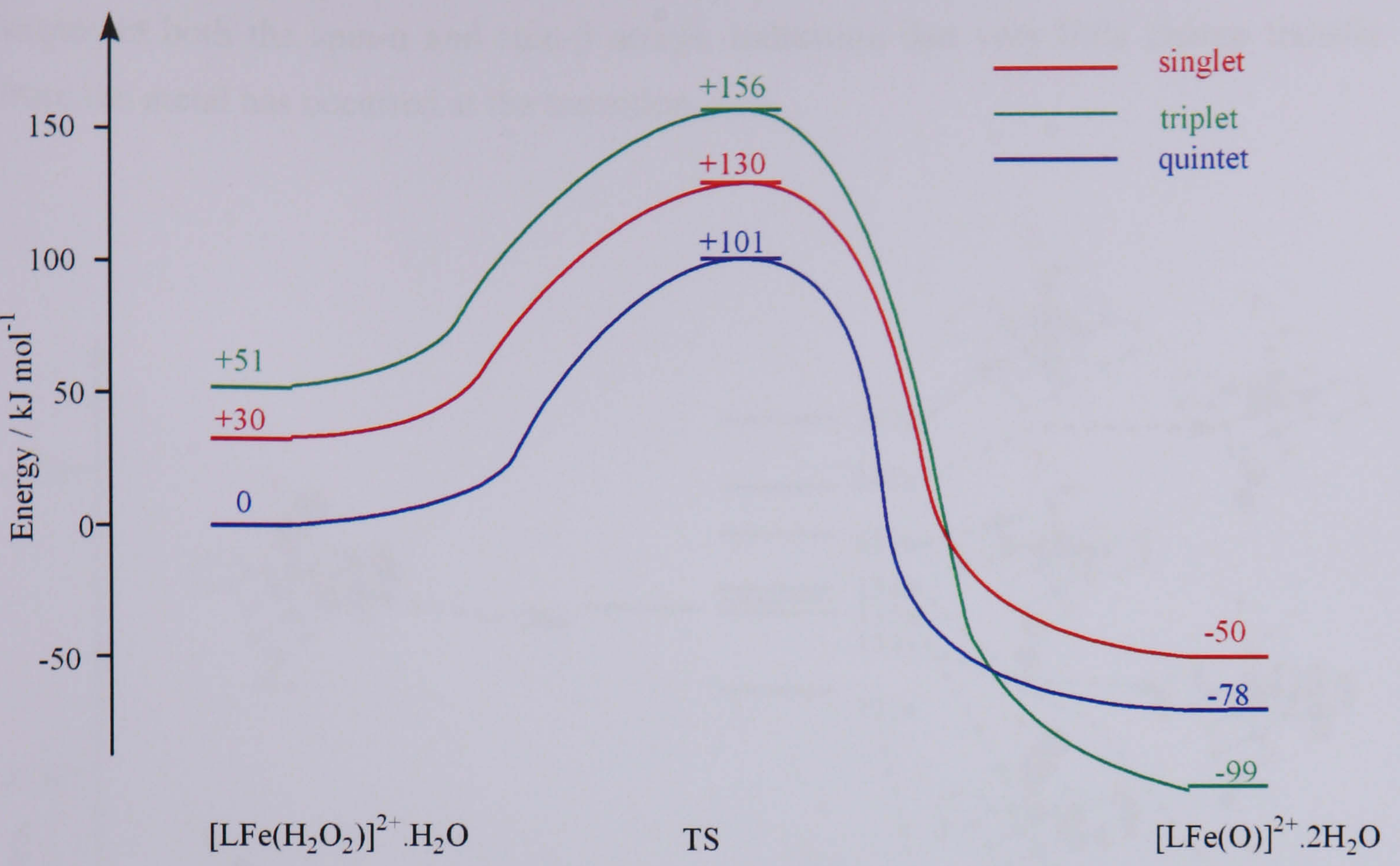

Figure 3-33 – Energetics of the direct mechanism for the singlet, triplet and quintet spin states {original in colour}

The electronic structure of the transition state corresponds to a closed shell H_3O^+ molecule, and an L-Fe moiety upon which all the spin density is located (Figure 3-34).

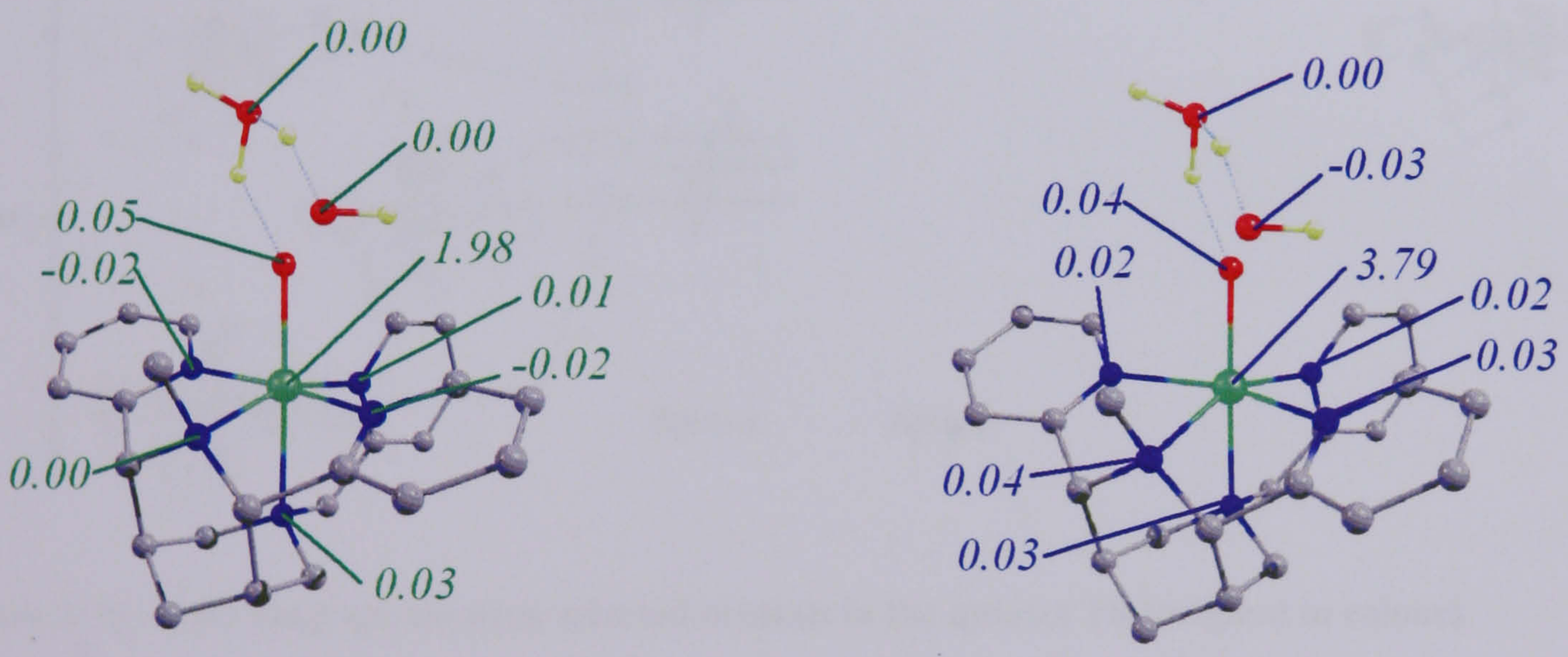

Figure 3-34 – Mulliken spin densities of the triplet and quintet transition states† {original in colour}

The electronic structure of the quintet transition state is shown in Figure 3-35. The occupation of the t_{2g}-like orbitals is similar to in the quintet $[LFe(H_2O_2)]^{2+}$ complex, with all five spin-α MOs and one spin-β orbital filled. The σ* orbital of the O-O bond is

† The singlet spin state is a closed shell species and so there is no spin density associated with any atom

vacant in both the spin-α and spin-β arrays, indicating that very little charge transfer from the metal has occurred at the transition state.

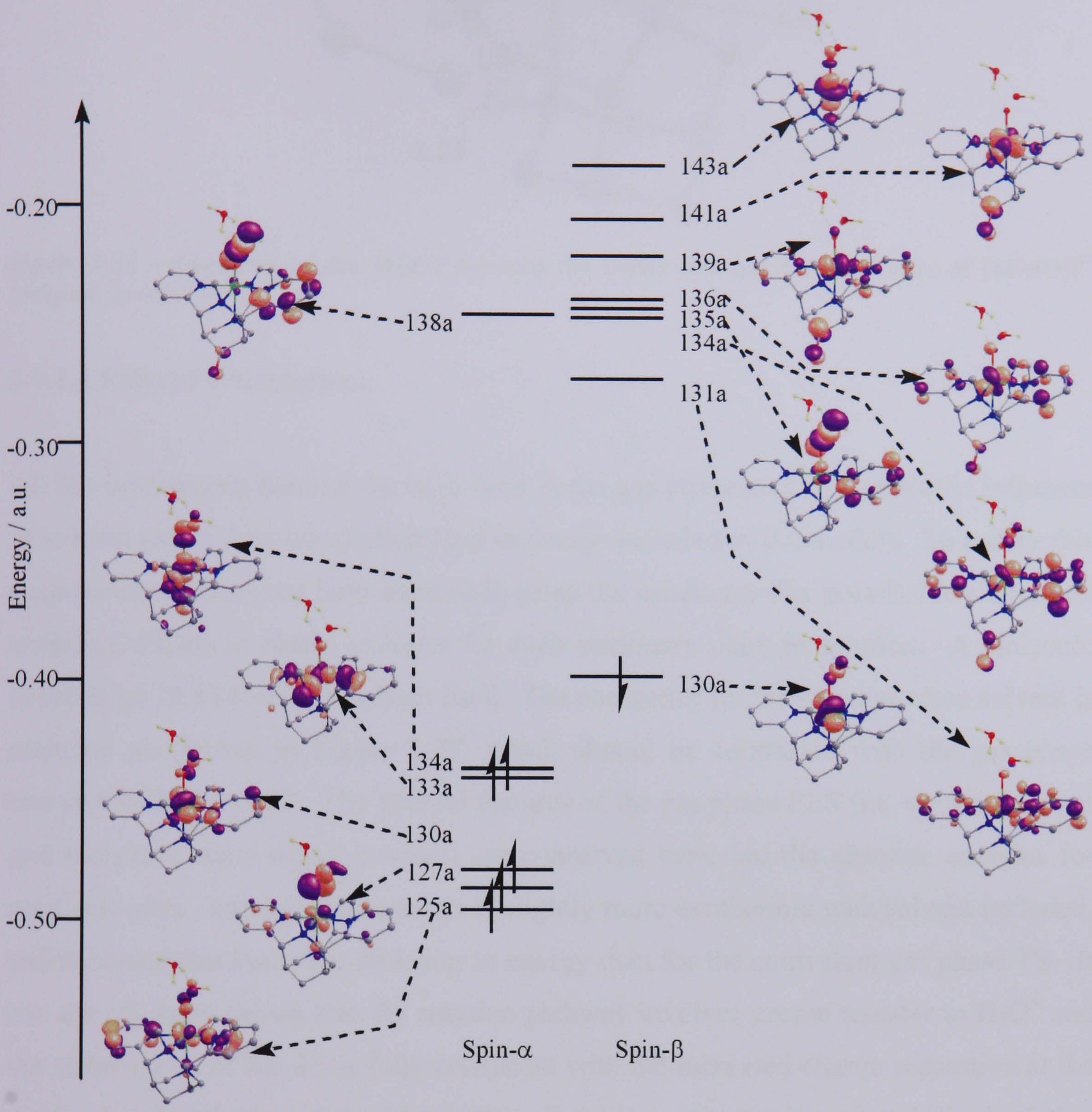

Figure 3-35 – MO diagram showing selected orbitals in the quintet TS {original in colour}

3.8.1.1 Two State Reactivity Calculations

The MECP between the triplet and quintet spin states of the isolated $[LFe(O)]^{2+}$ complex has been located only 23 kJ mol^{-1} higher than, and with a similar geometry to the ground state of $[LFe(O)]^{2+}$ (Figure 3-36). This suggests that the quintet TS will be rate-determining and spin crossover will not play a key role in the reaction.

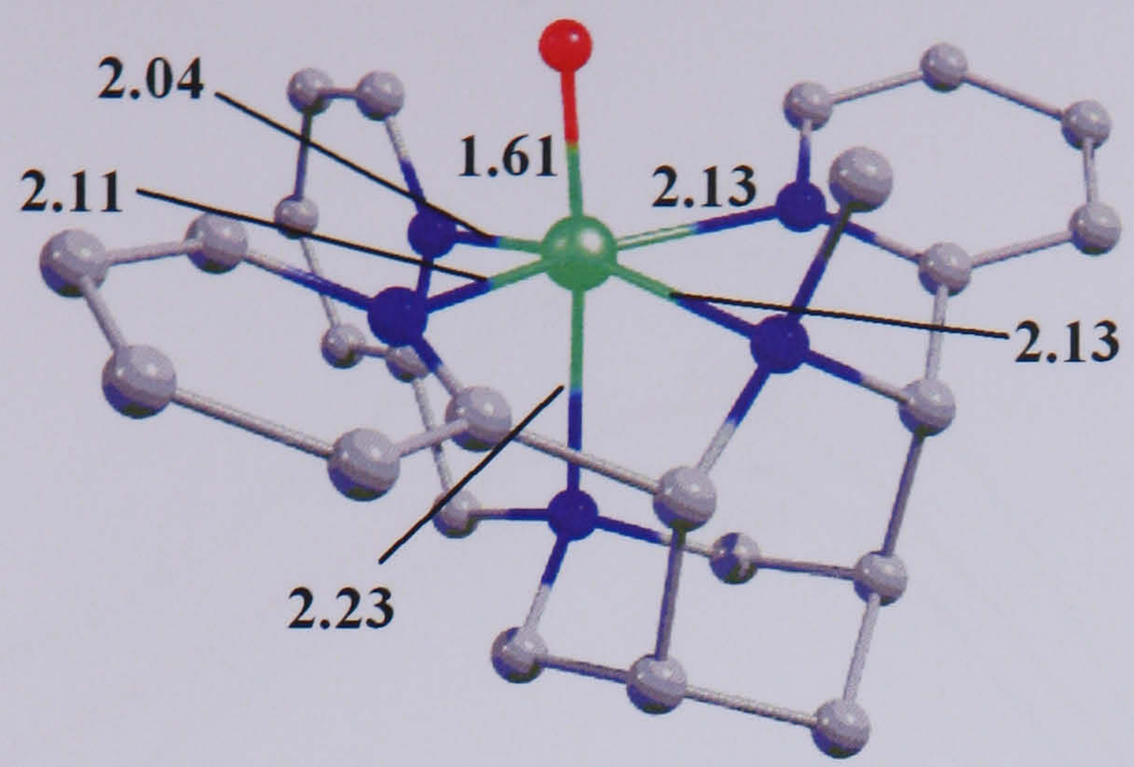

Figure 3-36 – Geometry of the MECP between the triplet and quintet spin states of $[LFe(O)]^{2+}$ {original in colour}

3.8.1.2 Solvent Calculations

All the calculations done so far have been in the gas phase, and so neglect the influence of solvent (other than the explicit H_2O molecule included in the model). To rectify this single point calculations have been done using the conductor-like polarisable continuum model (C-PCM) to obtain energies for each stationary point in solution. A dielectric constant of 78.39 (water) has been used. The energetics for the reaction when solvent is included are shown in Figure 3-37, which should be contrasted with the gas phase energies in Figure 3-33. The general features of the gas phase PES (i.e. quintet reactant and transition state, triplet product) are conserved here, but the absolute energies for each step alter. Overall, the reaction is slightly more exothermic with solvent included, and the transition states are all lower in energy than for the equivalent gas phase TS. It has already been shown that the reaction pathway involves proton transfer to H_3O^+ and the stabilisation of the TS is fully consistent with the increased charge separation at the point. Another feature of the PES is that all the low spin species are stabilised relative to the equivalent high spin ones. This can be attributed to the smaller size of the low spin complexes resulting in a smaller molecular cavity and higher charge density to be stabilised.

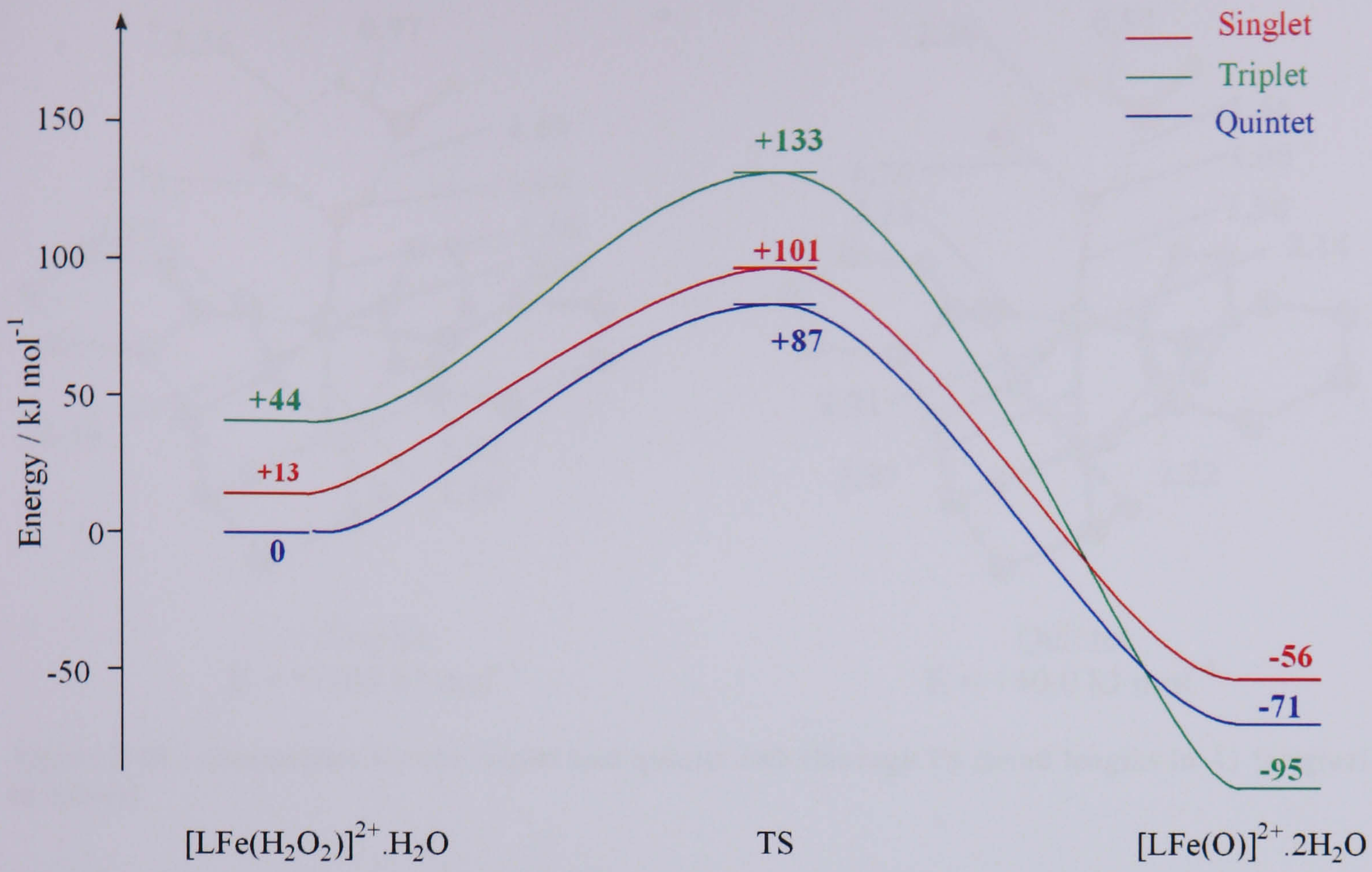

Figure 3-37 – Energetics of the direct mechanism using C-PCM {original in colour}

3.8.2 Indirect Mechanism

Earlier in this chapter, we established that formation of a radical intermediate species, $[LFe(OH)]^{2+}$…HO•, that could, in principle, lie on the PES between the $[LFe(H_2O_2)]^{2+}$ species and the $[LFeO]^{2+}$ species is not energetically unreasonable, and like for the $[LFe(H_2O_2)]^{2+}$ reactant has a quintet ground state. To explore the viability of this pathway, we now consider transition states connecting these minima. Two distinct transition states been located for the triplet and quintet pathways, one linking reactants with the $Fe^{3+}OH$…OH• intermediate, the other linking the intermediate with $[LFe(O)]^{2+}$ and H_2O.

3.8.3 Transition States

3.8.3.1 First Transition State

The first transition state involves the homolytic cleavage of the O-O bond. The quintet TS is lower in energy than the triplet TS, and lies 40 kJ mol^{-1} above the starting complex. Its geometry is shown in Figure 3-38.

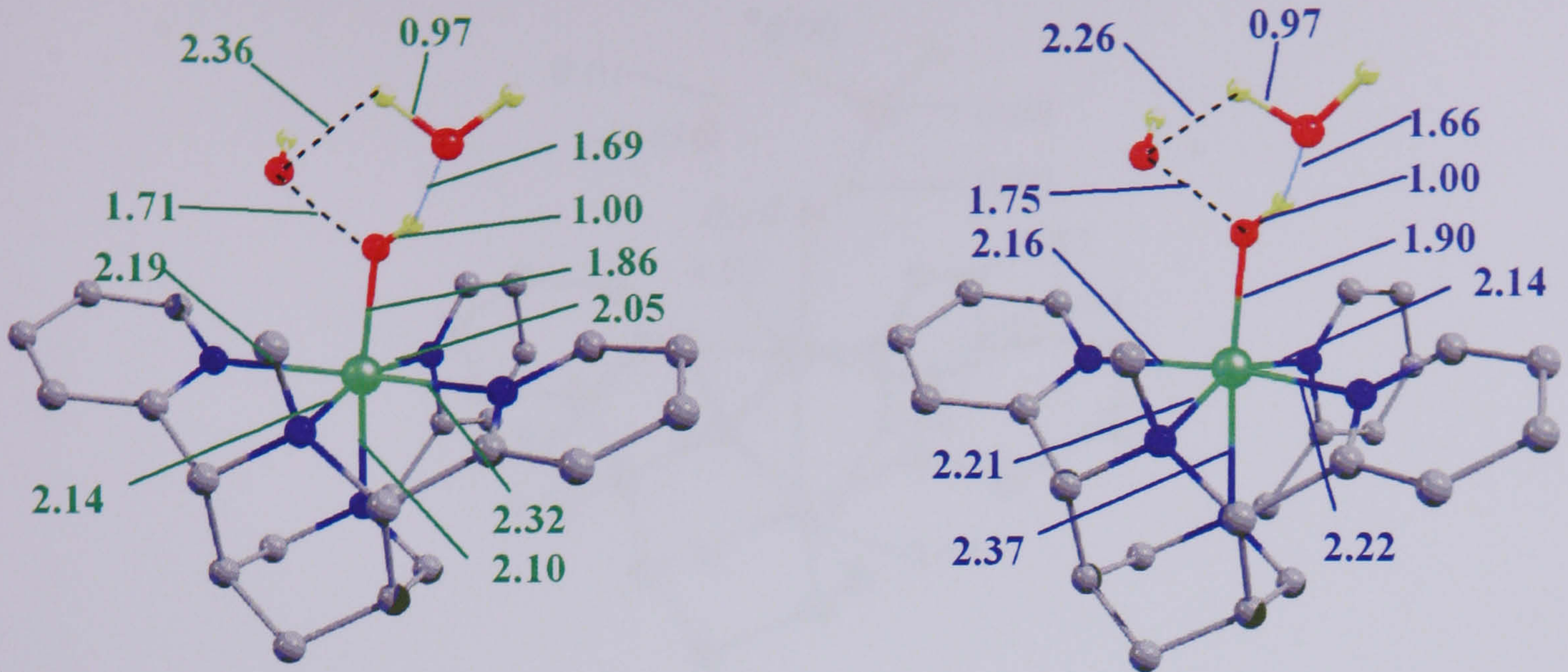

Triplet
$E = +105$ kJ mol^{-1}

Quintet
$E = +40.0$ kJ mol^{-1}

Figure 3-38 – Geometries for the triplet and quintet OO cleavage TS (bond lengths in Å) {original in colour}

The geometry of the quintet transition state has an O-O bond length of 1.75 Å, intermediate between that of the H_2O_2 complex (1.45 Å) and the radical intermediate (2.35 Å), indicating significant O-O bond cleavage. The Fe-O bond length is shorter than in the quintet $[LFe(H_2O_2)]^{2+}$ species, but longer than in the radical intermediates. This is also consistent with the TS corresponding to O-O homolytic cleavage as this results in the one-electron oxidation of Fe. The Fe-N bond lengths are also partway between those found in the quintet spin states of $[LFe(H_2O_2)]^{2+}$ and $[LFe(OH)]^{2+}.H_2O.OH$. The O-H distance between the terminal O of H_2O_2 and the closest H atom of the water molecule is 2.26 Å, which is much shorter than the equivalent distance in the initial complex, but longer than in the radical intermediate and too long to expect a significant interaction. The O-H distance within the water molecule is 0.97 Å, equal to the equivalent bond length in the initial complex and showing that there is no significant additional hydrogen bonding between the OH radical being formed and the water molecule at this stage. However, this interaction is clearly of some importance in stabilising the transition state as without the water molecule present we were unable to locate the equivalent TS.

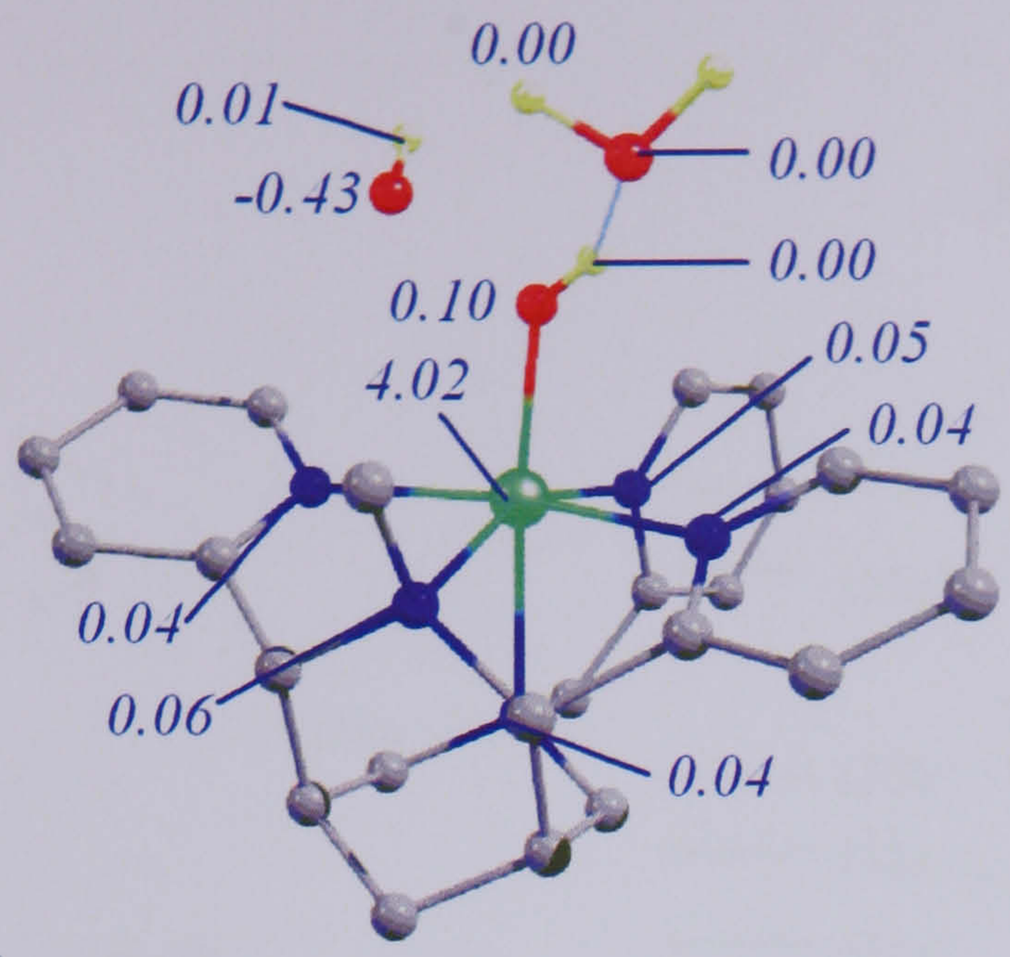

Figure 3-39 – Mulliken spin densities of the quintet transition state {original in colour}

The spin densities of the quintet TS (Figure 3-39) indicate significant radical character (−0.43 units) on the lone OH molecule, clearly partway between the spin densities in $[LFe(H_2O_2)]^{2+}.H_2O$ and $[LFe(OH)]^{2+}.OH.H_2O$. This radical character is anti-ferromagnetically coupled to the spin on the Fe, consistent with the scenario in the radical intermediate. The amount of spin density on Fe is lower than in the intermediate, but greater than that of the H_2O_2 complex, again representing an intermediate between these two extremes.

The electronic structure of the quintet transition state (Figure 3-40) shows that in the spin-α array all the d-orbitals are filled, and there is a vacant orbital corresponding to the O-O σ*.‡ In the spin-β array, there is a lot of mixing between the O-O σ* and the d_{xz} orbital. The bonding combination of this is filled, and the anti-bonding combination is vacant. Therefore, a significant amount of electron density is being pushed into the σ* orbital, helping to break the O-O bond.

‡ The PES around the triplet transition state is extremely soft, and the TS was difficult to locate, largely due to an electron 'hopping' between two orbitals. Therefore the triplet radical TS is not a true stationary point, but an approximation. Due to the difficulty in optimising this spin state, a minimum was found in Jaguar, and reoptimised using Gaussian 03, but a true stationary point has not been found.

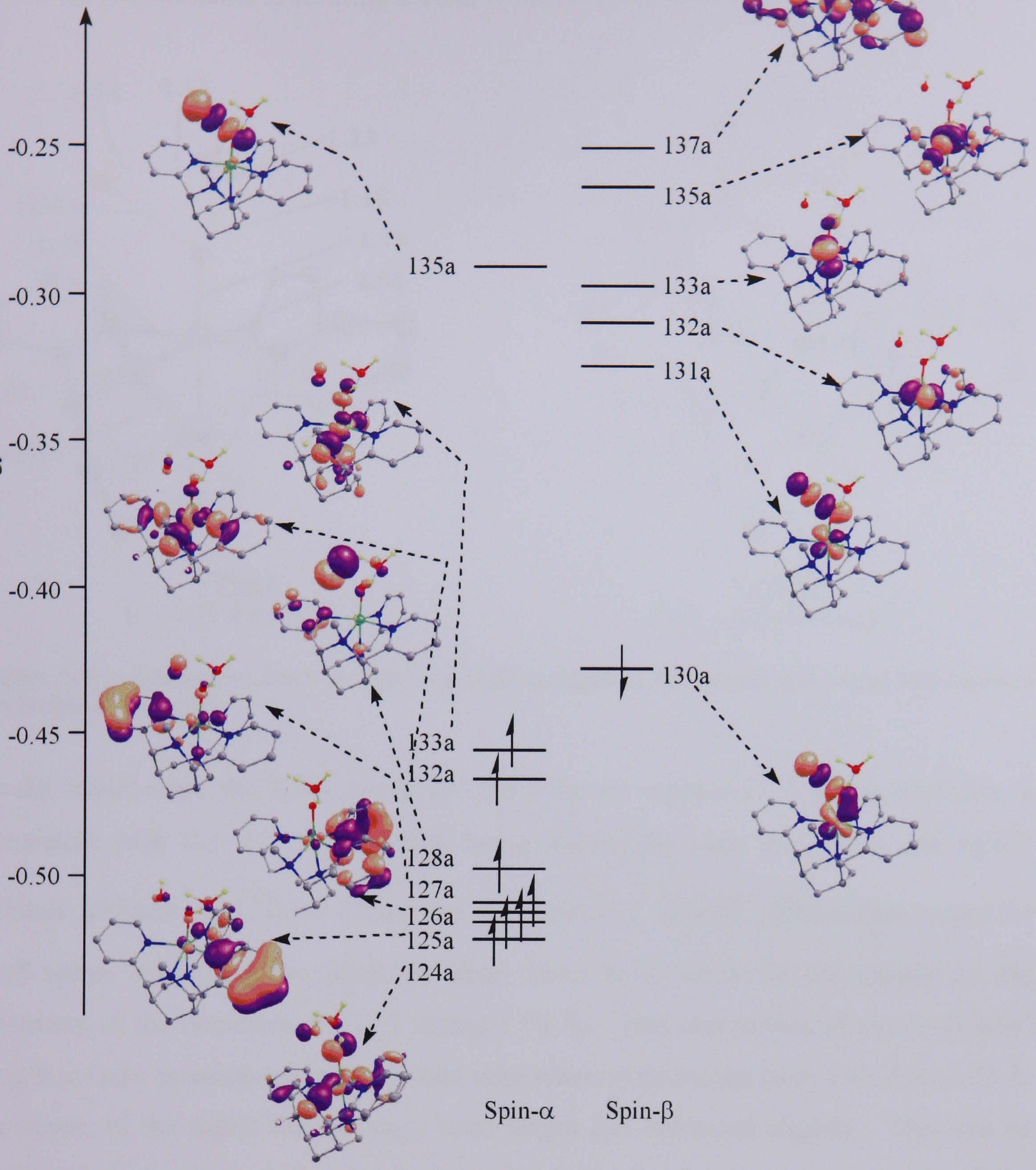

Figure 3-40 – MO diagram showing selected orbitals for the quintet TS for O-O cleavage {original in colour}

3.8.3 Second Transition State

Transition states linking the radical intermediates and the $[LFeO]^{2+}$ products have been found for the triplet and quintet spin states. Their geometries and energies are shown in Figure 3-41. The imaginary frequency of the transition states for both spin state corresponds to the FeO-H bond breaking and concomitant formation of an O-H(OH_2)

bond, and is simultaneously accompanied by a H-O bond of the water molecule breaking, and the same H forming a bond to the O of the OH radical.

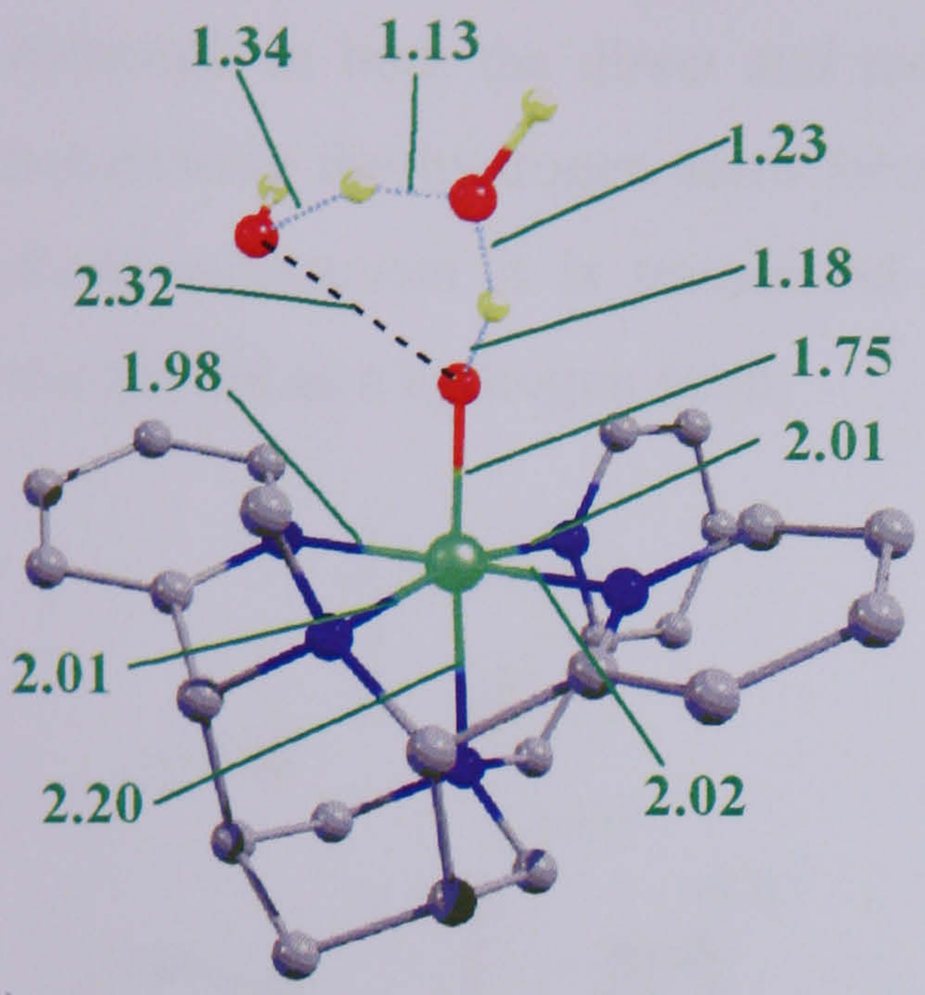

Triplet
E = +78.8 kJ mol^{-1}

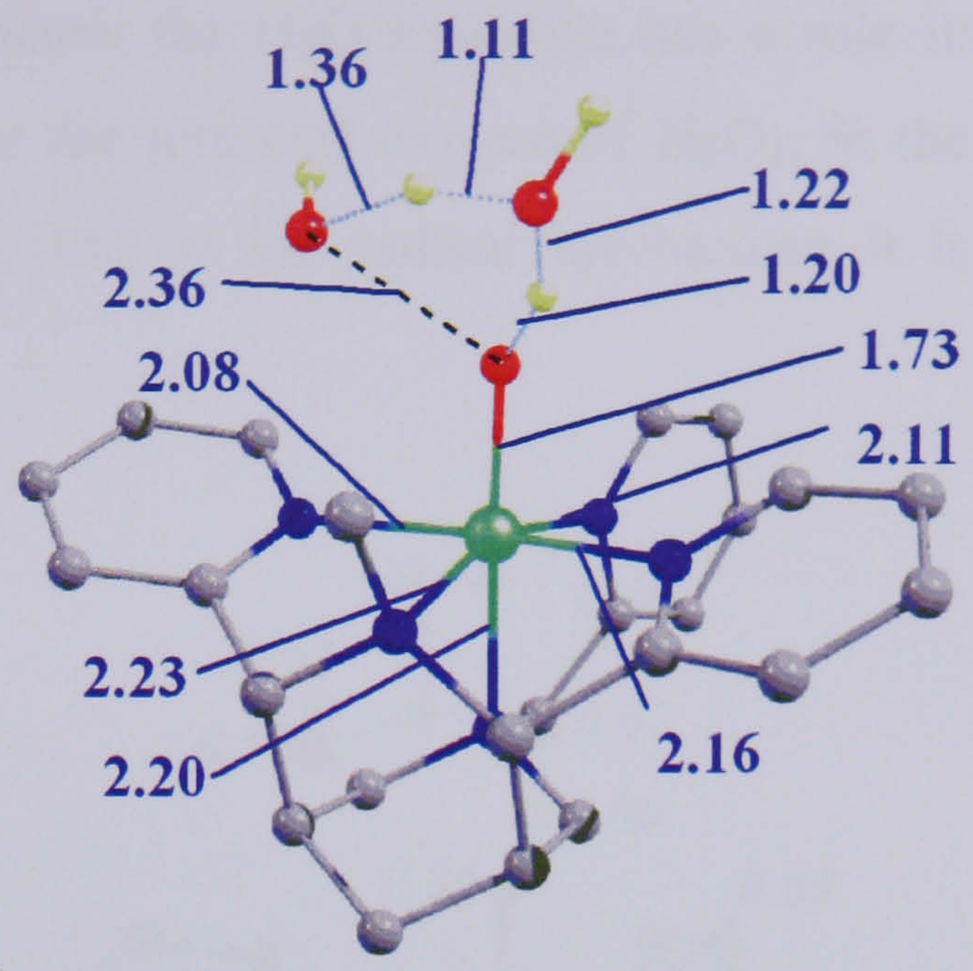

Quintet
E = +103.6 kJ mol^{-1}

Figure 3-41 – Geometries (bond lengths in Å) and energies of the quintet and triplet OH rebound TS {original in colour}

In the triplet state the Fe-N bonds are short for all equatorial N atoms, and this is consistent with the $d_{x^2-y^2}$ like orbital being vacant for both the spin-α and spin-β orbitals. (Figure , α, 134a; β, 136a) The d_{z^2} orbital (α, 135a; β, 140a) is also vacant for both spins, explaining the relatively short Fe-O bond length in comparison to the geometry of the intermediate (1.75 versus 1.79 Å). This contraction of the Fe-O bond length is more pronounced in the quintet state where it decreases from 1.81 Å to 1.73 Å. However, in the triplet the Fe-N_{trans} bond length has increased slightly. This can be attributed to the increased π-donor strength of the O atom as the magnitude of the charge on O increases.

In the second coordination sphere, the distance between the O of the OH radical and the closest H of H_2O is around 1.35 Å for both spin states. This is a significant decrease from the intermediate (2.35 Å for the quintet and 2.53 Å for the triplet), and is accompanied by a significant increase in the O-H bond length of the water molecule, from around 1.00 Å to 1.12 Å. Overall, this shows that the reaction coordinate involves

hydrogen atom transfer, with the water molecule second coordination sphere acting as a shuttle between the proximal and terminal oxygen atoms of H_2O_2.

Although in both the direct and radical mechanisms the H_2O molecule has a role in transferring the hydrogen atom from proximal to the terminal oxygen of H_2O_2, in the direct mechanism it is transferred as a proton, and in the radical mechanism it is transferred as a hydrogen atom.

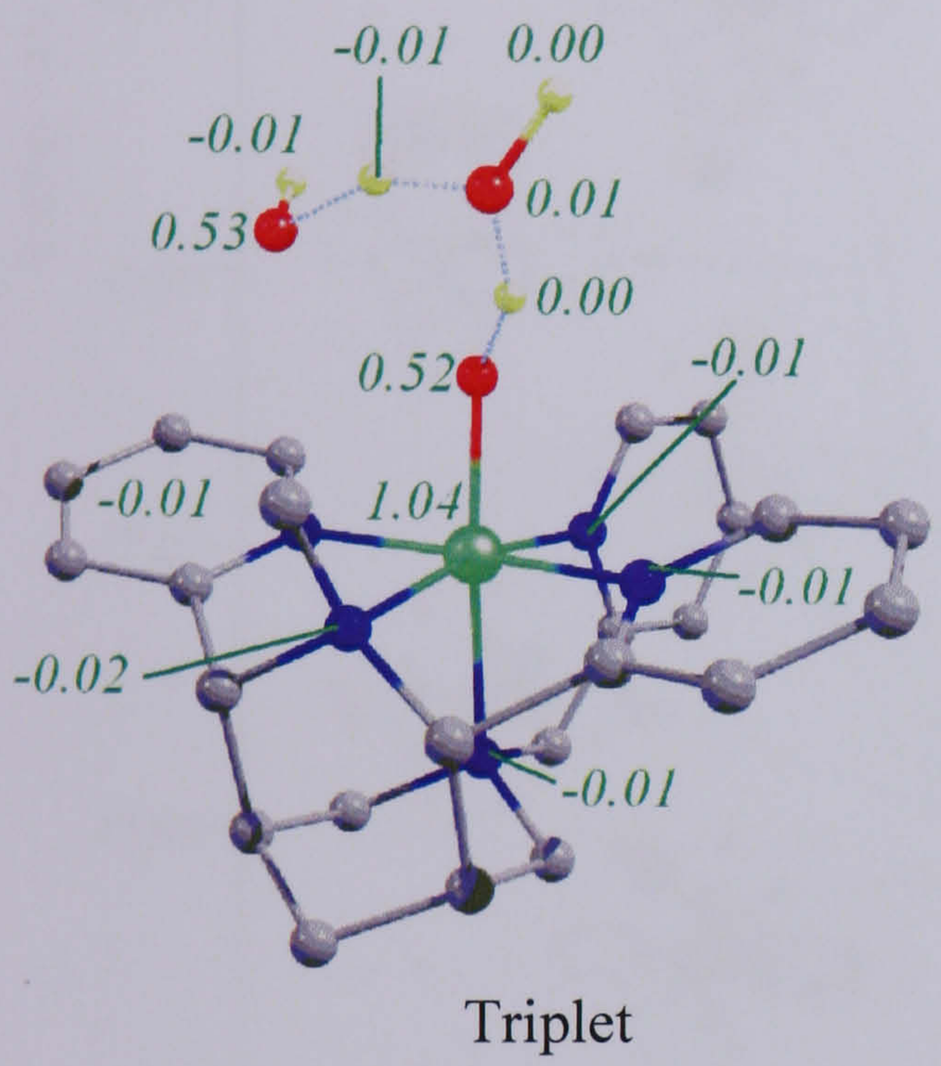

Triplet Quintet

Figure 3-42 – Mulliken spin densities for TS2 {original in colour}

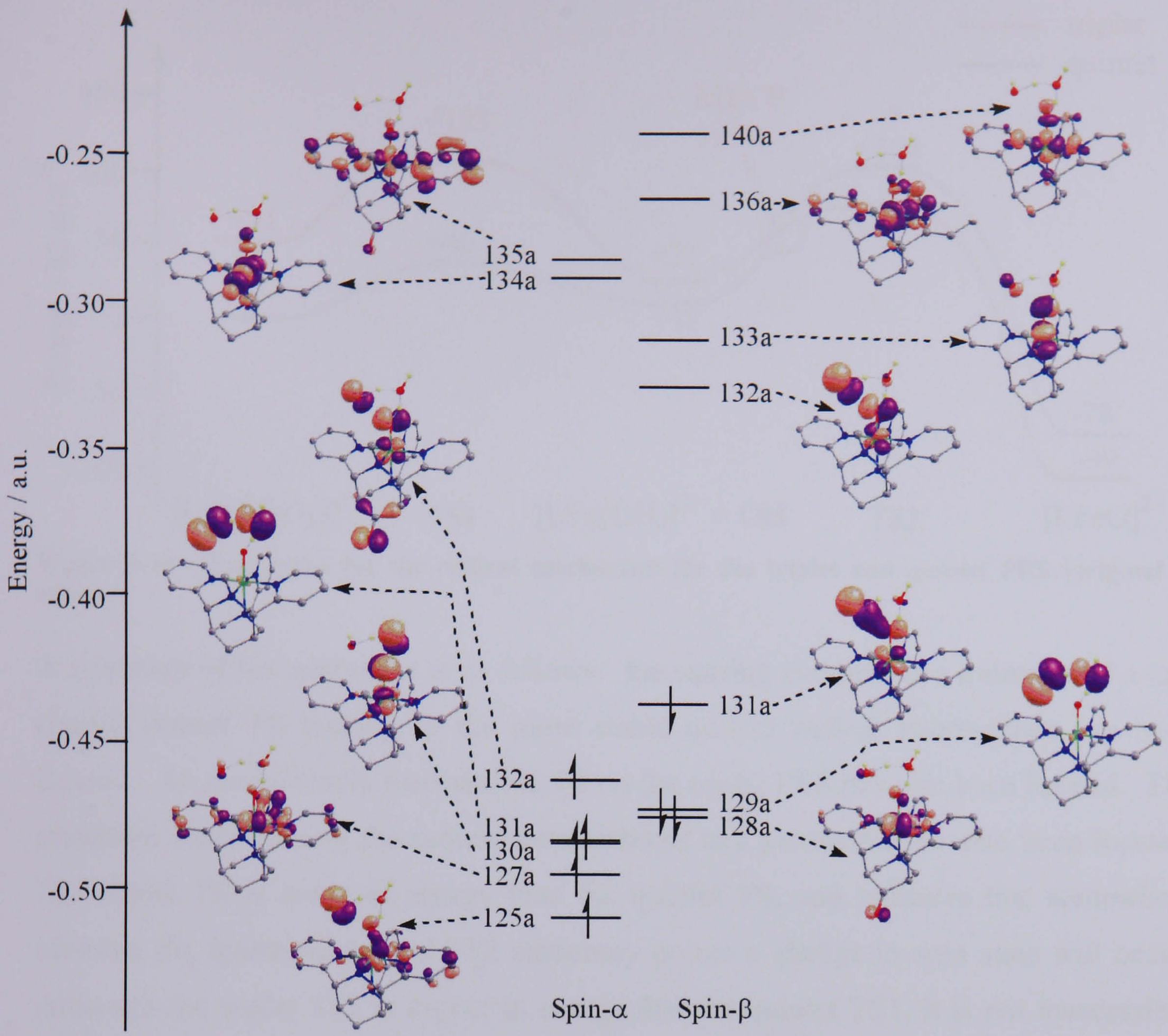

Figure 3-43 – MO diagram showing selected orbitals of the triplet transition state, TS2 {original in colour}

The geometry of the hydrogen bonded network reflects the fact that some O-H bonds are being broken and others are being formed. Consideration of the molecular orbital diagram (Figure 3-43) shows that there is some $Fe^{4+}O$ character developing with large amounts of π* character developing between the p-orbitals of O and the Fe based d_{xy} and d_{yz} orbitals (α: 130a, 132a; β: 132a, 133a). These show similar characteristics to orbitals α: 121a, 122a and β: 122a, 123a in Figure 3-22 (triplet).

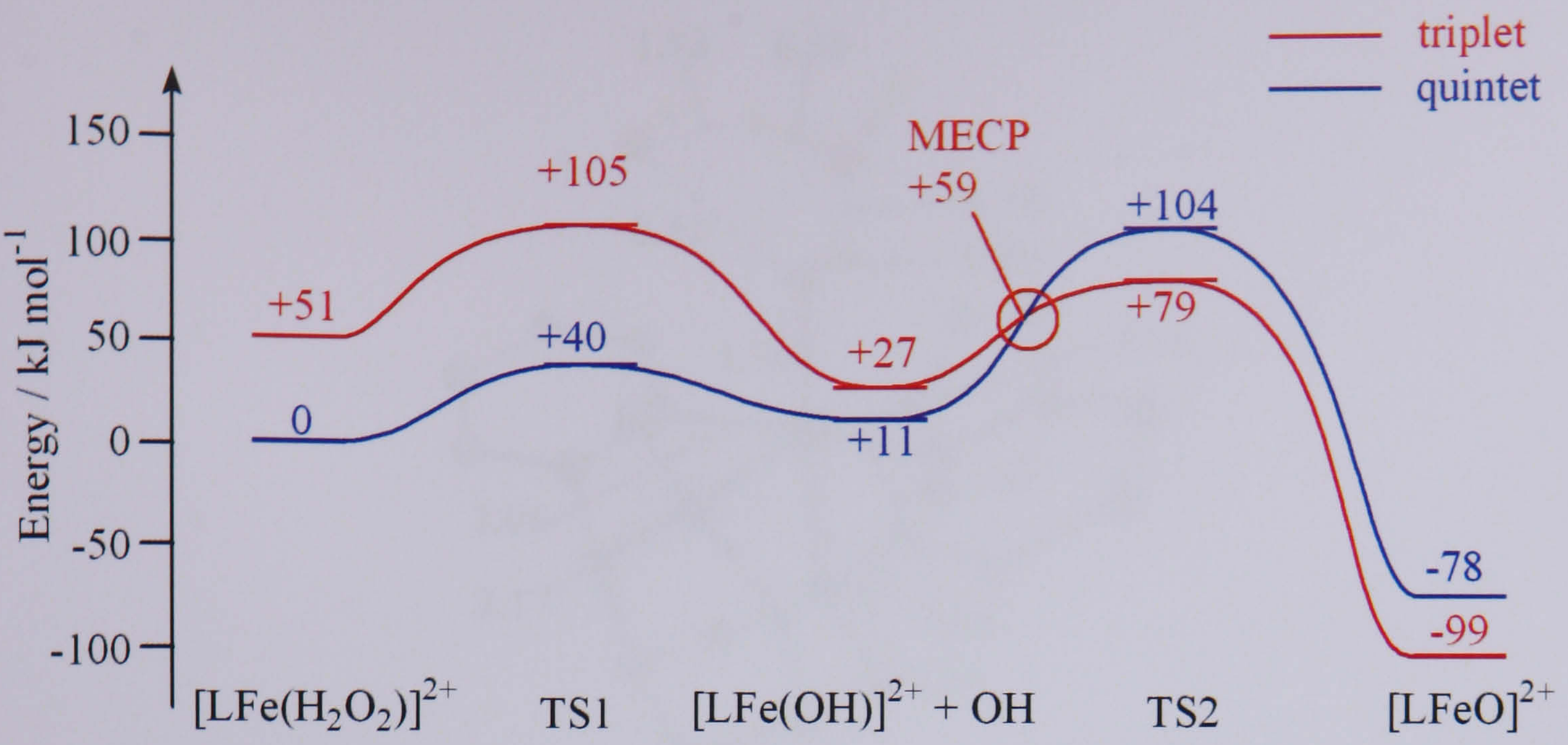

Figure 3-44 - Energetics for the radical mechanism for the triplet and quintet PES {original in colour}

A summary of the energetics is as follows: the starting complex is a quintet, and a low energy quintet TS leading to the more stable quintet radical intermediate has been located. An energetically inaccessible TS on the triplet PES has also been located. The transition states linking the radical intermediates and products have also been located. The triplet TS is lower in energy than the quintet TS, and indicates that somewhere between the intermediate and TS2 stationary points a change in spin state will occur. Although the triplet TS2 is higher in energy that the quintet TS1, it is not inaccessibly high so the reaction will proceed.

The geometry and energy of the aforementioned MECP has been located, and is shown in Figure 3-45. It lies 48 kJ mol^{-1} higher in energy than the quintet radical intermediate, but lower in energy than the triplet TS2. On both the triplet and quintet PES, it leads to the radical intermediate when optimised.

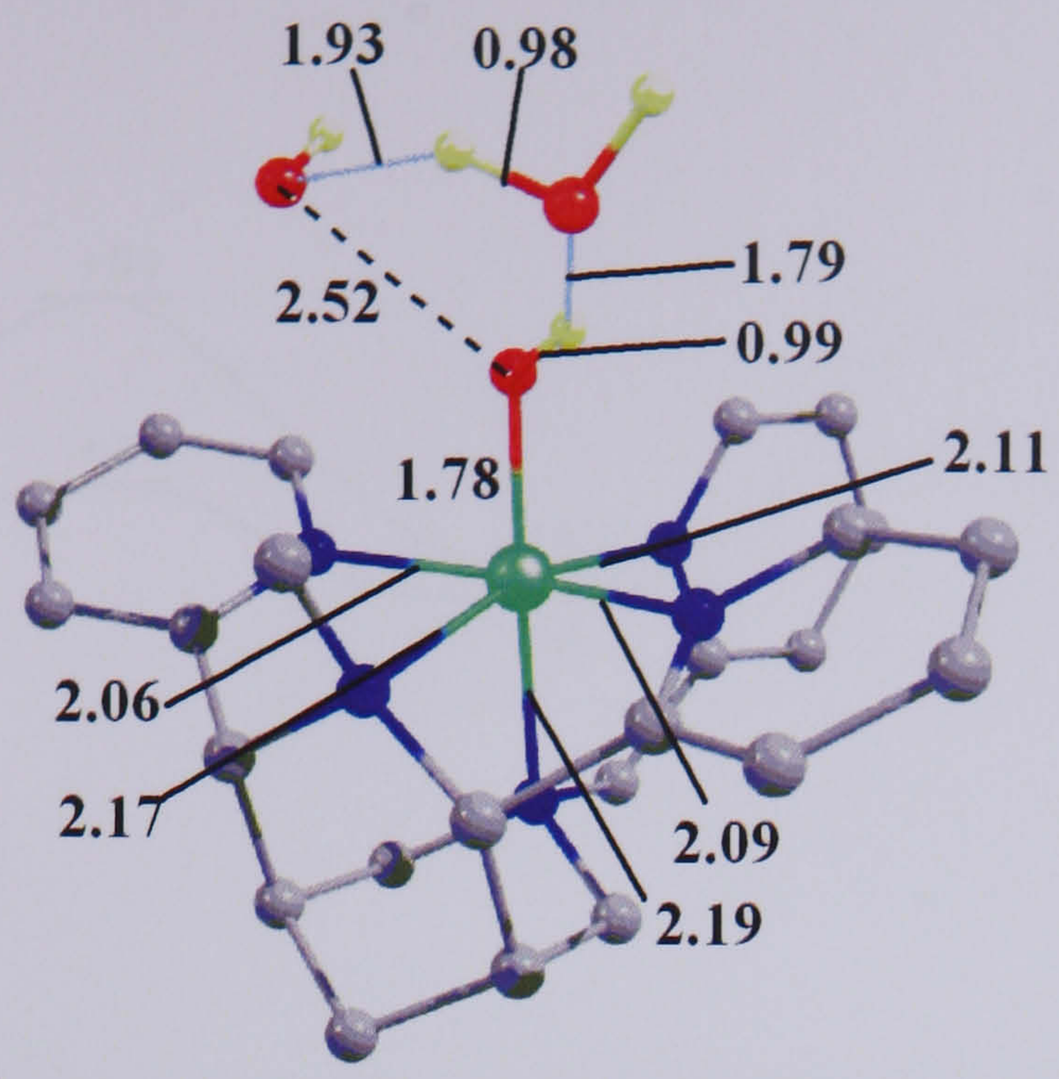

Figure 3-45 – Geometry of the S=1/S=2 MECP (bond lengths in Å) {original in colour}

The geometry of the Fe-O, Fe-N_{trans} and around the •OH radical and water molecule is similar to that found in the triplet intermediate. In contrast, the Fe-N_{eq} are either similar to the quintet spin state, or an intermediate between the two spin states. The geometry, especially around the second coordination sphere is consistent with the radical intermediate rather than the TS.

3.8.4 Solvent Calculations

We have again performed single point calculations including a solvent correction using C-PCM with a dielectric constant equal to that of water, and the results are shown in Figure 3-46. Like before, inclusion of solvent has the effect of reducing the height of the transition states relative to the reactants, and also in this case, the energy of the radical intermediate so that it is only slightly higher than the reactant. The first (quintet) transition state has been stabilised by 6 kJ mol^{-1} and so this step of the reaction is fast. The second, rate-limiting triplet transition state has been lowered considerably in energy, and there is now only a barrier of +41 kJ mol^{-1} to go from the radical intermediate. Therefore this step is also expected to occur rapidly and any radical intermediate would be very short-lived.

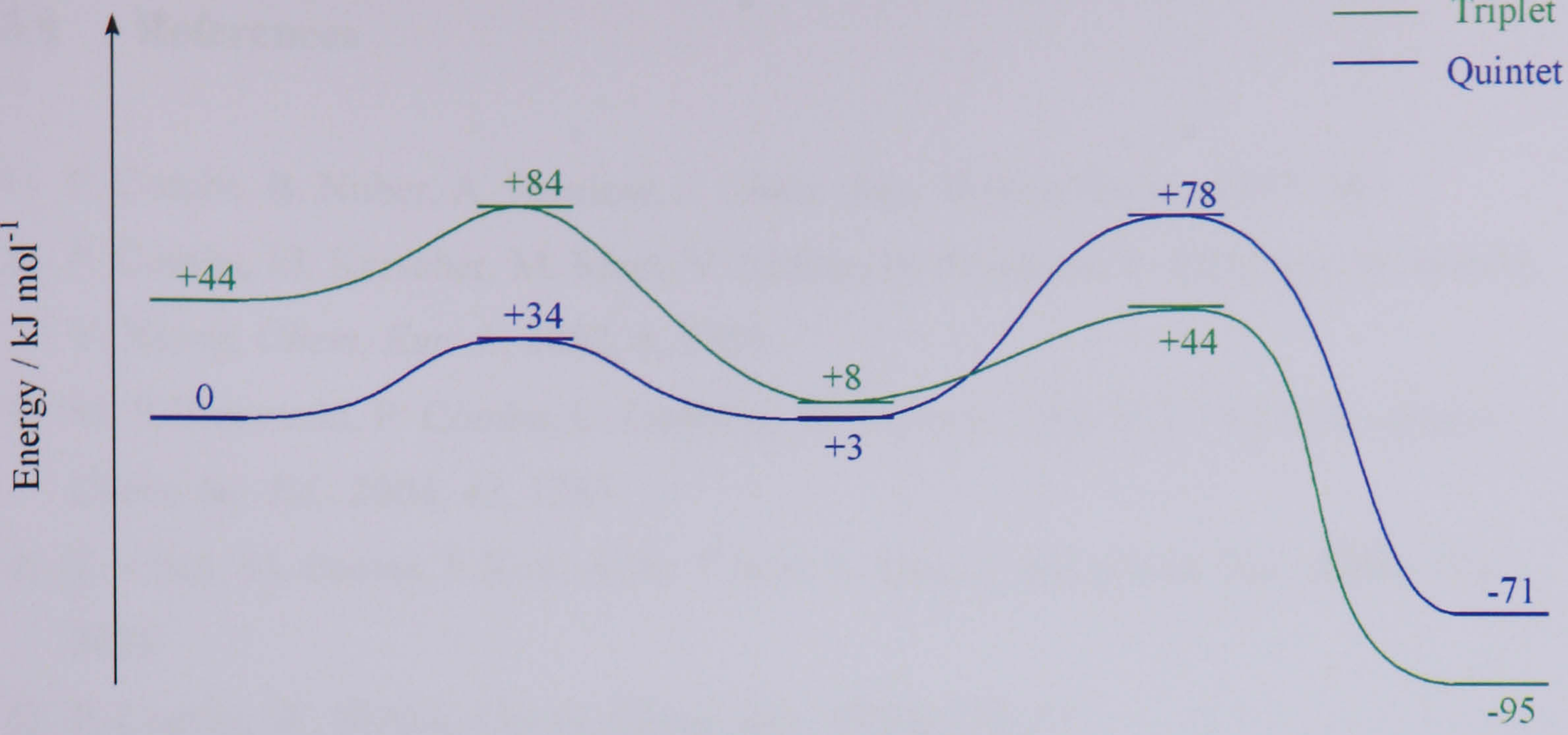

Figure 3-46 – Energetics of the radical mechanism using C-PCM {original in colour}

The second transition state is lowered in energy a lot more than the first transition state. A possible reason for this is the relative sizes of the Fe complexes in the transition states. In the first transition state, corresponding to O-O homolysis, the Fe complex is reasonably large. In the second transition state, corresponding to H abstraction by an OH radical, the Fe-O bonds are already much shorter, therefore the charge on the complex is more concentrated. This means that more electrostatic stabilisation will occur (due to the higher charge density) and due to the smaller size of the $[LFe(O)]^{2+}$ fragment there will be less disruption to the network of water overall.

3.9 References

1) P. Comba, B. Nuber, A. Ramlow, *J. Chem. Soc., Dalton Trans.*, **1997**, 347
2) P. Comba, M. Kerscher, M. Merz, V. Müller, H. Pritzkow, R. Remenyi, W. Schiek, Y. Xiong, *Chem. Eur. J.*, **2002**, *8*, 5750
3) M. R Bukowski, P. Comba, C. Limberg, M. Merz, L. Que, T. L. Wistuba, *Angew. Chem. Int. Ed.*, **2004**, *43*, 1283
4) K. Chen, M. Costas, J. Kim, A. K. Tipton, L. Que, *J. Am. Chem. Soc.*, **2002**, *124*, 3026
5) P. Comba, W. Schiek, *Coord. Chem. Rev.*, **2003**, *238*, 21
6) K. Chen, L. Que, *J. Am. Chem. Soc.*, **2001**, *123*, 6327
7) A. Bassan, M. R. A. Blomberg, P. E. M. Siegbahn, L. Que, *Chem. Eur. J.*, **2005**, *11*, 692
8) D. Kumar, H. Hirao, L. Que, S. Shaik, *J. Am. Chem. Soc.*, **2005**, *22*, 8026
9) A. M. I. Payeras, R. Y. N. Ho, M. Fujita, L. Que, *Chem. Eur. J.*, **2004**, *10*, 4944
10) M. Fujita, L. Que, *Adv. Syn. Cat.*, **2004**, *346*, 190
11) N. Lehnert, F. Neese, R. Y. N. Ho, L. Que, E. I. Solomon, *J. Am. Chem. Soc.*, **2002**, *124*, 10810
12) K. Chen, M. Costas, J. H. Kim, A. K. Tipton, L. Que, *J. Am. Chem. Soc.*, **2002**, *124*, 3026
13) G. Roelfes, M. Lubben, R. Hage, L. Que, B. L. Feringa, *Chem. Eur. J.*, **2000**, *6*, 2152
14) J. H. Kim, C. Kim, R. G. Harrison, E. C. Wilkinson, L. Que, *J. Mol. Catal. A*, **1997**, *117*, 83
15) Y. Mekmouche, S. Ménage, J. Pécaut, C. Lebrun, L. Reilly, V. Schuenemann, A. Trautwein, M. Fontecave, *Eur. J. Inorg. Chem.*, **2004**, 3163
16) M. J. Hamor, T. A. Hamor, J. L. Hoard, *Inorg. Chem.*, **1964**, *3*, 34
17) Y. Zang, J. Kim, Y. Dong, E. C. Wilkinson, E. H. Appelman, L. Que, *J. Am. Chem. Soc.*, **1997**, *119*, 4197
18) M. Merkel, M. Pascaly, B. Krebs, J. Astner, S. P. Foxon, S. Schlindler, *Inorg. Chem.*, **2005**, *44*, 7582
19) K. Chen, L. Que, *Chem. Commun.*, **1999**, 1375
20) K. Chen, M. Costas, L. Que, *J. Chem. Soc., Dalton Trans.*, **2002,** 672

21) P. Comba, W. Schiek, *Coord. Chem. Rev.*, **2003**, *238*, 21

22) H. Börzel, P. Comba, K. S. Hagen, Y. S. Lampeka, A. Lienke, G. Linti, M. Merz, H. Pritzkow, L.V. Tsymbal, *Inorg. Chim. Acta*, **2002**, *337*, 407

23) M. Costas, K. Chem, L. Que, *Coord. Chem. Rev.*, **2000**, *200-202*, 517

24) C. Kim, K. Chen, J. Kim, L. Que, *J. Am. Chem. Soc.*, **1997**, *119*, 5964

25) M. Klopstra, G. Roelfes, R. Hage, R. M. Kellogg, B. L. Feringa, *Eur. J. Inorg. Chem.*, **2004**, 846

26) S. Autzen, H-G. Korth, H. de Groot, R. Sustmann, *Eur. J. Org. Chem.*, **2001**, 3119

27) R. Y. N. Ho, G. Roelfes, B. Feringa, L. Que, *J. Am. Chem. Soc.*, **1999**, *121*, 264

28) A. Hazell, C. J. McKenzie, L. P. Nielsen, S. Schindler, *J. Chem. Soc., Dalton Trans.*, **2002**, 310

29) C. Nguyen, R. J. Guajardo, P. K. Mascharak, *Inorg. Chem.*, **1996**, *35*, 6273

30) G. J. P. Britovsek, J. England, S. K. Spitzmesser, A. J. P. White, D. J. Williams, *Dalton Trans.*, **2005**, 945

31) K. Chen. L. Que, *Angew. Chem. Int. Ed*, **1999**, *38*, 2227

32) I. G. Denisov, T. M. Makris, S. G. Sligar, I. Schlichting, *Chem. Rev.*, **2005**, *105*, 2253

33) T. E. Westre, K. E. Leob, J. M. Zakeski, B. Hedman, K. O. Hodgson, E. I. Solomon, *J. Am. Chem. Soc.*, **1995**, *117*, 1309

34) J. W. Sam, X. J. Tang, J. Peisach, *J. Am. Chem. Soc.*, **1994**, *116*, 5250

35) F. Neese, J. M. Zaleski, K. L. Zaleski, E. I. Solomon, *J. Am. Chem. Soc.*, **2000**, *122*, 11703

36) M. J. Park, J. Lee, Y. Suh, J. Kim, W. Nam, *J. Am. Chem. Soc.*, **2006**, *128*, 2630

37) L. Que, *J. Biol. Inorg. Chem.*, **2004**, *9*, 684

38) W. Nam, R. Ho, J. S. Valentine, *J. Am. Chem. Soc.*, **1991**, *113*, 7052

39) F. Ogliaro, S. P. de Visser, S. Cohen, P. K. Sharma, S. Shaik, *J. Am. Chem. Soc*, **2002**, *124*, 2806

40) G. Roelfes, M. Lubben, K. Chen, R. Y. N. Ho, A. Meetsma, S. Genseberger, R. M. Hermant, R. Hage, S. K. Mandal, *Inorg. Chem.*, **1999**, *38*, 1929

41) J. Annaraj, Y. Suh, M. S. Seo, S. O. Kim, W. Nam, *Chem. Commun.*, **2005**, 4529

42) H. Miyake, K. Chen, S. J. Lange, L. Que, *Inorg. Chem.*, **2001**, *40*, 3534

43) J-U. Rohde, J-H. In, M. H. Lim, W. W. Brennessel, M. R. Bukowski, A. Stubna, E. Münck, W. Nam, L. Que, *Science*, **2003**, *299*, 1037

44) C. V. Sastri, M. S. Seo, M. J. Park, K. M. Kim, W. Nam, *Chem. Commum.*, **2005**, 1405

45) S. O. Kim, C. V. Sastri, M. S. Seo, J. Kim, W. Nam, *J. Am. Chem. Soc*, **2005**, *127*, 4178

46) S. J. Lange, H. Miyake, L. Que, *J. Am. Chem. Soc.*, **1999**, *121*, 6330

47) N. Y. Oh, Y. Suh, M. J. Park., M. S. Seo, J. Kim, W. Nam, *Angew. Chem. Int. Ed.*, **2005**, *44*, 4235

48) A. Bassan, M. R. A. Blomberg, P. E. M. Siegbahn, L. Que, *J. Am. Chem. Soc.*, **2002**, *124*, 11056

49) D. Quiñonero, K. Morojuma, D. G. Musaev, *J. Am. Chem. Soc.*, **2005**, *127*, 6548

50) H. Börzel, P. Comba, R. Hage, M. Kerscher, A. Lienke, M. Merz , *Chem. Abstr.* **2002**, *137*, 48918

51) H. Börzel, P. Comba, K. S. Hagen, Y. D. Lampeka, A. Lienke, G. Linti, M. Merz, H. Pritzkow, L. V. Tsymbal, *Inorg. Chim. Acta*, **2002**, *337*, 407

52) H. J. H. Fenton, *J. Chem. Soc. Trans.*, **1894**, *65*, 899

53) F. Haber, J. Weiss, *Proc. R. Soc. London A*, **1934**, *147*, 332

54) W. C. Bray, M. H. Gorin, *J. Am. Chem. Soc.*, **1932**, *54*, 2124

55) A. Masarwa, S. Rachmilovich-Calis, N. Meyerstein, D. Meyerstein, *Coord. Chem. Rev.*, **2005**, *249*, 1937

56) G. A. Russell, *J. Am. Chem. Soc.*, **1957**, *79* 3871

57) W. G. Barb, J. H. Baxendale, P. George, K. R. Hargrave, *Trans. Far. Soc.*, **1951**, *47*, 462

58) C. Walling, *Acc. Chem. Res.*, **1998**, *31*, 155

59) W. T. Dixon, R. O. C. Norman, *Nature*, **1962**, *196*, 891

60) C. R. E. Jefcoate, J. R. Lindsay Smith, R. O. C. Norman, *J. Chem, Soc. B Physo. Org.*, **1969**, *8*, 1013

61) M. J. Burkitt, *Prog. React. Kin. Mech.*, **2003**, *28*, 75

62) M. L. Kremer, *Phys. Chem. Chem. Phys.*, **1999**, *1*, 3595

63) O. Pestovsky, S. Stoian, E. L. Bominaar, X. P. Shan, E. Munck, L. Que, A. Bakac, *Angew. Chem. Int. Ed.*, **2005**, *44*, 6871

64) H. C. Sutton. C. C. Winterbourn, *Free Radic. Biol. Med.*, **1989**, *6*, 53

65) T. Shiga, *J. Phys. Chem.*, **1965**, *69*, 3805

66) F. Buda, B. Ensing, M. C. M. Gribnau, E. J. Baerends, *Chem. Eur. J.*, **2001**. *7*, 2775

67) B. Ensing, F. Buda, P. E. Blochl, E. J. Baerends, *Phys. Chem. Chem. Phys.*, **2002**, *4*, 3619

68) H. Börzel, P. Comba, K. S, Hagen, Y. D. Lampeka, A. Lienke, G. Linti, M. Merz, H. Pritzkow, L. V. Tsymbal, *Inorg. Chim. Acta*, **2002**, *337*, 407

69) N. Lehnert, R. Y. N. Ho, L. Que, E. I. Solomon, *J. Am. Chem. Soc.*, **2001**, *123*, 8271

70) A. Ghosh, E. Tangen, H. Ryeng, P. R. Taylor, *Eur. J. Inorg. Chem.*, **2004**, *23*, 4555

Chapter 4 - Reaction of $[LFe(O)]^{2+}$ with Propene

4.1 Introduction

$[Fe(N2Py3o)(O)]^{2+}$ is thought to be a potential intermediate in the oxidation of key chromophores such as β-carotene and curcumin (chapter 1, Figure 1-2) found in certain stains. To assess whether this oxoiron(IV) species is competent to affect such reactions we describe a series of calculations on the hydroxylation and epoxidation of propene by $[Fe(N2Py3o)(O)]^{2+}$. Propene was chosen as the model substrate as, like fatty acids and the chromophores mentioned above, it contains both a C=C double bond and an allylic C-H bond that can be oxidised.

Oxoiron(IV) species are known to effect the epoxidation of olefins (via O atom transfer) or hydroxylation of hydrocarbons (via H atom abstraction followed by a rebound mechanism as proposed by Groves for the oxidation of C-H bonds by cytochrome P450.[1] There have been several computational studies on these mechanisms, primarily by Shaik and co-workers on the reactivity of **compound I** of cytochrome P450, and a summary of these results provides the background to this chapter. The electronic structure of **compound I** is shown schematically in Figure 4-1.

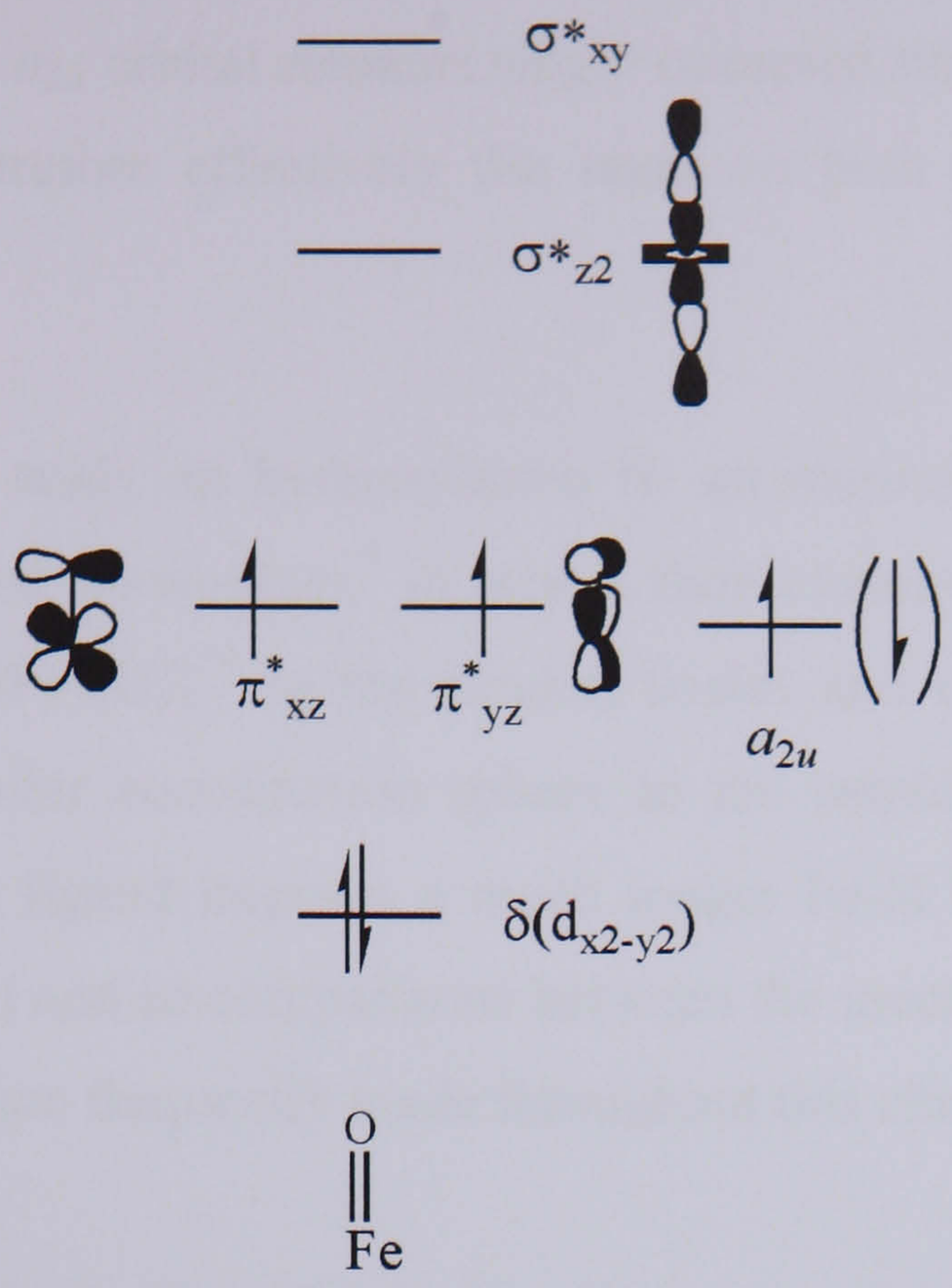

Figure 4-1 – Schematic MO diagram of Cytochrome P450, compound I, adapted from reference 2

Compound I corresponds to a triplet oxoiron(IV) species ferromagnetically or anti-ferromagnetically coupled to an unpaired electron in the a_{2u} orbital of the porphyrin ring, leading to quartet and doublet species that are virtually energetically identical.[3] Reduction of this species by one electron can either lead to an Fe^{3+} centre coupled to the electron in the singly occupied a_{2u} orbital, or, alternatively, the a_{2u} orbital can be filled to give an oxoiron(IV) species in the triplet spin state. In this chapter we focus on the reactivity of the oxoiron(IV) species, $[Fe(N2Py3o)(O)]^{2+}$ produced by the reaction of H_2O_2 and Fe^{2+}, and discussed in detail in the previous chapter. In this case reduction must lead to an Fe^{3+} species and so when comparisons to **compound I** are made, the focus is on cases where the iron centre is reduced rather than the porphyrin ring.

4.1.1 Hydroxylation by Oxoiron(IV) Species

The hydroxylation of both methane and propene by **compound I** have been studied using DFT by Shaik and co-workers.[4,5] With methane, **compound I** forms a weakly bound cluster stabilised by 0.98 kcal mol^{-1} (4 kJ mol^{-1}) relative to the isolated species. A similar comparison is not reported for propene. From the cluster complexes, oxidation of both hydrocarbons occurs via initial H atom abstraction. For methane, the transition states for the doublet and quartet spin states are almost isoenergetic, primarily because the electron transfer occurs from the C-H σ orbital to the π* Fe-O orbital in

both spin states and the a_{2u} orbital remains singly occupied throughout. The spin state of the Fe centre is therefore effectively the same on both the doublet and quartet surface.[5]

Another computational study on hydroxylation by an oxoiron(IV) complex has been carried out by Shaik and co-workers,[7] in which they examined the hydroxylation of cyclohexane by $[Fe(N4Py)(O)]^{2+}$ in the singlet, triplet and quintet spin states. The N4Py ligand has a similar coordination sphere to the bispidone ligand studied here (although the bispidone ligand imposes a much longer Fe-N bond length *trans* to the vacant coordination site) and so comparisons between the mechanisms discussed in this chapter and reference 1 are frequently made throughout this chapter.

Initially a reactant cluster is formed between the iron oxo complex and cyclohexane, which is more stable than the isolated reactants by 0.1 and 1.5 kcal mol^{-1} depending on the spin state. This is followed by a transition state corresponding to H atom abstraction from a C-H bond by the oxo group, and accompanied by a change in spin state from the triplet surface (for the reactants) to the quintet surface (for the transition state). The barrier is 7.3 kcal mol^{-1}, and the imaginary frequency leads to an intermediate corresponding to $[Fe(N4Py)(OH)]^{2+}$ and an alkyl radical. The alkyl radical then rebounds to give the alcohol coordinated to Fe^{2+} as the product.[7]

A similar mechanism for hydroxylation is proposed in this chapter, and its potential energy surface is calculated using DFT. Like for the calculations reported in chapter 3, the B3LYP functional and 6-31G(d) basis set as implemented in Gaussian03 have been used.

4.1.2 Epoxidation by Oxoiron(IV) Species

Oxoiron(IV) complexes can also effect epoxidation of C=C double bonds. Shaik and co-workers have studied the reaction of **compound I** with ethene and propene, both of which give similar results.[2,4] The initial step for alkene epoxidation by **compound I** is the formation of a C-O bond between the oxo group coordinated to iron and the terminal carbon atom (in propene). The transition state for this step corresponds to single electron transfer from the π orbital of the C=C double bond to either an Fe-O π^* orbital

resulting in the one electron reduction of iron, or to the a_{2u} of the porphyrin ring giving an Fe^{4+} species. As the reactant studied in this chapter does not have a radical ligand, only the first scenario (electron transfer from the C=C double bond to the iron centre) is of interest to us despite the fact that it is at higher in energy in **compound** I.

In the doublet spin state there are two possible stationary points in which the iron centre is reduced, differing in the coupling between the electron in the a_{2u} orbital and the iron centre, which can be ferro (^{2}TS1-III) or anti-ferromagnetic (^{2}TS1-III'). These possibilities are shown schematically in Figure 4-2. The a_{2u} and the carbon centred orbitals are both singly occupied and the electrons in them are anti-ferromagnetically coupled to each other. The ^{2}TS1-III' transition state is a real transition state with only one imaginary frequency. The ^{2}TS1-III stationary point, however, is a second order saddle point which also leads to the intermediates or reactants. In the complex studied here, the ligand orbitals are always filled so an issue similar to coupling between the iron centre and the a_{2u} orbital does not occur. However, we do consider the effect of ferro- versus anti-ferromagnetic coupling between the iron-oxo group and the substrate.

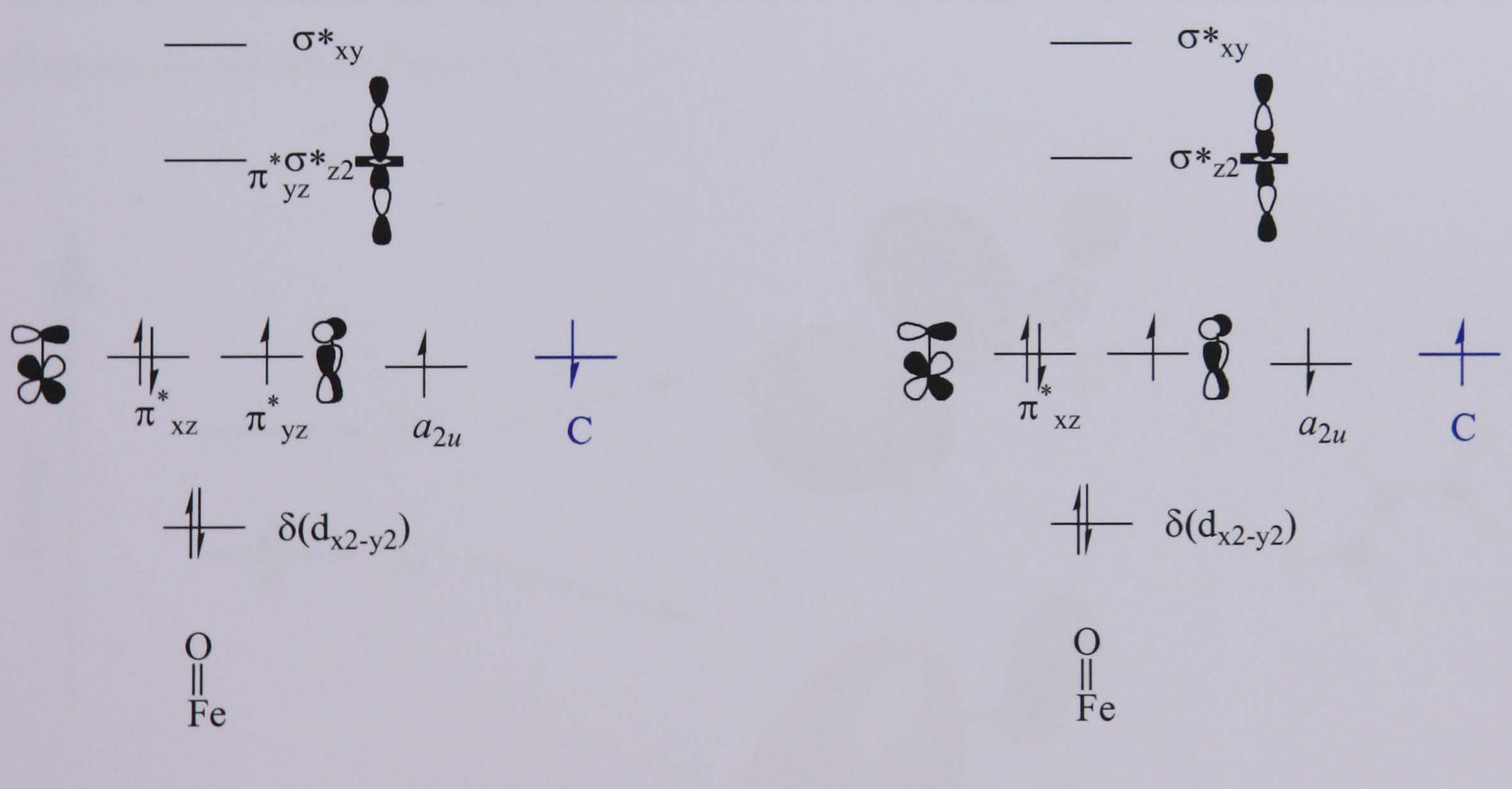

Figure 4-2 – Schematic MO diagrams showing the coupling between electrons in different doublet stationary points for epoxidation {original in colour}

The 'rebound' step of epoxidation by **compound I** is the attack of the carbon centred radical on the oxygen atom. However, rather than further reduction of the iron centre resulting in an Fe^{2+} product, the porphyrin hole is filled. In this sense it is quite distinct

from the oxoiron(IV) species of interest here, where there is no analogous ligand 'hole', and so the second step for the two complexes hasn't been compared.

4.2 Results

In our study, propene is used as a model substrate. It was chosen as it has both a C=C double bond that can undergo oxidation via oxygen atom transfer, and a methyl group that can undergo hydroxylation via hydrogen atom abstraction. During the discussion of the different mechanisms, comparisons are drawn between our calculations and those carried out on similar systems – in particular the $[(N4Py)Fe(O)]^{2+}$ catalyst. However, in this case the substrate is cyclohexane which has a stronger C-H bond.

4.2.1 Electronic Structure of Propene

To understand the mechanism of reaction between oxoiron(IV) and propene, it is useful to discuss the frontier molecular orbitals of the two species: The HOMO and LUMO of propene are shown in Figure 4-3.

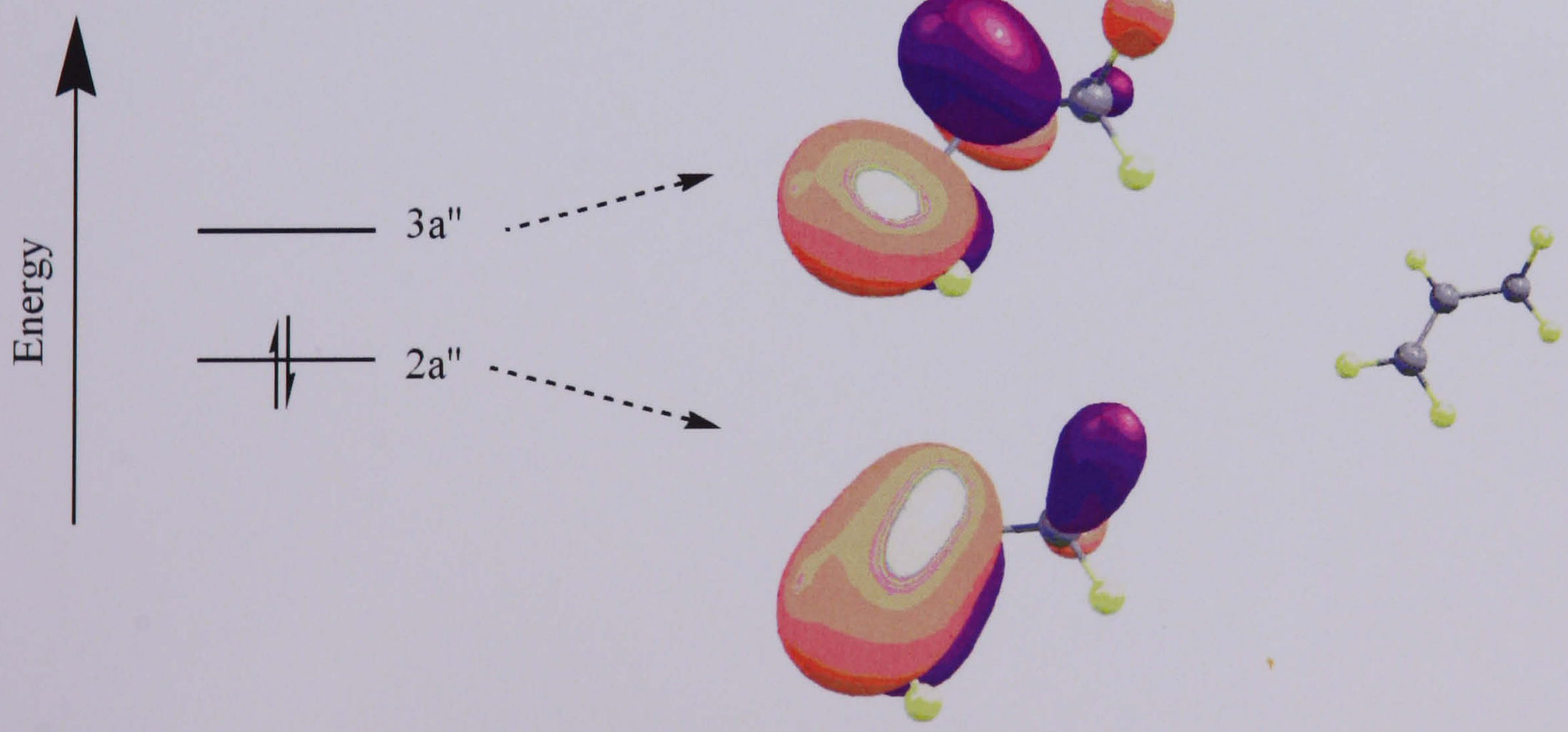

Figure 4-3 – HOMO and LUMO of propene {original in colour}

The HOMO (2a") of propene corresponds to the C=C π bonding orbital with some contribution from the p_z orbital located on the sp^3 carbon atom. The LUMO (3a") is the

π* orbital of the C=C bond. The electronic structure of $[LFe(O)]^{2+}$ has been discussed in the chapter 3, section 3.6.3.

4.2.2 Geometries of the Precursor Complex

The initial step in both the hydroxylation and epoxidation reactions is the formation of a weak complex between propene and $[LFe(O)]^{2+}$, the geometries of which are shown in Figure 4-4 for the singlet, triplet, quintet and septet spin states. Although the septet spin state is high in energy and would not usually be considered for an oxoiron(IV) species, it is included here for completeness as the septet PES is important in the hydroxylation reaction mechanism, discussed later.

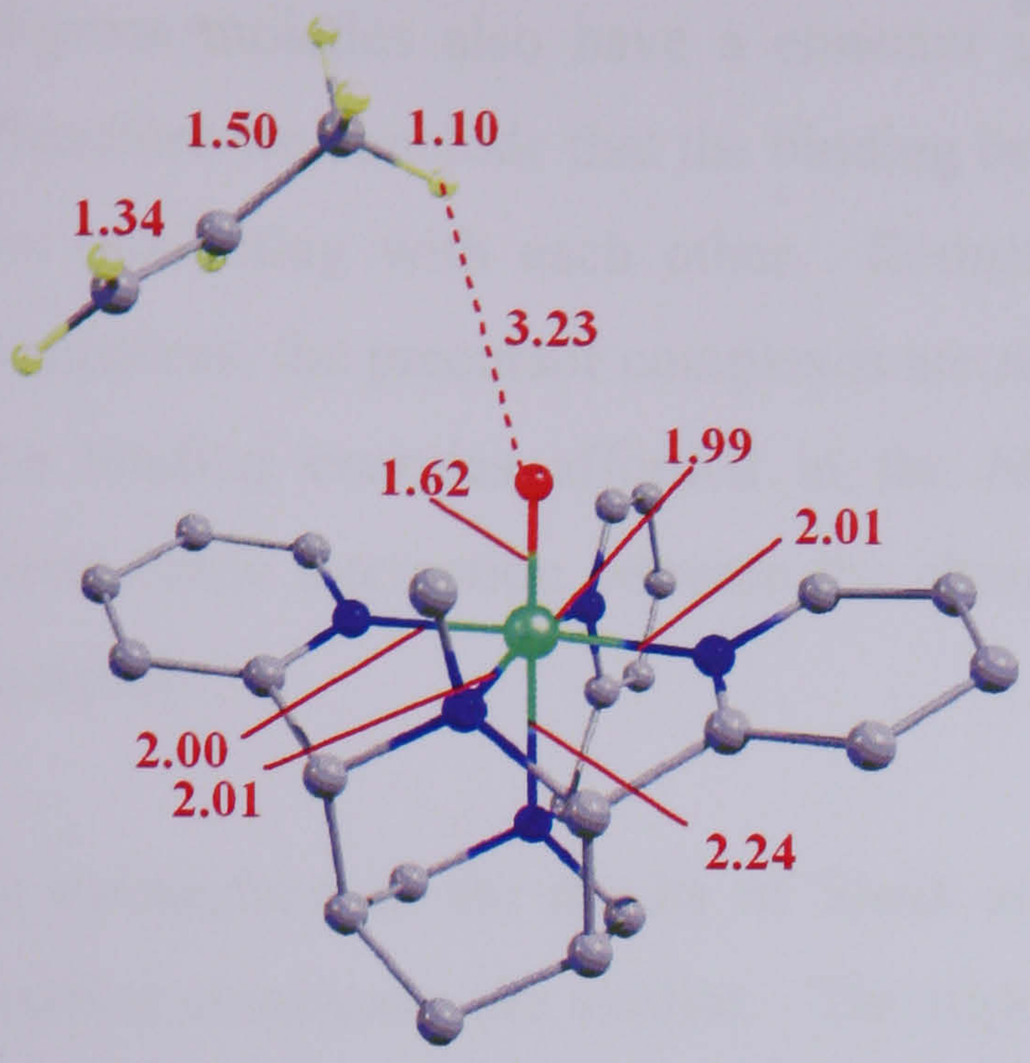

Singlet (^{1}PC)
E = +38.1 kJ mol^{-1}

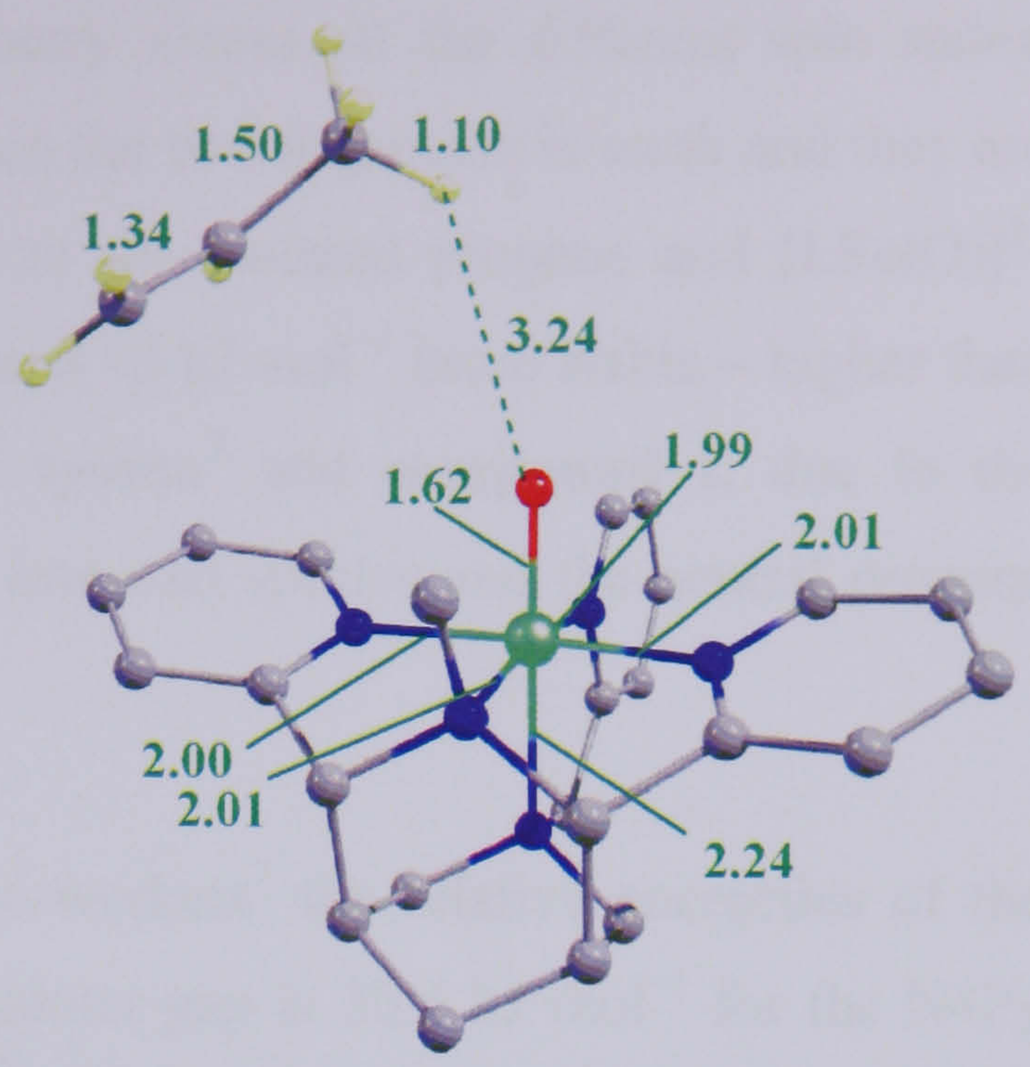

Triplet (^{3}PC)
E = 0.0 kJ mol^{-1*}

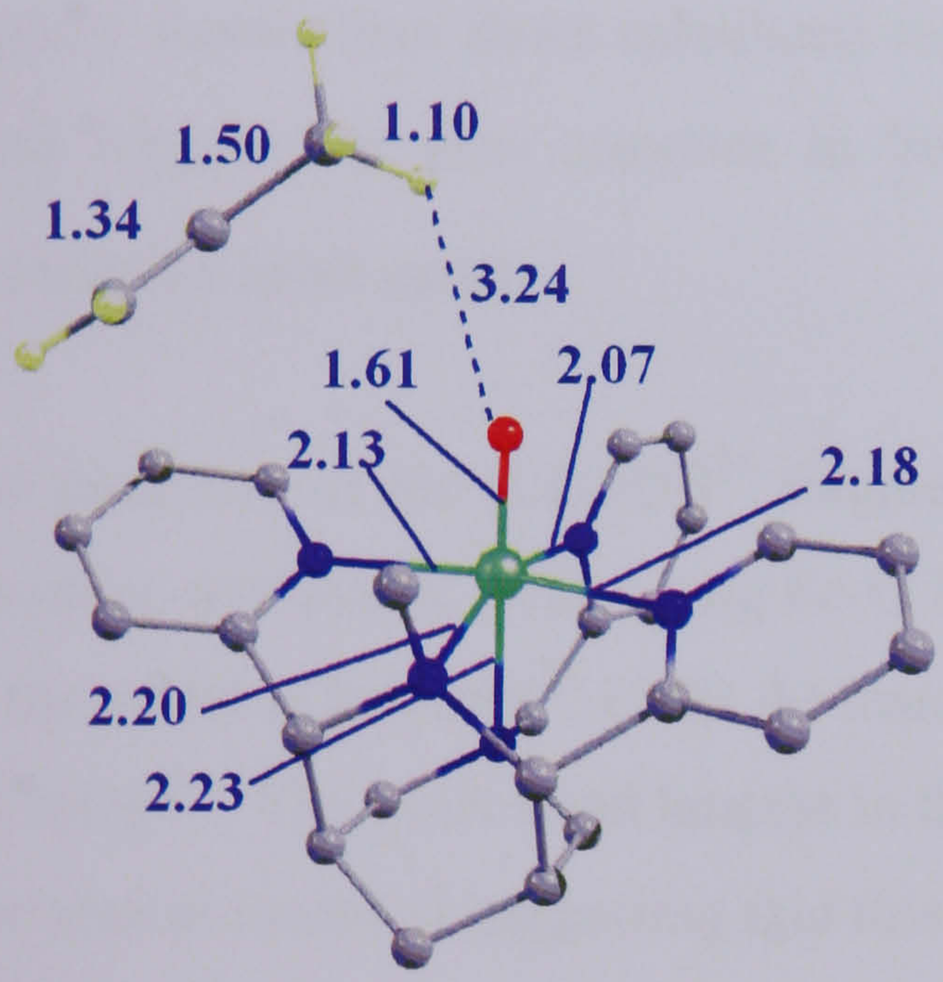

Quintet (^{5}PC)
E = +20.2 kJ mol^{-1}

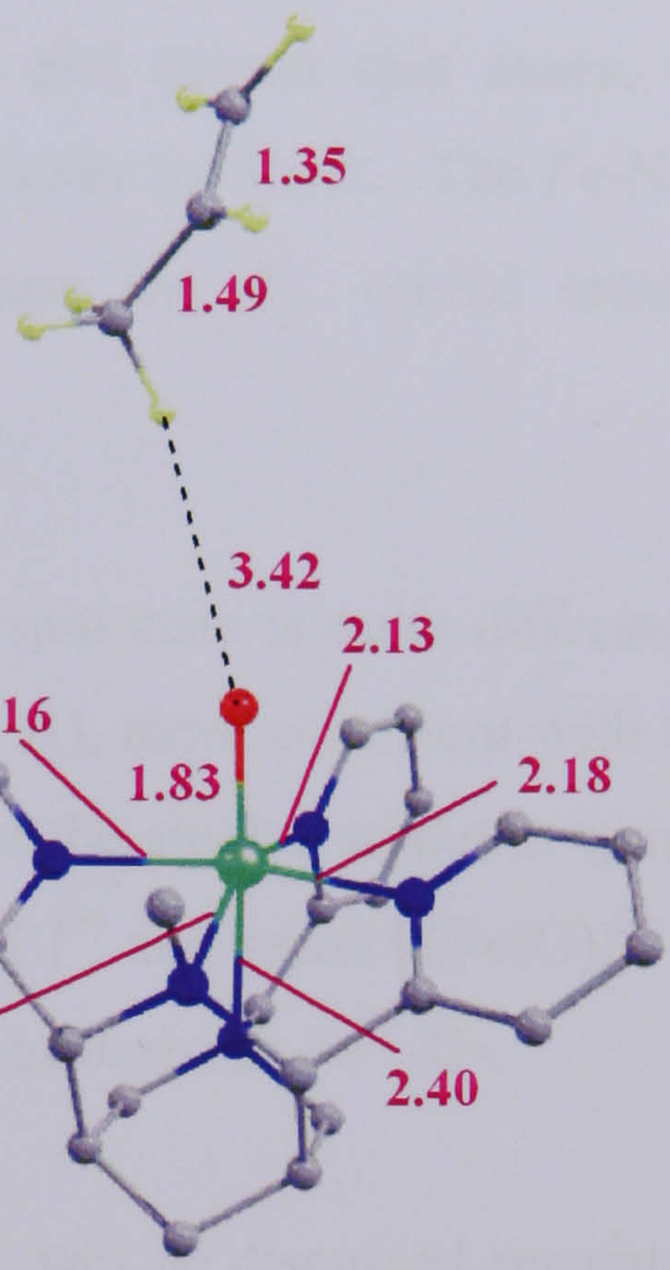

Septet (^{7}PC)
E = + 116.2 kJ mol^{-1}

Figure 4-4 – Geometries (bond length in Å) and energies of starting species {original in colour}

The most stable spin state for the initial geometry is, as expected, a triplet, consistent with isolated $[LFe(O)]^{2+}$. The quintet lies 20.2 kJ mol^{-1} higher in energy than the triplet, and the open shell singlet is 38.1 kJ mol^{-1} higher in energy than the triplet. These energy differences are consistent with those that have been calculated for the isolated $[LFe(O)]^{2+}$ species, as are the geometries of the $[LFe(O)]^{2+}$ fragments. The

propene moieties also have a constant geometry across all the different spin states. Therefore we conclude that the binding between the two fragments is weak and they are not interacting with each other. Compared to the isolated propene and $[LFe(O)]^{2+}$ complexes, the precursor complexes are all about 13 kJ mol^{-1} more stable – higher than the binding energies afforded in the N4Py system[7] and **compound I**, due to the electrostatic interaction between the charged iron-oxo species and the neutral propene molecule.

In comparison to the results of Shaik and co-workers[7] the relative energetics of the starting complexes are similar. The triplet-quintet gap is 30.6 kJ mol^{-1} for the N4Py complex, compared to 20.2 kJ mol^{-1} for this study, while the triplet-singlet gap is 39.5 kJ mol^{-1} for N4Py, compared with 38.1 kJ mol^{-1} for this complex. The calculated Fe-O bond lengths are fairly constant for the singlet, triplet and quintet spin states, and slightly shorter than those calculated for the N4Py complexes by Shaik. The Fe-N_{trans} bond lengths are also constant in both systems because the d_{z^2} orbital remains unoccupied in all cases.

The geometry of the $[LFe(O)]^{2+}$ fragment for the septet spin state is quite different to the other spin states, with a long Fe-O bond length (1.83 Å), more consistent with that in the sextet $[LFe(OH)]^{2+}$ (1.80 Å) than the geometries of the singlet, triplet or quintet $[LFe(O)]^{2+}$. The Fe-N bond lengths in the sextet $[LFe(OH)]^{2+}$ and septet $[LFe(O)]^{2+}$ are also almost identical suggesting that this species can be considered as Fe^{3+}-O•.

The reaction pathways for epoxidation and hydroxylation will be discussed separately. The hydroxylation pathway is compared to that calculated for hydroxylation of cyclohexene by $[(N4Py)Fe(O)]^{2+}$. Although the energetics are not directly comparable due to the different methods used and the different substrate, qualitative similarities between the two mechanisms offer insight into the general reactivity of oxoiron{(IV) complexes.

---

* All energies reported in this chapter are taken relative to this species

4.3 Hydroxylation

The hydroxylation of propene by $[LFe(O)]^{2+}$ has been considered for the singlet, triplet, quintet and septet spin states. The mechanism proposed is analogous to that described by Shaik and co-workers for the oxidation of cyclohexane by $[Fe(N4Py)(O)]^{2+}$.[7] The hydrogen atom that is abstracted is one of those bonded to the sp^3 hybridised carbon atom, leaving an allyl radical as an intermediate. A schematic diagram of the proposed reaction is shown in Figure 4-5, and the energetics for the hydroxylation pathway are summarised in Figure 4-6.

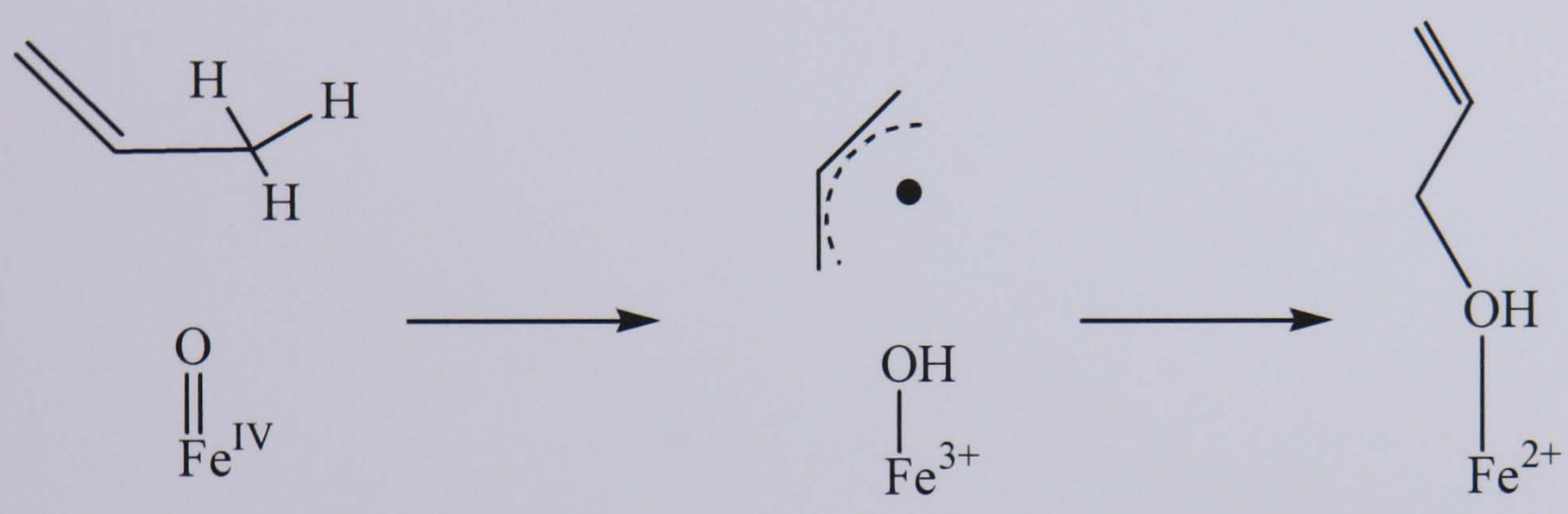

Figure 4-5 – Schematic diagram of the mechanism for hydroxylation of propene by oxoiron(IV)

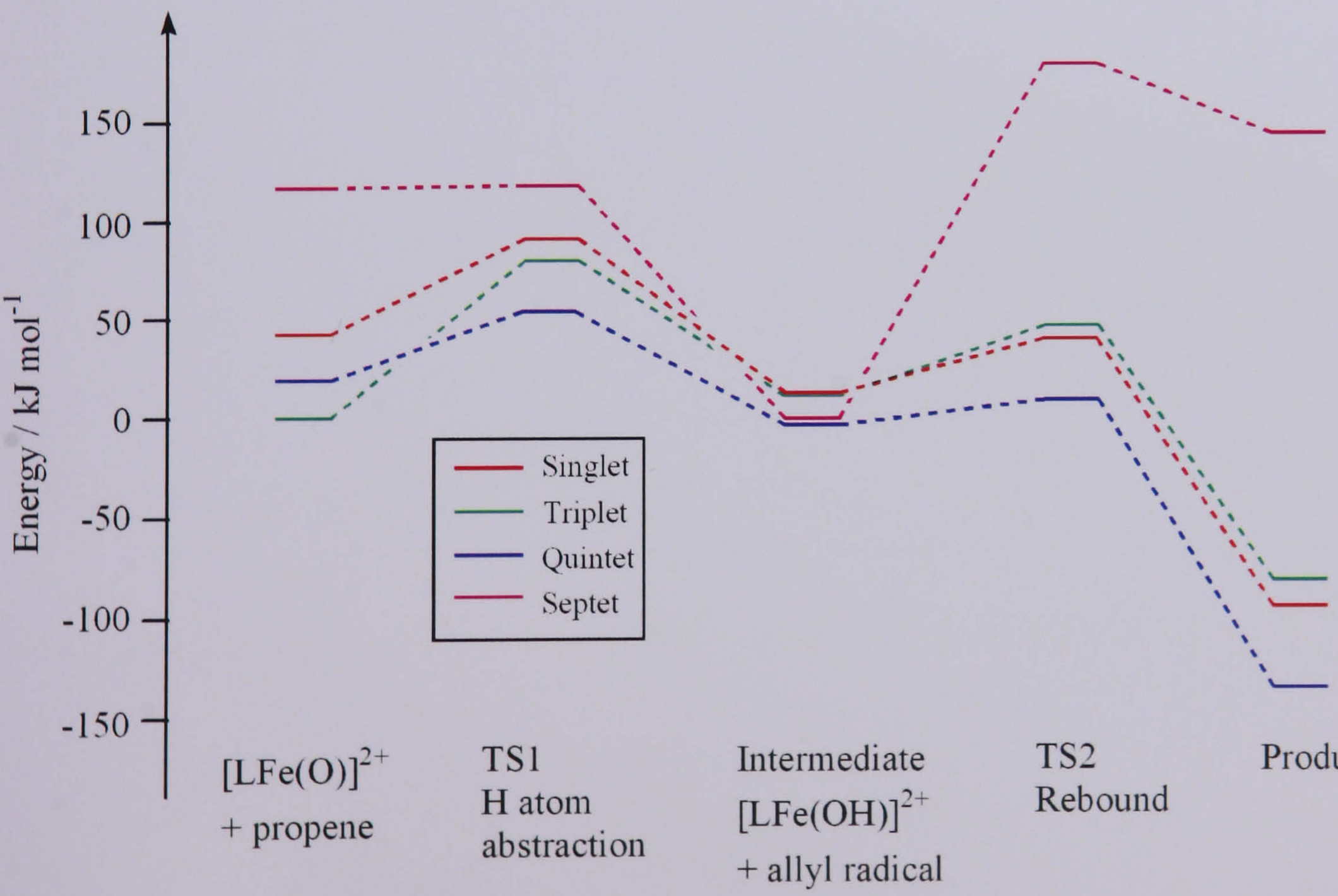

Figure 4-6 – Energetics for the hydroxylation reaction of $[LFe(O)]^{2+}$ and propene {original in colour}

4.3.1 Product Geometries – Hydroxylation

The hydroxylation of propene by $[LFe(O)]^{2+}$ leads to a propenol molecule coordinated to Fe^{2+}. This complex has been located for the singlet, triplet, quintet and septet transition states, and the geometries and relative energies are shown in Figure 4-7. The quintet state is the most stable, as for the equivalent water and H_2O_2 complexes. The triplet and septet spin states are unstable, and will not be discussed further.

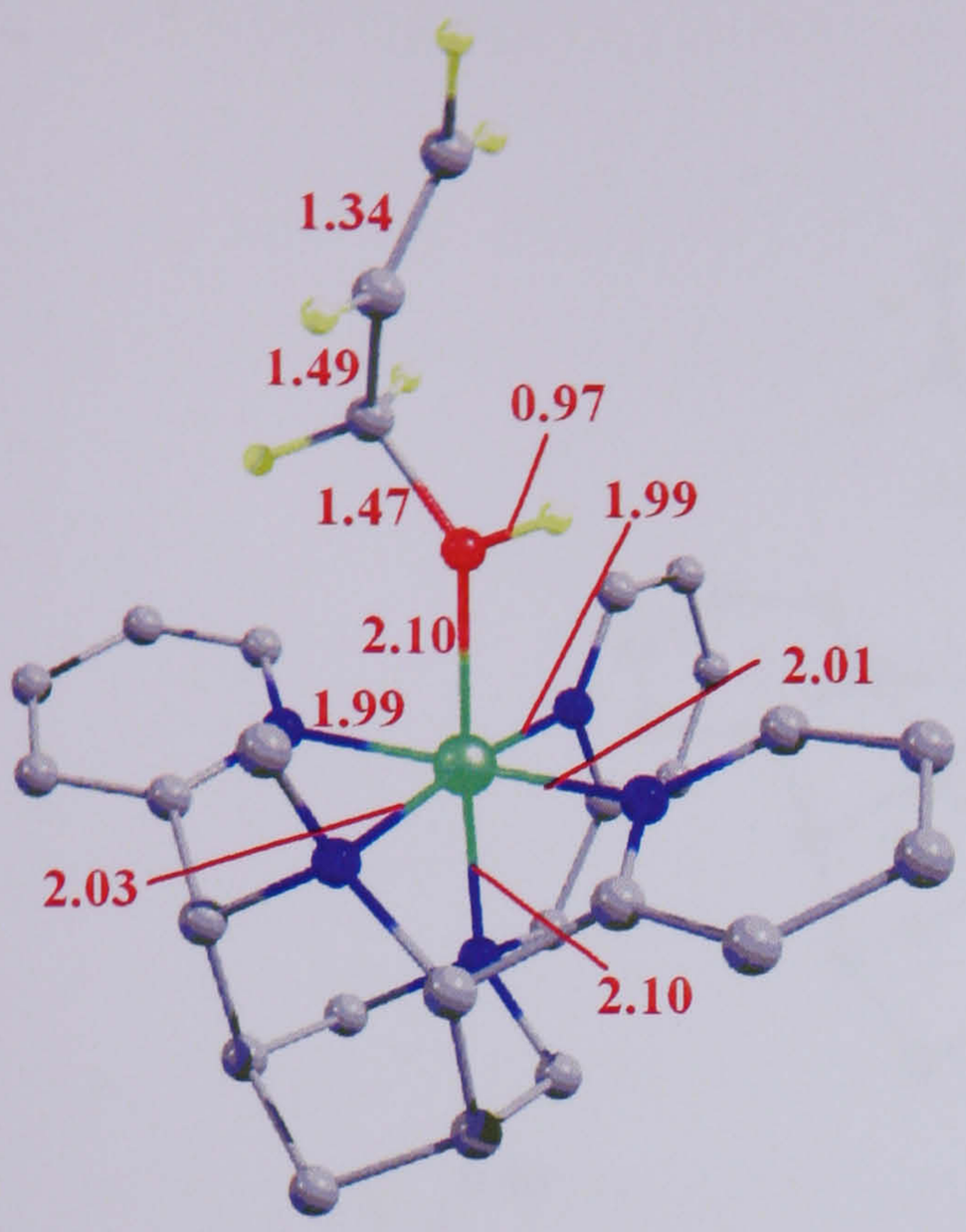

Singlet (^{1}HP)
Energy = −96.1 kJ mol^{-1}

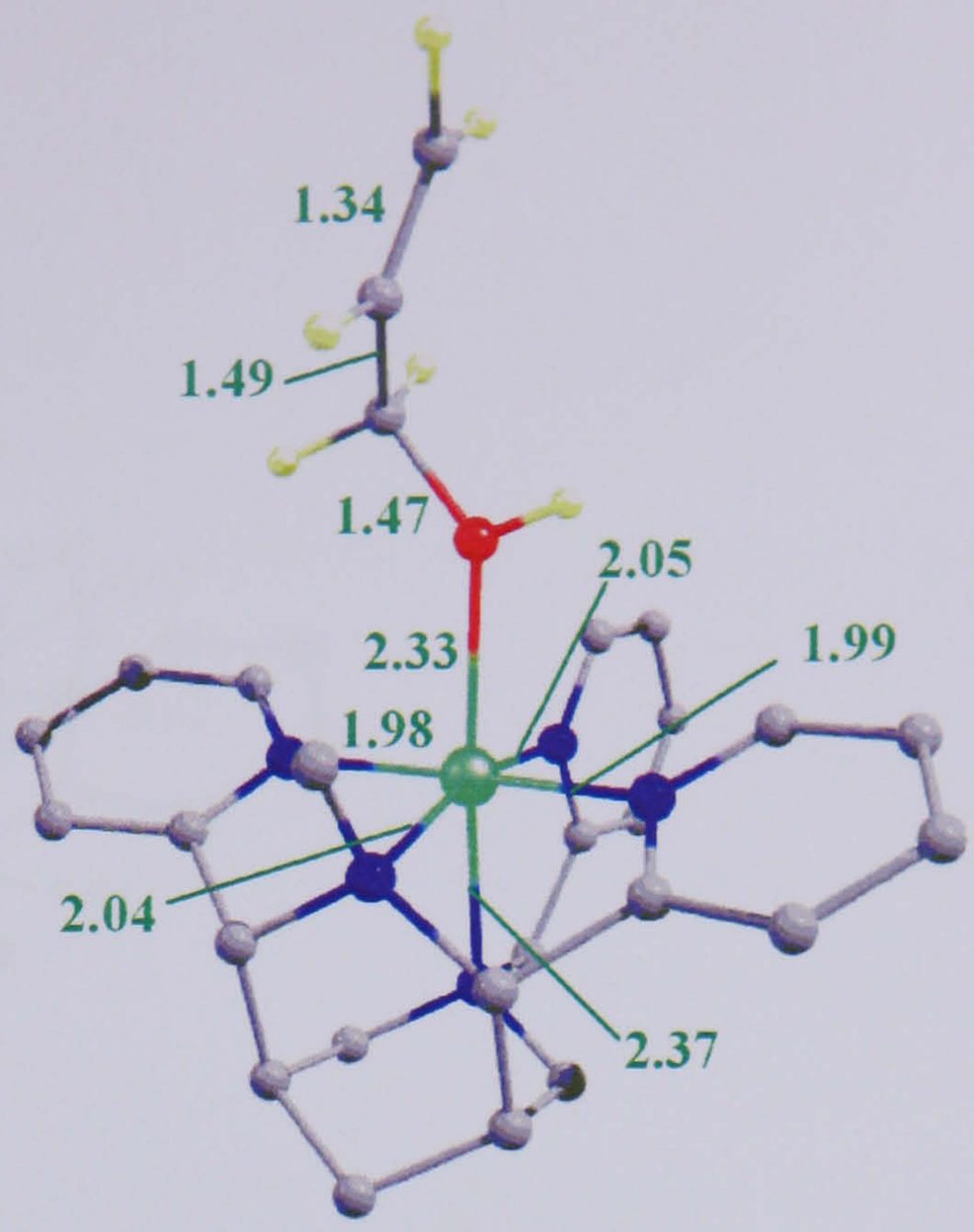

Triplet (^{3}HP)
Energy = −82.0 kJ mol^{-1}

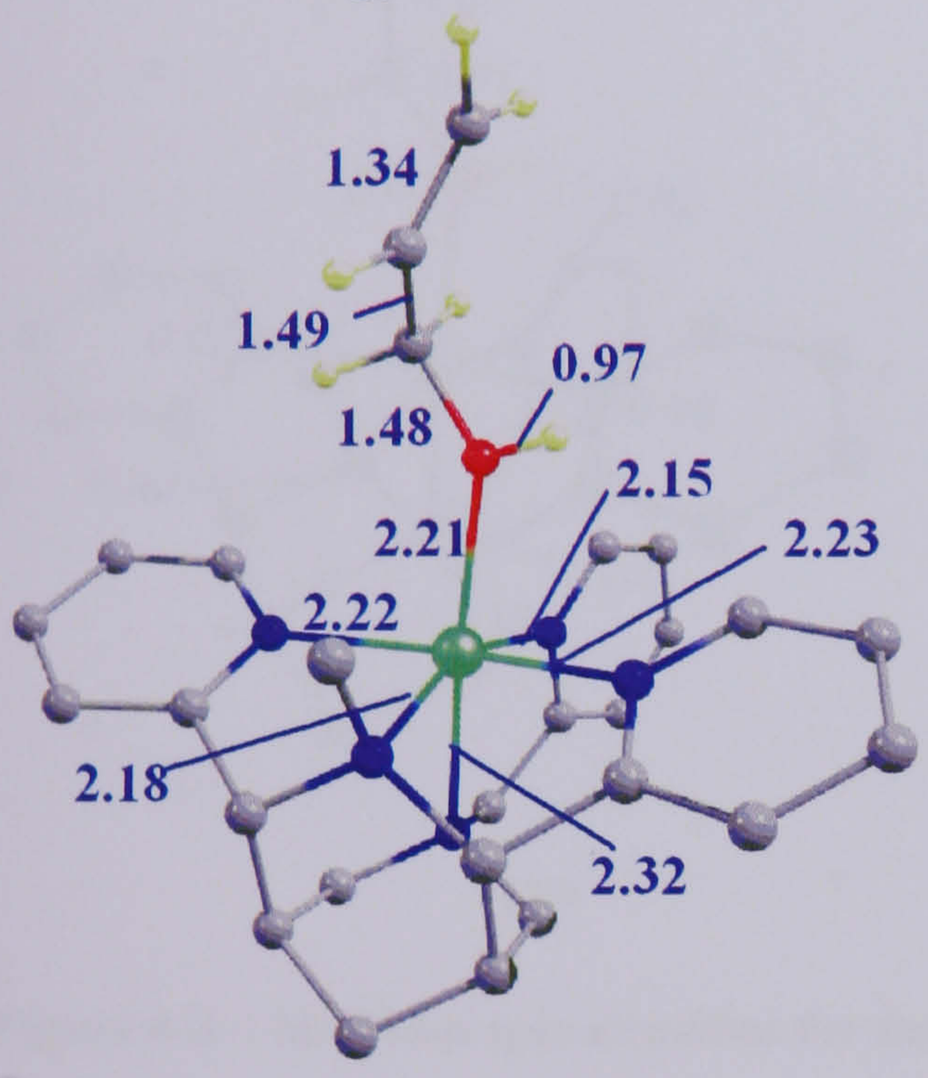

Quintet (^{5}HP)
Energy = −134.8 kJ mol^{-1}

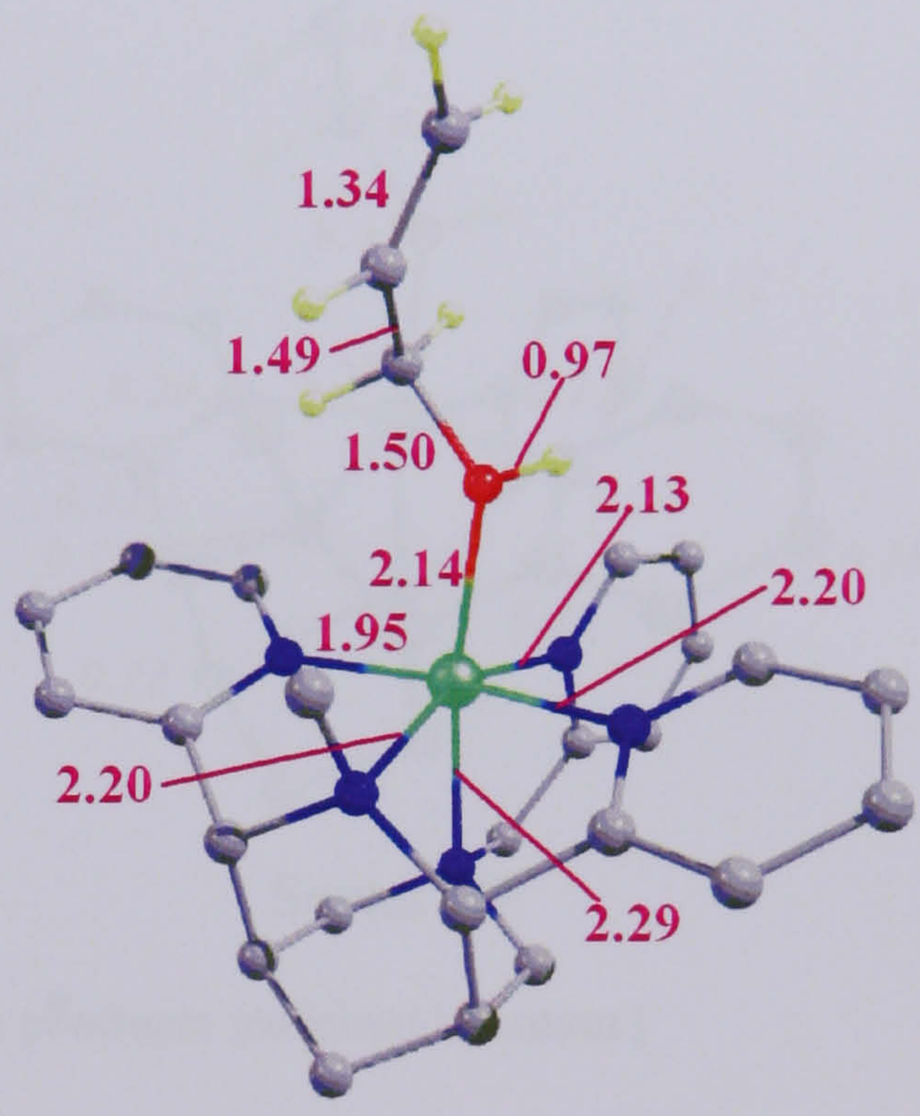

Septet (^{7}HP)
Energy = +143.8 kJ mol^{-1}

Figure 4-7 – Geometries (bond lengths in Å) and energies of the propene H-atom abstraction products {original in colour}

The geometry of the propenol fragment is insensitive to spin state, and the Mulliken spin densities (shown in Figure 4-8) confirm that it is a closed shell ligand. The singlet, triplet and quintet states therefore differ only in the electronic structure at the iron centre. The (highly unstable) septet spin state, in contrast, has considerable radical character delocalised over the nitrogen ligands and two of the pyridine rings.

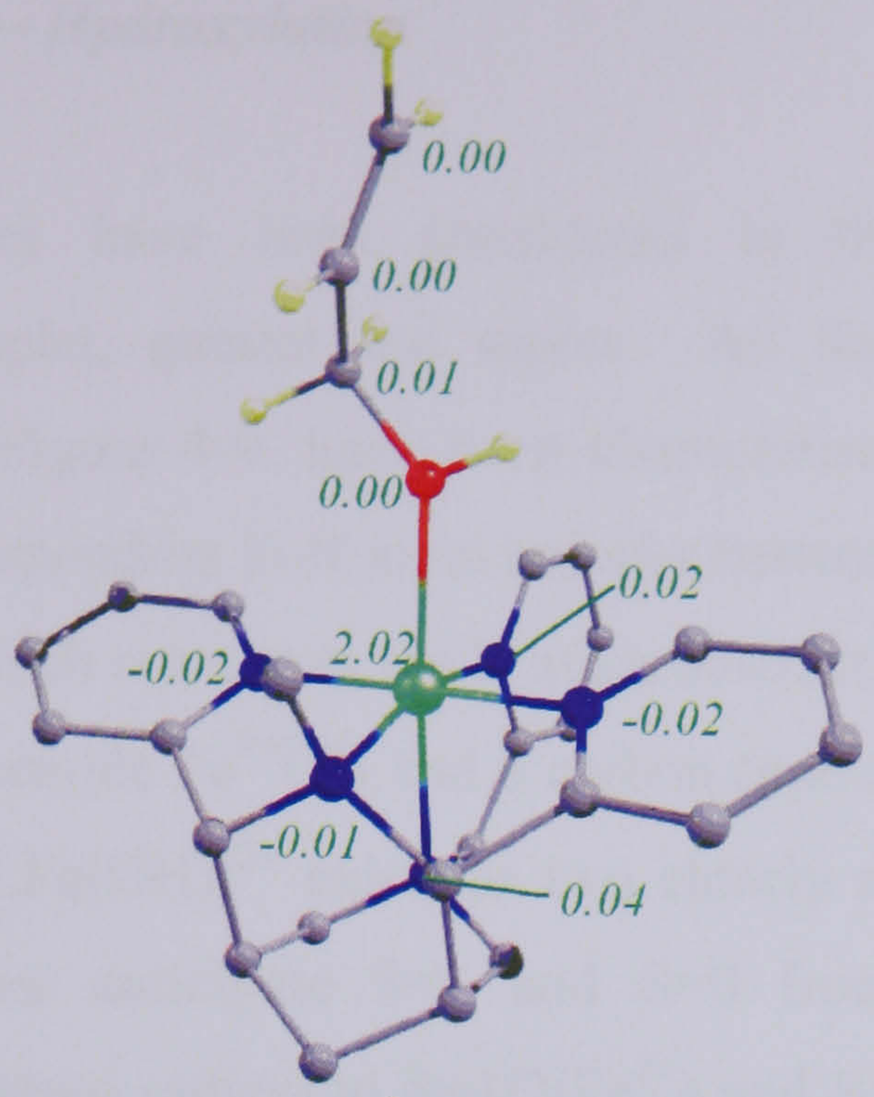

^{3}HP

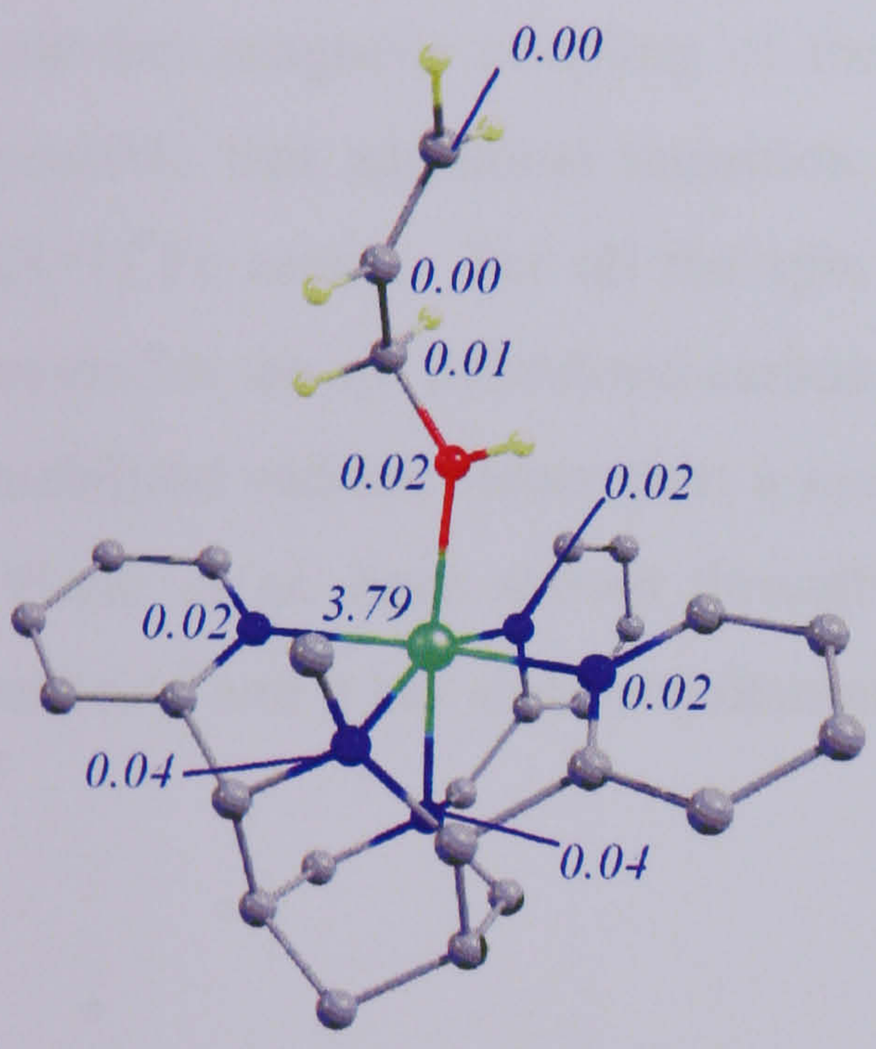

^{5}HP

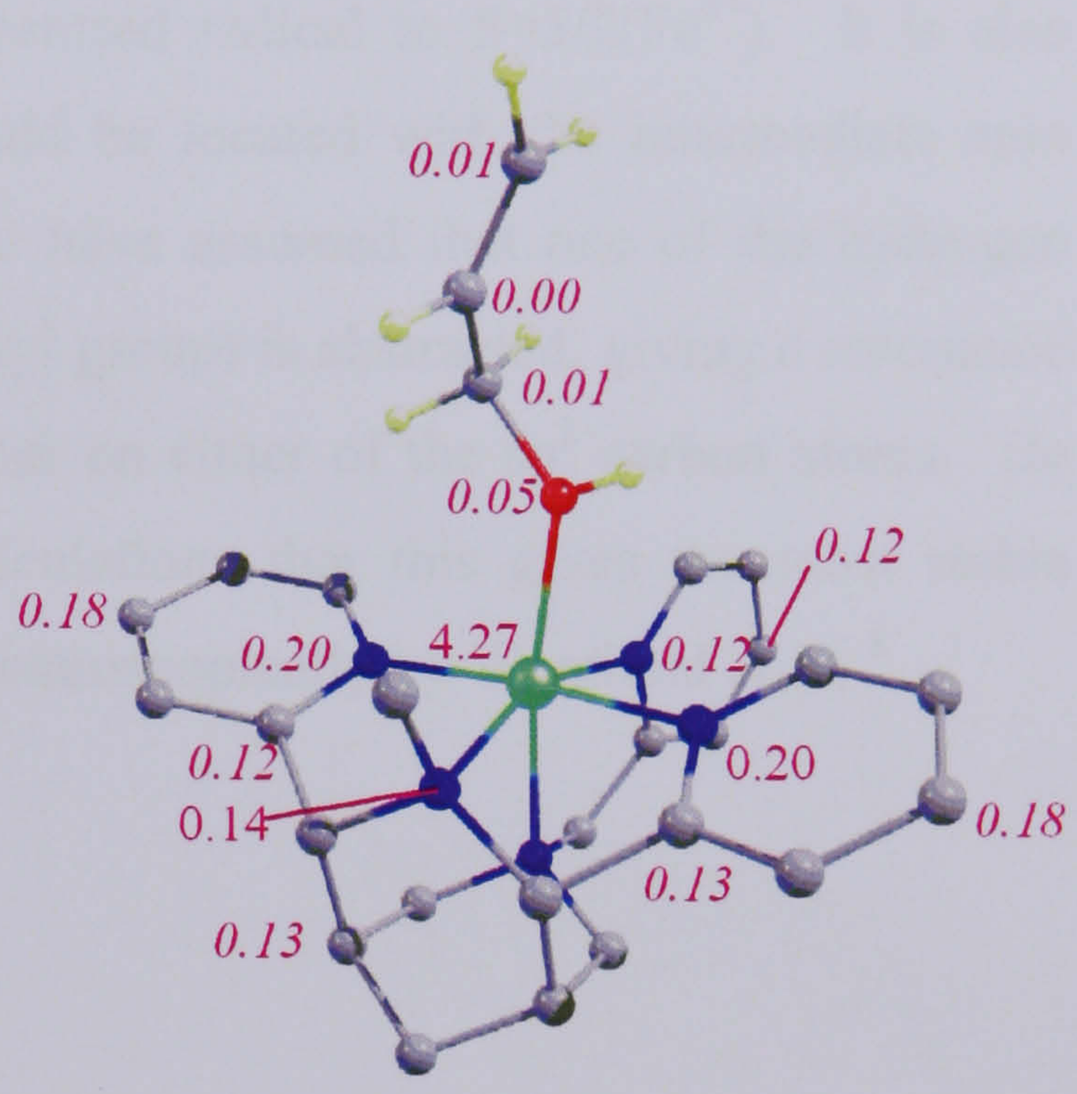

Septet^{7}HP

Figure 4-8 – Mullkien spin densities for the hydroxylation products {original in colour}

Overall, the results presented for the hydroxylation products are consistent with those of Shaik and co-workers, particularly with regard to the ordering of spin states.[7] However, the energy differences – especially for the singlet-triplet gap – are smaller in our system than the N4Py system. We attribute this difference to the role of the nitrogen based ligand, which has a longer Fe-N_{trans} distance in the bispidone ligand than the N4Py ligand, stabilising the d_{z^2} orbital.

4.3.2 Transition State 1 – Hydroxylation

Four possible spin states have been considered in the reaction pathway for hydroxylation: singlet, triplet, quintet and septet. All the transition states, whose geometries are shown in Figure 4-9, have been characterised by the presence of one imaginary frequency corresponding to H atom transfer between the O and C atoms. For the first transition state, which represents the H atom abstraction step, we anticipate that the transition state will resemble $Fe^{3+}OH$ and a carbon centred radical. In the previous chapter we showed that $[LFe(OH)]^{2+}$ exists as two closely spaced spin states – S=1/2 and S=5/2. We therefore anticipate S=1 and S=0 from ferro/anti-ferromagnetic coupling of the carbon centred radical to S=1/2(Fe^{3+}) and S=3 and S=2 for ferro- and anti-ferromagnetic coupling of the carbon centred radical to S=5/2(Fe^{3+}). It is also possible that additional transition states could be located with the intermediate spin (S=1) Fe centre. For all the spin states, we have assumed that one of the hydrogen atoms on the sp^3 hybridised carbon (the methyl group) is abstracted, giving a resonance stabilised radical, rather than a hydrogen atom on either of the sp^2 carbon atoms. De Visser *et al.* have shown through DFT calculations that this gives the most stable radical,[4] and it has also been demonstrated spectroscopically by Wenthold *et al.* [8]

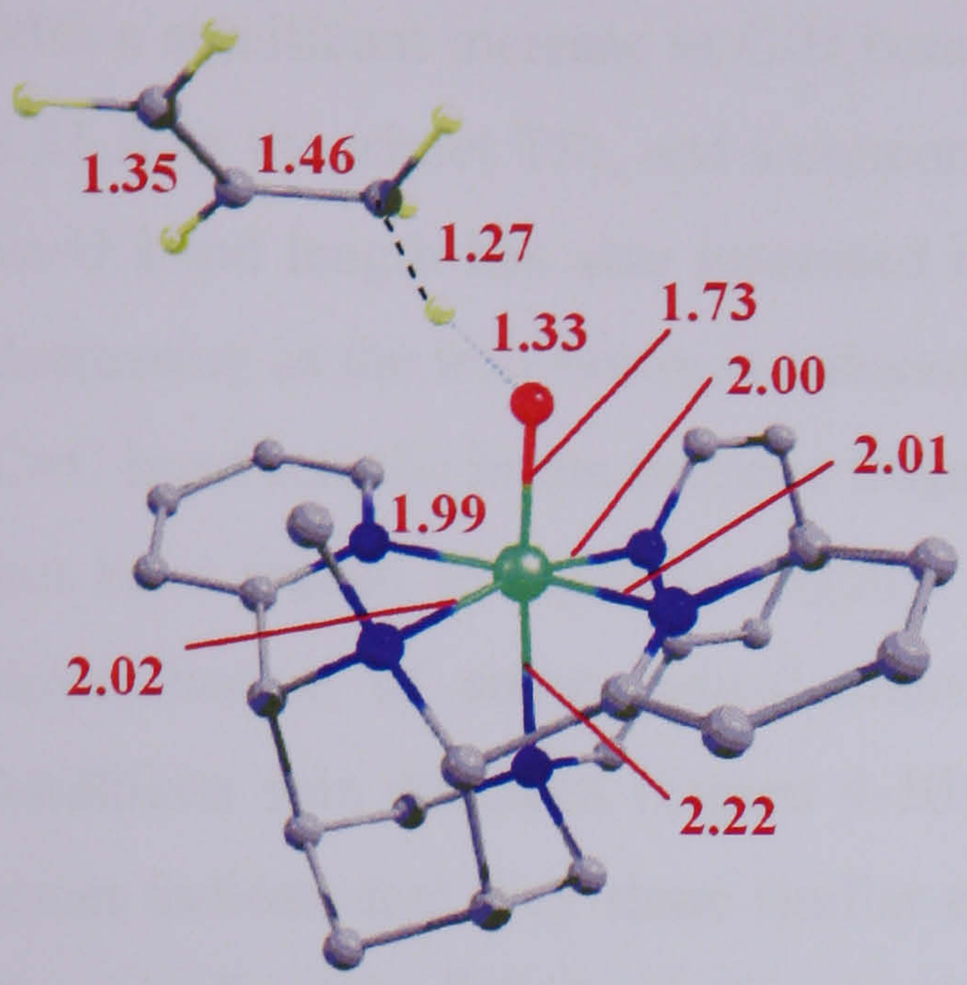

Singlet (^{1}HTS1)
E = +93.3 kJ mol^{-1}

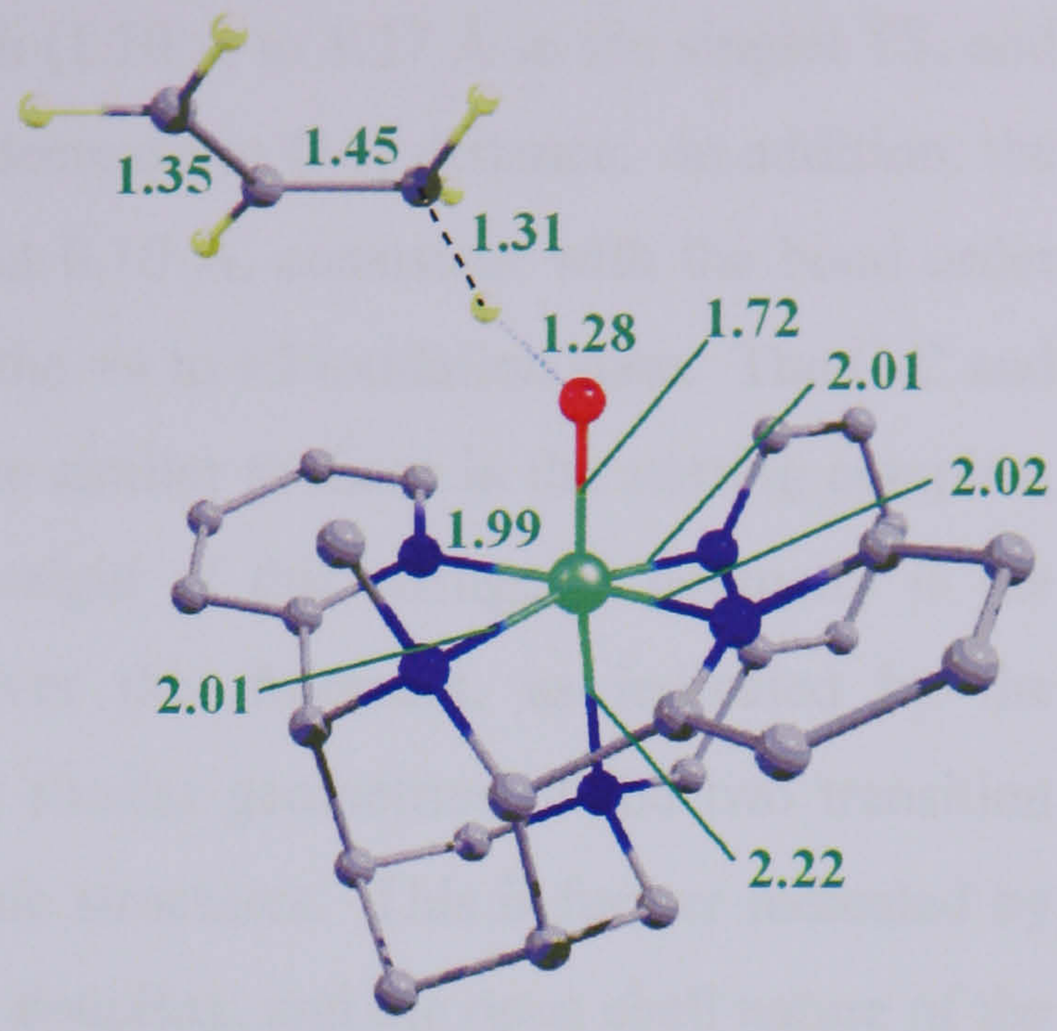

Triplet (^{3}HTS1)
E = +80.1 kJ mol^{-1}

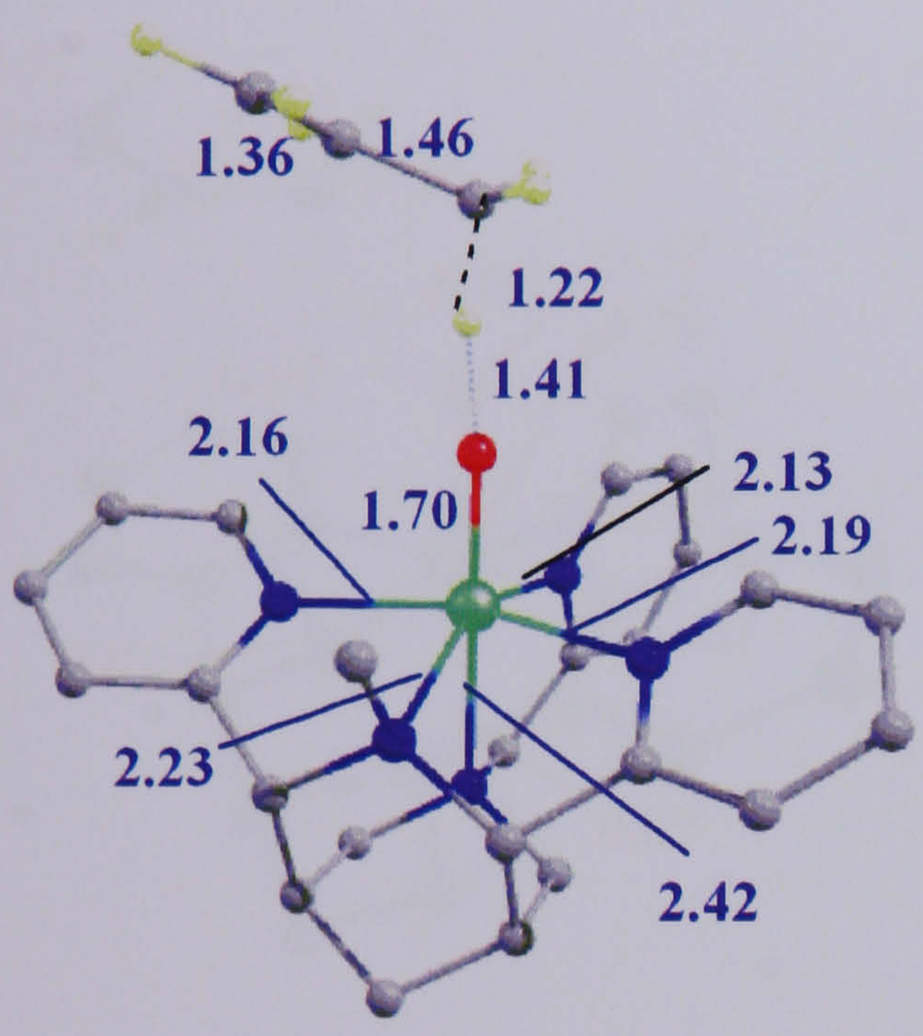

Quintet (^{5}HTS1)
E = +53.2 kJ mol^{-1}

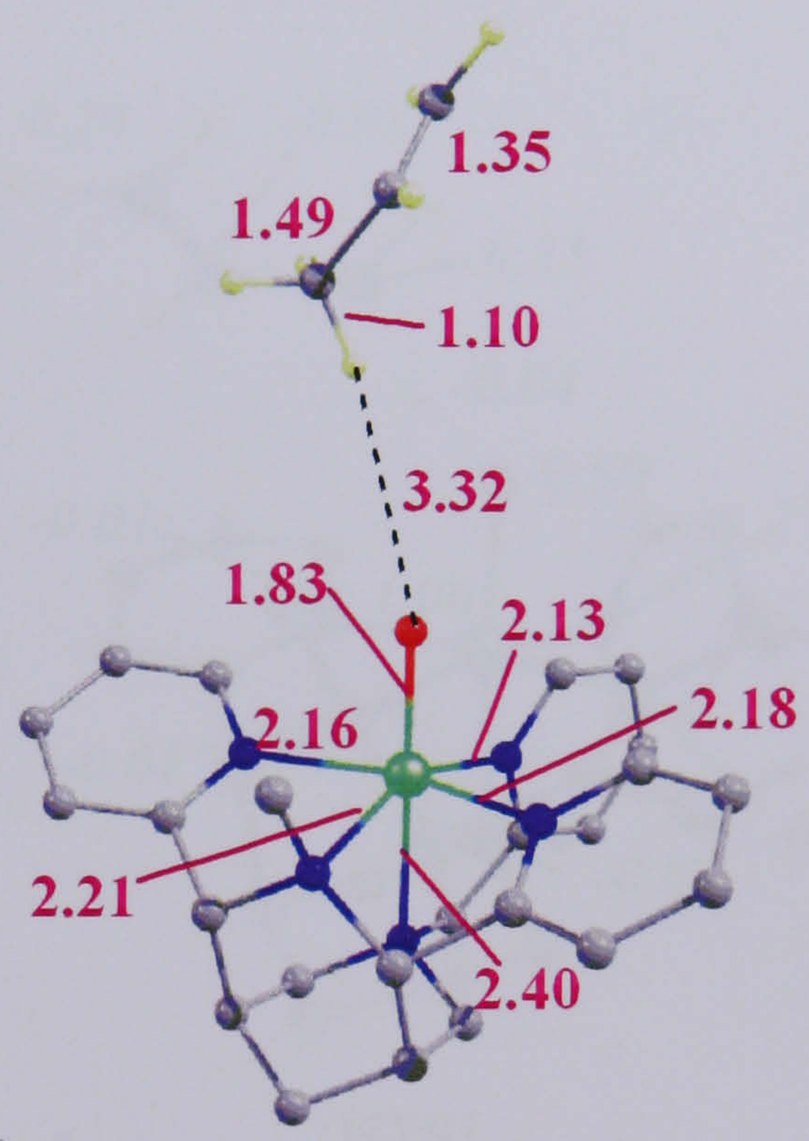

Septet (^{7}HTS1)
E = +116.7 kJ mol^{-1}

Figure 4-9 – Geometries (bond lengths in Å) and energies of TS1 for hydroxylation {original in colour}

4.3.2.1 Singlet and Triplet Transition States

The singlet and triplet transition states have similar geometries, although the triplet state is more stable by 13 kJ mol^{-1}. This is consistent with the difference between the singlet and triplet spin state in the N4Py system suggesting that the transition states are electronically similar in both systems. Both transition states in the bispidone system

correspond to H atom abstraction from the CH_3 group of propene by the oxo group, with a significant increase in C-H bond length (1.10 Å to 1.27 Å in the singlet TS, and 1.31 Å in the triplet TS), and a concomitant decrease in O-H distance. In addition, the Fe-O bond length has also increased by about 0.10 Å, consistent with the bond order decreasing as the iron centre is reduced from the +4 to +3 oxidation state. The C-C and C=C bond lengths in the propene fragment are similar to those in the starting complex, but have started to equalise slightly. The origin of this change in geometry is the delocalisation of some radical character over this fragment, as indicated by the Mullliken spin densities (Figure 4-10). The similar geometries of the two transition states indicate that they share similar electronic structures. This is further indicated by the spin densities, which confirm S=1/2 ± 1/2 coupling, and the open shell nature of the singlet.

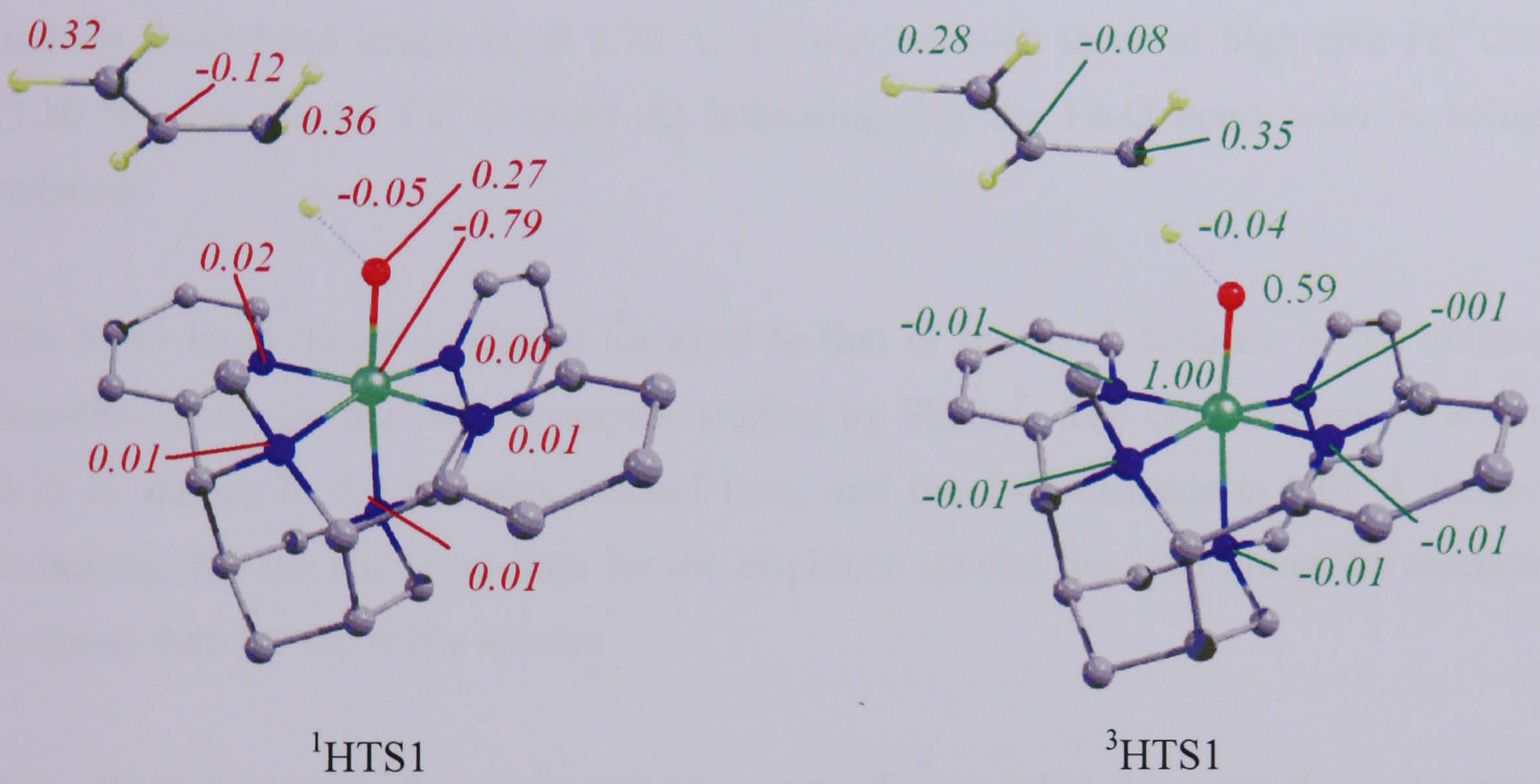

^{1}HTS1 ^{3}HTS1

Figure 4-10 – Spin densities for the singlet and triplet spin states {original in colour}

The singlet and triplet geometries of the HTS1 stationary points with the bispidone ligands are comparable to the equivalent points on the PES of the N4Py complexes, particularly for the Fe-N, O-H and C-H distances. The relatively long Fe-N_{trans} bond lengths observed in other Fe-bispidone complexes discussed in this thesis are also seen here, and are longer than the Fe-N_{trans} bond lengths in the N4Py complexes. The Fe-O distance is also calculated to be shorter in the bispidone than the N4Py complexes as a result of the reduced *trans* influence in the bispidone species.

The geometry of the C…H…O fragment is similar for the singlet states of both the bispidone and N4Py species. The triplet geometries are also fairly similar, but the triplet transition state for the N4Py complex lies further along the reaction pathway than the bispidone triplet TS, as indicated by the shorter O-H and longer C-H distances. The energy differences between the singlet and triplet spin states are also similar in both complexes, with ferromagnetic coupling preferred over anti-ferromagnetic coupling.

4.3.2.2 Quintet Transition State

The quintet transition state has the lowest barrier of the spin states considered, consistent with the results of Shaik and co-workers.[7] The hydrogen atom being transferred has both a long C-H and even longer O-H bond (1.22 and 1.41 Å respectively). The Fe-N bond lengths are typical of those expected for high spin Fe^{3+}, and the Fe-O bond length is, at 1.70 Å, midway between those of high spin $Fe^{3+}OH$ (1.80 Å) and quintet $Fe^{4+}O$ (1.61 Å) indicating that the Fe-O bond order is being reduced.

The Fe-O bond length is almost identical to that of the Fe-O distance in the quintet transition state for the N4Py complex studied by Shaik.[7] The O-H distance is about 0.23 Å shorter in the complex studied here, and the C-H distance is 0.07 Å longer indicating that the transition state for the bispidone species lies later along the reaction pathway than for the N4Py species.

The spin densities for the quintet transition state (Figure 4-11) show that the iron centre has four majority spin electrons associated with it. The oxygen atom also has a large amount of radical character associated with it and is ferromagnetically coupled to iron. The propene fragment, including the hydrogen atom being transferred, also has a considerable degree of radical character, but of the opposite spin to that on Fe. In the singlet and triplet spin states, the radical character associated with the propene fragment is largely localised on the two primary carbon centres. with a small amount of spin density of the opposite spin on the secondary carbon, and virtually no spin density on the hydrogen atom being transferred. This is consistent with allyl radical character, and single occupancy of the non-bonding orbital. The situation for the quintet transition state is reversed: the secondary carbon atom and the hydrogen atom bear most of the

radical character, and there is virtually none on the two primary carbon centres. The O-H and C-H bond lengths show that the quintet transition state lies earlier than for the singlet and triplet, and the propene fragment has not yet developed much allyl character, explaining the different distribution of electrons.

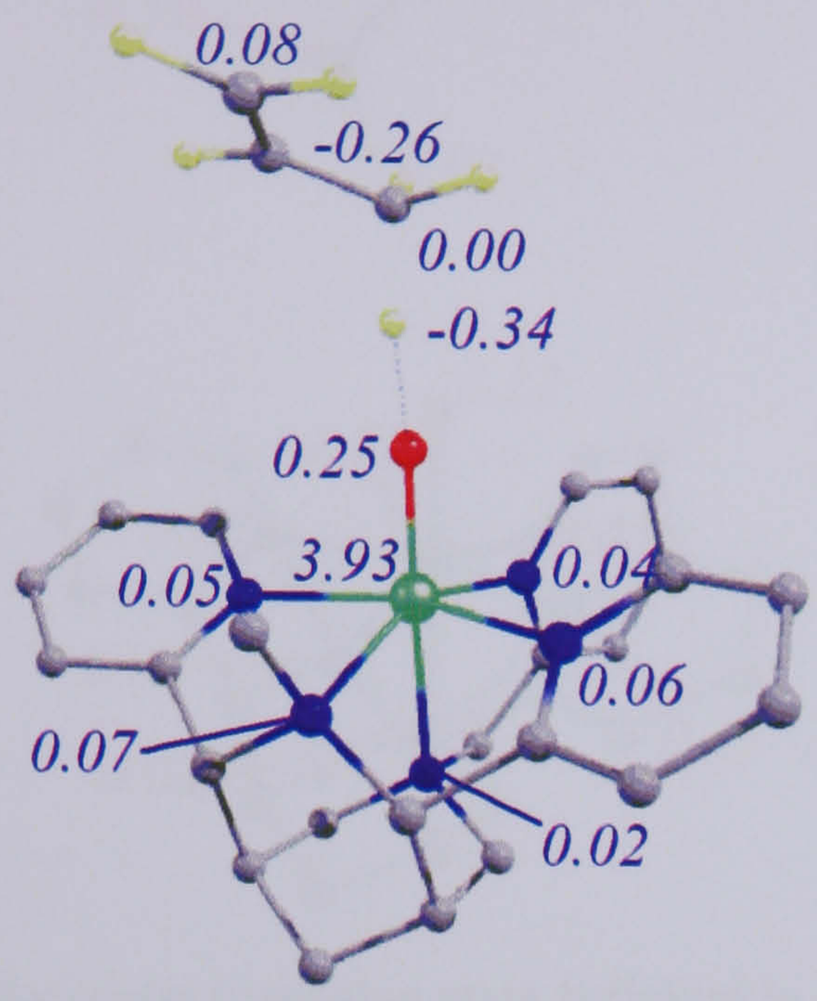

Figure 4-11 – Spin densities for the quintet TS

4.3.2.3 Septet Transition State

The structure of the septet transition state we have located is unlike that of the other spin states, and lies much earlier along the reaction pathway. The geometry of the propene fragment is essentially the same as that of ground state propene, and the $[LFe(O)]^{2+}$ geometry is almost identical to that of the reactant, and can therefore still be described as Fe^{3+}-O•, rather than Fe^{4+}=O. This description is supported by the spin densities of 4.13 on iron and 1.22 on oxygen, shown in Figure 4-12. As stated in section 4.2, the Fe^{3+}-O• is an excited state, and the oxo group is expected to be extremely reactive due to the high amount of radical character associated with it. Therefore it is able to abstract a hydrogen atom from propene with only a very small energetic barrier to leave a comparatively stable allyl radical. This is reflected in the extremely small difference of less that 1 kJ mol^{-1} between the septet reactant and transition state. Unlike in the singlet, triplet and quintet spin states, the propene fragment has very little spin density associated with it, again showing that the septet transition state very closely resembles the reactants. However, due to the high energy of

both the septet starting complex and transition state, this spin state is not expected to influence to reaction at all at this point.

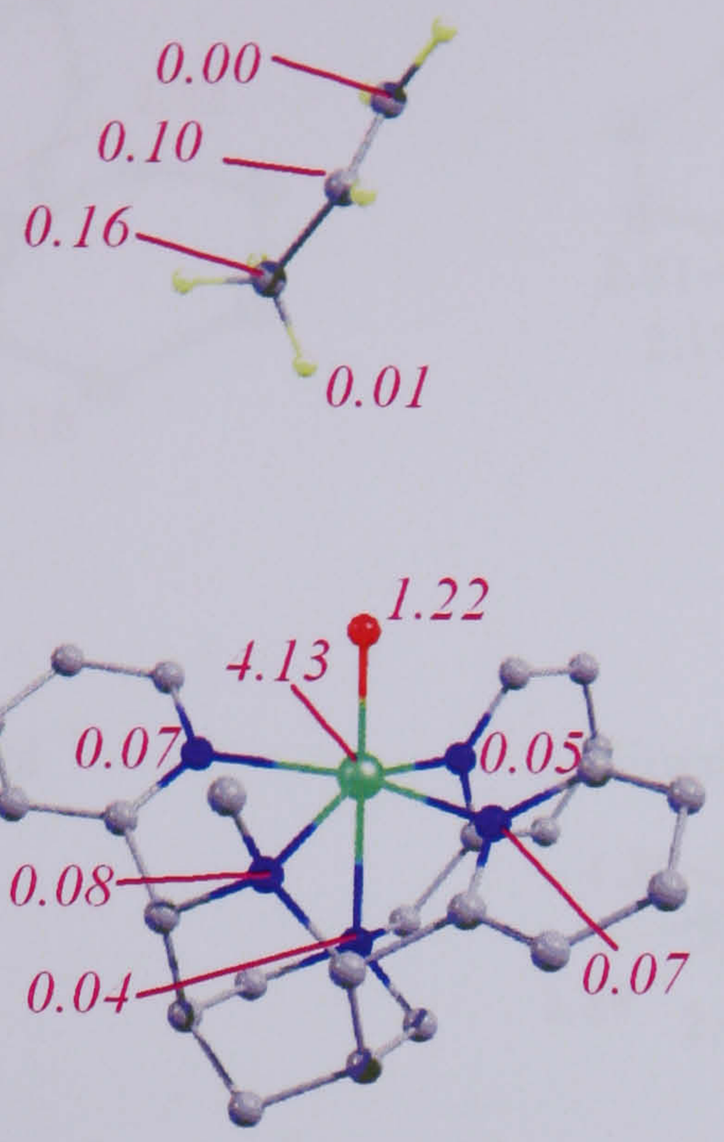

Figure 4-12 – Spin densities of the septet transition state {original in colour}

In the N4Py system, the substrate is cyclohexane whereas in this study the substrate is propene. Typical CH bond strengths for secondary carbons such as those in cyclohexane are around 414 kJ mol^{-1}, compared to 364 kJ mol^{-1} for the CH bond strengths in propene (we are considering the CH_3 bond strengths here).[7,8] Therefore, we expect the transition state to be approximately 50 kJ mol^{-1} higher in the N4Py system if the reactivities of the two complexes are the same. In fact, the energies of the equivalent transition states relative to the triplet oxoiron(IV) species and substrate are approximately equal for both species: +53 kJ mol^{-1} in the complex studied here versus +46 kJ mol^{-1} in the N4Py complex. This indicates that the N4Py species is expected to be faster at hydroxylating hydrocarbons than the $[Fe(N2Py3o)(O)]^{2+}$ species assuming that the rate of formation of the oxoiron(IV) species is the same.

4.3.6 Intermediates for the Hydroxylation of Propene

The transition states discussed in the previous section lead to intermediates corresponding to $[LFe(OH)]^{2+}$ and an allyl radical, the geometries and energies of which are shown in Figure 4-13.

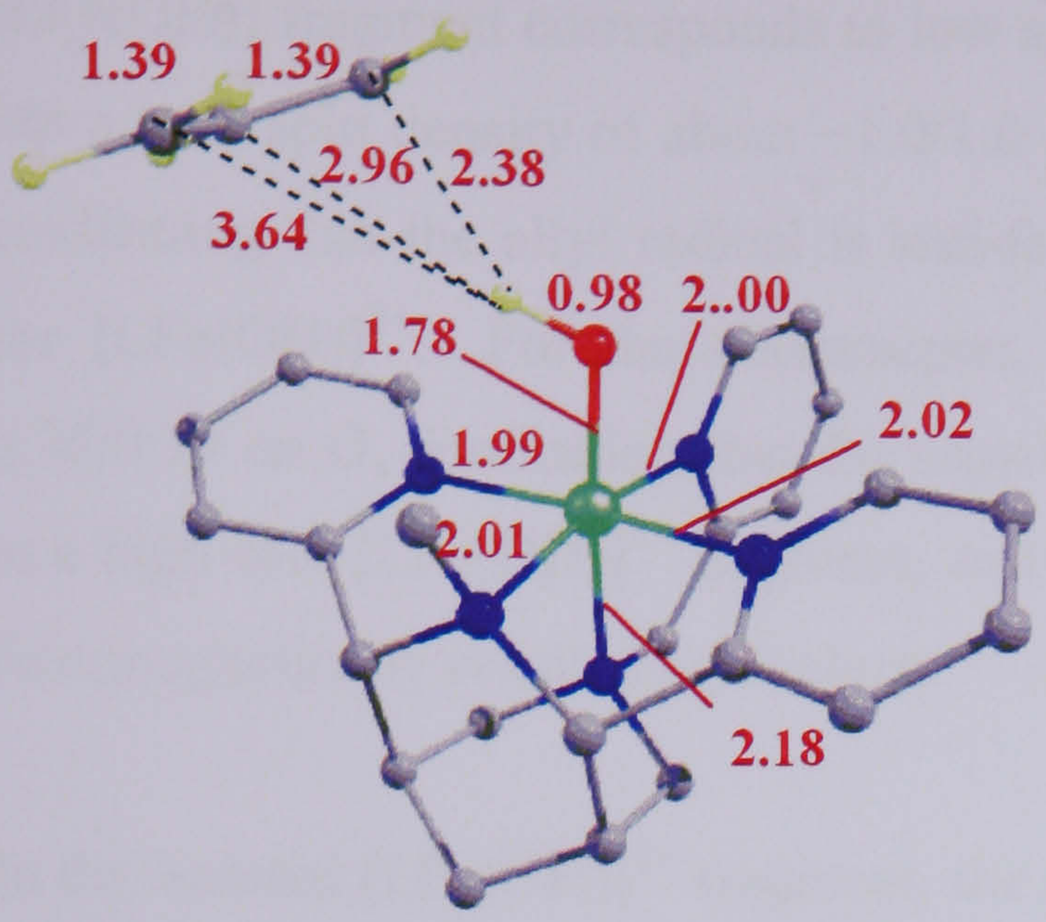

Singlet (^{1}HI)
Energy = +10.2 kJ mol^{-1}

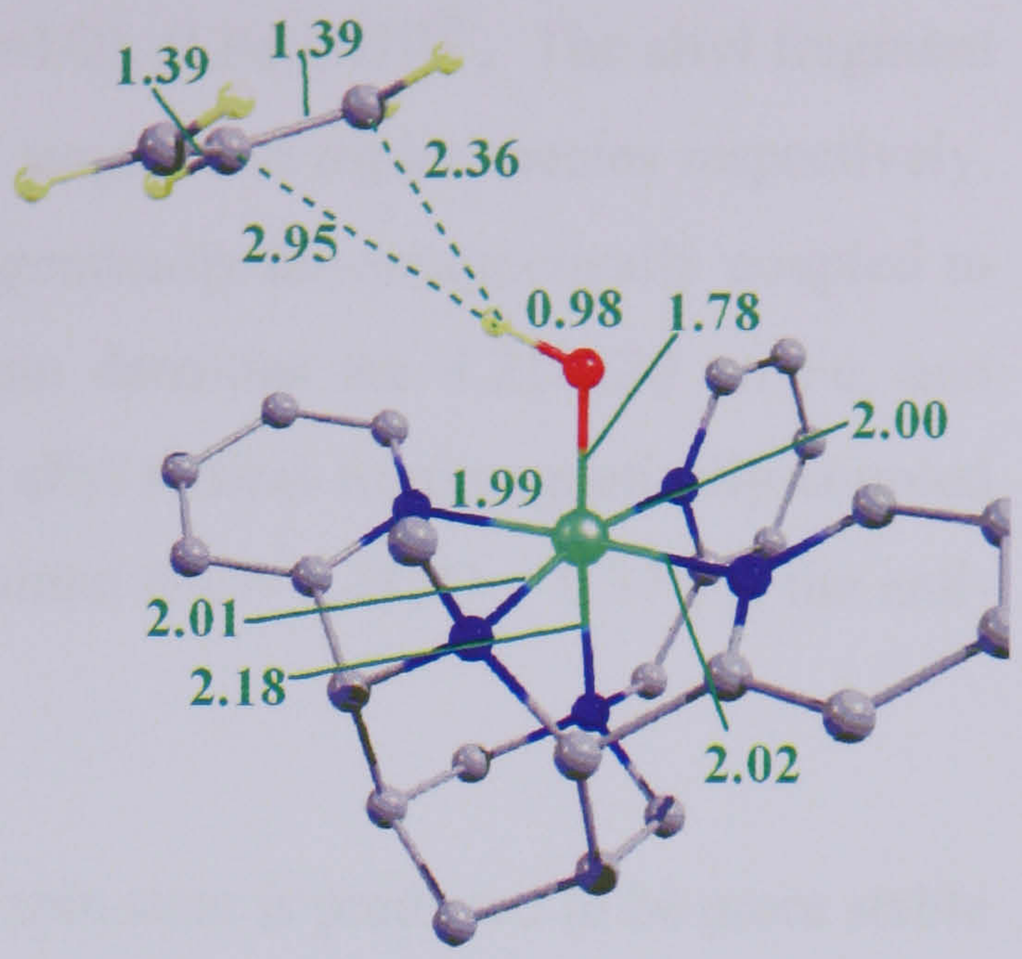

Triplet (^{3}HI)
Energy = +9.8 kJ mol^{-1}

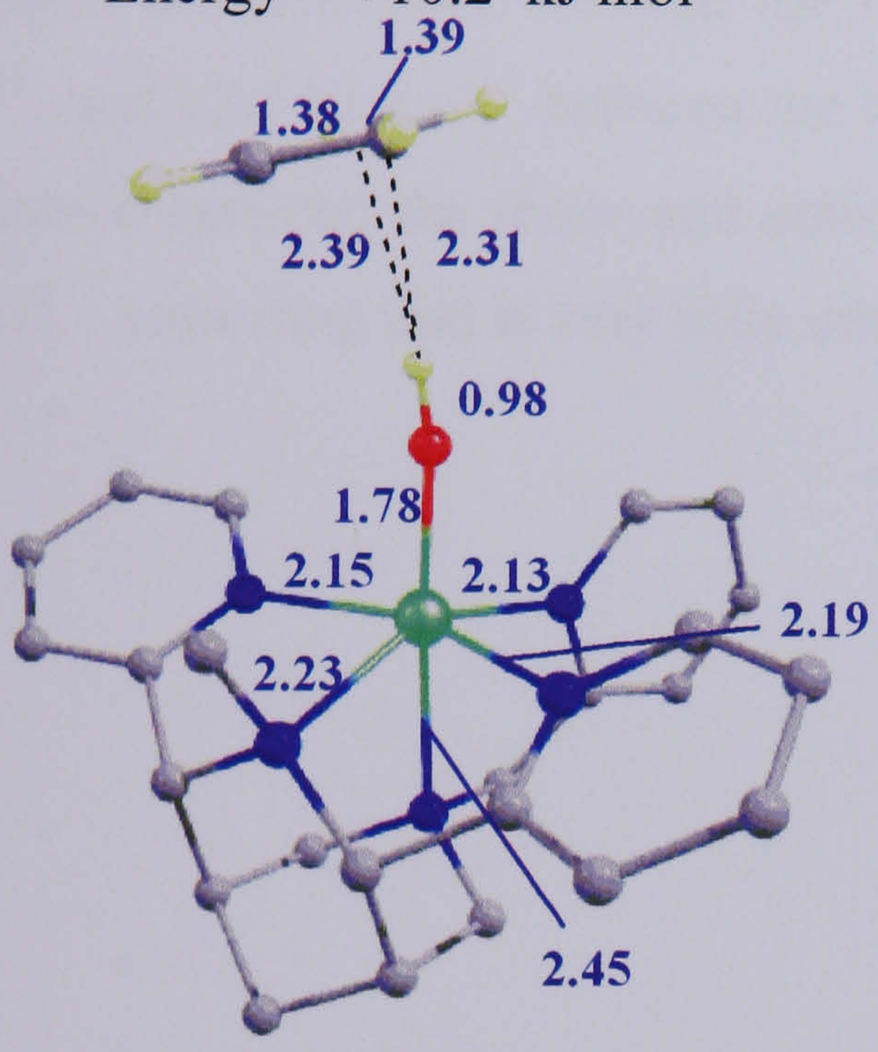

Quintet (^{5}HI)
Energy = −2.5 kJ mol^{-1}

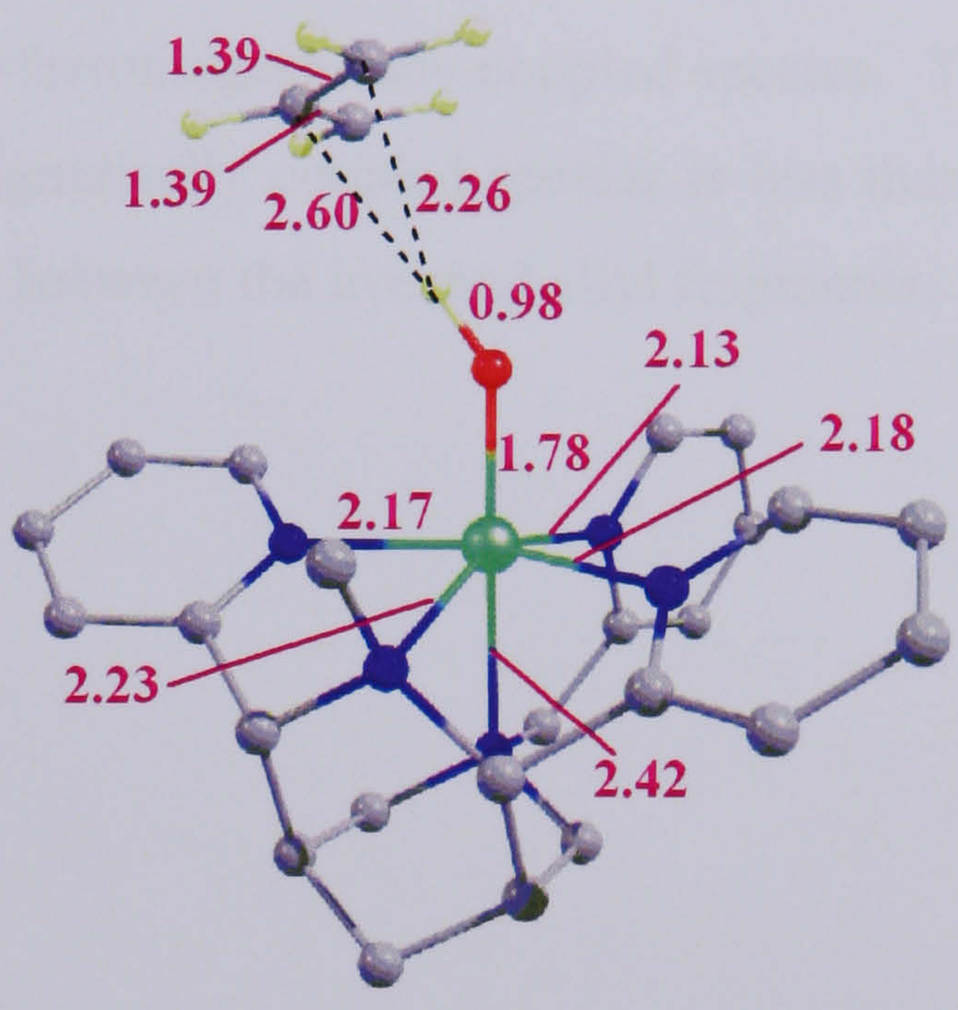

Septet (^{7}HI)
Energy = −0.7 kJ mol^{-1}

Figure 4-13 – Geometries (bond length in Å) and energies of the radical intermediates for hydroxylation {original in colour}

The geometries of the allyl radicals are identical for all the spin states, and comparison of the spin densities shows that they all have approximately one electron isolated on the carbon framework. The geometry of the [LFe(OH)] fragments in the singlet and triplet states are almost identical to that of isolated $[LFe(OH)]^{2+}$ in the doublet state. Similarly, the [LFe(OH)] fragments of the quintet and septet species are very similar to each other, and almost identical in geometry to the sextet minimum for the isolated species. Comparison of spin densities of isolated $[LFe(OH)]^{2+}$ (doublet) with the [LFe(OH)] fragments for ^{1,3}HI [(Figure 4-14) show that are very similar: 0.95 compared with 0.93/0.96 on Fe, and 0.12 compared with 0.12/0.14 on O, confirming that the

[LFe(OH)] fragment corresponds to low spin (S=1/2), $[LFe(OH)]^{2+}$. The allyl fragment has a total spin density of about −1.0/1.0 on the singlet and triplet species respectively, confirming that the allyl radical is anti-ferromagentically/ferromagnetically coupled to the $[LFe(OH)]^{2+}$. For the sextet/septet, the spin densities are 4.21/4.20 on Fe, and 0.35/0.39 on O, confirming that the septet is an allyl radical ferromagnetically coupled to a high spin $[LFe(OH)]^{2+}$ fragment, and the quintet (Fe = 4.18, O = 0.37) is the anti-ferromagnetically coupled equivalent.

In the isolated $[LFe(OH)]^{2+}$ fragment, the sextet spin state is predicted to be more stable than the doublet by 8 kJ mol^{-1}, and this difference is retained in the intermediates. For example, the difference between the two ferromagnetically coupled species is 9.5 kJ mol^{-1}, and 12.7 kJ mol^{-1} between the two anti-ferromagnetically coupled species. The difference between the ferro- and anti-ferromagnetically coupled species is less than 2 kJ mol^{-1} indicating that is very little interaction between the iron and allyl fragments.

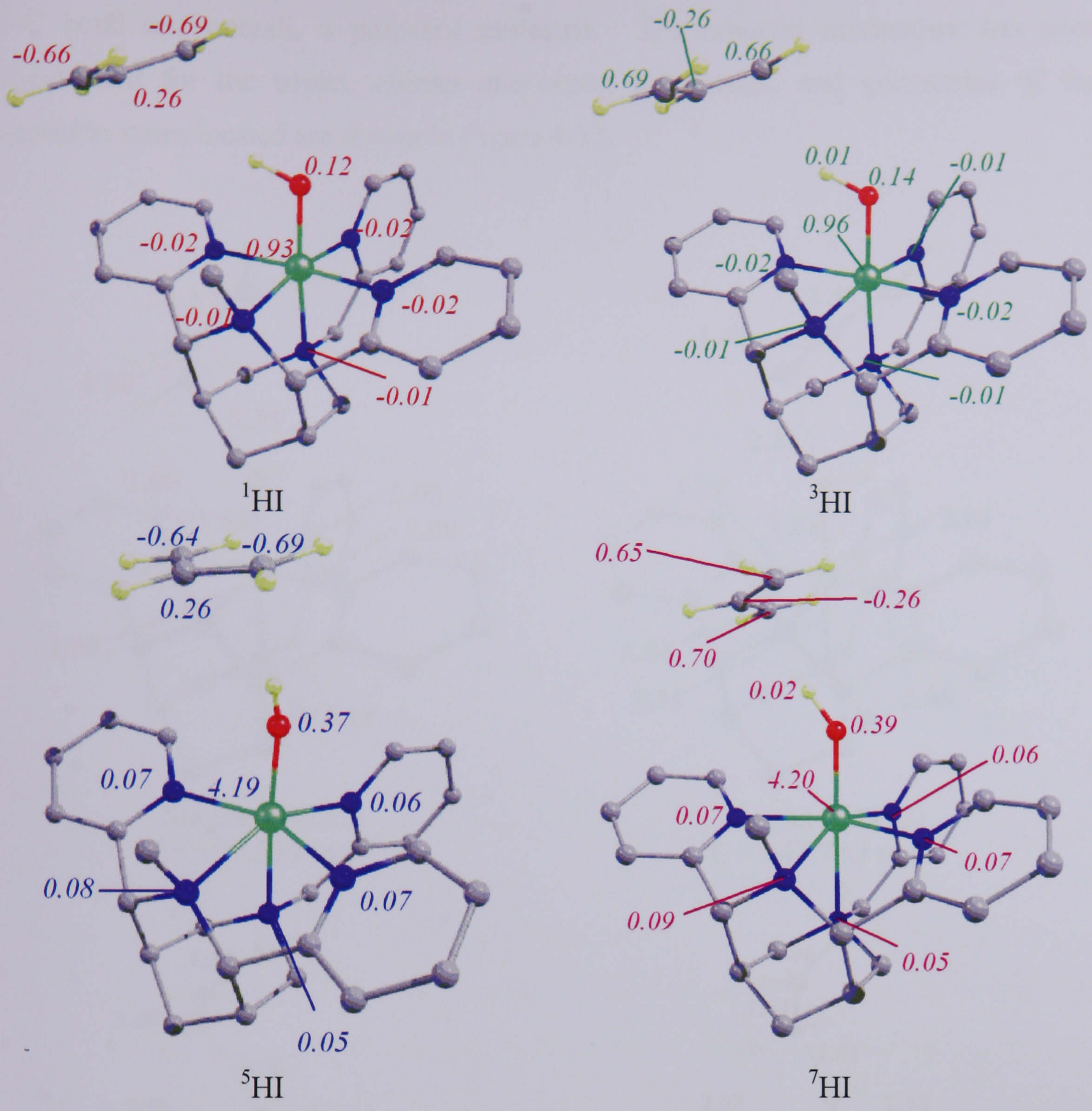

Figure 4-14 – Mulliken spin densities of the radical intermediates for hydroxylation {original in colour}

In the study by Shaik and co-workers, the quintet spin state is predicted to be the most stable intermediate, consistent with our results. They have not calculated the septet spin state so no comparisons can be drawn with this.

4.3.7 Hydroxylation Transition State 2

The intermediate can potentially react in a number of ways: the allyl radical can leave the vicinity of the Fe complex, and then go on and react with solvent, O_2 dissolved in the solvent, or other organic substrates dissolved in the solvent. Alternatively, the allyl radical can react in a rebound mechanism with the $[LFe(OH)]^{2+}$ complex to form a new

O-C bond and overall, a propenol molecule. The rebound mechanism has been investigated for the triplet, quintet and septet spin states, and geometries of the transition states located are shown in Figure 4-15.

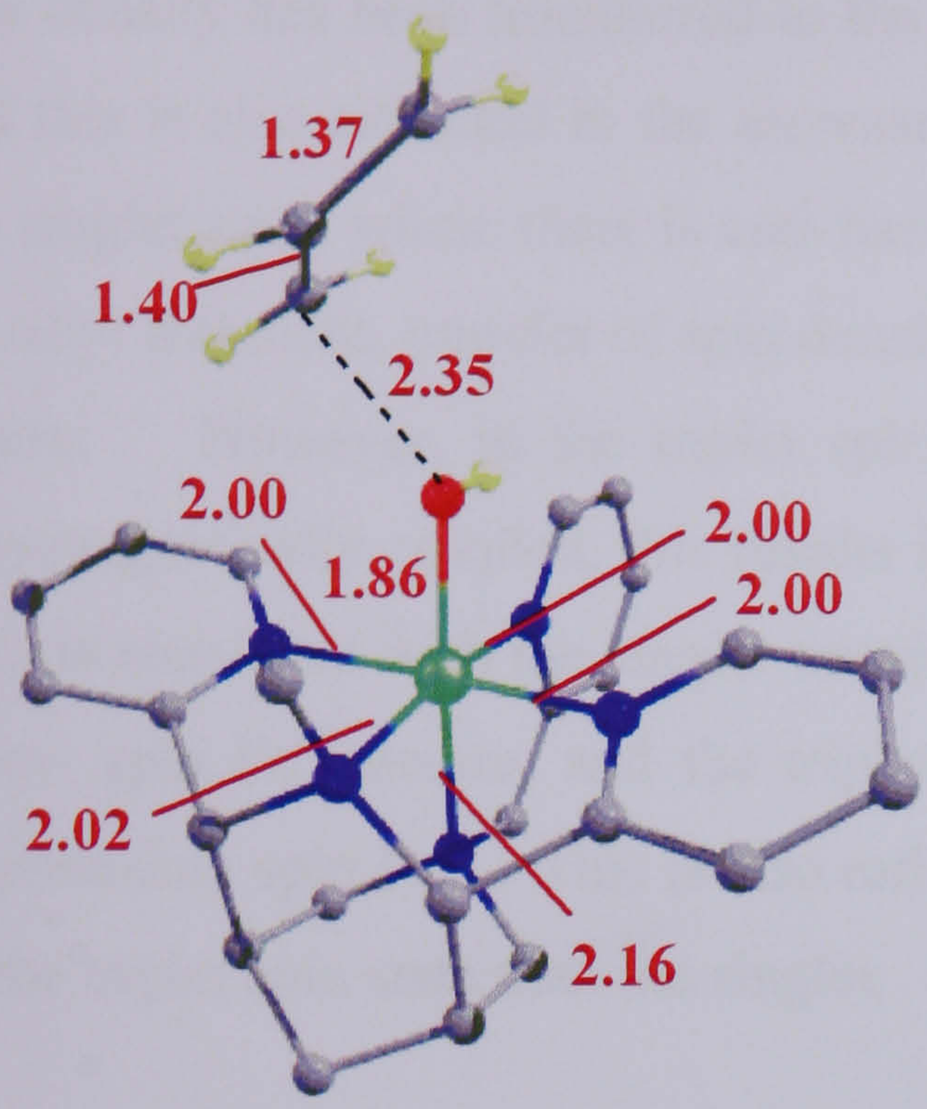

Singlet (^{1}HTS2)
E = +39.5 kJ mol^{-1}

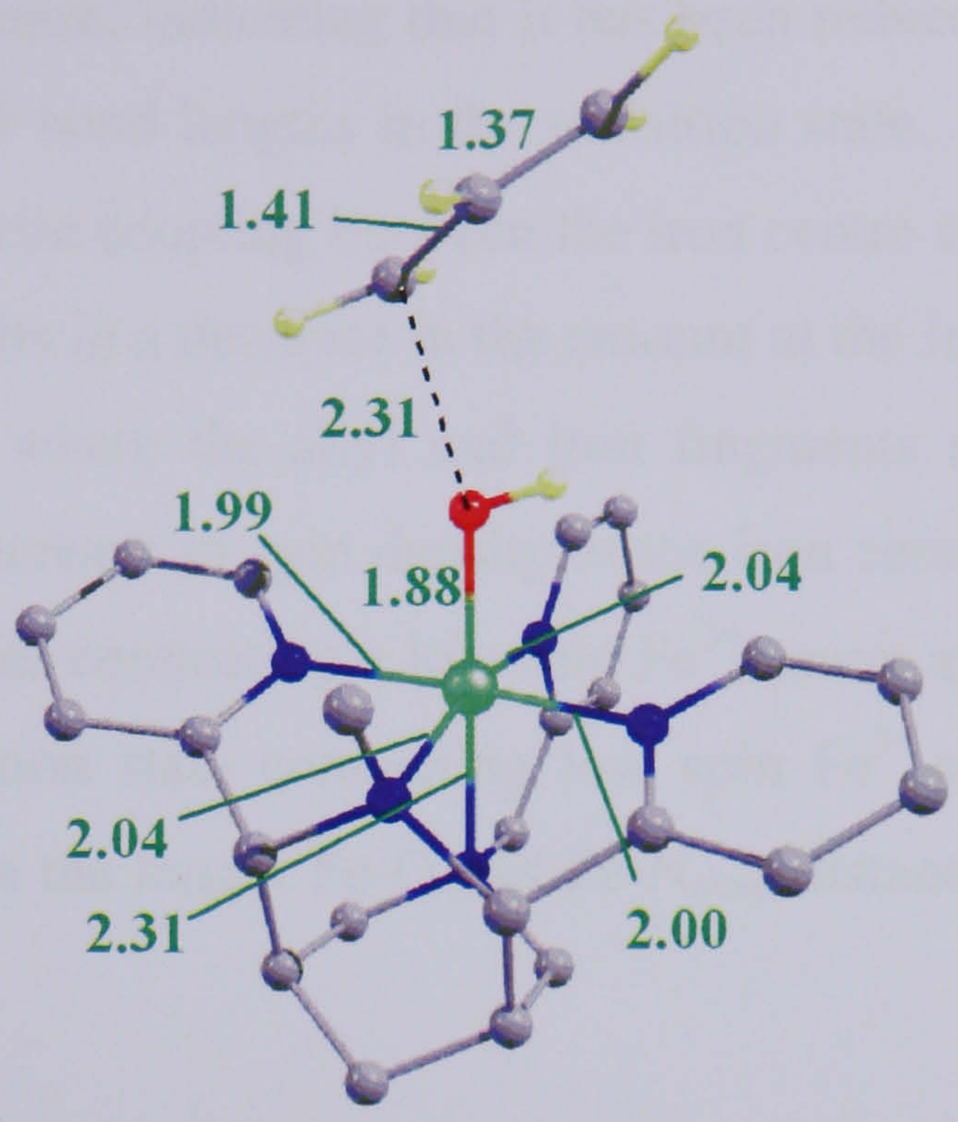

Triplet (^{3}HTS2)
E = +47.7 kJ mol^{-1}

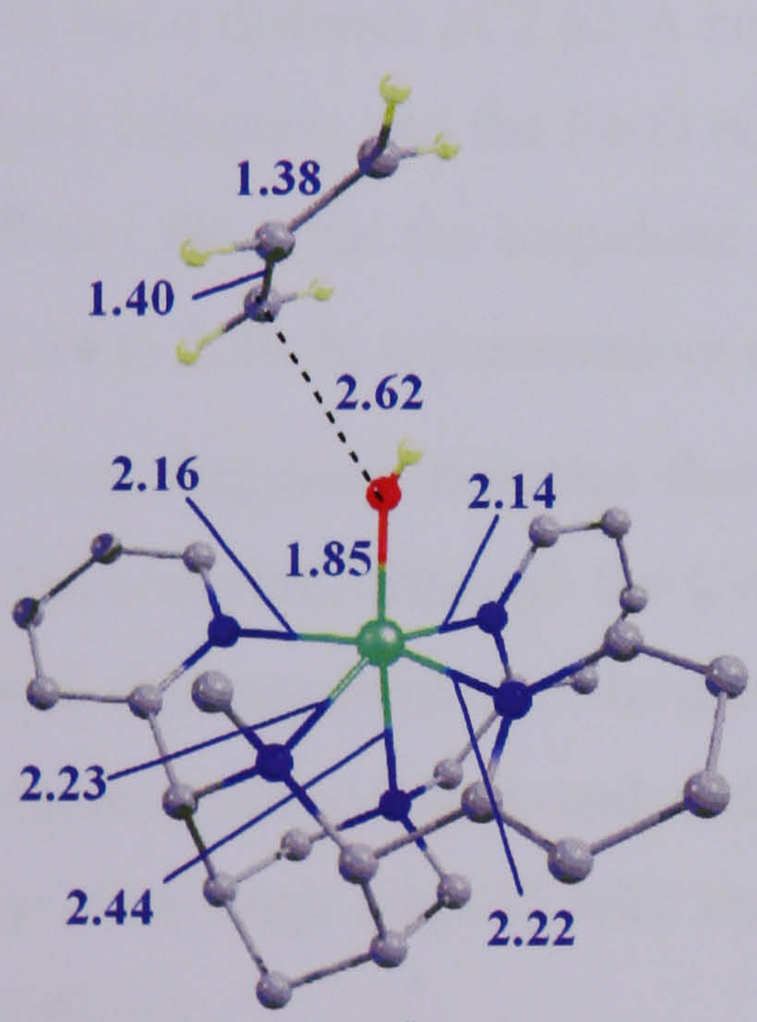

Quintet (^{5}HTS2)
E = +10.1 kJ mol^{-1}

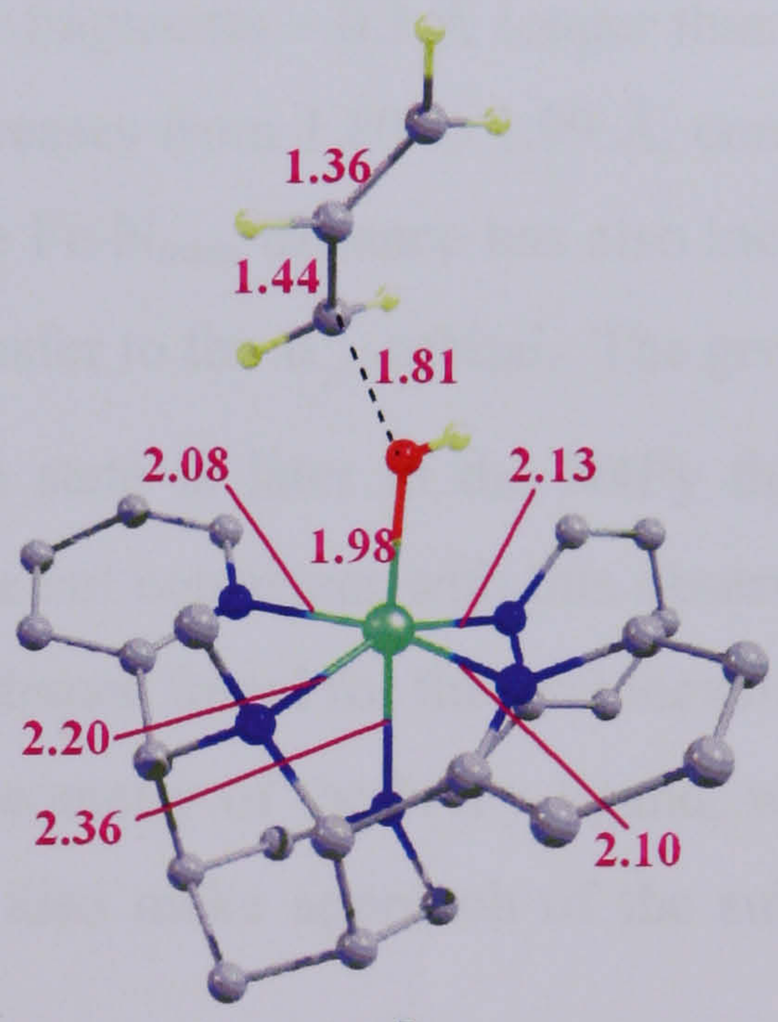

Septet (^{7}HTS2)
E = +177.8 kJ mol^{-1}

Figure 4-15 – Geometries (bond length in Å) and energies of the rebound transition states {original in colour}

The quintet transition state is lowest in energy, and only 12 kJ mol^{-1} higher than the quintet intermediate. In contrast the septet is very high in energy, and will not be considered further. The geometry of the quintet, triplet and singlet transition states, in particular the near equal C-C bond lengths, shows that the allyl fragment still has a lot

of radical character – a fact that is confirmed by the spin densities (Figure 4-16). In both the triplet and quintet spin states, the amount of spin density associated with the allyl fragment has been reduced by about 0.3 electrons in comparison to the intermediate, still leaving a large amount of radical character on the allyl group. The spin density has been transferred to the iron centre, indicating that it has been reduced, and this is also reflected in the increased Fe-O bond lengths in the transition state. In the singlet state, where there is anti-ferromagnetic coupling between the iron centre and the allyl fragment, transfer of spin density results in a decrease in the amount at the iron centre. However, in the triplet spin state, where the allyl and iron fragments are ferromagnetically coupled, this results in an increase in spin density at the iron centre. This is consistent with the singlet transition state connecting a low spin Fe^{3+} centre and a low spin Fe^{2+} centre, and the triplet transition state connecting low spin Fe^{3+} and intermediate spin Fe^{2+}. This is also reflected in the longer Fe-O and Fe-N_{trans} distances in the triplet spin state than the singlet.

Shaik and co-workers only managed to locate a transition state for the triplet spin state, and this has a distance of 2.62 Å between the two fragments – 0.3 Å longer than in the bispidone complex, and the Fe-O bond length increases from 1.80 to 1.99 Å, compared to 1.78 to 1.88 Å for the bispidone complex. The Fe-N_{trans} distance has also increased from 2.04 to 2.20 Å, representative of electron transfer to the d_{z^2} orbital. The geometry of the iron fragment indicates that the transition state is later in the N4Py than the bispidone complex, although the C-O distances are not consistent with this observation. However, this may be due to the greater steric hindrance found for the cyclohexane than the propene hydroxylation, and additionally the geometry of the N4Py ligand, with all four pyridine rings aligned with the z-axis, may also make approach of the substrate more difficult.

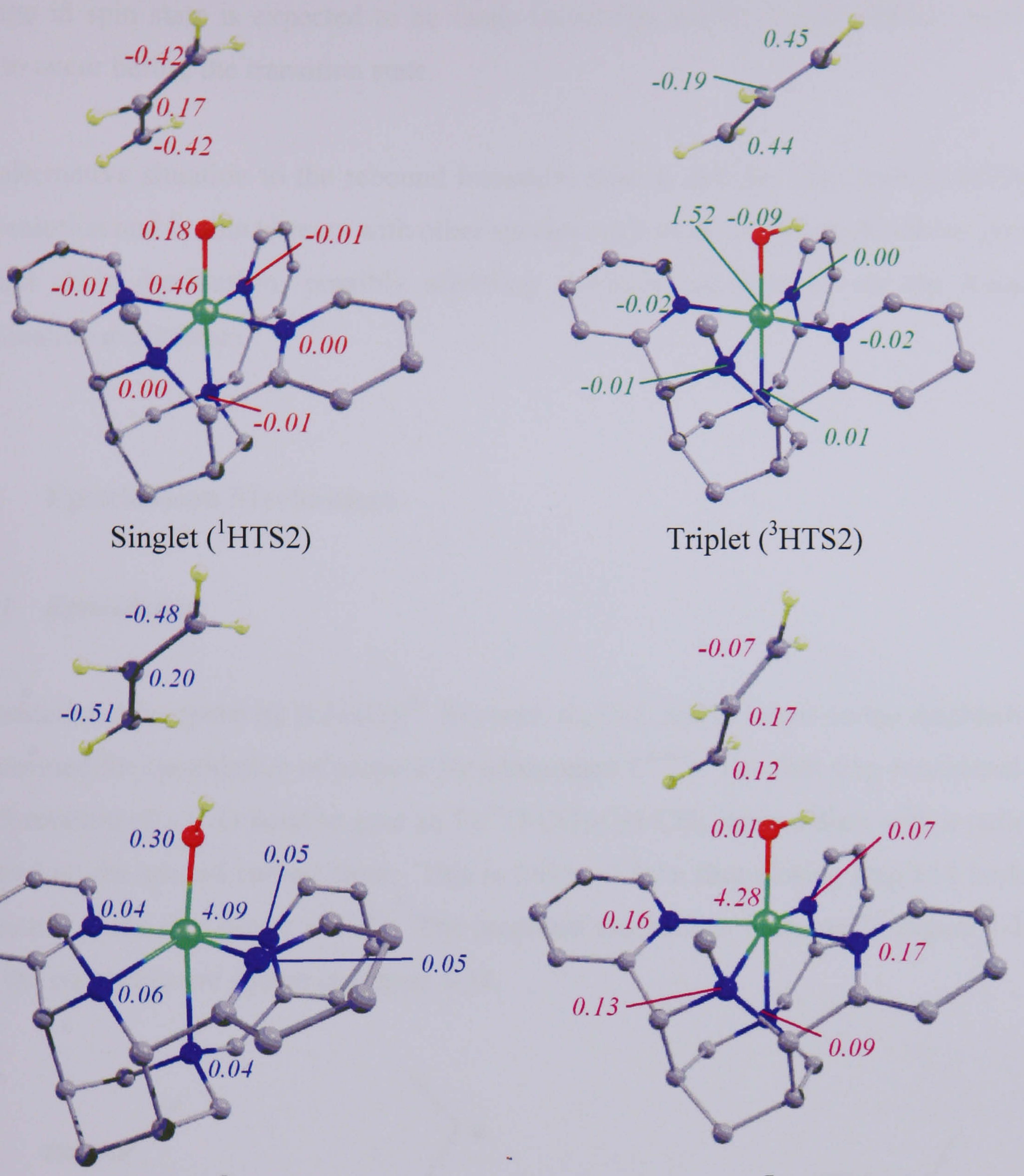

Singlet (^{1}HTS2) Triplet (^{3}HTS2)

Quintet (^{5}HTS2) Septet (^{7}HTS2)

Figure 4-16 – Mulliken spin densities for the rebound transition states

4.3.8 Overall conclusions about the reaction mechanism

The energetics of the hydroxylation mechanism indicate that the first step in the reaction is hydrogen atom abstraction from the CH_3 group of propene by the $[LFe(O)]^{2+}$ species with a barrier of 53.2 kJ mol^{-1} on the quintet surface. Therefore a change in spin state between the reactants and first transition state must occur. We have located the MECP between the triplet and quintet spin states for the isolated $[LFe(O)]^{2+}$ species and found that it lies only 24 kJ mol^{-1} higher in energy than the triplet minimum. Therefore this

change in spin state is expected to be facile (assuming sufficient spin-orbit coupling) and to occur before the transition state.

An alternative situation to the rebound transition state is that the allyl radical diffuses into solution and is able to react with other species such as an oxygen molecule to give a radical chain mechanism, possibly affording alcohols and ketones via the Russell termination mechanism.[9]

4.4 Epoxidation Mechanism

4.4.1 Epoxidation

Epoxidation of propene by $[LFe(O)]^{2+}$ has been studied, and is based on the mechanism determined for epoxidation of propene by **compound I**.[4-6,10] The first step considered is the formation of a C-O bond to give an $Fe^{3+}O\text{-}CH_2\text{-}CH\text{-}CH_3$ intermediate with a radical centred on the second carbon atom. This is followed by a ring closing step and further reduction of the iron centre to Fe^{2+}. The proposed mechanism is shown in Figure 4-17, and the energetics are shown in Figure 4-18.

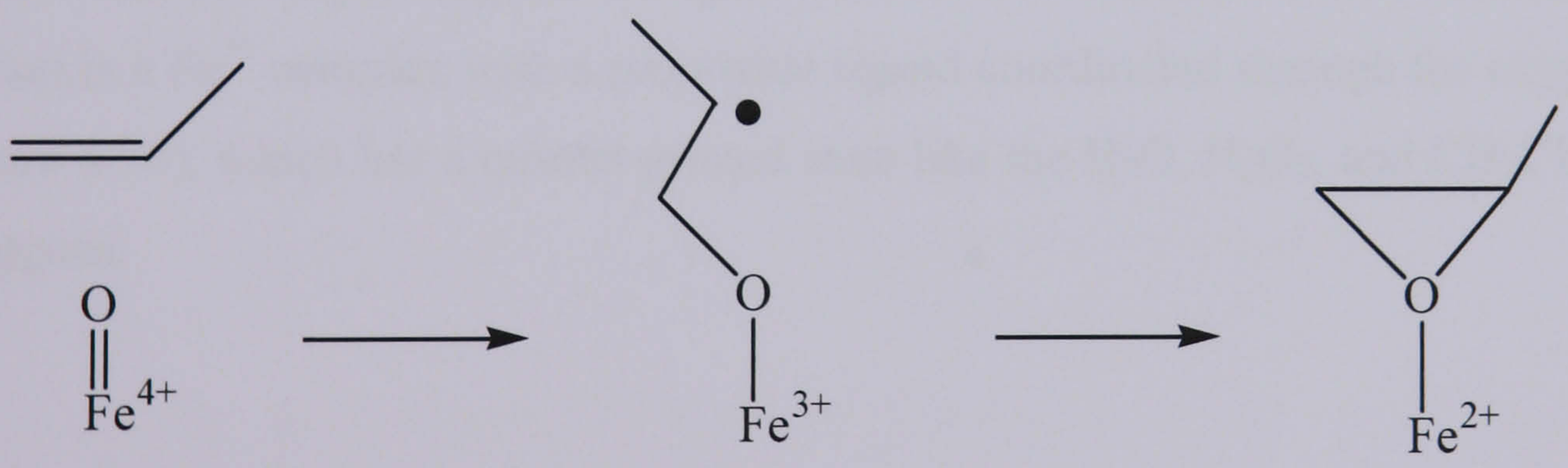

Figure 4-17 – Schematic diagram showing the proposed route for epoxidation of propene by $[LFe(O)]^{2+}$

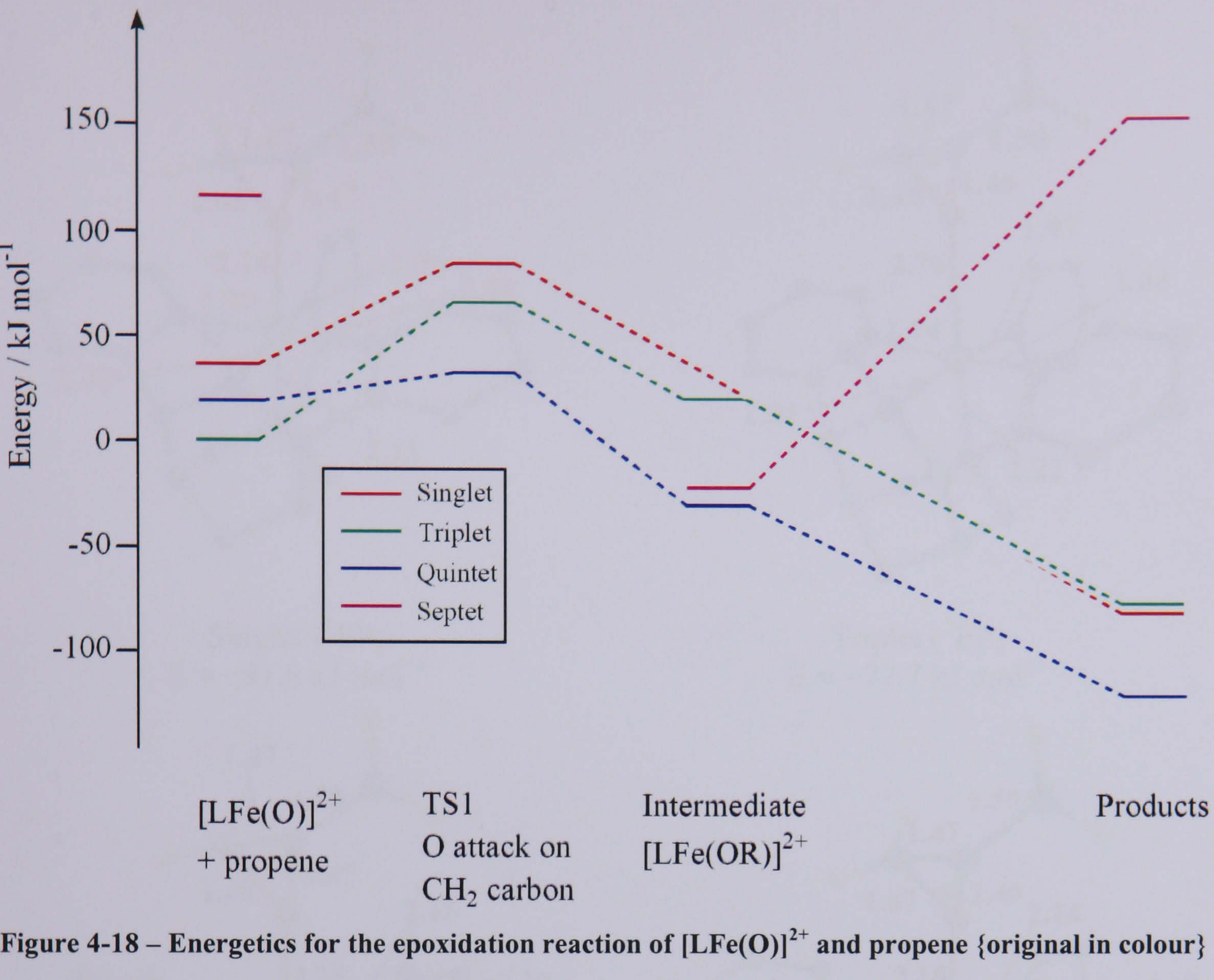

Figure 4-18 – Energetics for the epoxidation reaction of $[LFe(O)]^{2+}$ and propene {original in colour}

The pathway for epoxidation involves the insertion of the oxygen atom coordinated to the iron centre into the C=C double bond. Different mechanisms have been identified for this reaction depending on the spin state of the transition state. Ultimately, the product is a Fe^{2+} complex with a propoxide ligand coordinated through the oxygen atom (Figure 4-19), which has a quintet ground state like the H_2O, H_2O_2, and CH_2CHCH_2OH analogues.

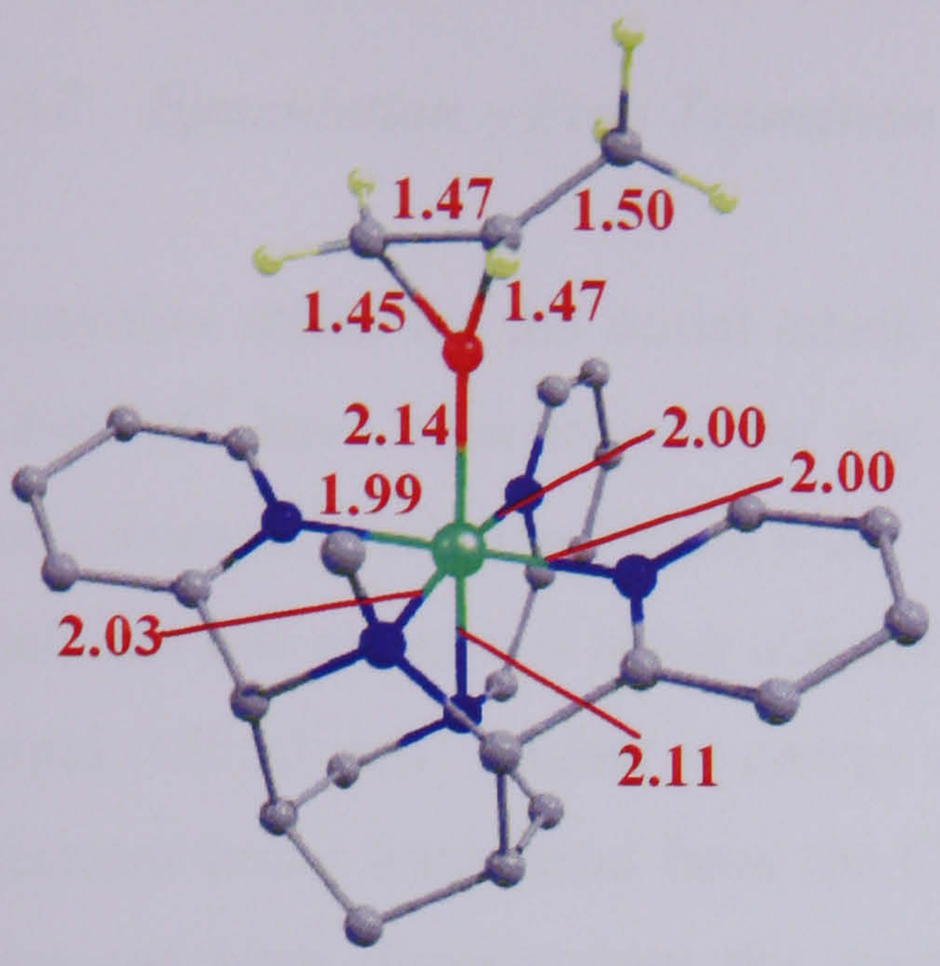

Singlet (^{1}EP)
E = −81.8 kJ mol^{-1}

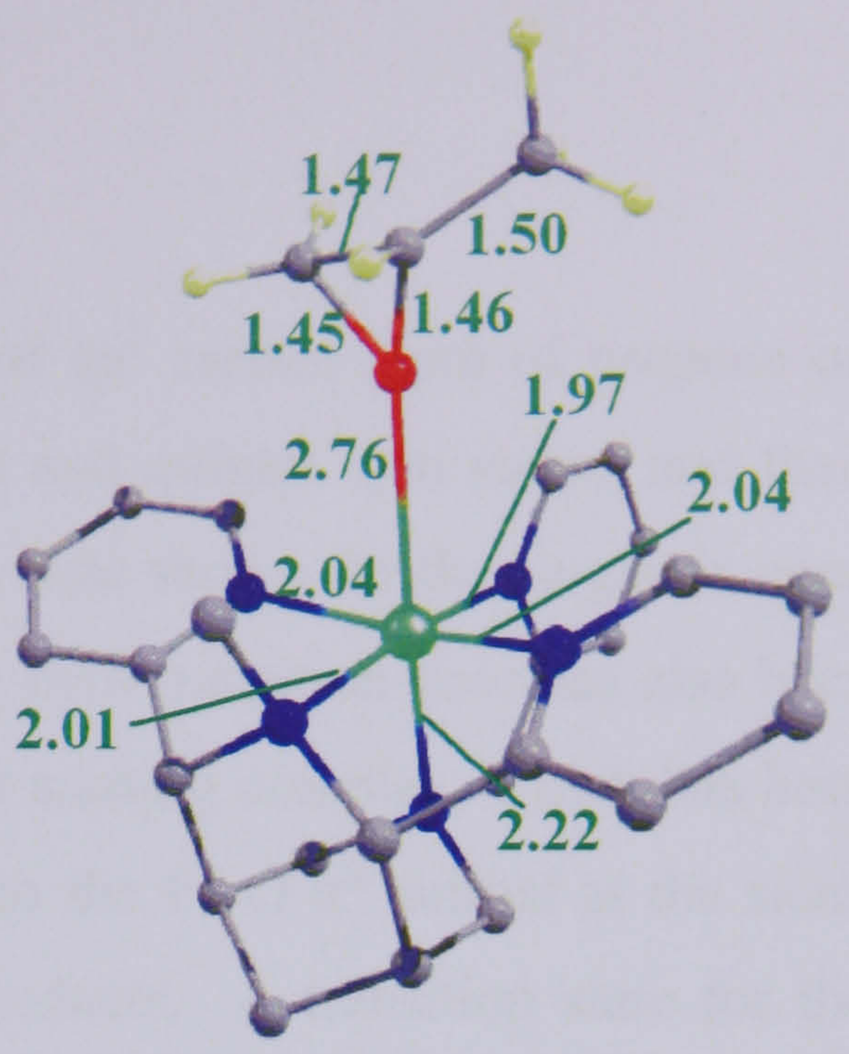

Triplet (^{3}EP)
E = −77.7 kJ mol^{-1}

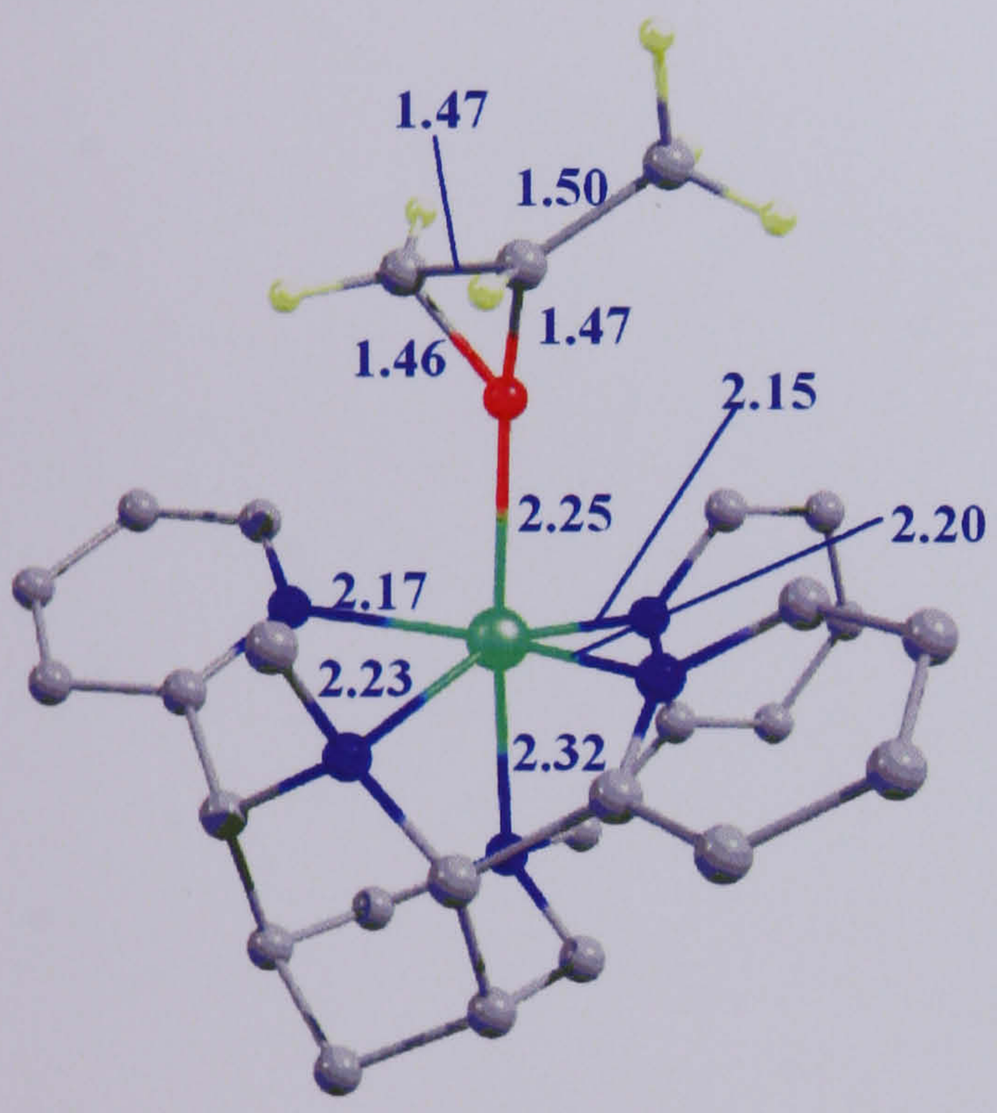

Quintet (^{5}EP)
E = −125.2 kJ mol^{-1}

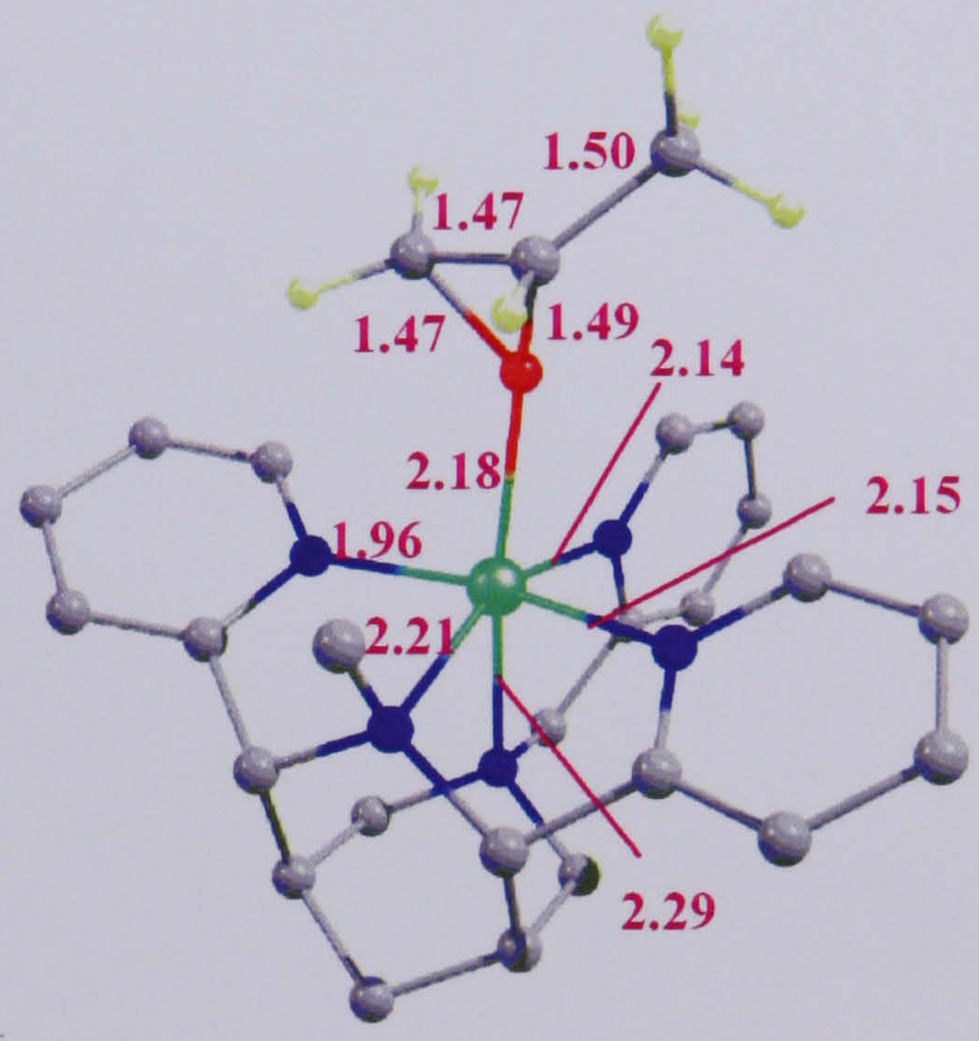

Septet (^{7}EP)
E = +153.2 kJ mol^{-1}

Figure 4-19 – Geometries (bond lengths in Å) and energies of the epoxide product {original in colour}

The epoxide fragment of the product has a fairly uniform geometry across the different spin states. Mulliken spin densities (not shown) show that it is essentially a closed shell species with all the spin density located on the iron centre, and therefore all the changes in electronic structure related to the spin state occur in the $[LFe]^{2+}$ fragment. The geometries of the iron moieties are generally very similar to the case of propenol coordination, differing mainly in the Fe-O and Fe-N_{trans} bond lengths due to the different π donor character of epoxide and alcohol ligands.

4.4.2 Epoxidation – First Transition state

Transition states for the initial attack of the terminal sp^2 carbon atom of propene on $[LFe(O)]^{2+}$ have been located for the singlet, triplet and quintet spin states, and their geometries are shown in Figure 4-20. The transition state shown for the singlet is open shell and one electron is being transferred. A closed shell transition state has also been found, 128 kJ mol^{-1} higher in energy than the triplet starting complex, which has both electrons being transferred from the C=C π orbital to the Fe-O π^* orbital at the same time and leads directly from the reactants to the products. A transition state for the septet species has not been located, but it is expected to be high in energy, like the septet TS1.

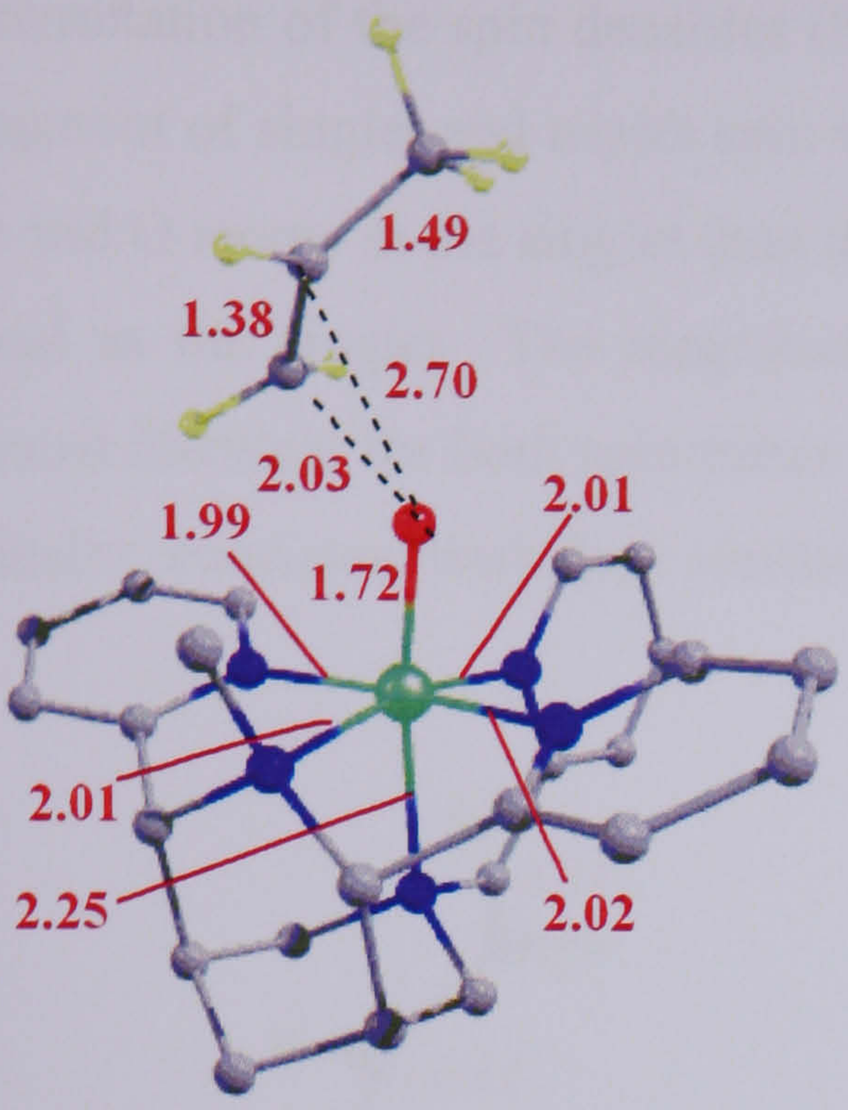

Singlet (^{1}TSE1)
E = +82.2 kJ mol^{-1}

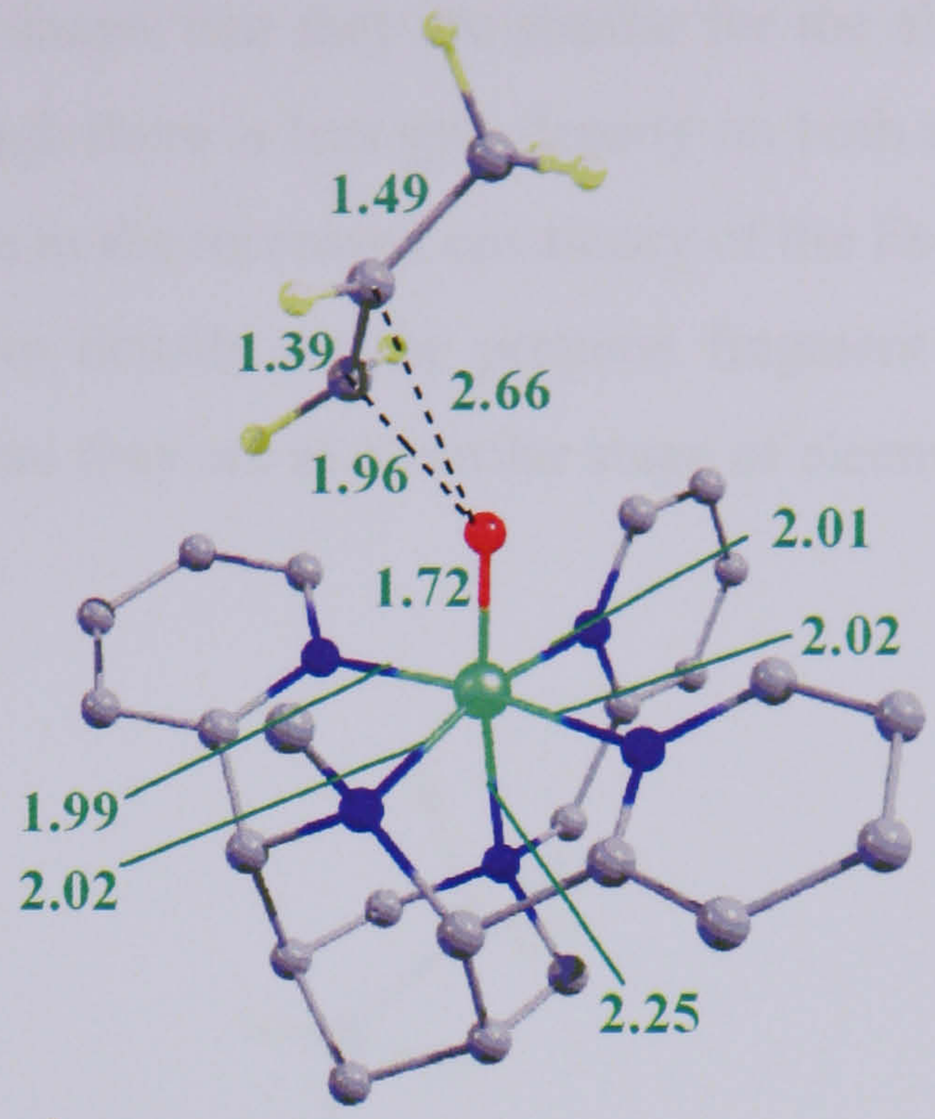

Triplet (^{3}TSE1)
E= +66.3 kJ mol^{-1}

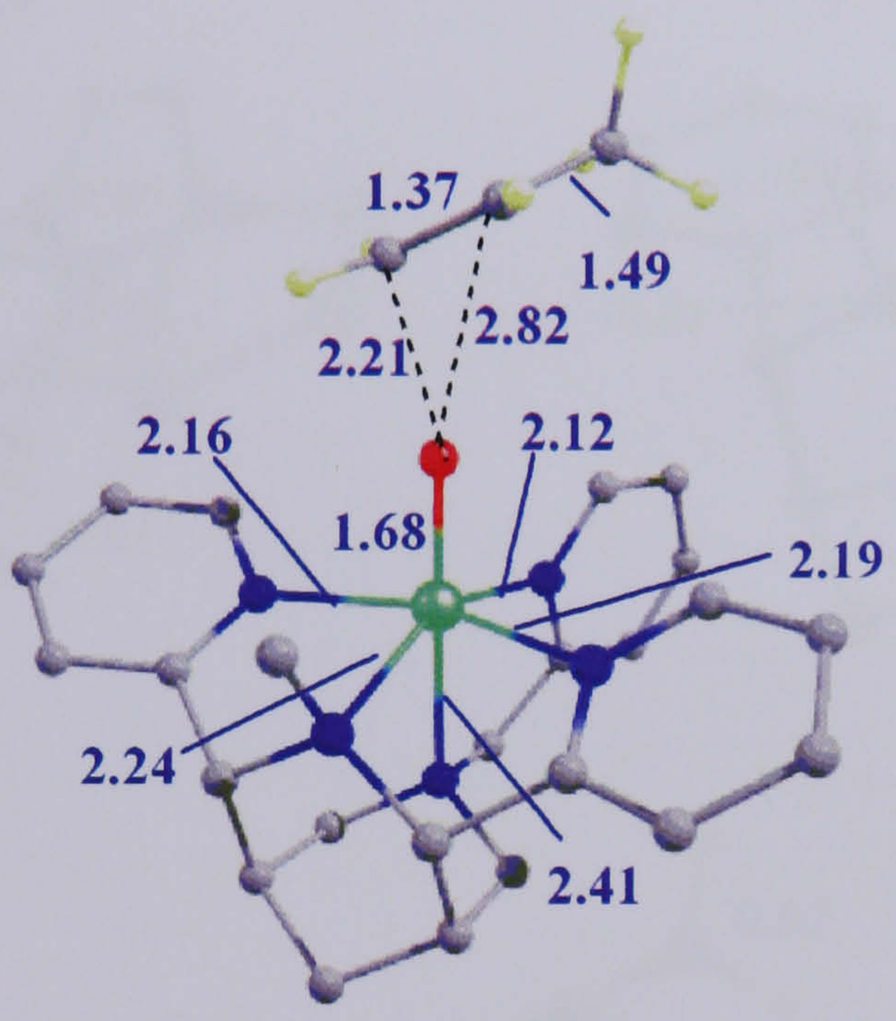

Quintet (^{5}TSE1)
E = +32.8 kJ mol^{-1}

Figure 4-20 – Geometries (bond lengths in Å) and energies of the epoxide TS1 {original in colour}

The singlet and triplet transition states have identical geometries for the coordination sphere of iron, indicating that they also have a similar electronic structure. In both spin states the Fe-O bond lengths have increased by about 0.1 Å compared to the reactants indicating that the Fe centre is being reduced. The geometry of the propene fragment in each case is also very similar, with a C=C bond that has only slightly increased in length from the reactants (1.34 Å and 1.38 Å). However, the propene fragment is closer to the Fe fragment in the triplet case than the singlet case and the triplet transition state is 16 kJ mol^{-1} lower in energy than the singlet.

Examination of the spin densities (Figure 4-21) shows that they are similar for the allyl fragment of singlet and triplet spin states, although there is less spin density on both the Fe and O atoms in the singlet than the triplet due to the increased covalency of the Fe-O bond in the singlet The magnitude of the spin density on the propene fragment is almost identical for both spin states indicating that they are at a similar stage of electron transfer, consistent with their similar geometries.

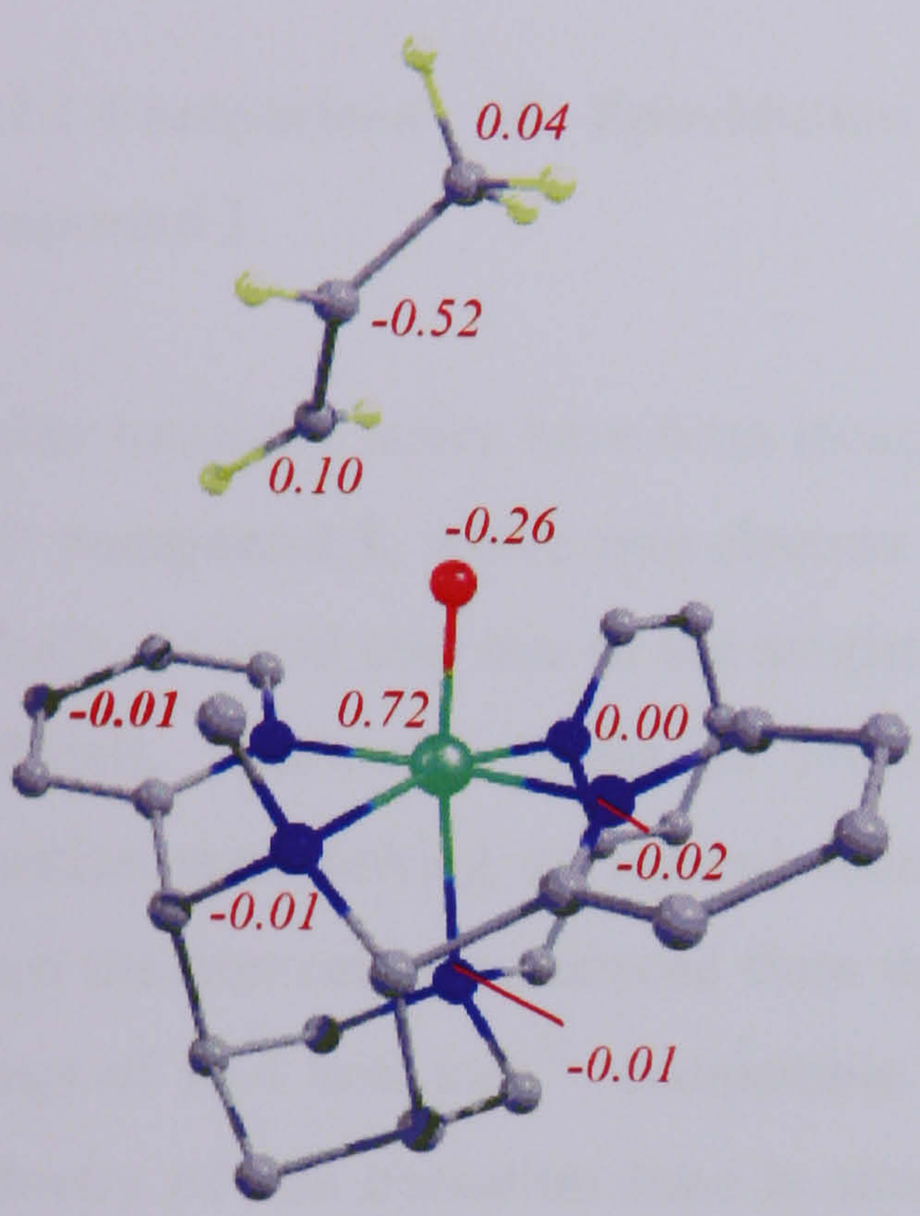

^{1}TSE1

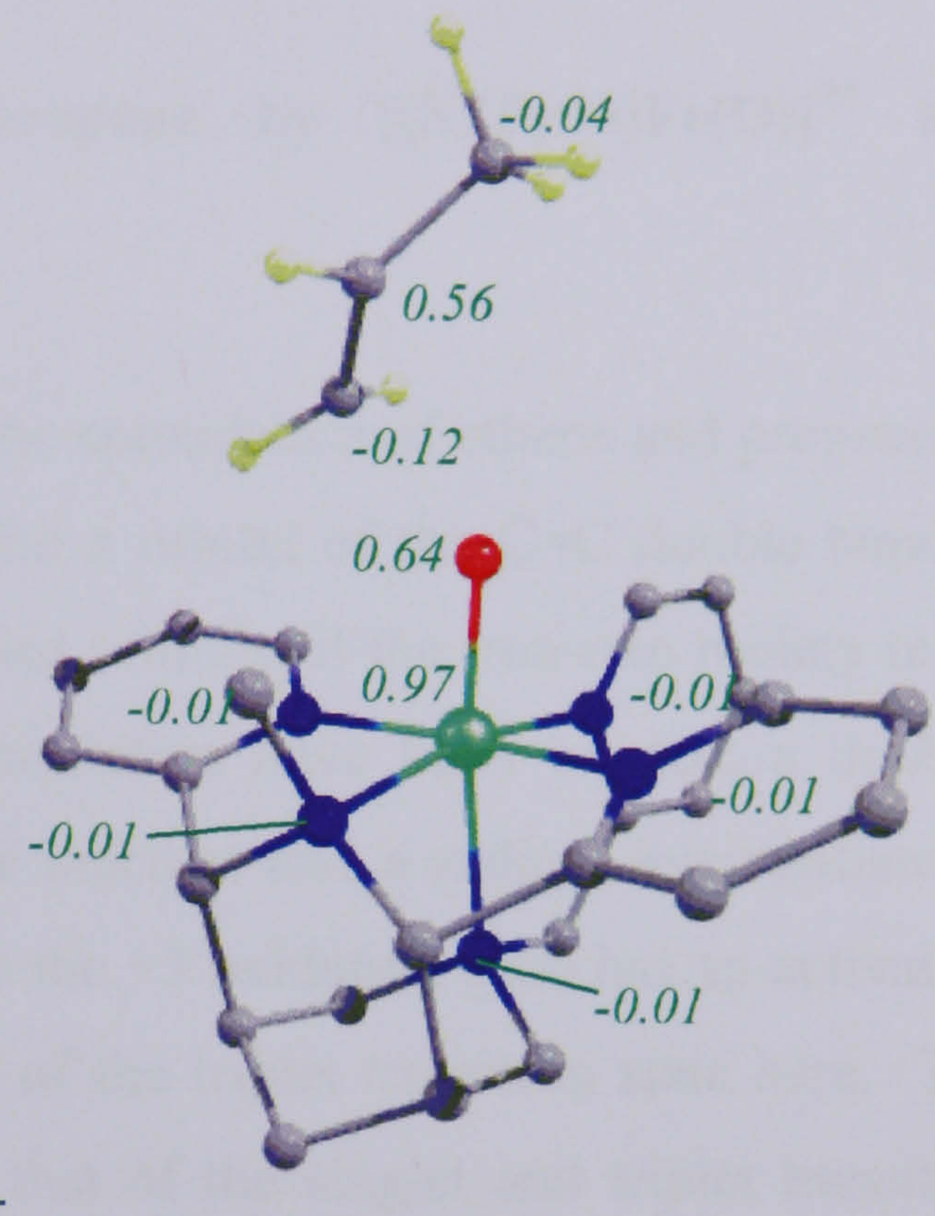

^{3}TSE1

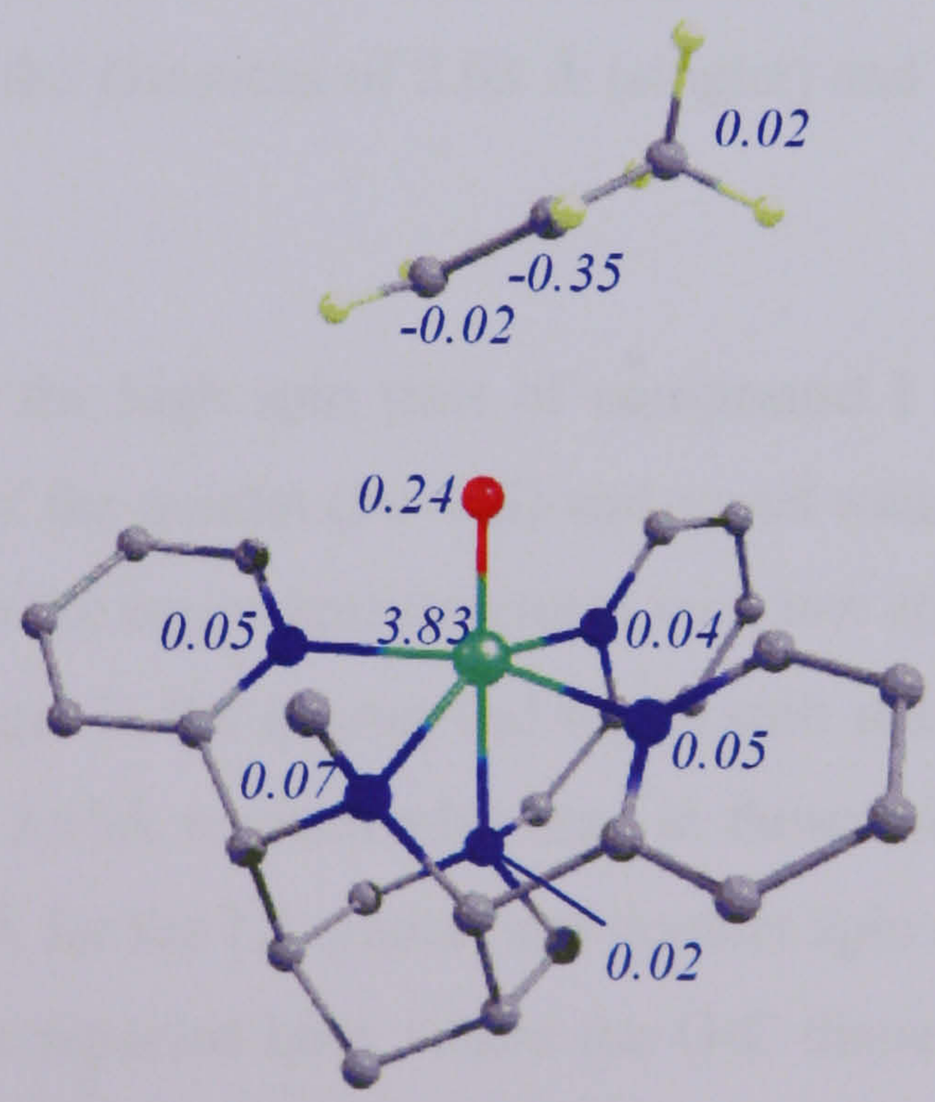

^{5}TSE1

Figure 4-21 – Spin densities for the singlet, triplet and quintet transition states for epoxidation {original in colour}

The quintet transition state shows a similar change in geometry compared to the reactants as the singlet and triplet do. However, the C=C bond length has not increased as much and the Fe-O bond length has only increased by 0.06 Å. There is also a larger build up of spin density on the allyl fragment for the singlet and triplet transition states than the quintet transition states, indicating that less electron transfer has occurred in the latter case. Therefore the quintet transition state is more like the reagents than the triplet and singlet transition states.

4.4.2.1 Comparison of Epoxidation of propene by $[(N2Py3o)Fe(O)]^{2+}$ and Compound I

Similar transition states have been located for the epoxidation of ethene and propene by CYP **compound I**, where one electron from the π orbital of the C=C double bond is formally donated into one of the singlet occupied orbitals of the iron-oxo moiety (a π* d-orbital). Stationary points for propene epoxidation have been located; a doublet transition state linking an excited state of the reactant and a radical intermediate in which the iron centre is reduced from the +4 to the +3 oxidation state has an activation energy of 14.4 kcal mol^{-1}, comparable to that of the triplet transition state here. The geometry of this transition state is similar to that of the singlet and triplet transition states located here with an identical Fe-O bond length of 1.72 Å. The O-C distance of 2.07 Å is comparable to the distances of 2.03 Å (singlet) and 1.96 Å (triplet) observed here.[6]

Oxidation of propene by the high spin state of **compound I** has also been studied by Shaik.[10] The geometry of the quartet (Fe=HS) and sextet transition states show similar Fe-O distances to those in the equivalent structures with low spin Fe^{4+} centres. The O-C distance is, however, longer in the quartet and septet spin states containing a high spin Fe^{4+} centre (2.19 Å and 2.13Å respectively) than in those containing a low spin Fe^{4+} centre (2.00 Å and 2.07 Å for the LS quartet and doublet spin states respectively). This is consistent with what is reported here, where the O-C distance is about 0.2 Å longer for quintet scenario than the triplet or singlet ones. In addition, the Fe-O-C angle is around 130° for **compound I** with low spin Fe^{4+} centres, compared to 133° for both the singlet and triplet complexes reported here. However, for the high spin Fe^{4+} centres, Shaik reports that this angle is 166° and 174° for the quartet and sextet states, which is

angles stems from the transfer of an electron from the π orbital of the C=C bond to the iron centre. In the low spin species, the electron is transferred to one of the Fe-O π* orbitals, and so to get maximum overlap between the two interacting orbitals an angle of around 130° is required. However, the quintet transition state links the high spin $Fe^{4+}O$ species and a high spin $Fe^{3+}OH$ species in which the d_{z^2} is filled so there is transfer of an electron to this orbital, requiring an angle of 180° for maximum overlap.

4.4.3 Epoxidation – Radical Intermediate

In the triplet, quintet and septet cases, the first transition states lead to a radical intermediate whose geometries are shown in Figure 4-22. For all these spin states, the intermediate corresponds to a Fe^{3+} centre with the substrate coordinated to the iron via the oxygen atom. The propyl chain has a radical centred on C^2, as indicated by the spin densities (Figure 4-23).

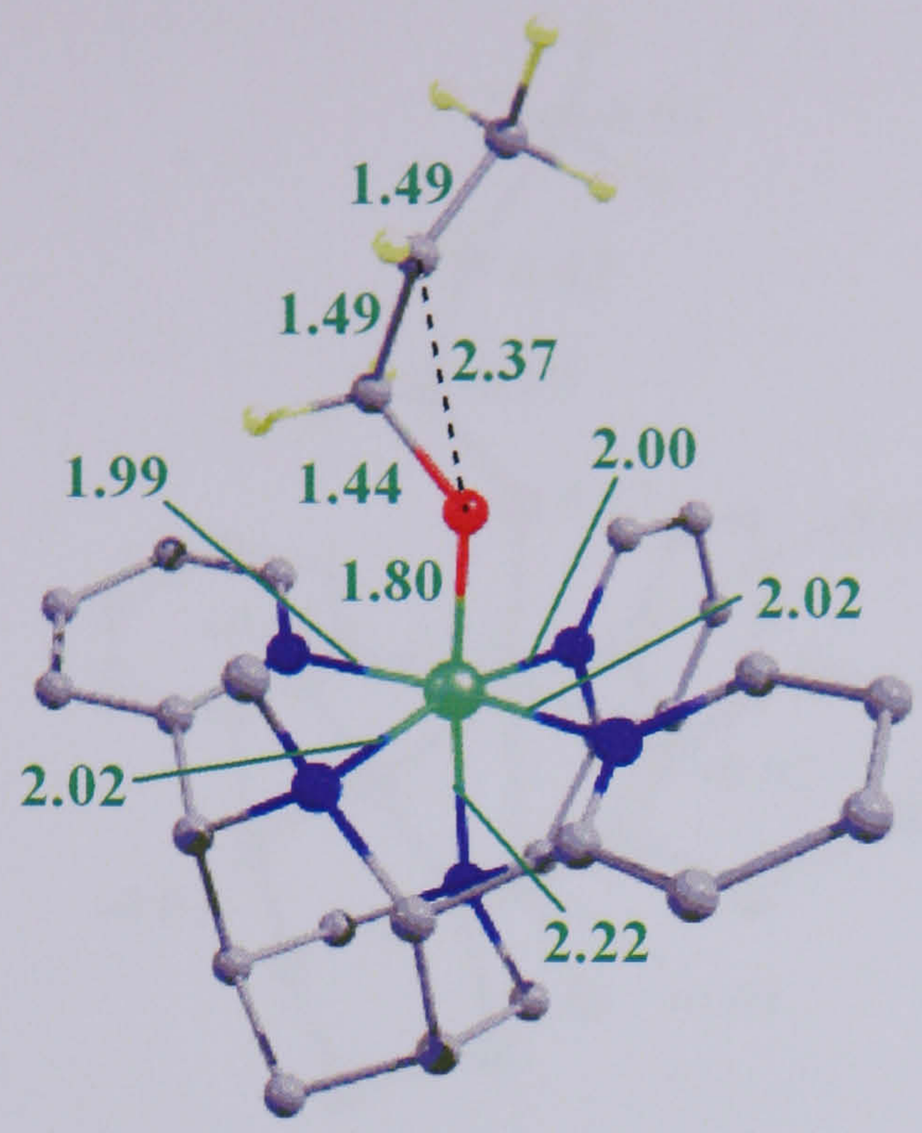

Triplet (^{3}EI)
E = +10.3 kJ mol^{-1}

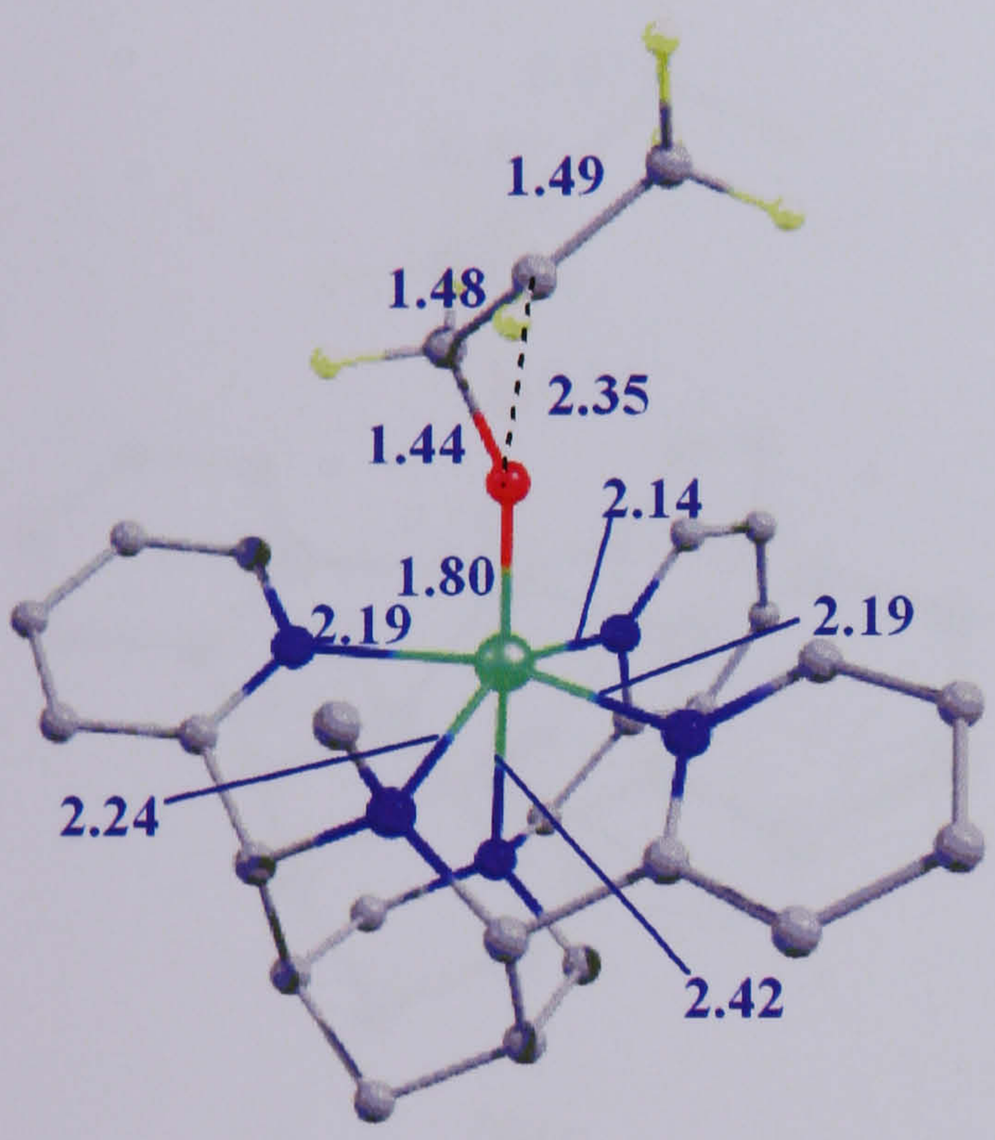

Quintet (^{5}EI)
E = −28.9 kJ mol^{-1}

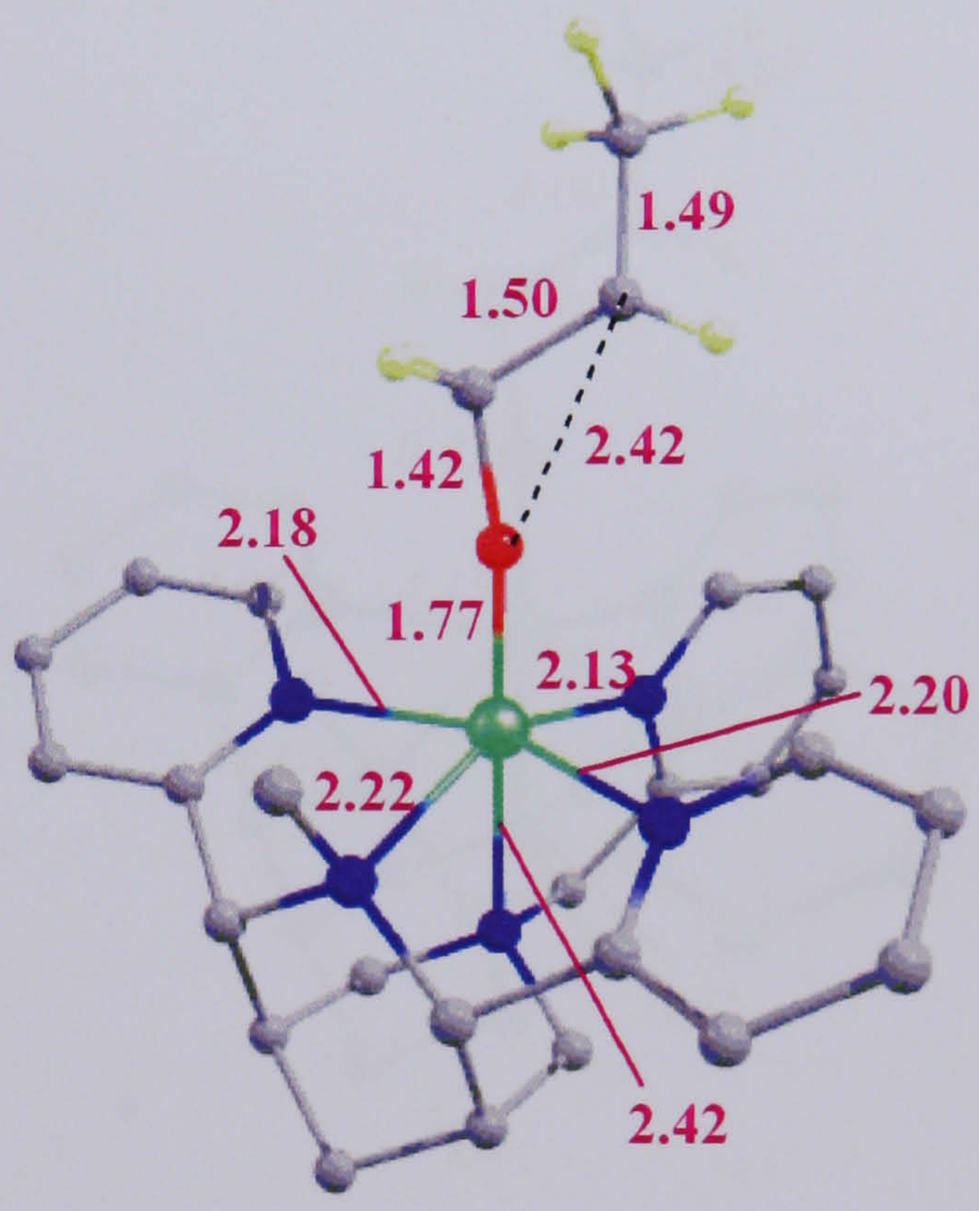

Septet (^{7}EI)
E = −22.6 kJ mol^{-1}

Figure 4-22 – Geometries (bond lengths in Å) and energies of the radical intermediates for epoxidation

The quintet and septet minima have similar geometries and energies, and their spin densities indicate that they correspond to an Fe^{3+} high spin centre, anti-ferro and ferromagnetically coupled to the carbon centred radical respectively.

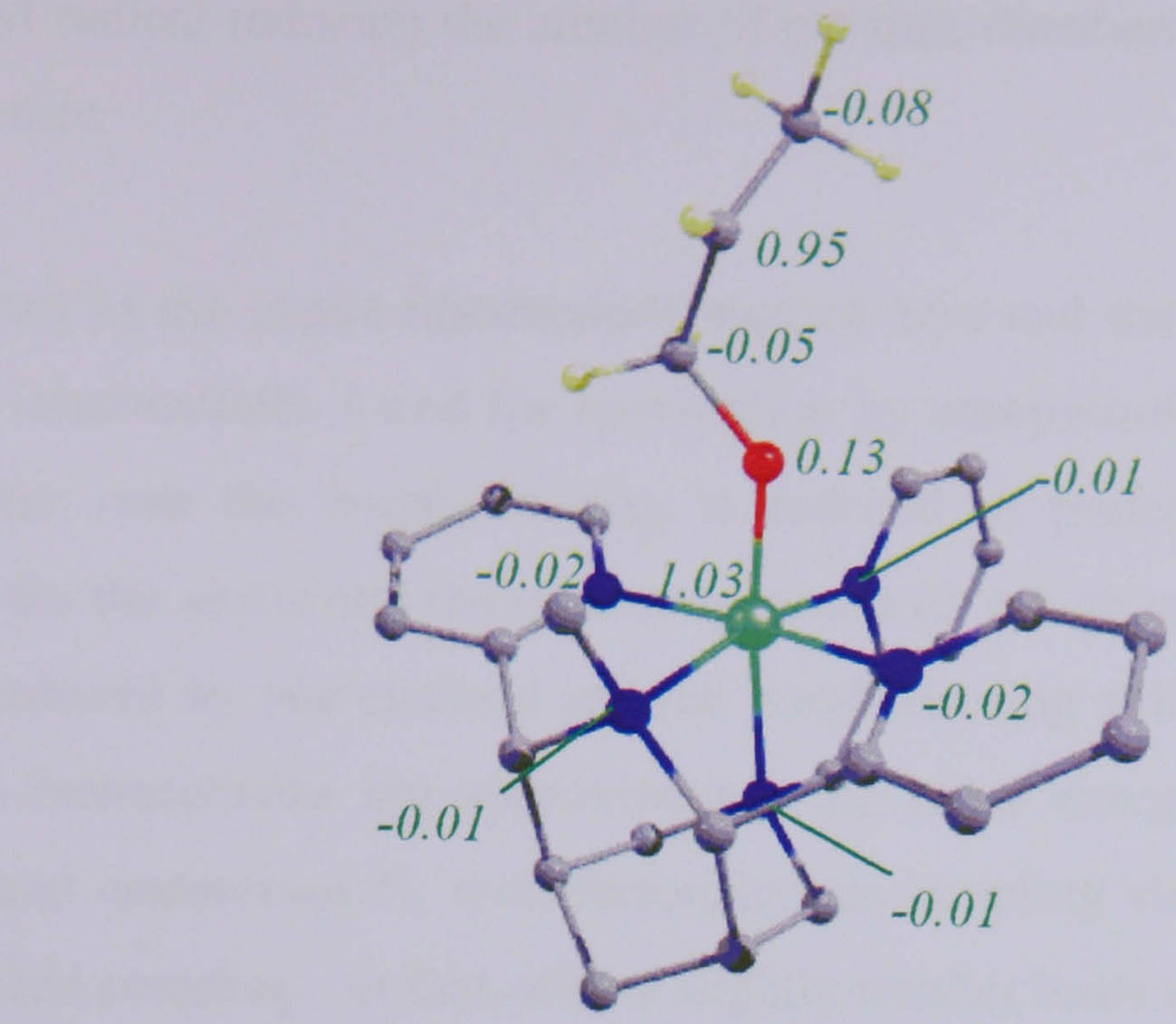

^{3}EI

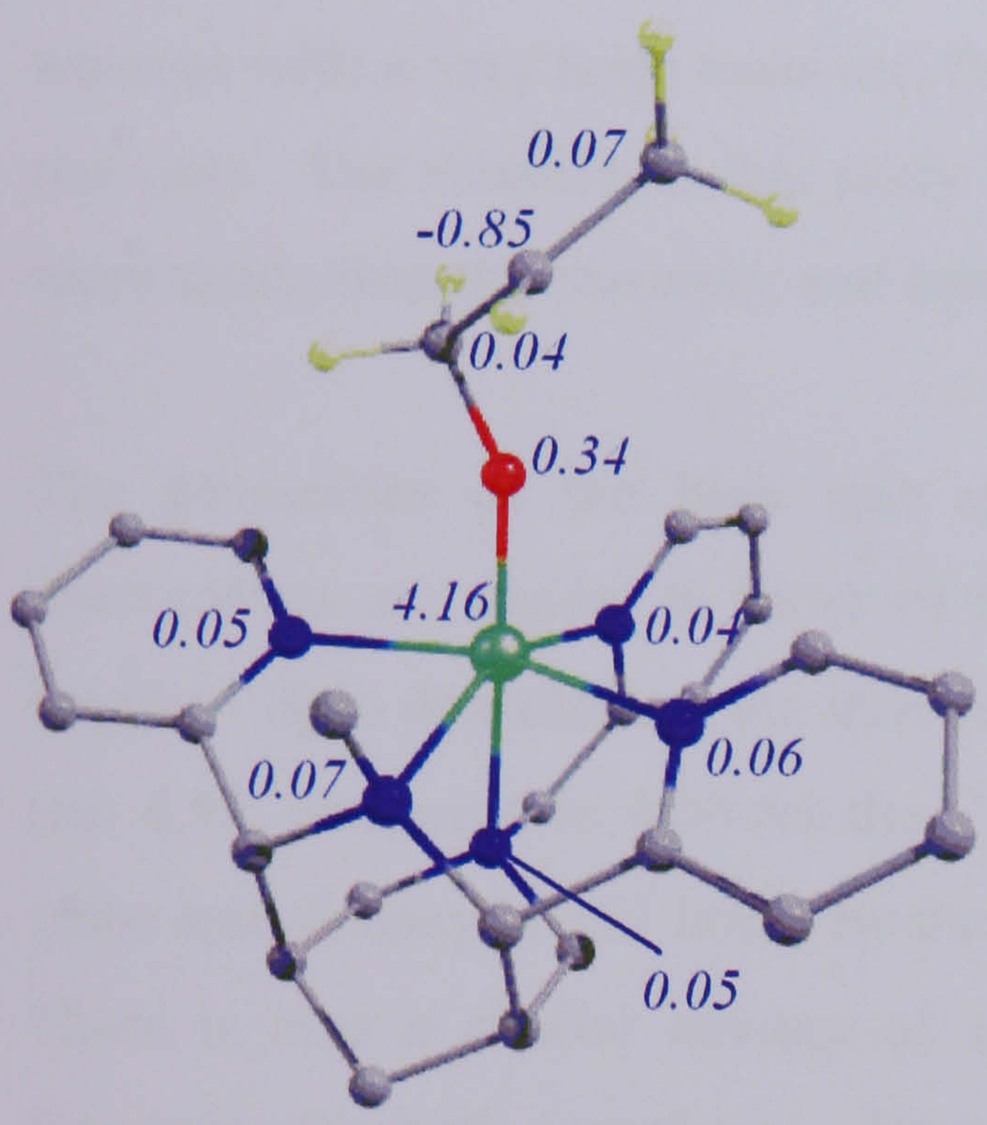

^{5}EI

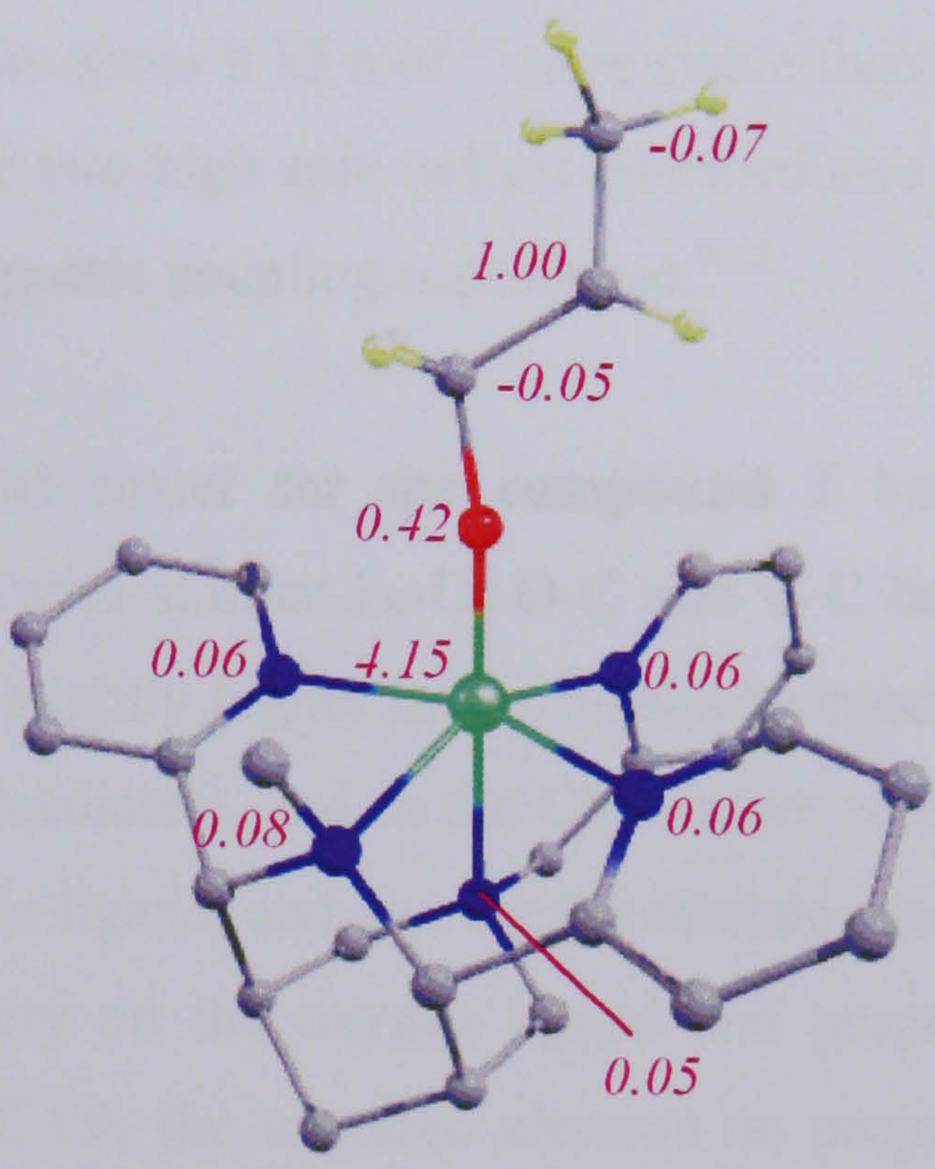

^{7}EI

Figure 4-23 – Spin densities of intermediates for epoxidation {original in colour}

It was not possible to obtain a minimum for an open shell singlet intermediate despite repeated attempts because the electronic structure always converged to a closed shell solution that led directly to the singlet product. The triplet spin state corresponds to low spin Fe^{3+} ferromagnetically coupled to a carbon centred radical on the propyl chain. Again, the geometry is consistent with low spin $[LFe(OH)]^{2+}$. In the hydroxide complex the high spin state is only just favoured whereas in the above complex, the high spin state is favoured by about 30 kJ mol^{-1}, possibly due to the electron deficiency

of the alkyl radical reducing the amount of electron donation from the oxygen atom to the iron centre.

Comparisons of the triplet intermediate studied here and the doublet and quartet (low spin iron) intermediates found for epoxidation by **compound I** have not been made as in the latter case the porphyrin ring is reduced in preference to the iron centre. However, for the sextet and the quartet species with a high spin iron centre, the iron is centre is reduced by one electron and the porphyrin ring still bears a charge. In these cases, the intermediates are approximately the same energy as the initial reactants (propene and **compound I**), with ferromagnetic coupling slightly favoured over anti-ferromagnetic coupling. In fact, with a slightly smaller basis set than that used here, the high spin intermediates are slightly less stable than the reactants (about 4-8 kJ mol^{-1}), whereas with a very large basis set, they become about 8 kJ mol^{-1} more stable than the reactants. The situation in this study is that the two high spin radical intermediates are more stable than the reactants, and anti-ferromagnetic coupling is preferred.[6,10]

The geometries of the high spin quartet and sextet for the **compound I** based intermediate are similar to those of the [5,7]EI, with similar Fe-O, O-C and C-C bond lengths. Spin densities on the iron centre are slightly higher in the bispidone species, (*ca.* 4.15, compared to 4.00 for the CYP intermediates), and in the CYP intermediates some spin density is still borne by the porphyrin ligand, and also by the thiolate group. There is also a similar amount of spin density on the oxygen ligand and propene fragments for both complexes. However, in CYP, the unpaired electron on propene fragment is anti-ferromagnetically coupled to the iron centre, and the difference in spin states is associated with the spin density (worth nearly one electron) associated with the thiolate group. In contrast, in the bispidone species there is no thiolate group and the change in spin state between the quintet and septet can be attributed to the coupling between the iron centre and the propene moiety.[10]

4.4.4 Epoxidation – Transition state 2

Although transition states are expected for O-C^2 bond formation, they are likely to be simple C-C rotations and very low in energy. Therefore we have been unable to find

these transition states and anticipate that they are sufficiently low in energy that the reaction can be considered barrierless.

4.4.4 Energetics of the Epoxidation Pathway

The epoxidation pathway begins with the reactants in the triplet spin state, but switches to the quintet surface before the first transition state occurs. This transition state has a barrier of +32.8 kJ mol^{-1} so it can easily be overcome at room temperature. After this an intermediate is formed and ring closure occurs to give the epoxide product.

4.5 Comparison of Different Mechanisms

Comparison of the epoxidation and hydroxylation pathways shows that epoxidation will occur in preference due to the low energy barrier of only 33 kJ mol^{-1} for the first transition state for epoxidation, compared to 53.2 kJ mol^{-1} for hydroxylation. The formation of radical intermediates opens up the possibility for different radical pathways to occur, and for O_2 to be incorporated into the product. However, due to the low barrier for the rebound mechanism in hydroxylation, and the anticipated low barriers for ring closure in epoxidation, this possibility remains unlikely. The low barriers to both the hydroxylation and epoxidation pathways indicate that the oxoiron(IV) species is a potent oxidant, and coupled with the conclusion from chapter 3 that formation of this intermediate can occur at room temperature, it is a likely oxidising agent for unsaturated hydrocarbons.

4.6 References

1) J. T. Groves, *J. Chem. Educ.*, **1985**, *62*, 928
2) J. McMurray, Organic Chemistry, **2004**, Brooks Cole
3) D. Kumar, H. Hirao, L. Que, S. Shaik, *J. Am. Chem. Soc.*, **2005**, *127*, 8026
4) S. P. de Visser, F. Ogliaro, P. K. Sharma, S. Shaik, *J. Am. Chem. Soc.*, **2002**, *124*, 11809
5) F. Ogliaro, N. Harris, S. Cohen, M. Filatov, S. P. de Visser, S. Shaik, *J. Am. Chem. Soc.*, **2000**, *122*, 8977
6) S. Shaik, S. P. de Visser, F. Ogliaro, H. Schwarz, D. Schröder, *Curr. Op. Chem. Biol.*, **2002**, *6*, 556
7) S. P. de Visser, F. Ogliaro, N. Harris, S. Shaik, *J. Am. Chem. Soc.*, **2001**, *123*, 3037
8) P. G. Wenthold, M. L. Polak, W. C. Linebergerm *J. Phys. Chem.*, **1996**, *100*, 6920
9) G. A. Russell, *J. Am. Chem. Soc.*, **1957**, *79* 3871
10) H. Hirao, D. Kumar, W. Thiel, S. Shaik, *J. Am. Chen. Soc.*, **2005**, *127*, 13007

Chapter 5 – Sulfide Oxidation by $[Mn_2(TMTACN)_2(O)_3]^{2+}$

5.1 Introduction

The manganese compound $[Mn_2(TMTACN)_2(O)_3](PF_6)_2$ (TMTACN = 1,4,7-trimethyl-1,4,7-triazacyclononane) shown in Figure 5-1, in acetonitrile or acetone solution in the presence of H_2O_2 has been shown to effect the oxidation of sulfides to sulfoxides and sulfones (Figure 5-2).[1,2] It is also able to effect the oxidation of sulfides to sulfones, with virtually no formation of sulfoxide or oxidation of other functional groups, in pyridine with periodic acid as the oxidant.[3] In particular, the oxidation of *para*-substituted phenyl methyl sulfides has been investigated experimentally, and kinetic investigations show that in the case of sulfides, those with an electron-donating substituent are oxidised fastest, and those with an electron-withdrawing substituent react slowest. Hammett plots of the rate of oxidation at 25°C in acetone with 5 equivalents H_2O_2 and 1 mol% catalyst give a ρ value of −0.28 when the substituents are compared using σ^+ values indicating that the oxidant is an electrophile. In contrast, Hammett plots for the oxidation of sulfoxides under the same conditions give a ρ value of +0.20 using σ values for the substituents, indicating that the oxidant is nucleophilic in nature, and hence that the mechanism is quite distinct from the oxidation of the sulfide. The selectivity for sulfide oxidation over sulfoxide oxidation can be tuned by various reaction conditions. Decreasing the amount (mol%) of catalyst present leads to a higher selectivity for sulfide oxidation, as does adding a carboxylate or carboxylic acid co-catalyst such as acetic acid that can coordinate to the Mn centre, or using a coordinating solvent. These observations indicate that the sulfoxide has to bind to the Mn centre before it is oxidised, and molecules that compete with this will inhibit the reaction.[1]

The fact that sulfides show a greater tendency to act as nucleophiles is no surprise as they are generally much more reactive than sulfoxides. The changes observed in these systems cannot, however, be accounted for simply by reduced reactivity of the sulfoxide because the rates of oxidation of the sulfide and sulfoxide are approximately equal.[4]

Only a very few examples of a marked switch in mechanism such as that described above have been documented in the literature.

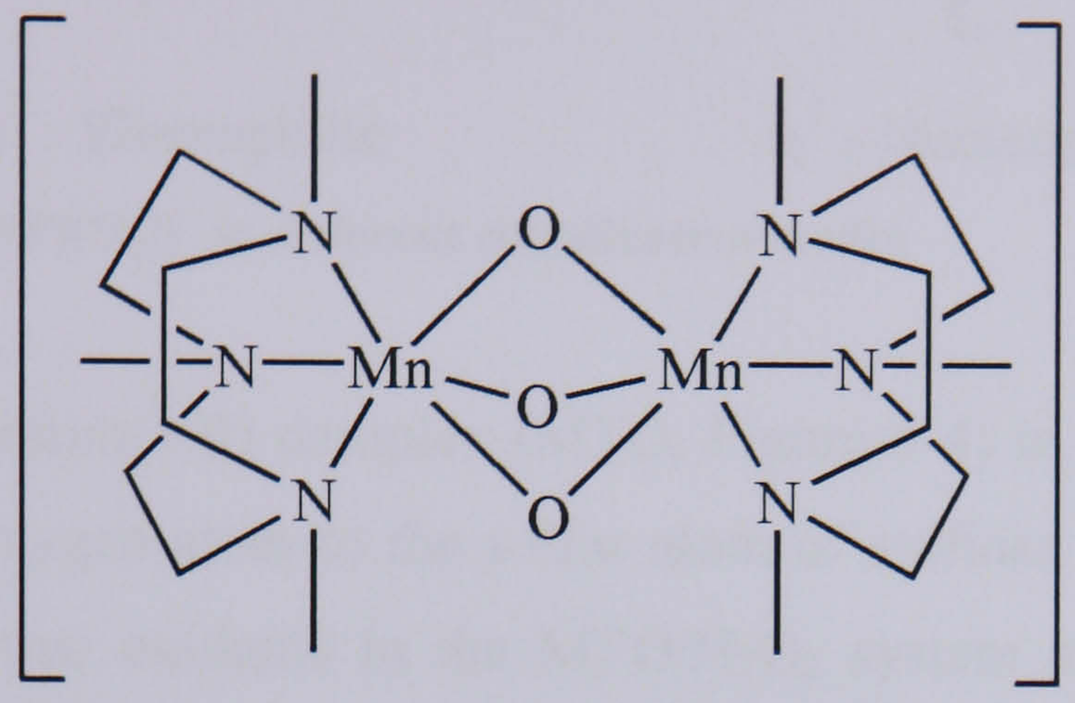

(5-1)

Figure 5-1 – Structure of $[Mn_2(TMTACN)_2(O)_3]^{2+}$

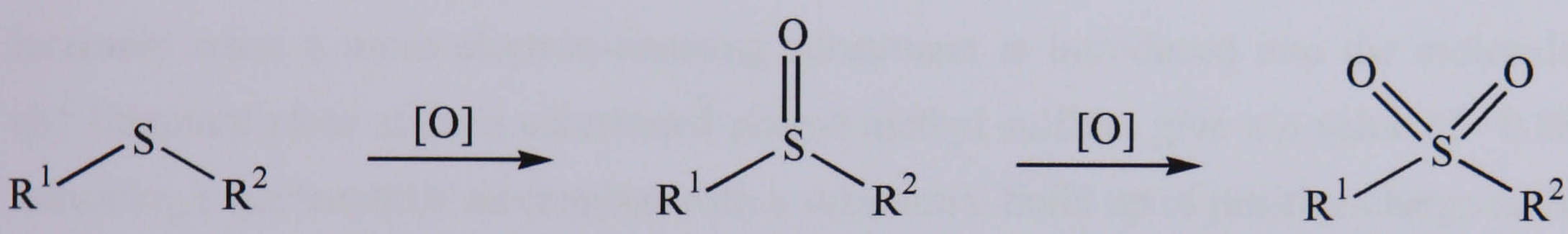

Sulfide Sulfoxide Sulfone

Figure 5-2 – General mechanism for sulfide oxidation

5.1.1 Circumstances Where a Change in the Nature of the Oxidant has been Observed

$[Fe^{3+}(O_2)(F_{20}TPP)]^-$ ($F_{20}TPP$ = 5,10,15,20-tetrakis(pentafluorophenyl)porphyrin) is able to epoxidise electron-rich olefins, but is able to react with their electron-poor analogues only in the presence of triphenyl phosphine.[5] Valentine and co-workers propose that in the absence of an additional axial ligand coordinated to Fe, the O_2 molecule is bonded in an η^2 fashion and acts as an electrophile, and is therefore unable to attack electron-poor species efficiently. However, upon coordination of PPh_3, the authors propose that the O_2 switches to an η^1 conformation and now acts as a nucleophile (Figure 5-3). The balance between these two modes of coordination can therefore have a significant effect on the reaction mechanism.

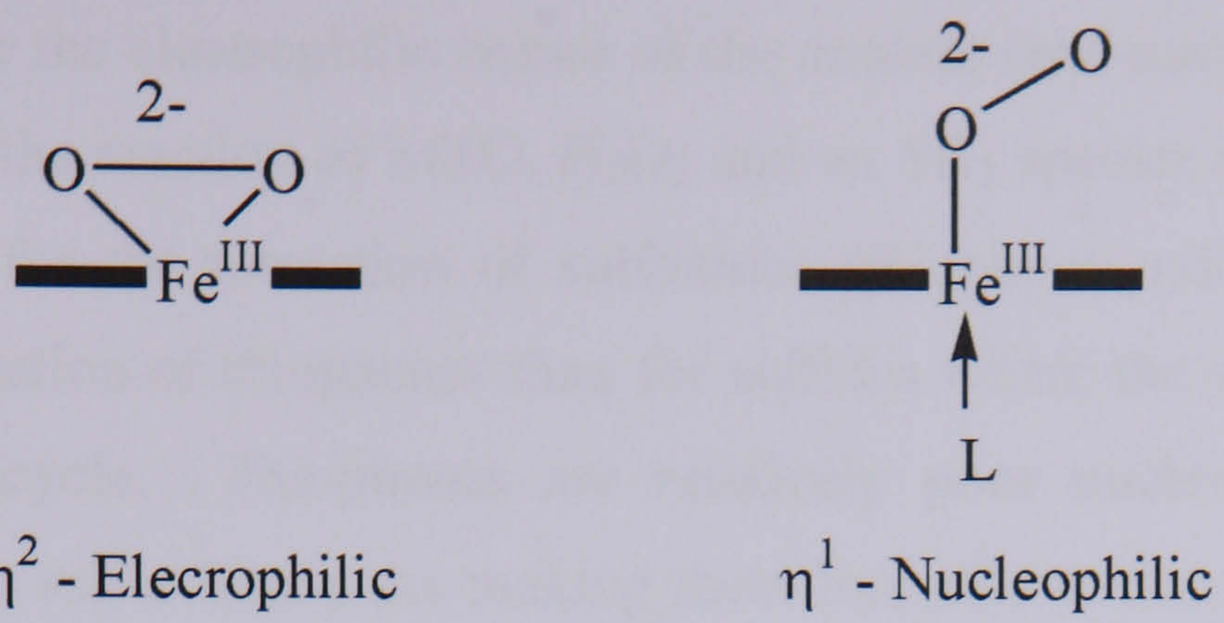

η^2 - Elecrophilic η^1 - Nucleophilic

Figure 5-3 – $[Fe^{3+}(F_{20}TPP)(O_2)]^-$ in different coordination modes

The methyltrioxorhenium(VII) complex (MTO, Figure 5-4) in the presence of H_2O_2 is able to transfer an oxygen atom to the sulfur atom of sulfides and thiophene and their derivatives.[6] The active oxidants in the MTO/H_2O_2 system are believed to be those shown in Figure 5-4, and both are thought to contribute to the mechanism. Evidence for this comes from both theoretical calculations[7] and experiment,[6,8,9] including a crystal structure of oxidant B. The rate constant for the conversion of a sulfide to a sulfoxide increases when a more electron-donating substituent is introduced into the molecule, and Hammett plots of *para* substituted phenyl methyl sulfides give a ρ value of −0.98, indicating a nucleophilic mechanism with a substantial build up of positive charge at the reaction centre.[10] The opposite trend is observed for the conversion of a sulfoxide to a sulfone,[8] analogous to the behaviour of the Mn complex that is the subject of this chapter. Kinetic monitoring of the oxidation of sulfines ($R_2C{=}S{=}O$, R=Ar) by MTO and H_2O_2 results in a Hammett plot with a distinct curvature. With electron withdrawing substituents on the aryl groups a nucleophilic oxidant is observed, but with electron donating substituents the oxidant is electrophilic.[11] This provides further support for the idea that the MTO species can behave as both a nucleophile and an electrophile under the same conditions.

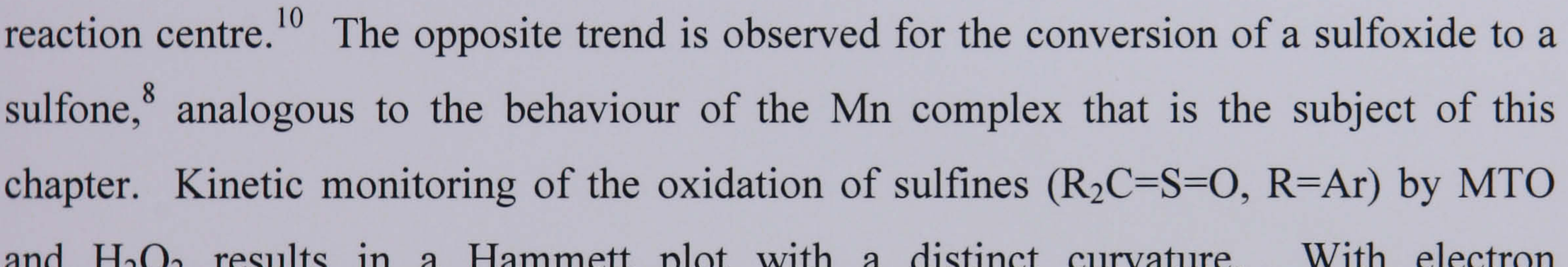

Methyltrioxorhenium Active Oxidant A Active Oxidant B

Figure 5-4 – MTO and the active oxidant from the reaction with H_2O_2

Further evidence for the electrophilic nature of the oxidant (and nucleophilic behaviour of the substrate) in the reaction of MTO, H_2O_2 and an SR_2 species is given by the fact that rate constants for the formation of sulfoxides (thiophene oxides) are 2–4 times smaller for the oxidation of thiophenes than for sulfides where the sulfur is not part of an aromatic heterocycle. Thiophenes are relatively poor nucleophiles due to the delocalisation of the sulfur lone pairs making them less able to donate electron density to reactants and explaining their lower activity.[8] In contrast, the rates of oxidation of the sulfoxides (and thiophen-1-oxides) by the same oxidant are much less influenced by the electronic properties of the substituent on the sulfur centre. The authors propose that this may signal a change in the oxygen-transfer mechanism, and that the peroxide may now be attacked by the coordinated sulfoxide and therefore act as an electrophile.[9] However, the Re^{7+} centre is electron deficient and it is questionable whether a coordinated peroxide group could behave as a nucleophile. Coordination of a sulfoxide ligand to the Re would, however, clearly aid such a process by increasing the electron density at the peroxide.

The concept of precoordination of the substrate highlighted in the previous paragraph has also been raised in the context of the titanium(IV)-(R,R,R)-tris(2-phenylethoxy)amine-alkylperoxo complex (Figure 5-5) studied by Nugent and co-workers.[12] For the oxidation of sulfides a linear Hammett correlation with a ρ value of −0.60 is obtained indicating that the oxidant is electrophilic, similar to the case studied here. However, the Hammett correlation for the oxidation of sulfoxides has a concave slope with a ρ value of +0.43 for electron withdrawing substituents and −0.15 for electron donating ones under identical conditions as for sulfide oxidation. This indicates a change in the mechanism of oxidation depending on the nature of substituents on the aryl methyl sulfoxides. The gradients of the Hammett plots for the Ti^{4+} complex are significantly steeper than those of the manganese complex studied here. This indicates that the sulfide and sulfoxide oxidation mechanisms are more sensitive to the electronic character of the substrate when oxidised by the Ti complex than the Mn complex.

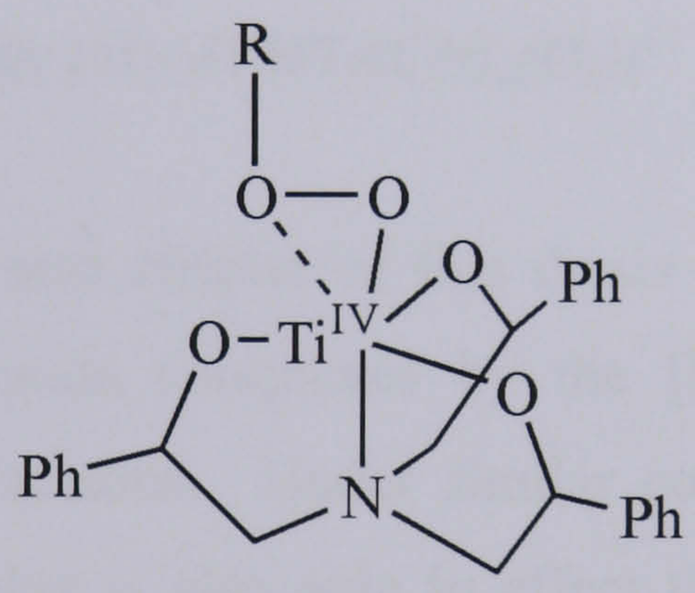

Figure 5-5 – Titanium(IV)-(R,R,R)-tris(2-phenylethoxy)amine – alkylperoxo complex

Nugent and co-workers propose that the change in the character of the oxidant is due to the ability of sulfoxides, but not sulfides, to coordinate to the Ti centre. Therefore sulfide oxidation occurs through an intermolecular electrophilic pathway and sulfoxide oxidation occurs via both an intramolecular nucleophilic pathway where the sulfoxide is coordinated to Ti (via the oxygen atom), and a competing intermolecular electrophilic pathway, explaining the non-linearity of the Hammett plot. Support for this mechanism is provided by the fact that the presence of a non-oxidisable coordinating ligand can suppress the coordination of the sulfoxide to the Ti centre and suppress the nucleophilic pathway.

Theoretical calculations by Nugent and co-workers[12,13] show that the energies and location of the frontier orbitals of the proposed oxidant (an alkyl peroxide coordinated

to Ti^{4+}, Figure 5-5) are consistent with the *umpolung* character of the peroxo functionality, and that the HOMO of the molecule (the O-O σ* orbital) and the LUMO (the $3p_y$ orbital of S) indicate that the key electronic interaction in the transition state could be the peroxo moiety donating electron density to the sulfoxide fragment, i.e a nucleophilic pathway. The role of the Ti^{4+} centre in this mechanism is to act as a template and activate both the hydroperoxide and sulfoxide fragments by holding them in close proximity. However, it should be noted that unlike the manganese systems of interest here, the formally d^0 Ti^{4+} centre cannot participate directly in the redox process.

DFT calculations show that when sulfoxide is coordinated to the titanium centre the alkyl peroxide ligand coordinates in a monodentate fashion.[12,13] However, when there is no sulfoxide ligand coordinated, the alkyl peroxide coordinates in a bidentate fashion. This is consistent with the observations of Valentine and co-workers, that monodentate peroxides act as nucleophiles and bidentate peroxides act as electrophiles.[5]

5.1.2 Examples of Oxidation by $[Mn_2(TMTACN)_2(O_3)]^{2+}$ and H_2O_2

As stated earlier, this and the next chapter of this thesis consider the mechanism of oxidation of sulfide and sulfoxide complexes by the $[Mn_2(TMTACN)_2(O)_3](PF_6)_2$ catalyst and aqueous H_2O_2 in acetone. Under similar conditions (although often in acetonitrile solution) this complex is also able to effect the oxidation of many other substrates including cinnamic acid, phenols and azo dyes.[14-19] Additives such as carboxylic acids (in particular acetic acid) are able to increase the rate of substrate oxidation,[20] and their presence broadens the range of substrates oxidised to include alkanes, alkenes, styrenes and alcohols.[20-28] Many of these functional groups are found in stains, and the catalyst is effective at stain bleaching.[29,30]

5.1.3 Identification of the Active Oxidant

The active oxidant in the systems mentioned above is the subject of some debate, and may not be the same for all complexes. However, there is compelling evidence for the presence of an oxomanganese(V) species (Figure 5-6) lending support to the mechanism proposed for the sulfide oxidation by Lindsay Smith and co-workers.[1]

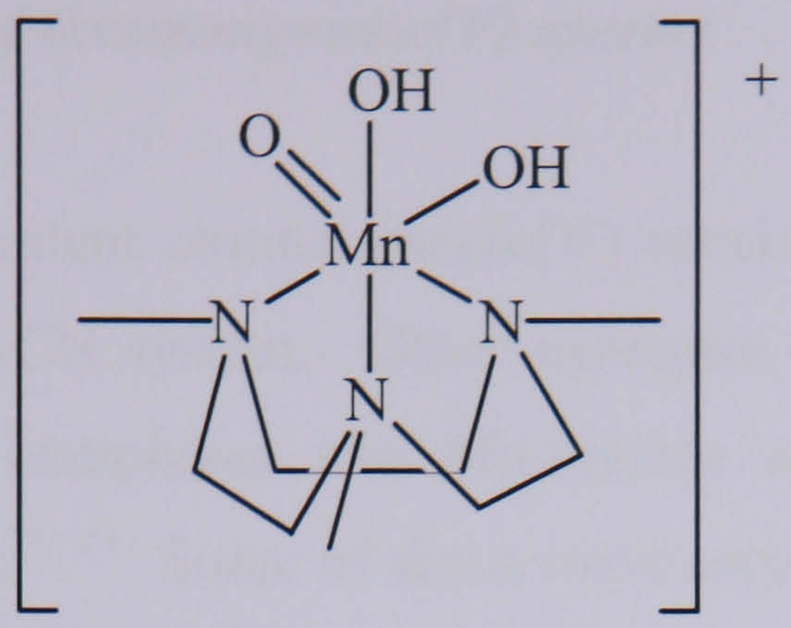

$[Mn(TMTACN)(OH)_2O]^+$

(5-2)

Figure 5-6 – Structure of the proposed active oxidant, $[Mn(TMTACN)(OH)_2(O)]^+$

Although no oxomanganese(V) species have been directly observed in the reaction between $[Mn_2(TMTACN)_2(\mu\text{-}O)_3]^{2+}$ and sulfides or sulfoxides in the presence of hydrogen peroxide, electrospray ionisation mass spectrometry shows evidence for fragmentation of the dimer. Moreover, identical reaction profiles are obtained when $[Mn(TMTACN)(OMe)_3]^+$ is used as the catalyst instead, supporting the proposal that a mononuclear species is involved. Studies on the oxidation of other substrates, such as alkenes and azo dyes, with the same complex and similar conditions do show evidence for an oxomanganese(V) species.[14-17] In particular, the reaction between **5-1** and phenols has been studied and oxomanganese(V) intermediates such as **5-3**, (Figure 5-7) have been identified by mass spectrometry. The observation of these species confirms that the phenols coordinate to the manganese, which in turn stabilises the high oxidation state on the metal centre and allows the oxomanganese(V) species to persist in solution for long enough to be detected by MS.

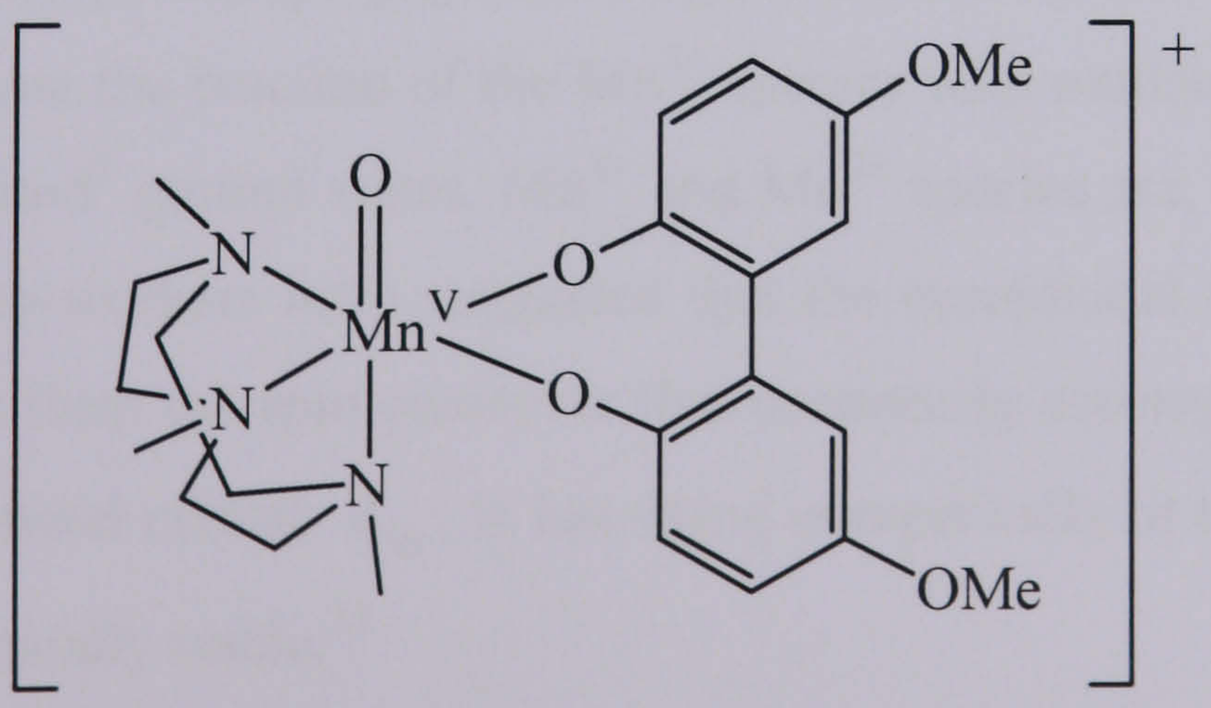

(5-3)

Figure 5-7 – Oxomanganese(V) species detected using ESI-MS

5.1.4 Other Examples of Oxomanganese(V) species

The proposal of a high valent oxomanganese(V) species as an active oxidant is not unique to the Mn-TMTACN system. Other examples include the (salen)manganese catalysts, Mn-porphyrin complexes and Mn-corrole complexes which give stable oxomanganese(V) species.[31-33] Some of these oxomanganese(V) complexes have been structurally characterised, and they are all found to have Mn=O bond lengths in the region of 1.55 Å.* All these complexes have macrocyclic tetradentate ligands which adopt a square planar geometry with the Mn centre sitting in, or just above the plane of the ligands.

5.1.4.1 Oxomanganese(V) Porphyrin Complexes

Evidence for several oxomanganese(V) porphyrin complexes has been gathered in recent years. These include the complex synthesised by Groves and co-workers, [Mn(TMPyP)(O)] (TMPyP = tetra-*N*-(methylpyridyl)porphyrinato) which is generated by the oxidation of the Mn^{3+}(TMPyP) complex.[34] Oxidants include *m*-chloroperoxybenzoic acid, HSO_5^- (oxone) and ClO^-, and the species is identified by the appearance of a Soret band at 443 nm in the UV/vis spectrum. In addition, experiments show that a limited amount of ^{18}O exchange occurs during olefin epoxidation, and that generation or reaction of the [Mn(TMPyP)(O)] in the presence of the one electron reductant, nitrite, gives the corresponding Mn^{4+} complex, implying that it is initially Mn^{5+}. The related oxomanganese(V) porphyrin complex with TM-2-PyP (chlorotetra(N-Me-2-pyridyl)porphyrinato) ligand and its isomer, TM-4-PyP, have also been generated from the reaction of the Mn^{3+} species with oxidants such as oxone, and both have low spin d^2 ground states. Mn^{4+} and Mn^{3+} species are, in contrast, high spin, and Groves and co-workers have suggested that the exceptional stability of the TM-2-PyP isomer arises from the spin crossover that necessarily accompanies reduction. The lowest occupied metal orbital, d_{xy}, is low-lying energetically in the TM-4-PyP isomer, which is less kinetically stable.[35]

---

* Low spin Mn-oxo bonds have a bond order of 3, and high spin ones have a bond order of 2.5. However, to aid discussion we refer to Mn-oxo bonds as Mn=O in the text, but this does not indicate that it has a bond order of 2.

The [Mn(TMPyP)(O)] complex, and other Mn porphyrin complexes (tetraphenylporphyrinato, TPP and tetrakis(pentafluorophenyl)porphyrinato, TPFPP) with an oxomanganese(V) group have also been generated by laser photolysis of the $Mn^{3+}(ClO_4)$ at 355 nm. The oxomanganese(V) complex is identified by its reactivity with stilbene and other olefins, affording the epoxide.[36,37] The most reactive oxomanganese(V) porphyrin species are obtained where the porphyrin has electron withdrawing groups, and all species are stabilised by the presence of water.

An oxomanganese(V) porphyrin complex has been generated directly from $[Mn(TF_4TMAP)](CF_3SO_3)_5$ (TF_4TMAP = *meso*-tetrakis-(2,3,5,6-tetrafluoro-*N,N,N*-trimethyl-4-aniliniumyl)porphinato dianion) and H_2O_2 in aqueous solution at 0°C and pH 10.5 rather than the strong oxygen transfer agents used in the previous examples.[38] The high valent species has a maximum in the UV/vis spectrum at 427 nm and is able to epoxidise alkenes, whereas the analogous Mn^{4+} species is unable to do this.

5.1.4.2 Oxomanganese(V) Corrole and Corrolazine Complexes

Corroles (tetrapyrroles) have been used as ligands to stabilise high oxidation states in a similar way to porphyrins.[39] The manganese(III) complex of one such corrole (5,10,15-tris(pentafluorophenyl)corrole (H_3(TPFC)), shown in Figure 5-8, is a good epoxidation catalyst, and in a reaction with ozone at −78°C (or with iodysyl benzene) leads to a stable oxomanganese(V) product characterised by a diamagnetic ^{19}F NMR spectrum, MS and UV/vis spectroscopy. This species is either able to epoxidise styrene or (more likely) is the precursor to such an oxidant.

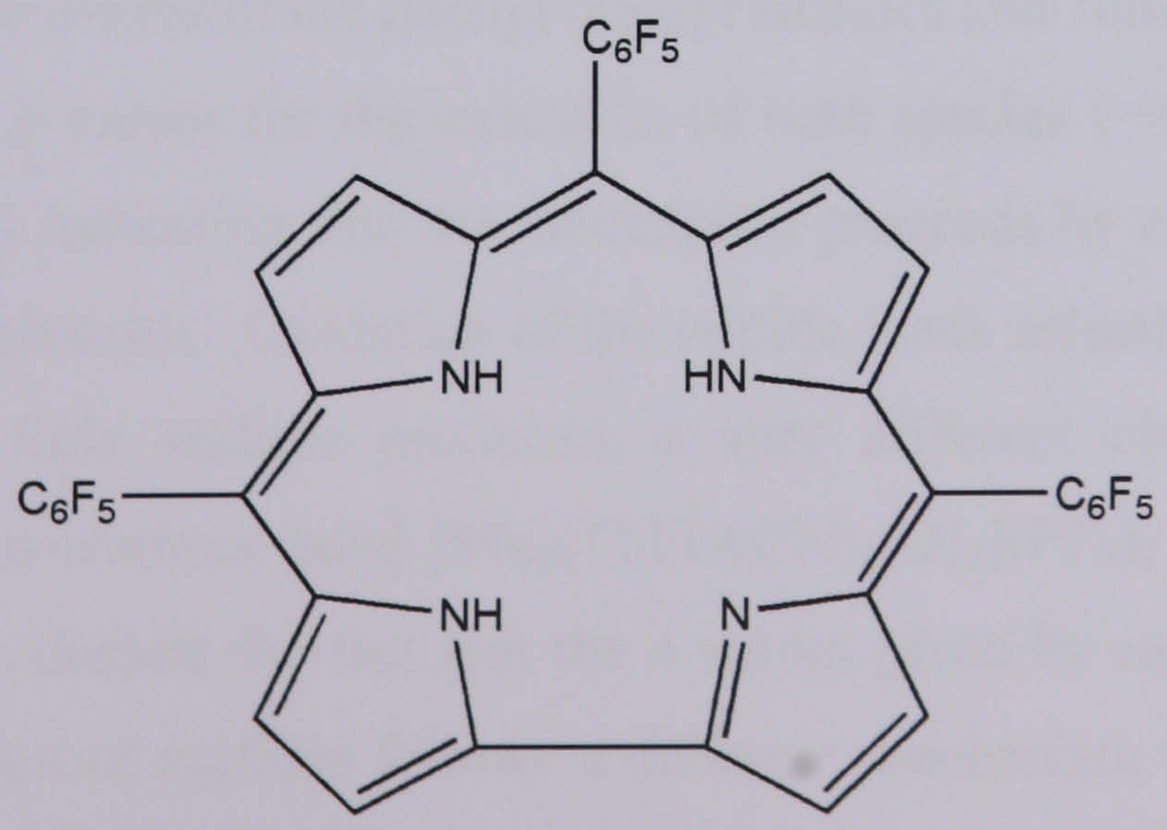

Figure 5-8 – 5,10,15-tris(pentafluorophenyl)corrole (H_3(TPFC))

The stability of oxomanganese(V) complexes with this type of ligand is further demonstrated by the isolation via flash column chromatography of $[(TBP)_8(Cz)Mn(O)]$ in 81% yield. This was characterised by ^1H NMR, high resolution LDI-TOF MS and resonance Raman spectroscopy where an Mn-O stretching band was identified at 979 cm^{-1}.[40]

5.1.4.3 Oxomanganese(V) Salen Complexes

The salen complex of Mn^{3+} catalyses the epoxidation of alkenes and other substrates by amine-*N*-oxides. ESI-MS experiments have detected the active oxidant and identified it as an oxo(salen)manganese(V) complex (Figure 5-9).[41] However, the authors report that this species reacts with (salen)manganese(III) to give a μ-oxo bridged complex, $[(salen)Mn^{4+}\text{-}O\text{-}Mn^{4+}(salen)]$ that can reversibly disproportionate to give the active species, but in the meantime stabilises it and allows it to persist.

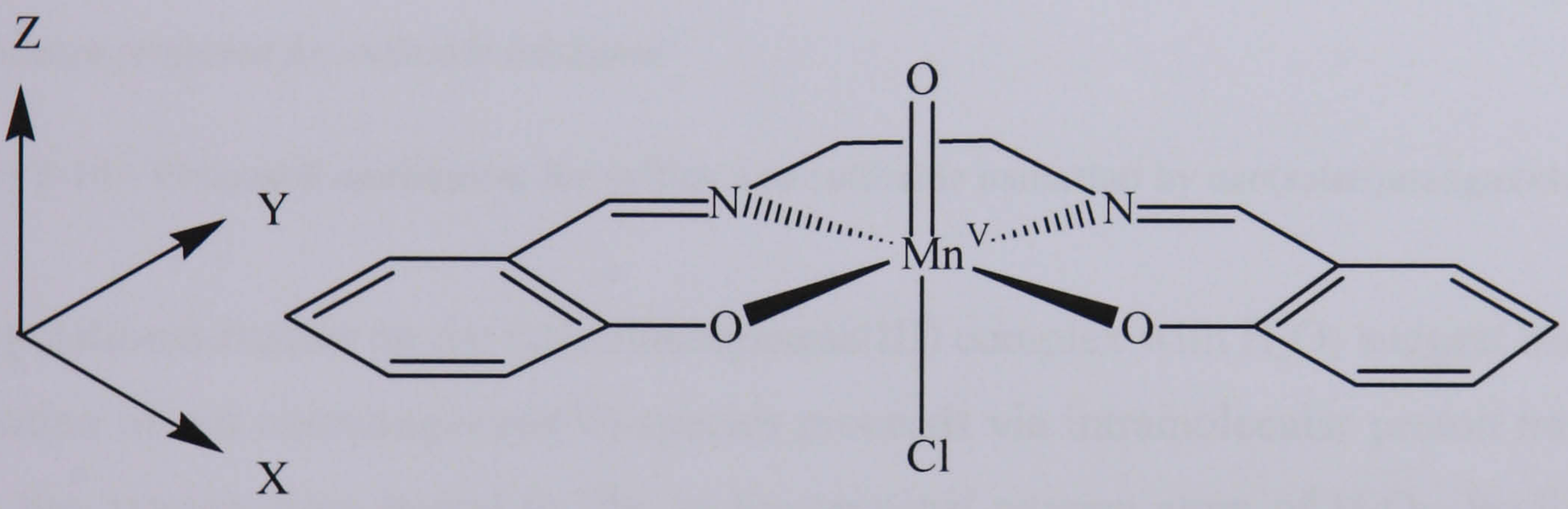

Figure 5-9 – Oxo(salen)manganese(V) with axial chloride ligand

Oxo(salen)manganese(V) complexes have been shown to oxidise many substrates[42] including sulfides and sulfoxides.[43,44] The mechanism of oxidation has been investigated using *para*-substituted phenyl methyl sulfides and sulfoxides, and Hammett plots show negative ρ values for the oxidation of both species (−1.86 for sulfides, and −2.44 for sulfoxides) indicating that the mechanism proceeds by electrophilic attack of the oxidant on the substrate. Oxidation of the sulfide leads selectively to the sulfoxide product, with very little sulfone produced, a very different observation to that of Lindsay Smith and co-workers using $[Mn_2(TMTACN)_2(O)_3](PF_6)_2$ as the oxidant.[1] The authors propose that, despite the fact that the ρ values given by each Hammett plot are negative, the oxidation of sulfides follows a different mechanism to that of sulfoxides; these two mechanisms are compared in Figure 5-10. For sulfides, single electron transfer is proposed to be the rate determining step, and then the sulfur radical is further

oxidised to give the sulfoxide product.[44,45] In contrast, sulfoxide oxidation goes via an S_N2 mechanism.[45]

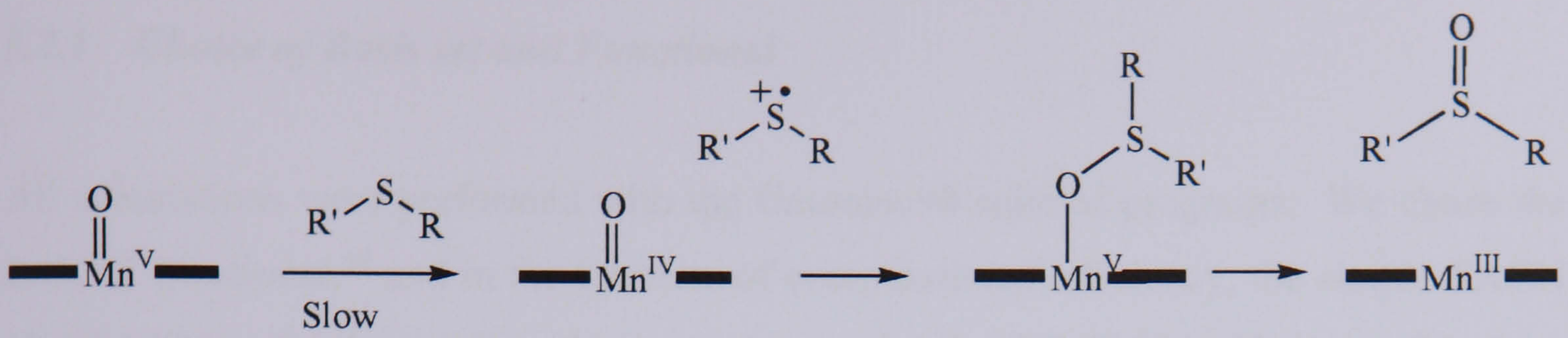

Mechanism proposed for sulfide oxidation

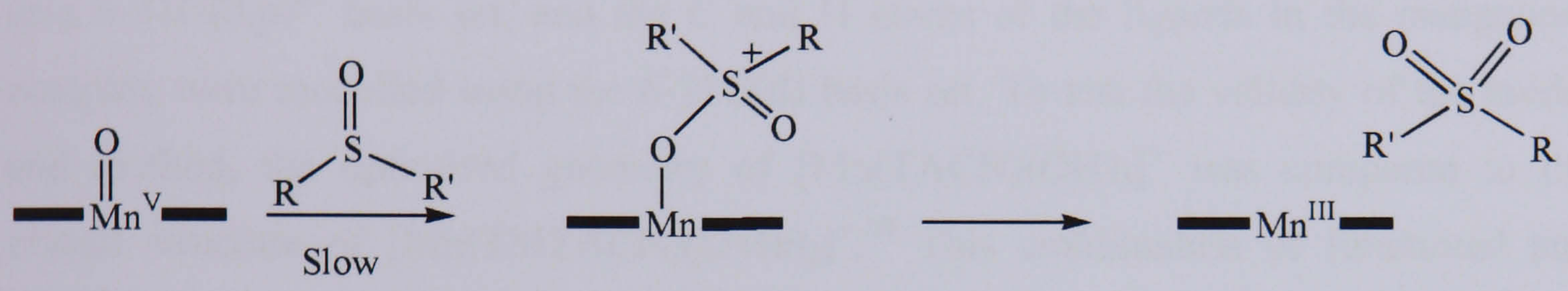

Mechanism proposed for sulfoxide oxidation

Figure 5-10 – Proposed mechanism for sulfide and sulfoxide oxidation by oxo(salen)manganese(V)

Computational studies on the (salen)manganese(III) complex with H_2O_2 suggest that the formation of an oxomanganese(V) species proceeds via intramolecular proton transfer from the oxygen atom bound to Mn, to the terminal oxygen atom of H_2O_2, leading to the loss of a water molecule. This reaction proceeds along a triplet pathway until after the transition state, when the complex undergoes a change in spin state to give a singlet oxomanganese(V) product. For the triplet pathway, the transition state barrier is 3.6 kcal mol^{-1} (15 kJ mol^{-1}) which is low enough to be overcome at ambient temperature.[46] With the explicit inclusion of a water molecule, the barrier is raised slightly to 4.0 kcal mol^{-1} (16 kJ mol^{-1}).

These examples of oxomanganese(V) porphyrin, corrole, corrolazine complexes and salen complexes illustrate that oxomanganese(V) species are plausible oxidation intermediates and offer support to the hypothesis that an oxomanganese(V) species is involved in the system we are studying.

5.2 Method validation

5.2.1 Choice of Basis set and Functional

All calculations were performed with the Gaussian98 suite of programs. We chose the B3LYP functional,[48] and in the interests of computational efficiency, the simple TACN (1,4,7-triazacyclononane) ligand was used to model the full TMTACN ligand. The Mn, O and N atoms, and the entire dimethyl sulfide molecule were modelled with the double zeta 6-31G(d,p)[49] basis set, and the C and H atoms of the ligands in the manganese complex were modelled using the 6-31G(d) basis set. To test the validity of the model and method, the optimised geometry of $[Mn(TACN)(OH)_3]^+$ was compared to the crystal structure of $[Mn(TMTACN)(OMe)_3]^+$.[50] This combination of functional and basis set with the model system $[Mn(TACN)(OH)_3]$ gives satisfactory agreement with the known crystal structure of $[Mn(TACN)(OMe)_3]$ (Figure 5-11). Initially the reaction pathway was modelled using dimethyl sulfide as the substrate, and the entire dimethyl sulfide molecule was modelled with the double zeta 6-31G(d,p)[49] basis set. When the dimethyl sulfide molecule was replaced with an aryl methyl sulfide group, all the atoms in the aryl group were modelled with the 6-31G(d) basis. The same basis sets were used for the sulfoxide system, and the additional oxygen atom coordinated to the sulfur was also modelled with a 6-31G(d) basis set.

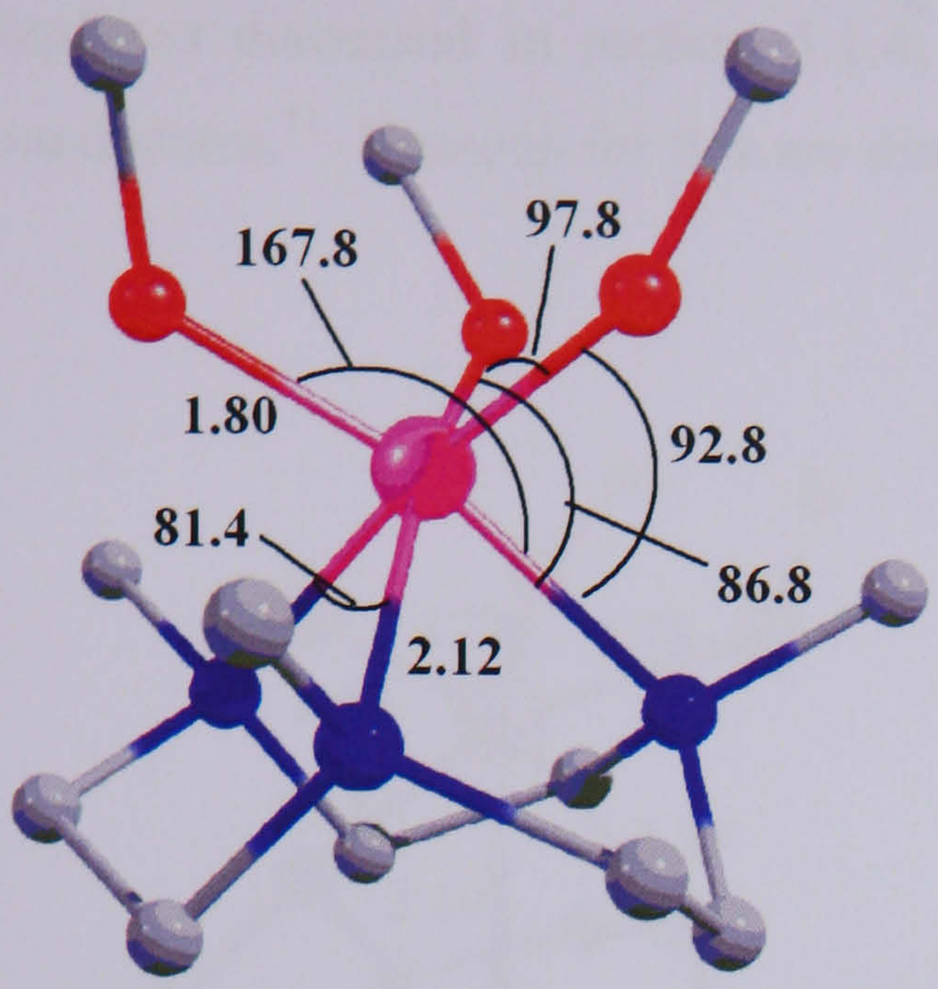

(5-4)

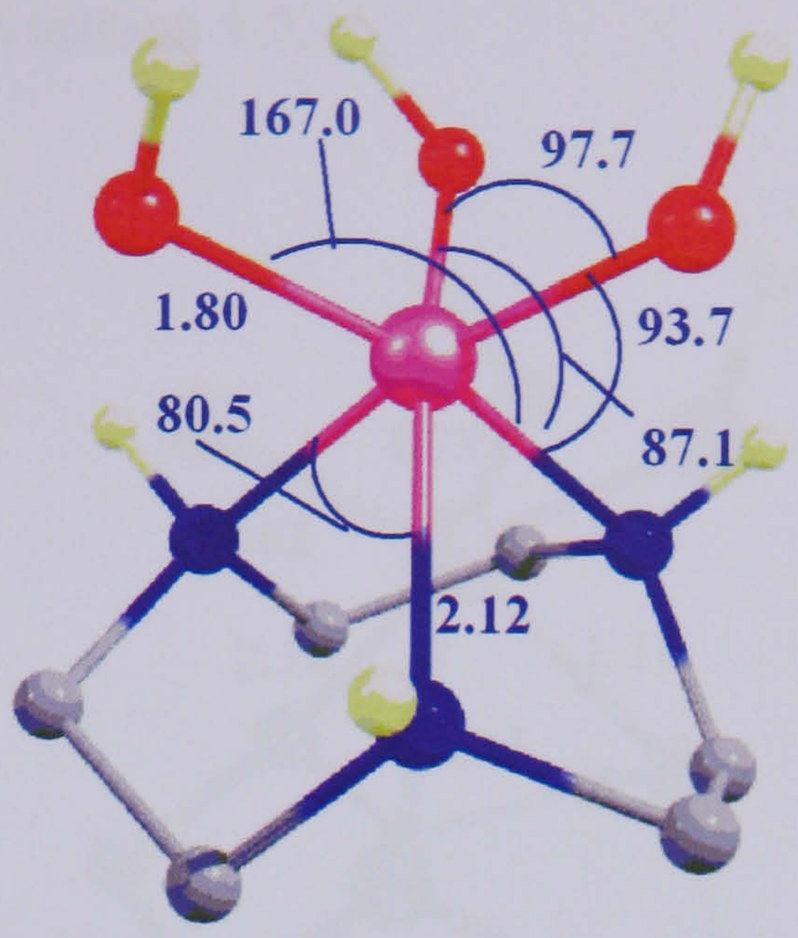

(5-5)

Figure 5-11 – Comparison of geometries of Mn^{4+} complexes (bond lengths in Å and angles in °) {original in colour}

5.2.2 Geometry and Spin State of the Oxomanganese(V) Complex: $[Mn(TACN)(OH)_2(O)]^+$

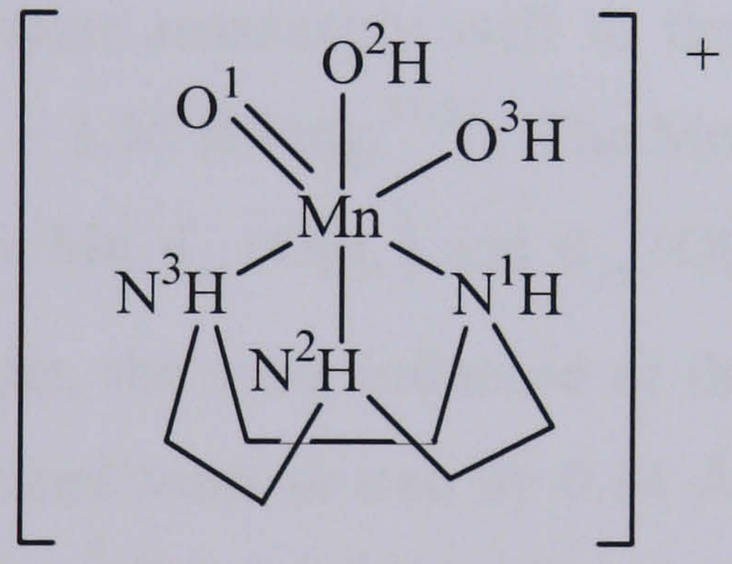

(5-6)

Figure 5-12 – $[Mn(TACN)(OH)_2(O)]^+$ including labelling of the atoms used in the discussion

On the basis of experimental results discussed in section 5.1.3, the active species in the reaction that we are studying is assumed to be $[Mn(TMTACN)(OH)_2(O)]^+$. By analogy to species **5-2**, the simplest model for the active oxidant is $[Mn(TACN)(OH)_2O]^+$ (**5-6**). The manganese centre of this species is in the +5 oxidation state, with a d^2 configuration giving rise to two possible spin states, a singlet (S=0) and a triplet (S=1). The geometry and energies of both the singlet and triplet spin states are summarised in Figure 5-13. The most stable spin state is the triplet, in marked contrast to the oxomanganese(V)

complexes discussed in section 5.1.4, which have been identified as having singlet ground states.[51] Reasons for this are discussed in section 5.2.4.

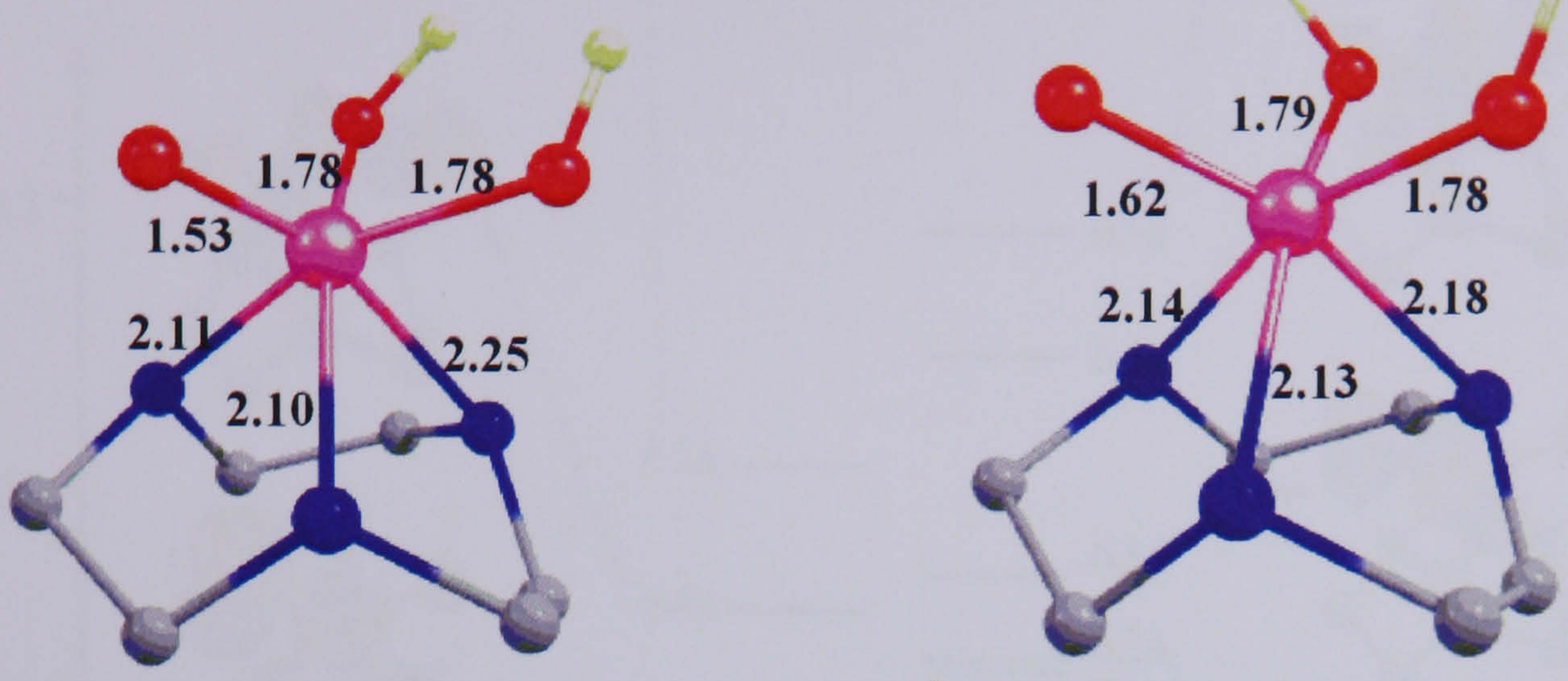

Singlet
$E = +41\ kJ\ mol^{-1}$

Triplet
$E = 0\ kJ\ mol^{-1}$

Figure 5-13 – Geometry of the singlet and triplet oxomanganese(V) species (bond lengths in Å) {original in colour}

Although the singlet spin state is not the lowest-energy minimum, its Mn-oxo bond length (1.53 Å) does compare reasonably well to those that have been structurally determined which are 1.55 – 1.56 Å long.[31-33]. The Mn=O bond in the triplet is longer due to the occupation of the Mn $d_{xz}/O(p_x)$ and $d_{yz}/O(p_y)$ π^* orbitals (Figure 5-14, α, 61a and 62a). In the singlet, the *trans* influence of the oxo group is reflected in the lengthening of the Mn-N bond *trans* to oxo by 0.14 Å compared to the Mn-N bonds *trans* to hydroxide ligands. The bond lengths of the Mn-OH groups are almost identical, as are the Mn-N bond lengths for the nitrogen atoms *cis* to the oxo group. In comparison, the triplet geometry shows a less pronounced *trans* influence and a longer Mn-oxo bond length due to the occupation of one π^* orbital.

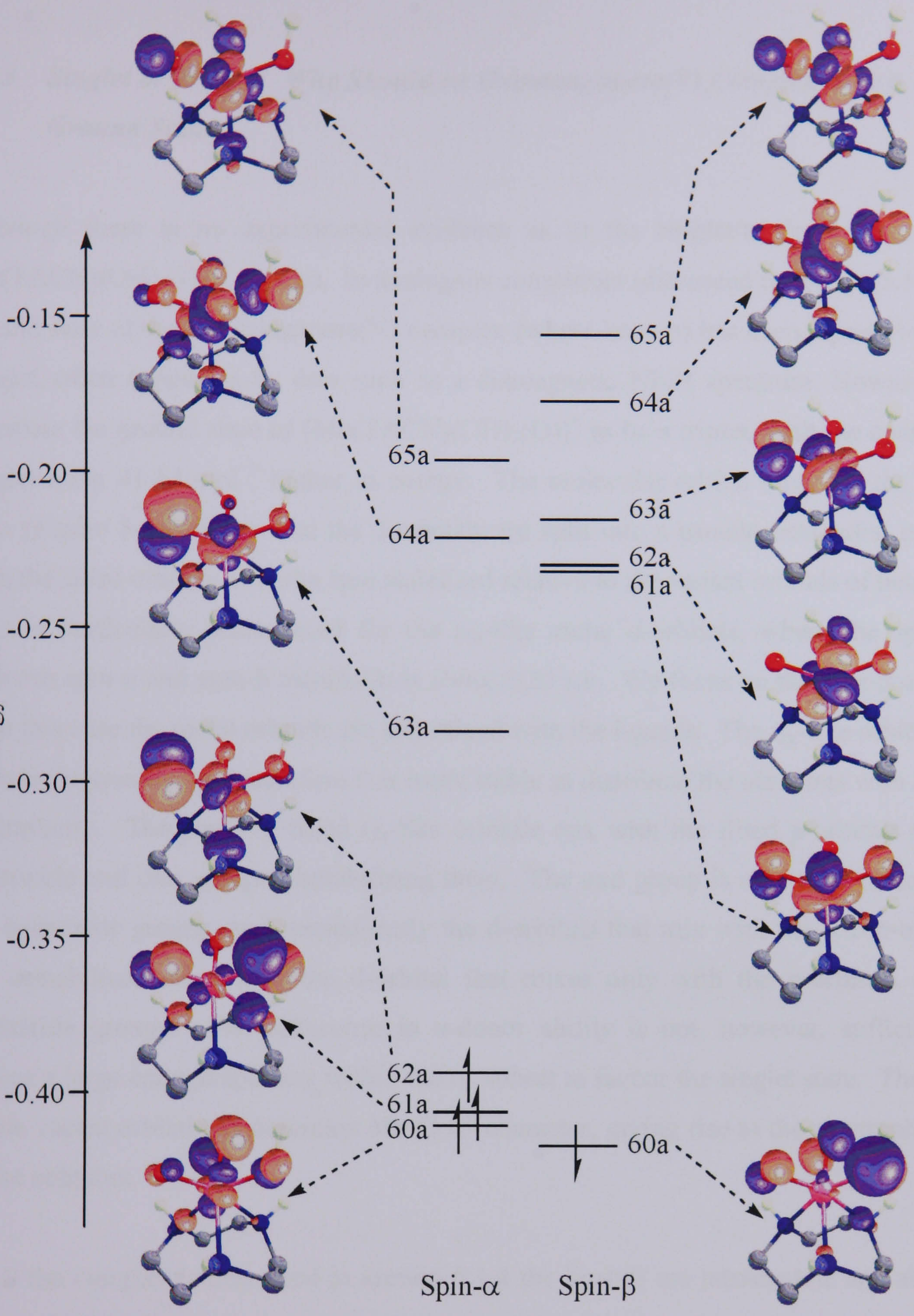

Figure 5-14 – Molecular Orbital array for $[Mn(TACN)(OH)_2(O)]^+$, S=1 {original in colour}

In the triplet state, the Mulliken spin density on the metal centre is greater than 2 (2.38) while that on the oxo ligand is high and of opposite sign (−0.38), indicating that there is significant radical character associated with the oxo ligand. The value of $\langle S^2 \rangle$ for the triplet state is also 15% higher than expected, consistent with significant radical character found on the oxo ligand, and suggests that there is some contribution from higher spin states due to a low lying O→Mn charge transfer excitation.

5.2.3 *Singlet or Triplet? Why Should an Oxomanganese(V) Complex have a Triplet Ground State?*

Although there is no experimental evidence as to the singlet/triplet nature of the $Mn(TACN)(OH)_2(O)]^+$ species, in analogous complexes (discussed in section 5.1.3) the ground state of the oxomanganese(V) complex (where known) has been reported to be a singlet, often supported by data such as a diamagnetic NMR spectrum. However, we calculate the ground state of $[Mn(TACN)(OH)_2(O)]^+$ to be a triplet, with the open shell singlet lying 41 kJ mol^{-1} higher in energy. The molecular orbital array for the triplet state (Figure 5-14) shows that the d-orbitals are split into a pseudo octahedral pattern, with the filled orbitals of alpha spin stabilised relative to the vacant orbitals of beta spin. This is particularly pronounced for the t_{2g}-like metal d-orbitals, where the splitting between spin-α and spin-β manifolds is about 0.20 a.u. We focus on the spin-β orbitals as in this case the metal orbitals are less mixed with the ligands. The t_{2g}-like orbitals are pseudo degenerate, and therefore it is more stable to distribute the electrons with higher multiplicity. The partially filled t_{2g}-like orbitals mix with the filled p-orbitals on the hydroxide and oxo groups, destabilising them. The oxo group is a better π-donor than the hydroxide groups, and consequently the d-orbitals that mix with the oxo p-orbitals are destabilised more than the d-orbital that mixes only with the p-orbitals of the hydroxide groups. The difference in π-donor ability is not, however, sufficient to induce a large enough splitting within the t_{2g} subset to favour the singlet state. The most stable vacant orbital has dominant Mn-O π* character, giving rise to the electrophilicity of the complex.

In all the complexes described in section 5.1.4 the ligands are tetradentate and all bind in one plane. Moreover, they have no strong π-donor groups other than the oxo group – even in the salen ligand, which has two oxygen donors, the p-orbitals of the oxygen atoms are involved in a π bond already and so their π-donor ability is diminished. Therefore in those cases the oxo group induces a strong splitting with the t_{2g} subset and favours the singlet state. The very different donor set here has π-donor ligands interacting with all the orbitals in the t_{2g} subset so these are not split so much and the triplet spin state is favoured.

5.3 Sulfide oxidation by Oxomanganese(V)

We have shown in the previous section that the oxo group in a $[Mn(TACN)(OH)_2(O)]^+$ **(5-6)** complex is electron deficient and therefore potentially a strong electrophile. Sulfides have an accessible lone pair of electrons on the sulfur that can act as a nucleophile towards the oxo group. In one possible mechanism for the oxidation of sulfides by **(5-6)**, the sulfide lone pair of electrons attacks the oxo group resulting in a manganese(III) species with a coordinated sulfoxide molecule (Figure 5-15). This mechanism is similar to the one proposed by Rajagopal and co-workers for the oxidation of sulfides by oxo manganese(salen).[44]

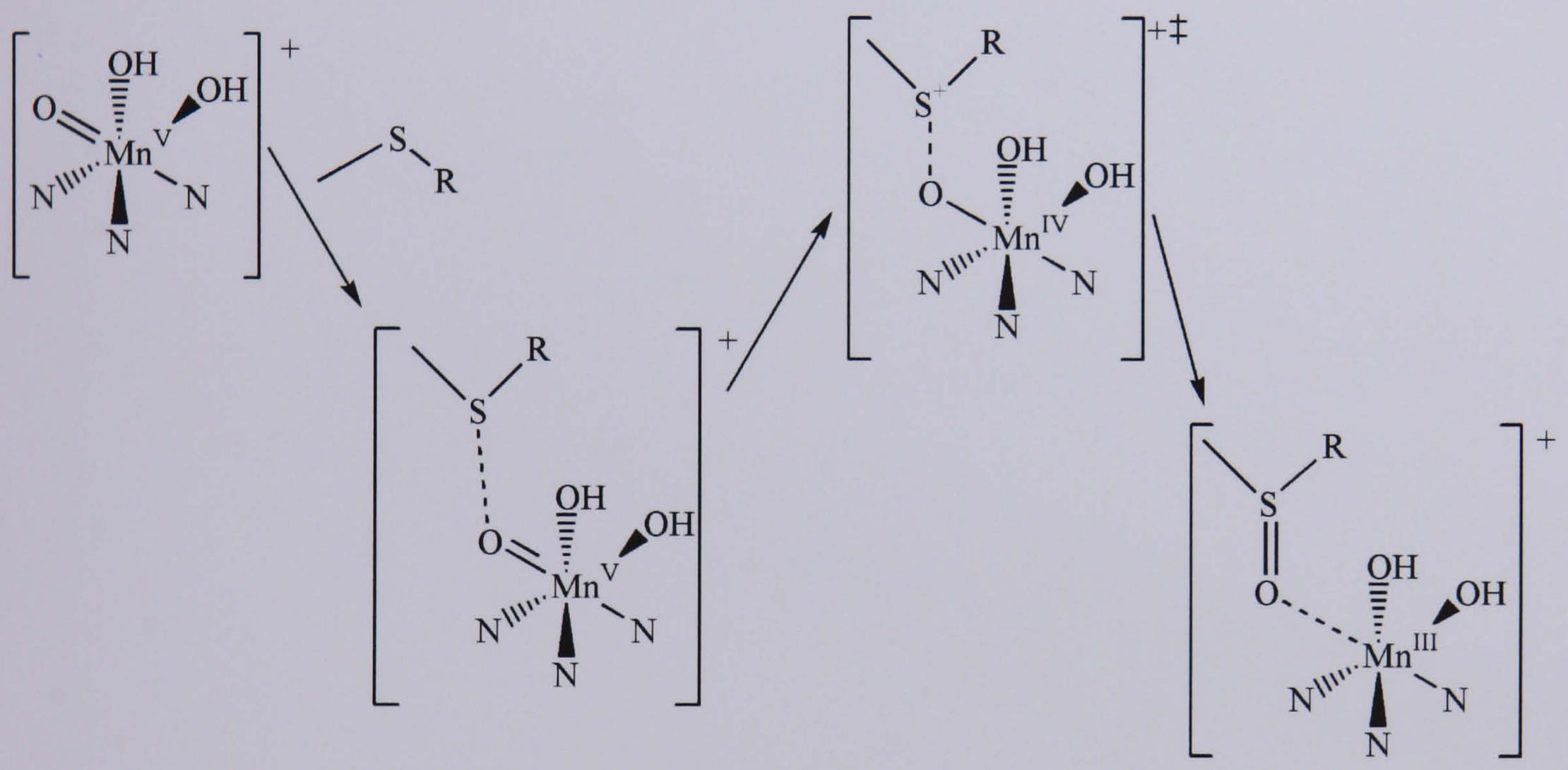

Figure 5-15 – Proposed mechanism for sulfide oxidation by $[Mn(TACN)(OH)_2(O)]^+$

The potential energy surface for the oxidation of sulfides to sulfoxides by $[Mn(TACN)(OH)_2(O)]^+$ for selected sulfides has been investigated using DFT. Initially, the reaction pathway was calculated with dimethyl sulfide as the nucleophile. The stationary points were then reoptimised with three *para*-substituted phenyl methyl sulfoxides: phenyl methyl sulfoxide, 4-nitro-phenyl methyl sulfoxide and 4-methoxy phenyl methyl sulfoxide, the last two having strongly electron withdrawing and donating substituents, respectively. The energetics of the reaction have been compared to see if they show the same qualitative trend as the experimental Hammett plots (i.e. a negative slope).[1]

5.3.1 Potential Energy Surface

The potential energy surface for the reaction between $[Mn(TACN)(OH)_2O]^+$ **(5-6)** and DMS is shown in Figure 5-16, below. The initial step is attack of the sulfide on the oxo group of $[Mn(TACN)(OH)_2(O)]^+$ to form a precursor complex, followed by transfer of the oxygen atom to the sulfur via the transition state to give a sulfoxide, loosely coordinated to the manganese via the oxygen atom. The geometry and electronic structure of the species at each stationary point will be discussed in turn. Where appropriate, more than one spin state has been considered. The energy barrier from the precursor complex to the transition state (which we consider as the activation energy) is +17 kJ mol^{-1}, a value consistent with rapid reaction at room temperature.

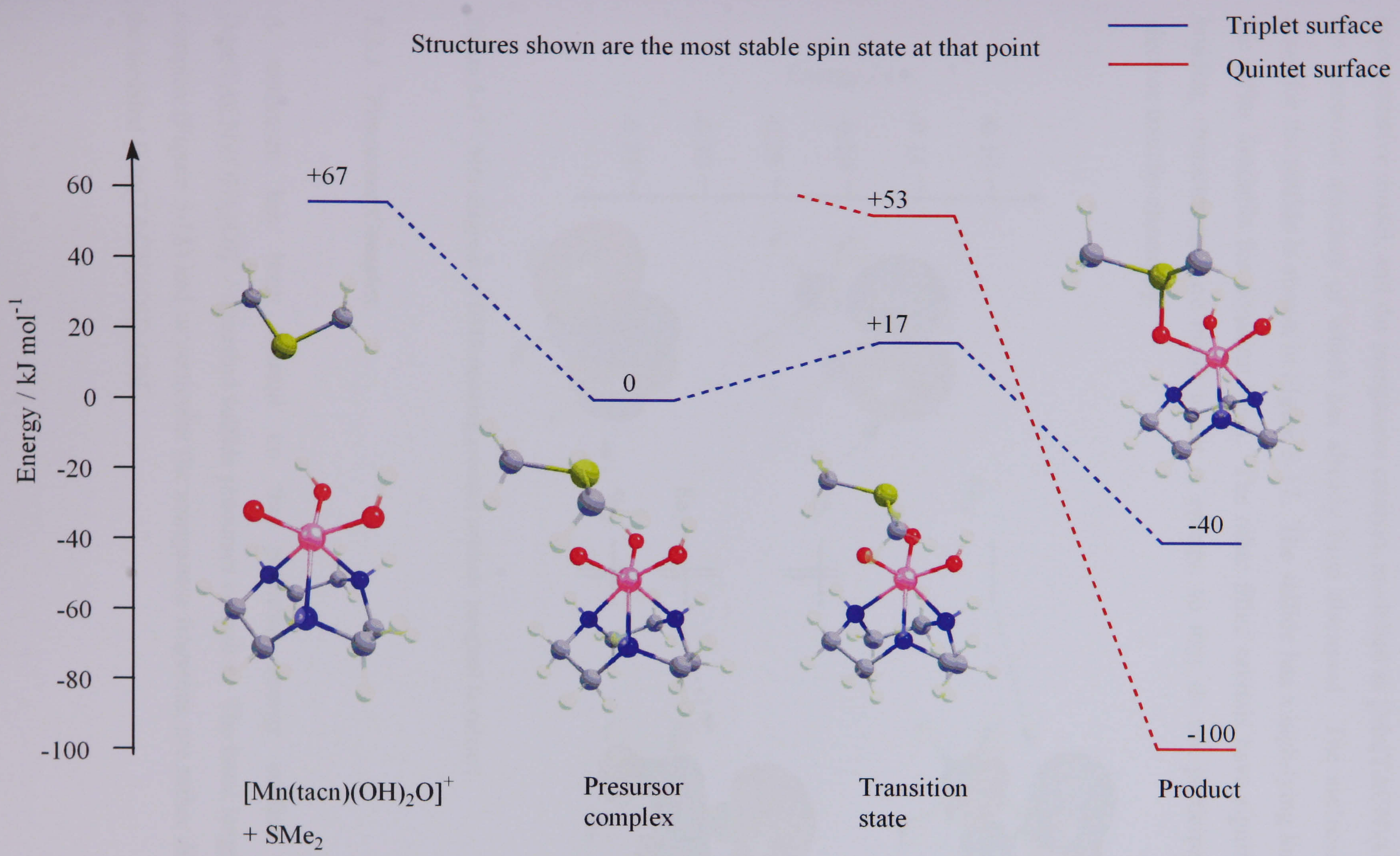

Figure 5-16 – Potential energy surface for the oxidation of dimethyl sulfide by 5-6 {original in colour}

5.3.2 Isolated Reactants

The reactants in this bimolecular reaction are a sulfide, for which DMS is used as a representative model, and the manganese catalyst, modelled as $[Mn(TACN)(OH)_2(O)]^+$, the electronic structure of which has already been discussed. The molecular orbital array for the sulfide is shown in Figure 5-17. The sulfide has a high-lying lone pair on the sulfur available for donation ($3b_1$). The other filled orbitals have significant C-S bonding character and are much lower in energy, so they do not participate in any electron transfer chemistry.

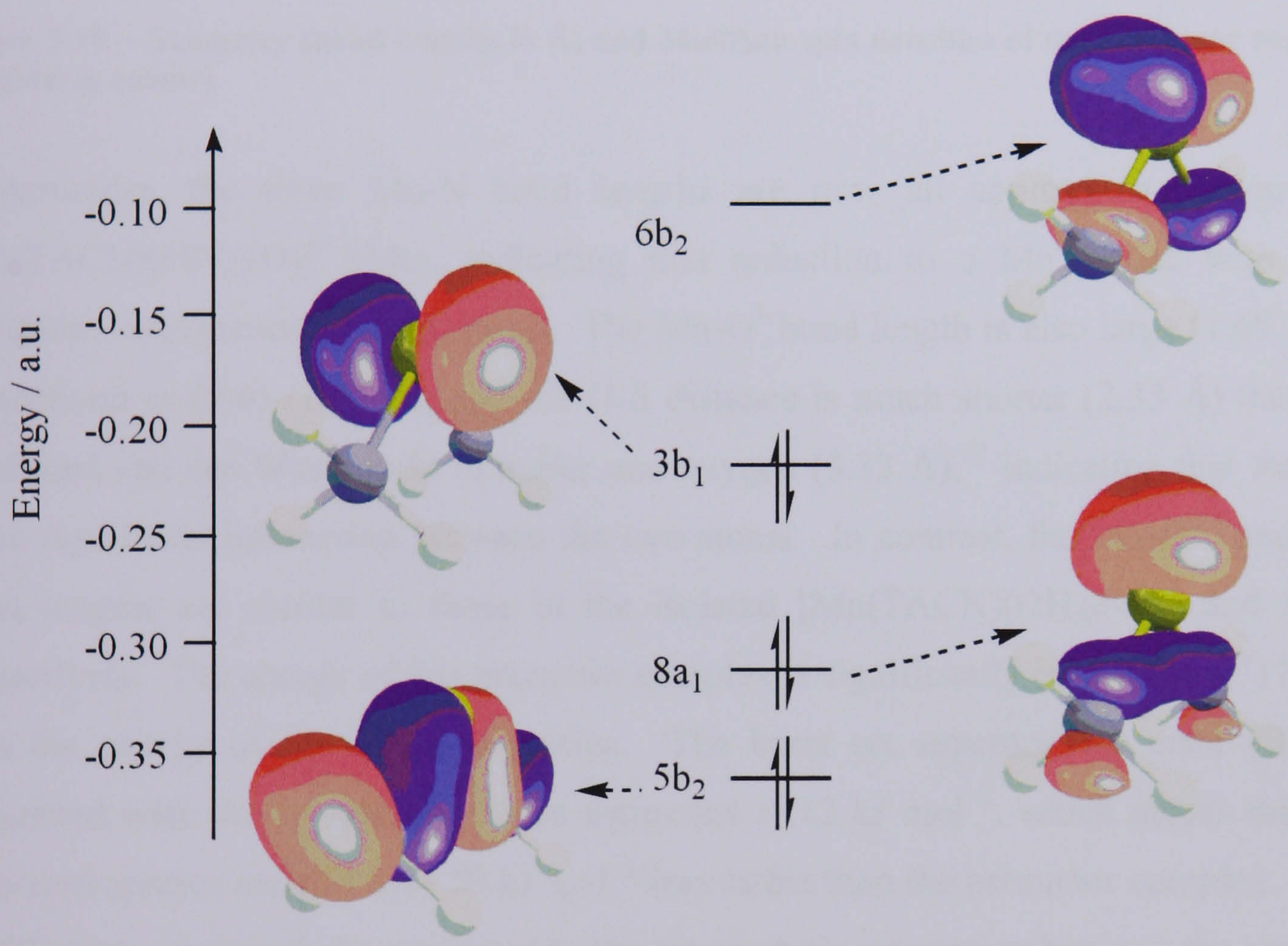

Figure 5-17 – MO diagram of DMS showing selected orbitals {original in colour}

5.3.3 Precursor Complex

A minimum has been located on the potential energy surface for the $[Mn(TACN)(OH)_2(O)]^+$ / dimethyl sulfide precursor complex. The bond lengths in this complex (Figure 5-18) and in particular the manganese fragment, are rather different to the isolated $[Mn(TACN)(OH)_2(O)]^+$.

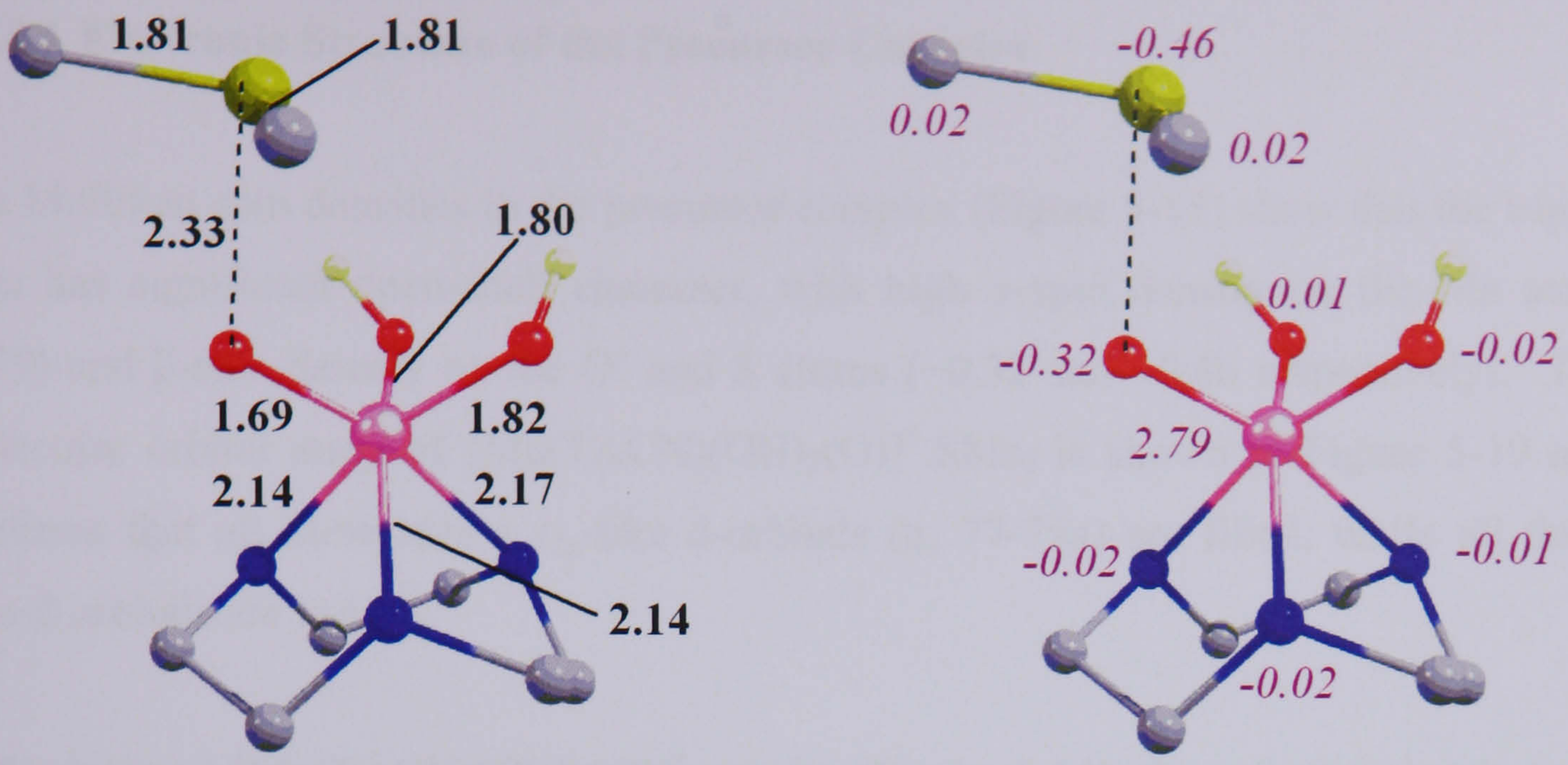

Figure 5-18 – Geometry (bond lengths in Å) and Mulliken spin densities of the precursor complex {original in colour}

In particular, the three Mn-N bond lengths are now all approximately equal in $[Mn(TACN)(OH)_2(O)]^+.SMe_2$, indicating that reduction to a Mn^{4+} state with a d^3 electronic configuration has occurred. The Mn-O^1 bond length is also large (1.69 Å) in comparison to **(5-6)** (1.62 Å), and the O-S distance is much shorter (2.33 Å) than the combined van der Waals radii of sulfur and oxygen (3.32 Å),[52] indicating that there is some significant interaction between the two atoms. In contrast, the Mn-$O^{2,3}$ and C-S bond lengths are similar to those in the isolated $[Mn(TACN)(OH)_2(O)]^+$ and SMe_2 respectively. The energy of this precursor complex is significantly (-69 kJ mol^{-1}) lower than the energy of the separate species. The basis set superposition error (BSSE) associated with the complex has been estimated at 12 kJ mol^{-1}, which means that the separated species are still over 50 kJ mol^{-1} less stable than the precursor complex. This stabilisation can largely be attributed to the electrostatic interaction between the charged Mn complex and the neutral sulfide. To confirm that there is no barrier to the formation of the precursor complex from the separate species, a linear transit calculation has been carried out in which the O-S distance has been constrained and increased by regular increments, starting at the optimised bond length. The energy rises as the O-S distance increases confirming that transfer of a spin-α electron from the manganese to the sulfur is barrierless.

5.3.3.1 Electronic Structure of the Precursor Complex

The Mulliken spin densities in the precursor complex (Figure 5-18) show that the triplet state has significant open-shell character, with high α-spin density on the Mn atom (2.79) and β-spin density on the O^1 and S atoms (−0.32 and −0.46 respectively). The molecular orbital array of $[Mn(TACN)(OH)_2(O)]^+.SMe_2$ is shown in Figure 5-19 and confirms that all three spin-α t_{2g}-like d-orbitals (α, 77-79a) are filled, while all three spin-β orbitals are vacant.

In the isolated $[Mn(TACN)(OH)_2(O)]^+$ species (Figure 5-14), the spin-β (minority) t_{2g}-like metal orbitals are destabilised by about 0.20 a.u. with respect to the spin-α (majority) array, and as a result the interactions with the sulfur lone pair are different for the spin-α and spin-β manifolds. The vacant spin-α M=O anti-bonding orbital (α, 63a in Figure 5-14) is lower in energy than its spin-β counterpart (β, 61a), and mixes with the sulfur p-orbital to give filled S-O bonding (α, 78a) (Figure 19) and virtual S-O anti-bonding (α, 80a) combinations. In the spin-β manifold, the higher energy of the M=O π* orbitals (β, 61a and β, 63a in Figure 5-14) means that they can not mix with the sulfur p-orbital as effectively. In fact, it is the spin-β Mn=O *bonding* orbital that lies closer in energy to the sulfur p-orbital and mixes to give a filled S-O anti-bonding combination (β, 77a) with very little Mn-O bonding character. The corresponding bonding combination lies much lower in energy. The net result is that there is significant sulfur lone pair character in the vacant spin-α manifold (80a α) but rather less in the vacant spin-β manifold, giving rise to the radical character at the sulfur centre. The precursor complex can, in fact, be viewed as a Mn^{4+} centre anti-ferromagnetically coupled to a sulfur radical centre via the bridging oxygen atom. The first step in the oxidation process can therefore be viewed as a one electron charge transfer from S to Mn^{5+}, the electron in question being in the spin-α manifold.

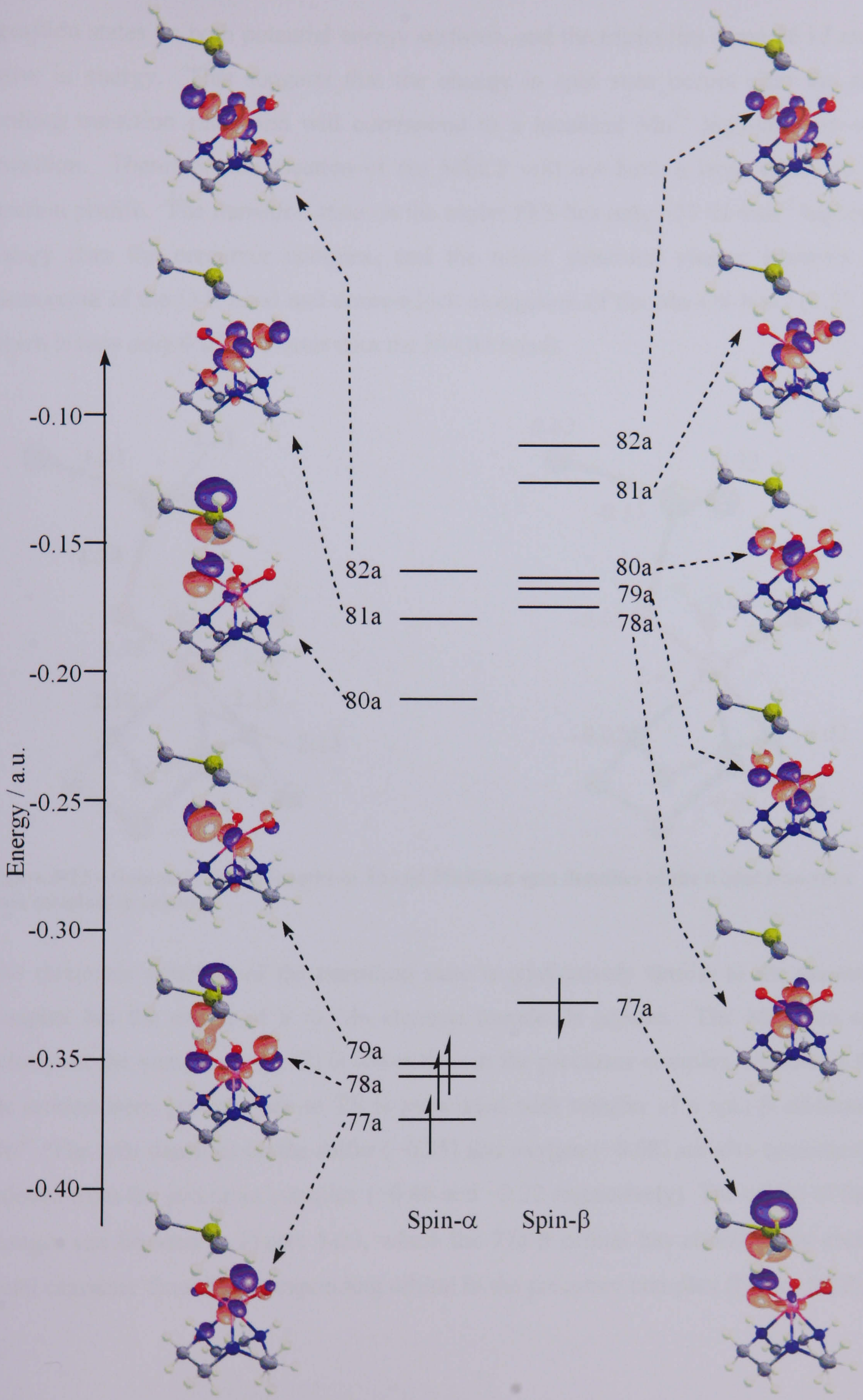

Figure 5-19 – MO diagram of $[Mn(TACN)(OH)_2(O)]^+.SMe_2$ {original in colour}

PAGE NUMBERING AS ORIGINAL

transition states on both potential energy surfaces, and the triplet lies some 36 kJ mol^{-1} lower in energy. This suggests that the change in spin state occurs after the rate-limiting transition state, and will correspond to a localised Mn^{3+} high-spin/low-spin transition. Therefore, the location of the MECP will not have a large effect on the reaction profile. The transition state on the triplet PES lies only +17 kJ mol^{-1} higher in energy than the precursor complex, and the major structural change involves the contraction of the O-S bond and concomitant elongation of the Mn-OS bond (1.75 Å), which is now only 0.05 Å shorter than the M-OH bonds.

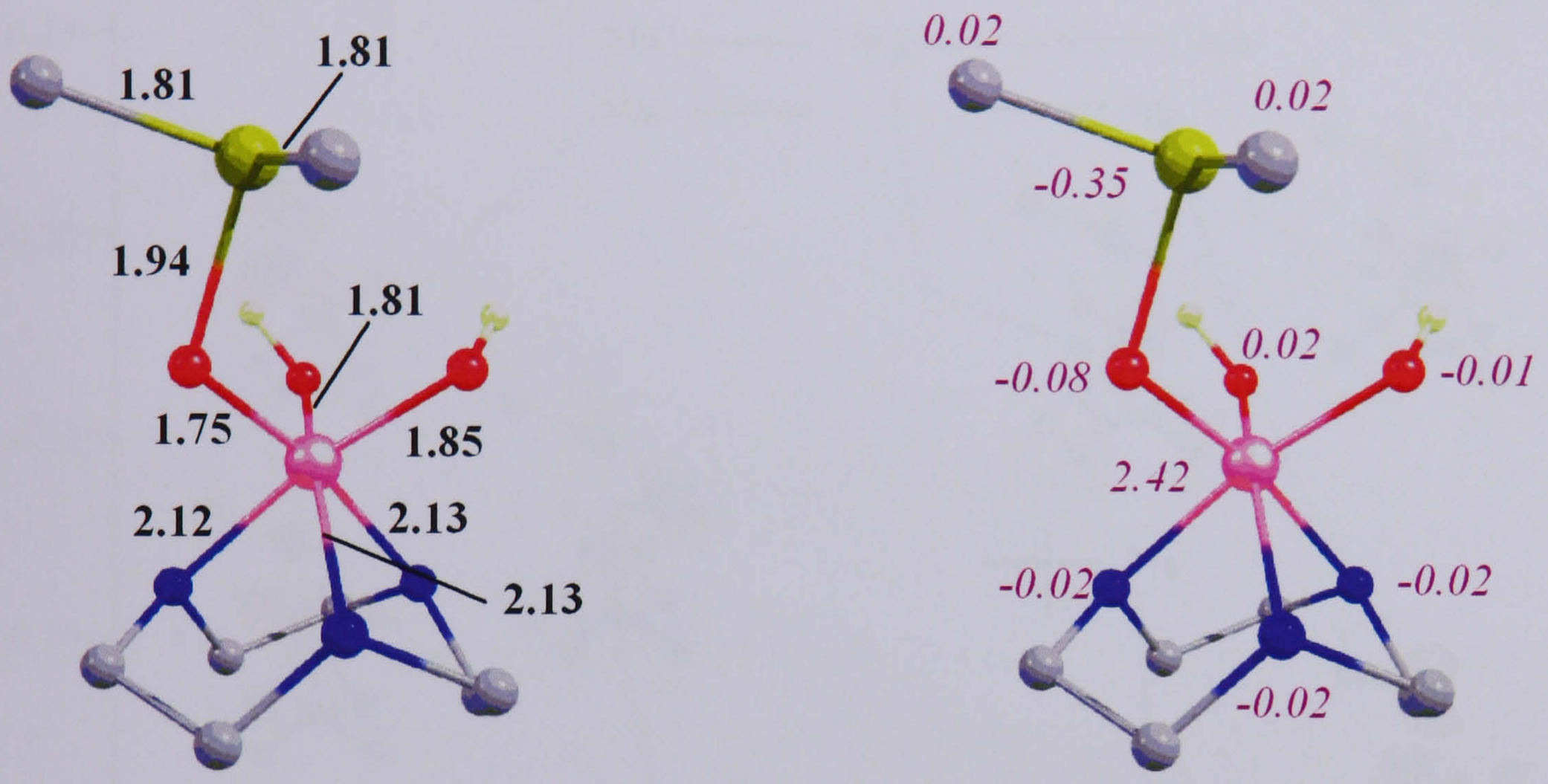

Figure 5-22 – Geometry (Bond lengths in Å) and Mulliken spin densities of the triplet transition state {original in colour}

The electronic structure of the transition state is qualitatively similar to the precursor complex but the extent of S to Mn electron transfer is greater. The Mulliken spin density on the manganese (2.42) is lower than in the precursor complex, indicating that the motion from ground state to TS is associated with transfer of a spin-β electron to Mn^{4+}. The spin densities on the sulfur (−0.35) and oxygen (−0.08) are also considerably reduced from the precursor complex (−0.46 and −0.32 respectively) The origin of these changes can be seen in Figure 5-23, where the 77a β orbital has considerably greater metal character than the corresponding orbital in the precursor complex (Figure 5-19).

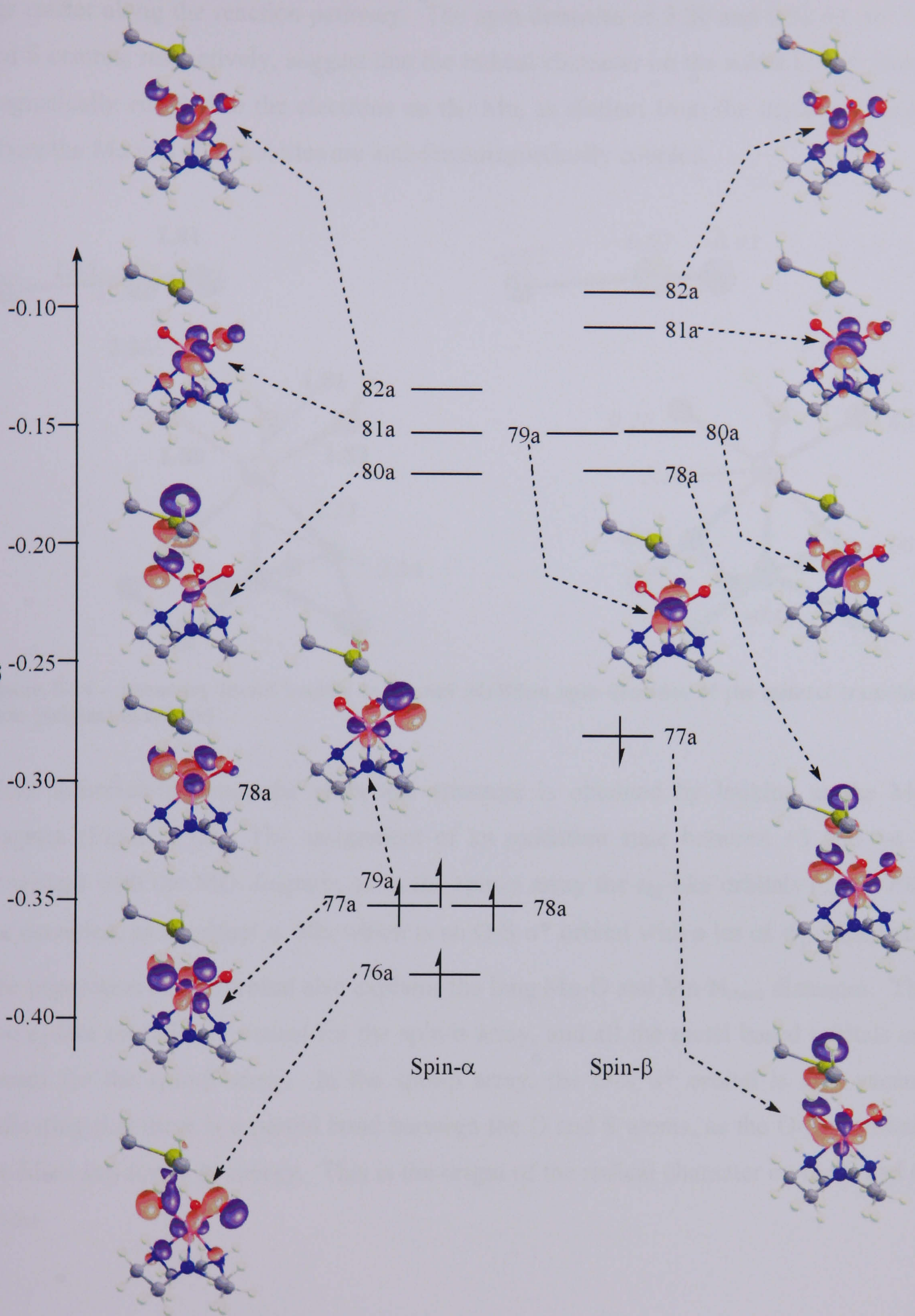

Figure 5-23 – MO array of the triplet transition state showing selected orbitals {original in colour}

The geometry of the quintet transition state (Figure 5-24) is similar in many respects to the triplet transition state (Figure 5-22). In the quintet transition state, however, the O-S distance is over 0.1 Å longer than in the triplet transition state suggesting that the TS

lies earlier along the reaction pathway. The spin densities of 3.20 and 0.52 on the Mn and S centres, respectively, suggest that the radical character on the sulfur is now ferromagnetically coupled to the electrons on the Mn, as distinct from the triplet spin state where the Mn and O-S moieties are anti-ferromagnetically coupled.

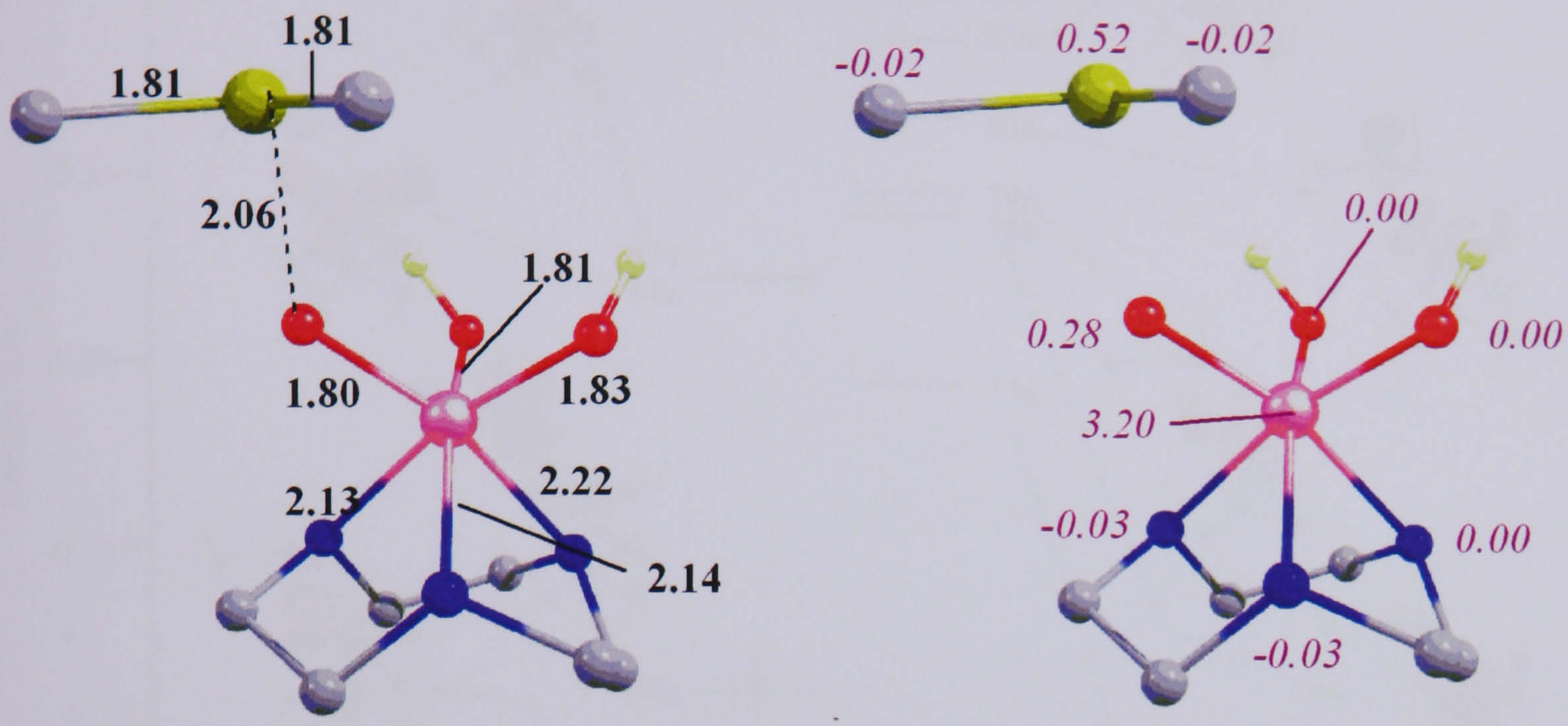

Figure 5-24 – geometry (bond lengths in Å) and Mulliken spin densities of the quintet transition state {original in colour}

More information about the electronic structure is obtained by looking at the MO diagram (Figure 5-25). The assignment of an oxidation state between +3 and +4 is consistent with the MO diagram, as in the spin-α array the t_{2g}-like orbitals (α, 77-79a) are occupied, as is orbital α, 80a which is an O-S σ* orbital with a lot of d_{z^2} character.

The population of this orbital also explains the long Mn-O and Mn-N_{trans} distances. The two e_g-like orbitals are vacant for the spin-α array, and all the metal based orbitals are vacant for the spin-β array. In the spin-β array, the O-S σ* orbital is also vacant, indicating that there is a partial bond between the O and S atoms, as the O-S σ orbitals are filled and lower in energy. This is the origin of the radical character on the S and O atoms.

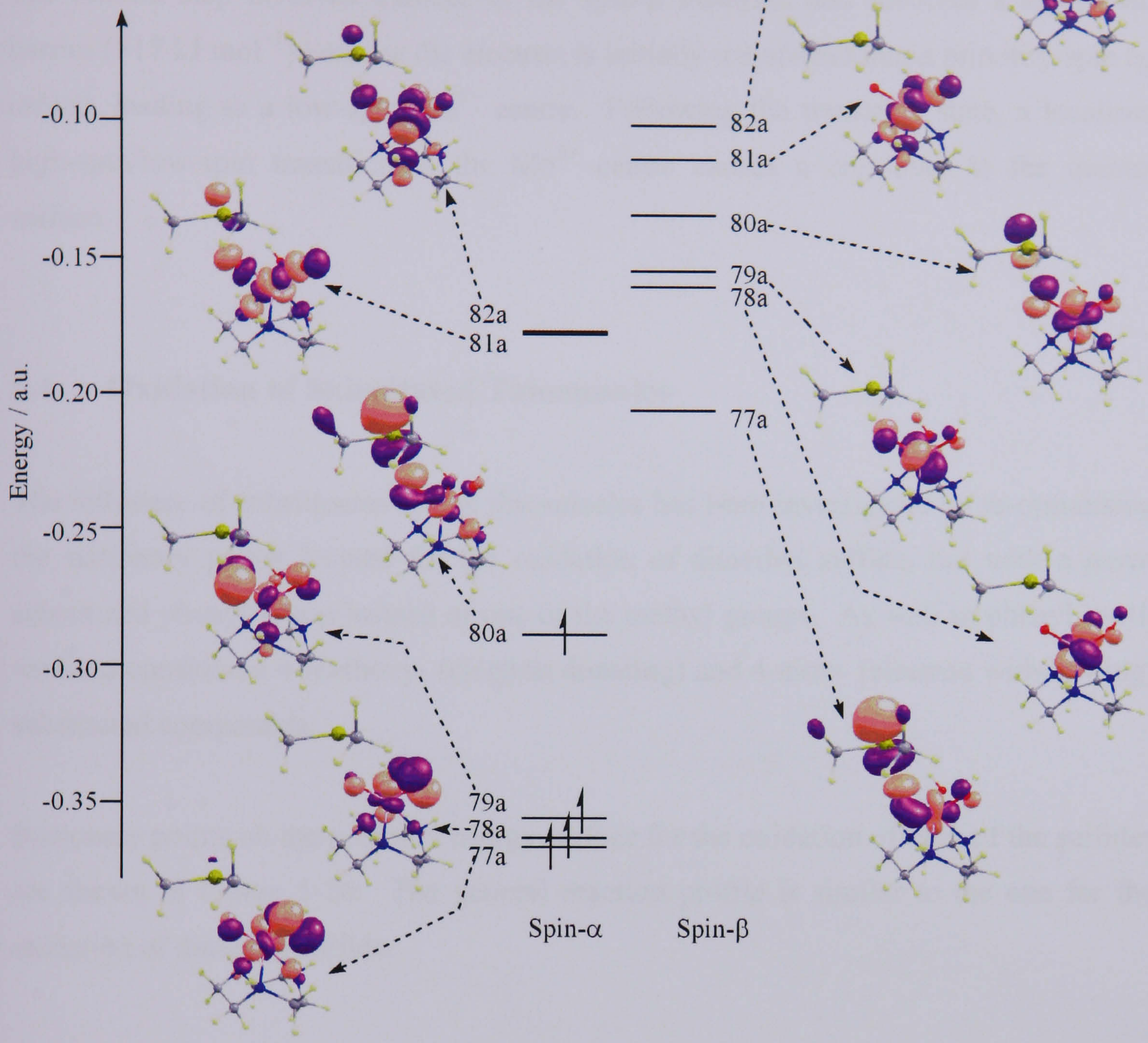

Figure 5-25 – MO diagram of the quintet transition state showing selected orbitals {original in colour}

In summary, the triplet transition state can be described as an S=3/2 Mn^{4+} centre anti-ferromagnetically coupled to a sulfur radical (S=1/2). Similarly, the quintet transition state can be described as an S=3/2 Mn^{4+} centre ferromagnetically coupled to a sulfur radical (S=1/2).

5.3.6 General Conclusions on the Reaction Mechanism

The reaction mechanism that has been established for the oxidation of dimethyl sulfide is as follows: A barrierless single-electron transfer results in the formation of the

precursor complex from **5-6** and sulfide. The electron transferred is spin-α, leading to a Mn^{4+} centre (S = 3/2) anti-ferromagnetically coupled to a sulfur-based radical (S = 1/2). The second step involves transfer of the spin-β electron, and involves a significant barrier (+17 kJ mol^{-1}) because the electron is initially transferred into a minority-spin t_{2g} orbital, leading to a low-spin Mn^{3+} centre. Following the transition state, a localised high-spin/low-spin transition at the Mn^{3+} centre causes a crossover to the quintet surface.

5.4 Oxidation of Substituted Thioanisoles

The influence of substituents on the thioanisoles has been investigated by re-optimising the stationary points located for the oxidation of dimethyl sulfide, but with a *para*-substituted phenyl group instead of one of the methyl groups. As well as phenyl itself, we have considered 4-methoxy- (electron donating) and 4-nitro- (electron withdrawing) substituted compounds.

Stationary points on the potential energy surface for the oxidation of each of the sulfides are shown in Figure 5-26. The general reaction profile is similar to the one for the oxidation of dimethyl sulfide.

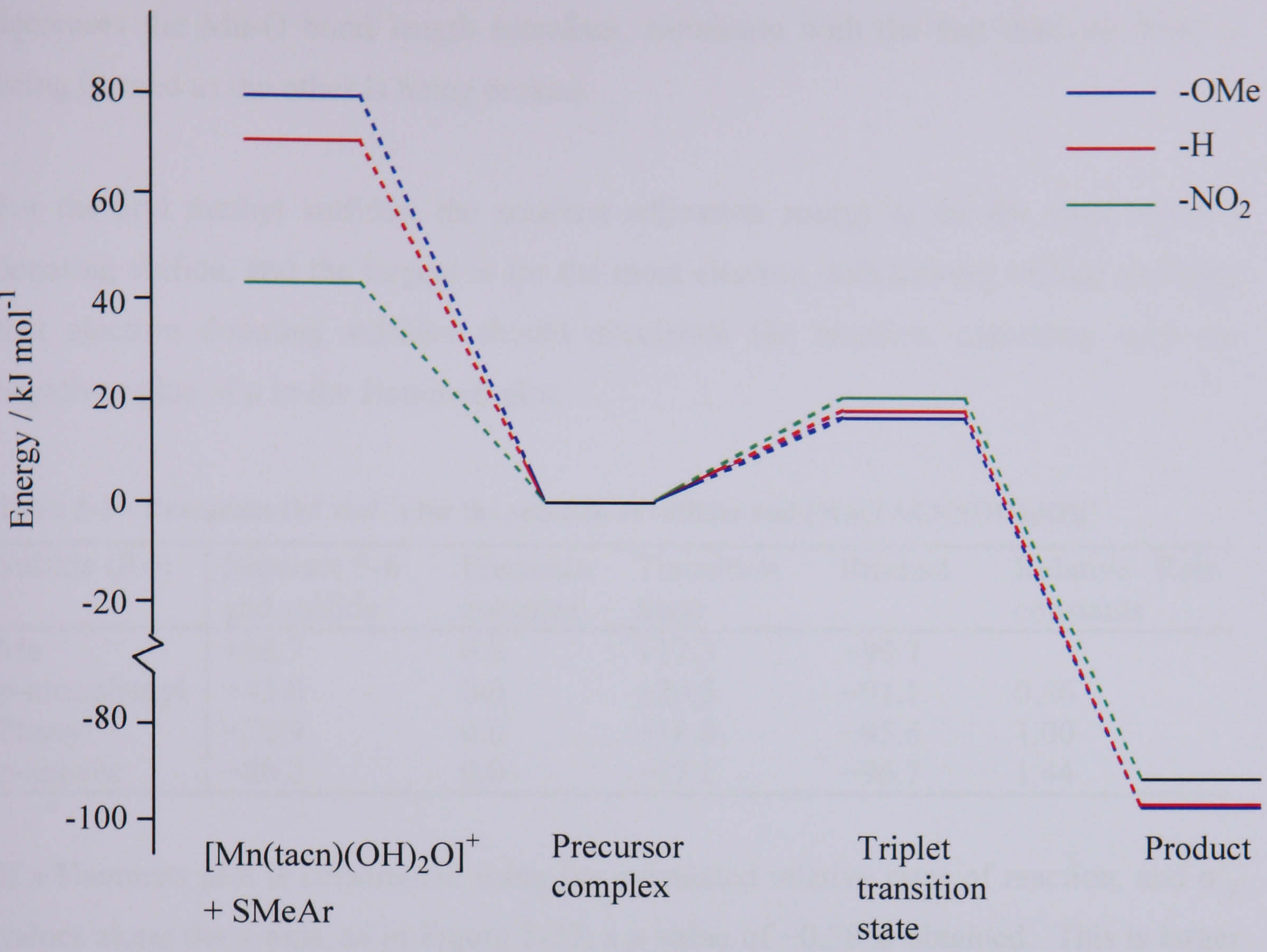

Figure 5-26 – PES for oxidation of substituted thioanisoles {original in colour}

The zero point for energy is taken as the energy of the precursor complex. In the first step, from the separated species to the precursor complex, the degree of stabilisation depends strongly on the substituent: the sulfide with the most electron donating substituent is most stabilised by the formation of the precursor complex, consistent with the electrophilic nature of **5-6**.

5.4.1 Transition State

The geometries of all the transition states are fairly similar,[†] and all have been characterised as true transition states by the presence of one imaginary frequency. The Mn-O[1] bond length increases as the sulfide becomes more electron withdrawing, and consistent with this, the S-O bond length is longest with the most electron withdrawing sulfide. This implies that there is an antagonistic effect, and as the S-O distance

[†] The geometries and Mulliken spin densities of all the transition states are summarised in the appendix, table A5-1

decreases the Mn-O bond length increases, consistent with the fact that one bond is being formed as the other is being broken.

For the aryl methyl sulfides, the smallest activation energy is for the most electron donating sulfide, and the largest is for the most electron withdrawing sulfide implying that electron donating sulfides should accelerate the reaction, consistent with the negative value of ρ in the Hammett plot.

Table 5-1 – Energetics (kJ mol^{-1}) for the reaction of sulfides and [Mn(TACN)(OH)$_2$(O)]$^+$

Sulfide (R=)	Separate **5-6** and sulfide	Precursor complex	Transition State	Product	Relative Rate constants
Me	+68.7	0.0	+17.3	−99.7	
p-nitrophenyl	+43.0	0.0	+20.5	−91.1	0.36
Phenyl	+70.9	0.0	+18.0	−95.6	1.00
p-anisole	+80.2	0.0	+17.1	−96.7	1.44

If a Hammett plot is constructed using the calculated relative rates of reaction, and σ^+_p values along the x-axis, as in Figure 5-27, a ρ value of −0.38 is obtained. This is larger (in magnitude) than found experimentally, but is still rather small and shows that the substituents do not have a large influence on sulfide oxidation. The 'line of best fit' has a rather poor R^2 value, but given that only three points are plotted this is not unduly worrying. If the σ_p values are used instead, the line of best fit has an R^2 value of 1.0, and a ρ value of −0.57, larger still than the experimental values but leading to the same conclusions.

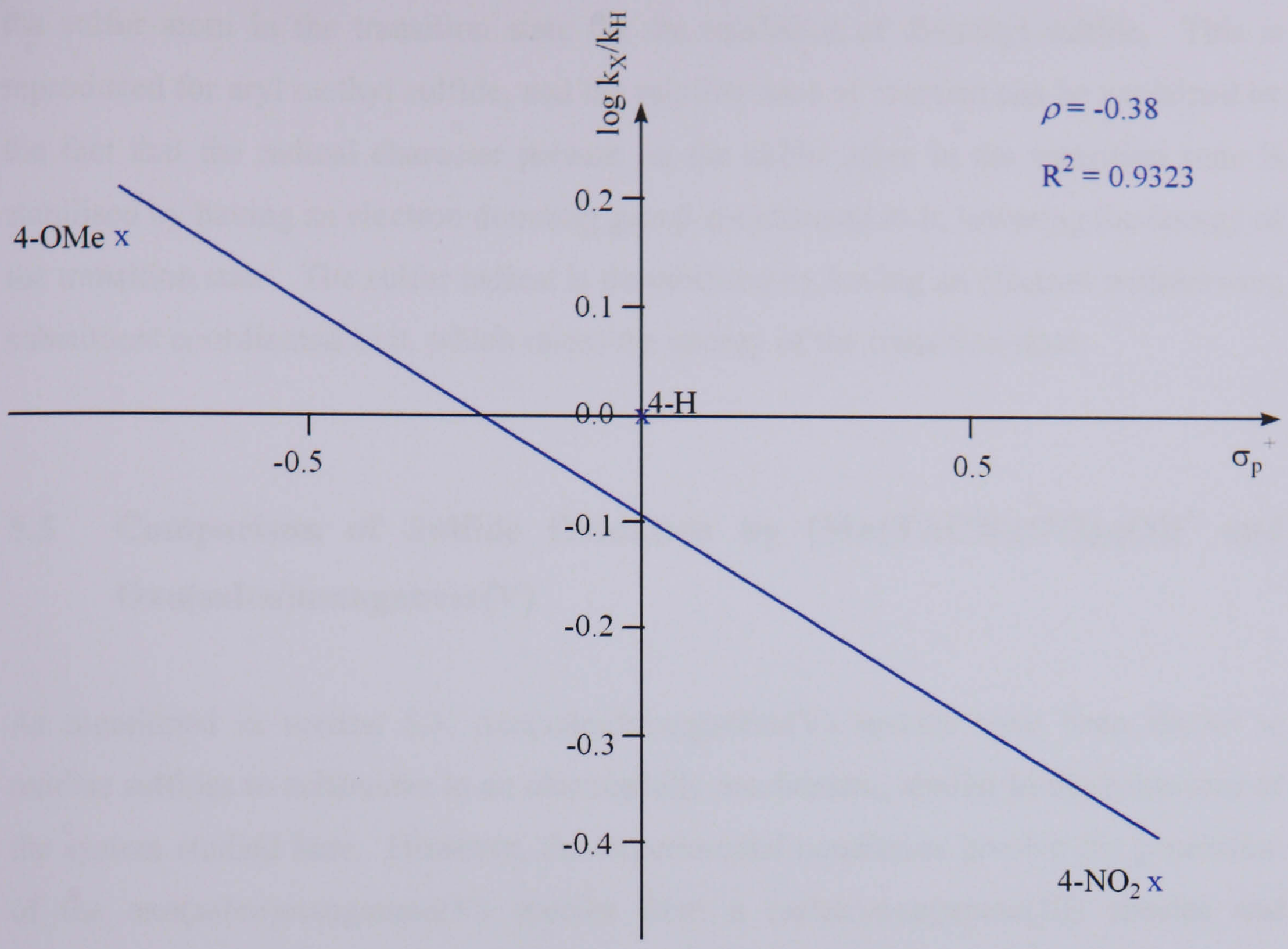

Figure 5-27 – Hammett plot of the theoretical data for the oxidation of sulfides by $[Mn(TACN)(OH)_2(O)]^+$ {original in colour}

Although the activation energy differences for the sulfides are small, the exponential dependence of the rate on activation energy (Arrhenius equation, $k = Ae^{-E_a/RT}$) means that this can translate into significant changes. In table 5-1 we define the relative rate constant, k_{rel}, as

$$k_{rel} = \frac{k_{ArX}}{k_{Ar}} = e^{\frac{-\Delta E_a}{RT}}$$

where k is the rate constant. E_a is the activation energy, R is the gas constant = 8.314 J K^{-1} mol^{-1} and T was taken as 298 K. We have taken the activation energy to be the difference in potential energy between the precursor complex and the transition state. We are relying on the assumption that the ZPE and ΔS are approximately constant in all cases.

We showed earlier that the proposed active oxidant, **5-6**, has an electrophilic oxo group with radical character, and there is a build up of radical character and formal charge on

the sulfur atom in the transition state for the oxidation of dimethyl sulfide. This is reproduced for aryl methyl sulfide, and the relative rates of reaction can be explained by the fact that the radical character present on the sulfur atom in the transition state is stabilised by having an electron donating group coordinated to it, lowering the energy of the transition state. The sulfur radical is destabilised by having an electron withdrawing substituent coordinated to it, which raises the energy of the transition state.

5.5 Comparison of Sulfide Oxidation by $[Mn(TACN)(OH)_2(O)]^+$ and Oxo(salen)manganese(V)

As mentioned in section 5.1, oxo(salen)manganese(V) species have been shown to oxidise sulfides to sulfoxides in an electrophilic mechanism, similar to the behaviour of the system studied here. However, the experimental conditions involve the generation of the oxo(salen)manganese(V) species from a (salen)manganese(III) species and iodosobenzene (an oxygen transfer agent) and not from H_2O_2, as in the case studied here. Rajagopal and co-workers observe yields of about 70% sulfoxide from the stoichiometric quantities of the reagents, and very little sulfone, unlike in the present system where sulfoxide and sulfone are obtained in similar yields. We attribute this to the different reaction conditions, and the fact that sulfoxide oxidation most likely occurs via a different mechanism and possibly a different oxidant.[45,54]

The reaction of *para*-substituted thioanisoles with both the oxo(salen)manganese(V) oxidant, and **5-6** gives a Hammett plot with a negative slope, indicative of an electrophilic oxidant and a build up of positive charge on the sulfur atom in the transition state. However, the magnitude of ρ is much larger for the salen complex, -1.86 (correlated with σ_p) compared to -0.28 (σ^+) for the TACN complex, suggesting that $[Mn(TACN)(OH)_2(O)]^+$ is a much more reactive and less selective oxidant than oxo(salen)manganese(V).[45,54]

Rajagopal and co-workers have shown that the mechanism for sulfide oxidation by oxo(salen)manganese(V) is second order overall, and first order with respect to both the substrate and the oxo complex. Two mechanisms for sulfide oxidation have been

proposed and are shown in Figure 5-28. Neither of these is the same as we have found for the oxidation of sulfides by **5-6**, although the first is similar, but instead of isolated single electron transfer, a precursor complex is formed at the same time.[43] Mechanism 1 is favoured by the authors for the oxidation of sulfides by oxo(salen)manganese(V).

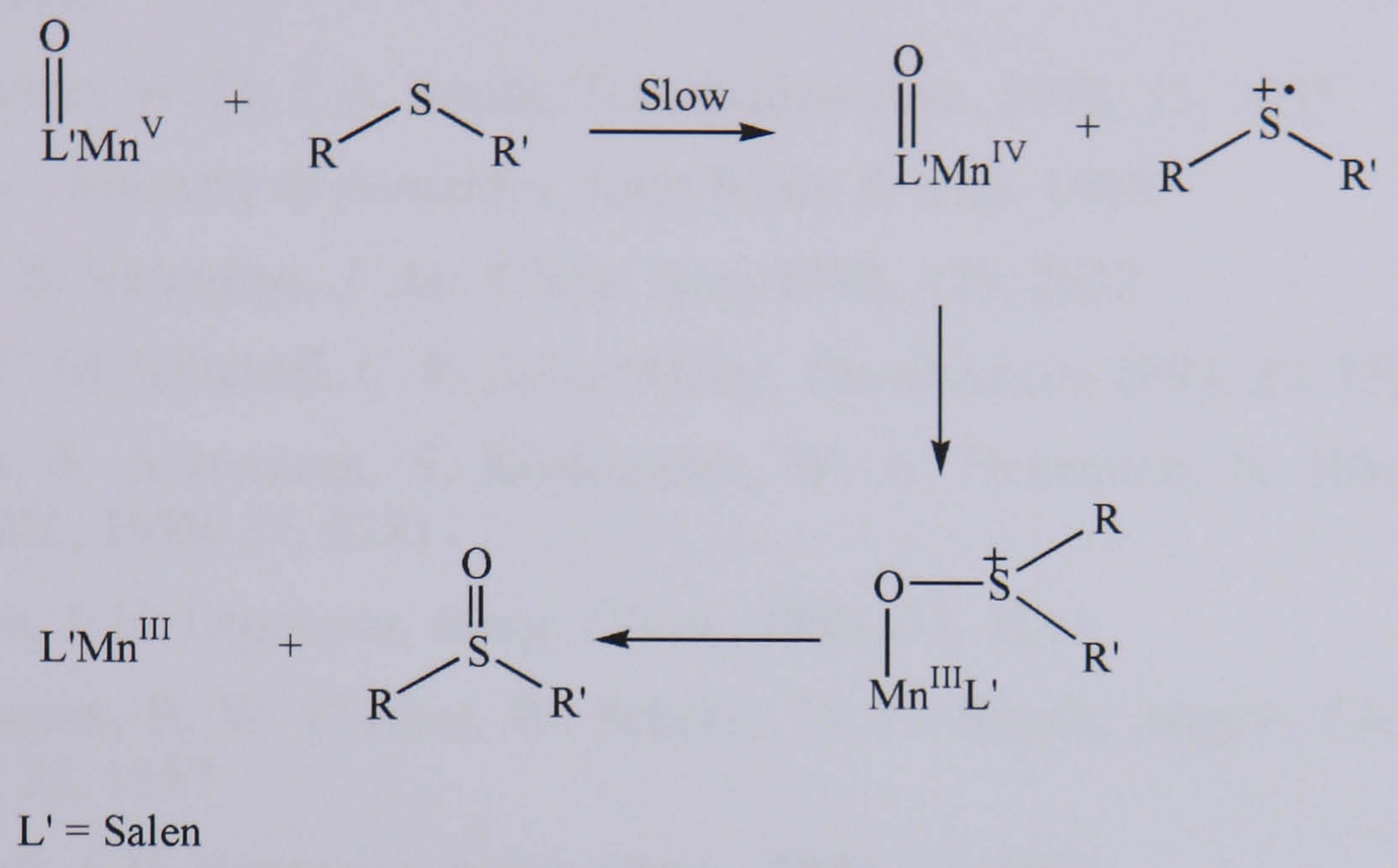

Figure 5-28 – Mechanism for sulfide oxidation by oxo(salen)manganese(V)

Rajagopal and co-workers also showed that by adding electron donating groups to the salen ligand, and thereby stabilising the oxomanganese(V) species, the rate of reaction is decreased, consistent with a reduction in charge at the metal centre. Although similar experiments have not been done with the TMTACN ligand, (either experimentally or computationally) it is likely that a similar effect would be observed.

5.6 References

1) J. R. Lindsay Smith, J. Murray, P. H. Walton, T. R. Lowdon, *Tetrahedron Lett.*, **2006**, *47*, 2005

2) J. Brinksma, R. La Crois, B. L. Feringa, M. I. Donnoli, C. Rosini, *Tetrahedron Lett.*, **2001**, *42*, 4049

3) D. H. R. Barton, W. Li, J. A. Smith, *Tetrahedron Lett.*, **1998**, *39*, 7055

4) S. Patai, *The chemistry of peroxides*, John Wiley & sons, **1983**

5) M. Selke, J. S. Valentine, *J. Am. Chem. Soc.*, **1998**, *120*, 2652

6) W. Adam, C. M. Mitchell, C. R. Saha-Möller, *Tetrahedron*, **1994**, *50*, 13121

7) P. Gisdakis, S. Antonczak, S. Kösklmeier, W. A. Herrmann, N. Rösch, *Angew. Chem. Int. Ed.*, **1998**, *37*, 2211

8) K. N. Brown, J. H. Espenson, *Inorg. Chem.*, **1996**, *35*, 7211

9) W. A. Hermann, R. W. Fischer, W. Scherer, M. U. Rauch, *Angew. Chem. Int. Ed. Eng.*, **1993**, *32*, 1157

10) K. A. Vassell, J. H. Espenson, *Inorg. Chem.*, **1994**, *33*, 5491

11) R. Huang, J. H. Espenson, *J. Org. Chem.*, **1999**, *64*, 6374

12) M. Bonchio, S. Calloni, F. Di Furia, G. Licini, G. Modena, S. Moro, W. A. Nugent, *J. Am. Chem. Soc.*, **1997**, *119*, 6935

13) G. Licini, M. Bonchio, G. Modena, W. A. Nugent, *Pure Appl. Chem.*, **1999**, *71*, 463

14) B. C. Gilbert, J. R. Lindsay Smith, M. S. Newton, J. Oakes, R. Pons I Prats, *Org. Biomol. Chem.*, **2003**, *1*, 1568

15) B. C. Gilbert, J. R. Lindsay Smith, A. Mairata I Payeras, J. Oakes, *Org. Biolmol. Chem.*, **2004**, *2*, 1176

16) B. C. Gilbert, N. W. J. Kamp, J. R. Lindsay Smith, J. Oakes, *J. Chem. Soc., Perkin Trans. 2*, **1998**, *9*, 1841

17) B. C. Gilbert, J. R. Lindsay Smith, A. Mairata I Payeras, J. Oakes, R. Pons I Prats, *J. mol. Catal. A*, **2004**, *219*, 265

18) D. E. De Vos, T. Brin, *Chem. Commun.*, **1996**, 917

19) C. Zondervan, R. Hage, B. L. Feringa, *Chem.. Commun.*, **1997**, 419

20) A. Berkessel, C. A. Sklorz, *Tetrahedron Lett.*, **1999**, *40*, 7965

21) G. B. Shul'pin, G. Süss-Fink, L. S. Shul'pina, *J. Mol. Catal. A.*, **2001**, *170*, 17

22) G. B. Shul`pin, G. V. Nizove, Y. N. Kozlov, I G. Pechenkina, *New J. Chem.*, **2002**, *26*, 1238

23) C. B. Woitiski, Y. N. Kozlov, D. Mandelli, G. V. Nizova, U. Schuchardt, G. B. Shul'pin, *J. Mol. Catal. A.*, **2004**, *222*, 103

24) D. Mandelli, J. B. Voitiski, U. Schuchardt, G. B. Shul`pin, *Chem. Nat. Com.*, **2002**, *38*, 243

25) J. Brinksma, L. Schmieder, G. van Vliet, R. Boaron, R. Hage, D. E. De Vos, P. L. Alsters, B. L. Feringa, *Tetrahedron lett.*, **2002**, *43*, 2619

26) G. B. Shul'pin, G. Süss-Fink, J. R. Lindsay Smith, *Tetrahedron*, **1999**, *55*, 5345

27) D. E. De Vos, B. F. Seld, M. Reynaers, Y. V. Subba Rao, P. A. Jacobs, *Tetrahedron Lett.*, **1998**, *39*, 3321

28) J. R. Lindsay Smith, G. B. Shul'pin, *Tetrahedron Lett.*, **1998**, *39*, 4909

29) R. Hage, J. E. Iburg, J. Kerschner, J. H. Koek, E. L. M. Lempers, R. J. Martens, U. S. Racheria, S. W. Russell, T. Swarthoff, M. R. P. van Vilet, J. B. Warnaar, L. van der Wolf, B. Krijnen, *Nature*, **1994**, *369*, 637

30) R. Hage, A. Lienke, *Angew. Chem. Int. Ed.*,**2006**, *45*, 206

31) F. M. MacDonnell, N. L. P. Fackler, C. Stern, T. V. O'Halloran, *J. Am. Chem. Soc.*, **1994**, *116*, 7431

32) T. J. Collins, R. D. Powell, C. Sledobnick, E. S. Uffelman, *J. Am. Chem. Soc.*, **1990**, *112*, 899

33) T. J. Collins, S. W. Gordon-Wylie, *J. Am. Chem. Soc*, **1989**, *111*, 4511

34) J. T. Groves, J. Lee, S. S. Marla, *J. Am. Chem. Soc.*, **1997**, *119*, 6269

35) N. Jin, J. T. Groves, *J. Am. Chem. Soc.*, **1999**, *121*, 2923

36) R. Zhang, M.Newcomb, *J. Am. Chem. Soc.*, **2003**, *125*, 12419

37) R. Zhang, J. H. Horner, M. Newcomb, *J. Am. Chem. Soc.*, **2005**, *127*, 6573

38) W. Nam, I. Kim, M. H. Lim, H. J. Choi, J. S. Lee, H. G. Jang, *Chem. Eur. J.*, **2002**, *8*, 2067

39) Z. Gross, G. Golubkov, L. Simkhovich, *Angew. Chem. Int. Ed.*, **2000**, *39*, 4045

40) B. S. Mandimutsira, B. Ramdhanie, R. C. Todd, H. L. Wang, A. A. Zareba, R. S. Czemuszewicz, D. P. Goldberg, *J. Am. Chem. Soc.*, **2002**, *124*, 15170

41) D. Feichtinger, D. A. Plattner, *Chem. Eur. J.*, **2001**, *7*, 591

42) N. S. Venkataramanan, G. Kuppuraj, S. Rajagopal, *Coord. Chem. Rev.*, **2005**, *249*, 1249

43) A. Chellamani, N. I. Alhaji, S. Rajagopal, R. Sevvel, C. Srinivasan, *Tetrahedron*, **1995**, *51*, 12677

44) A. Chellamani, P. Kulanthaipandi, S. Rajagopal, *J. Org. Chem.*, **1999**, *64*, 2232

45) A. Chellamani, N. M. I Alhaji, S. Rajagopal, *J. Chem. Soc., Perkin Trans. 2*, **1997**, 299

46) Y. G. Abashkin, S. K. Burt, *J. Phys. Chem. B*, **2004**, *108*, 2708

47) Gaussian 98, Revision A.11, M. J. Frisch, G. W. Trucks, H. B. Schlegel, G. E. Scuseria, M. A. Robb, J. R. Cheeseman, V. G. Zakrzewski, J. A. Montgomery, Jr., R. E. Stratmann, J. C. Burant, S. Dapprich, J. M. Millam, A. D. Daniels, K. N. Kudin, M. C. Strain, O. Farkas, J. Tomasi, V. Barone, M. Cossi, R. Cammi, B. Mennucci, C. Pomelli, C. Adamo, S. Clifford, J. Ochterski, G. A. Petersson, P. Y. Ayala, Q. Cui, K. Morokuma, P. Salvador, J. J. Dannenberg, D. K. Malick, A. D. Rabuck, K. Raghavachari, J. B. Foresman, J. Cioslowski, J. V. Ortiz, A. G. Baboul, B. B. Stefanov, G. Liu, A. Liashenko, P. Piskorz, I. Komaromi, R. Gomperts, R. L.

Martin, D. J. Fox, T. Keith, M. A. Al-Laham, C. Y. Peng, A. Nanayakkara, M. Challacombe, P. M. W. Gill, B. Johnson, W. Chen, M. W. Wong, J. L. Andres, C. Gonzalez, M. Head-Gordon, E. S. Replogle, and J. A. Pople, Gaussian Inc. Pittsburgh PA, USA

48) P. J. Stevens, J. F. Devlin, C. F. Chabalowski, M. J. Frisch, *J. Phys. Chem.*, **1994**, *98*, 11623

49) W. J. Hehre, R. Ditchfield, J. A. Pople, *J. Phys. Chem.*, **1972**, *56*, 2257

50) V. C. Quee-Smith, L. DelPizzo, S. H. Jureller, J. L. Kerschner, R. Hage, *Inorg. Chem.*, **1996**, *35*, 6461

51) Y. G. Abashkin, S. K. Burt, *Inorg. Chem.*, **2005**, *44*, 1425

52) A. Bondi, *J. Phys. Chem.*, **1964**, *68*, 441

53) M. Bonchio, O. Bortolini, G. Licini, S. Moro, W. A. Nugent, *Eur. J. Org. Chem.*, **2003**, 507

Chapter 6 – Sulfoxide Oxidation by $[Mn_2(TMTACN)_2(O)_3]^{2+}$

6.1 Introduction

In chapter 5 the mechanism of oxidation of sulfides by $[Mn_2(TMTACN)_2(O)_3]^{2+}$ and H_2O_2 was discussed, where electron donating substituents were found to accelerate the reaction by stabilisation of the developing positive charge on the sulfur centre. We now consider possible mechanisms for the oxidation of sulfoxides, where the experimental data suggest a quite distinct mechanism where the sulfur-containing species acts as an electrophile rather than a nucleophile.[1] Sulfoxides are, in general, less nucleophilic than their corresponding sulfides due to the electron withdrawing effect of the oxygen atom. The fact that the rates are comparable for the two classes of substrate is consistent with the presence of two or more competing mechanisms. Lindsay Smith and co-workers have proposed that oxidation of sulfoxides occurs via nucleophilic attack of a hydrogen peroxide molecule on a sulfoxide group coordinated to a Mn^{3+} centre (Figure 6-1).

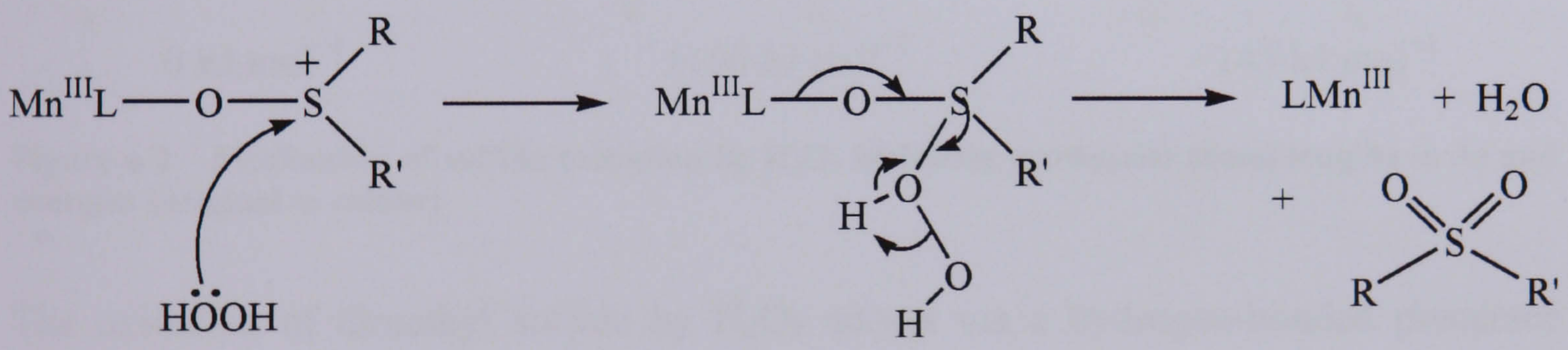

Figure 6-1 – Mechanism proposed by Lindsay Smith and co-workers for the oxidation of sulfoxides by H_2O_2 and Mn^{3+}

In this sense, the metal centre does not participate directly in the reaction, but instead acts as a Lewis acid catalyst. Experimentally it is known that the oxidation of sulfoxides is accelerated by base but oxidation of sulfides is not affected.[2] This is due to the deprotonation of hydrogen peroxide leading to increased nucleophilicity of the peroxide group, which is then able to attack the sulfur atom on the sulfoxide. We postulate that the Mn catalyst can, rather than deprotonating the hydrogen peroxide to increase its nucleophilicity relative to the sulfoxide, bind to the oxygen atom of sulfoxide and therefore increase the electrophilicity of the sulfur centre. In order to

explore whether this type of mechanism can account for the observed kinetics, we have first considered the oxidation of sulfides and sulfoxides by H_2O_2 in the presence of a generic Lewis acid catalyst (H^+).

6.2 Oxidation of Sulfides and Sulfoxides by H_2O_2

In this section we first consider the energetics of sulfide and sulfoxide oxidation by free H_2O_2, and then consider the influence of an acid catalyst. All geometries and energies have been calculated by DFT with the B3LYP functional and the 6-31G(d,p) basis set.

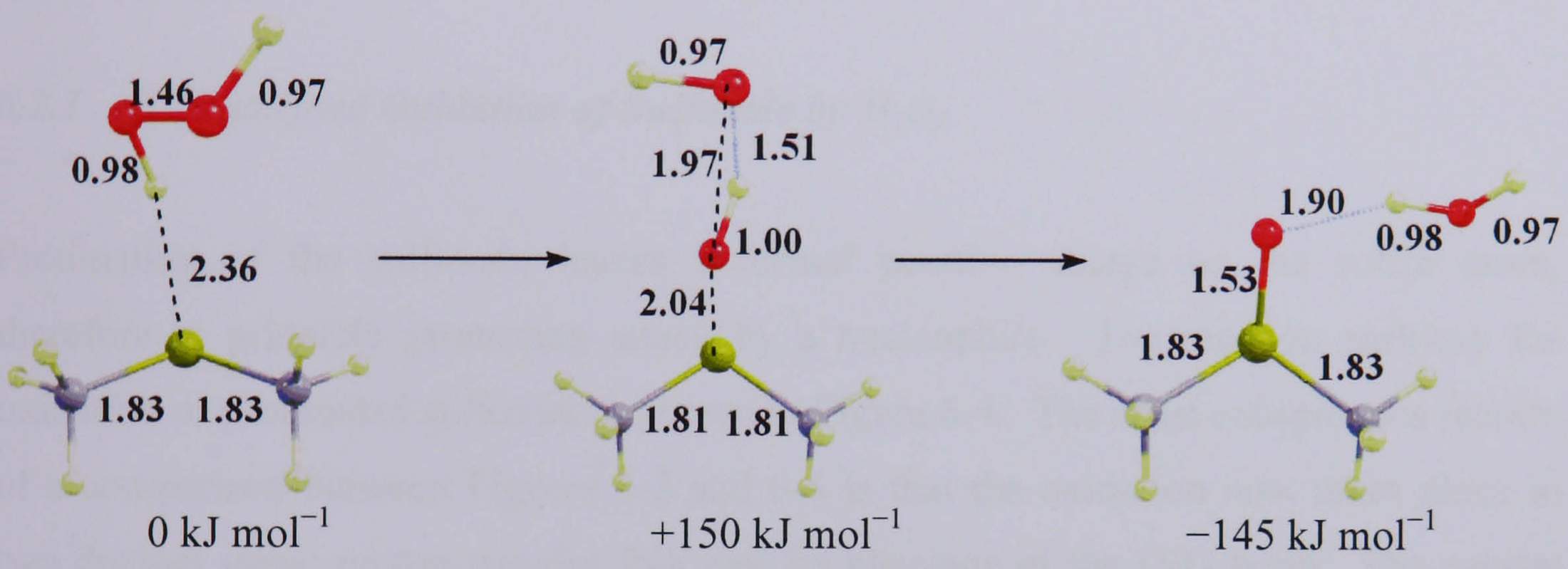

Figure 6-2 – Mechanism of sulfide oxidation by H_2O_2 including geometries (bond lengths in Å) and energies {original in colour}

The oxidation of dimethyl sulfide by H_2O_2 occurs via a hydrogen-bonded precursor complex, which then decomposes to dimethyl sulfoxide and water with a barrier of 150 kJ mol^{-1} – too high for the reaction to proceed at room temperature. The transition state involves significant donation of charge from the sulfur lone pair to the O-O σ* orbital, with concomitant migration of a proton to the distal oxygen centre. The corresponding process for the sulfoxide species is qualitatively similar, with a somewhat larger barrier of +169 kJ mol^{-1}, consistent with the lower nucleophilicity of this species.

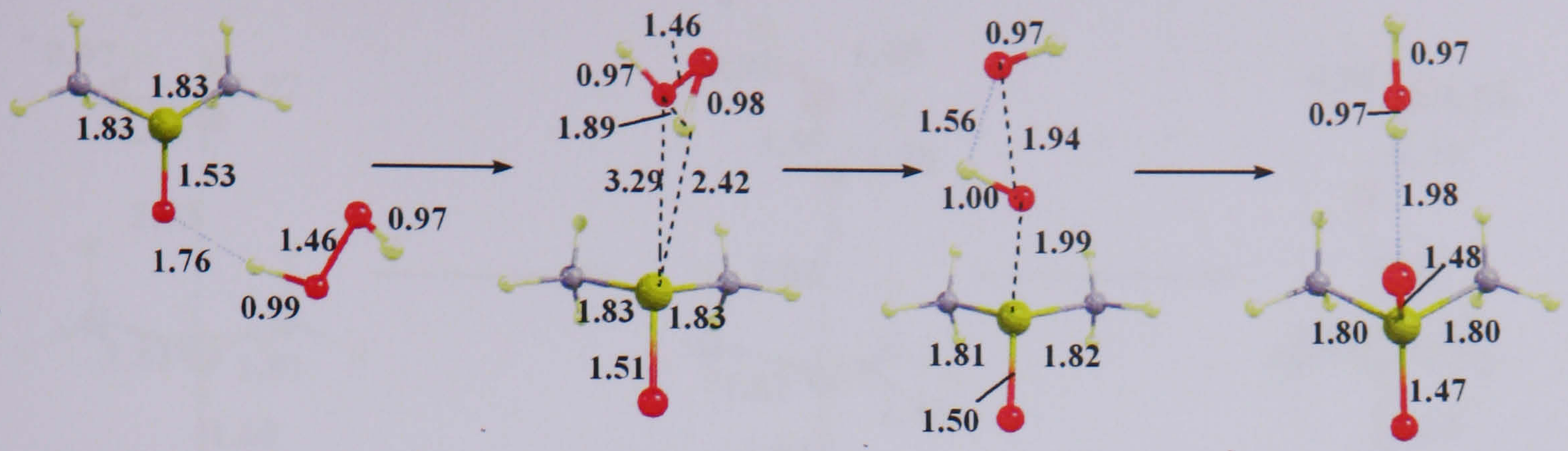

Reactants

$E = 0$ kJ mol^{-1}

High energy arrangement of reactants

TS

$E = +169$ kJ mol^{-1}

Product

$E = -206$ kJ mol^{-1}

Figure 6-3 – Geometries (bond lengths in Å) and energies for the uncatalysed oxidation of DMSO by H_2O_2 {original in colour}

6.2.1 H^+ Catalysed Oxidation of Sulfoxide by H_2O_2

Protonation of the sulfoxide leaves a formal positive charge on the sulfur atom, therefore in principle promoting attack by a nucleophile. The reaction pathway for oxidation of protonated sulfoxide is shown in Figure 6-4. The most conspicuous feature of a comparison between Figures 6-3 and 6-4 is that the oxidation now takes place in two distinct steps: proton transfer followed by cleavage of the O-O bond. The energy barrier to the proton transfer is high (>200 kJ mol^{-1}) and the barrier to O-O cleavage (238 kJ mol-1) is even higher, suggesting that Lewis acid catalysis will retard, rather than accelerate, the reaction. This observation is, of course, consistent with the dominant electron transfer pathway in the transition state which involves charge donation from the sulfur lone pair to the hydrogen peroxide, and not vice versa.

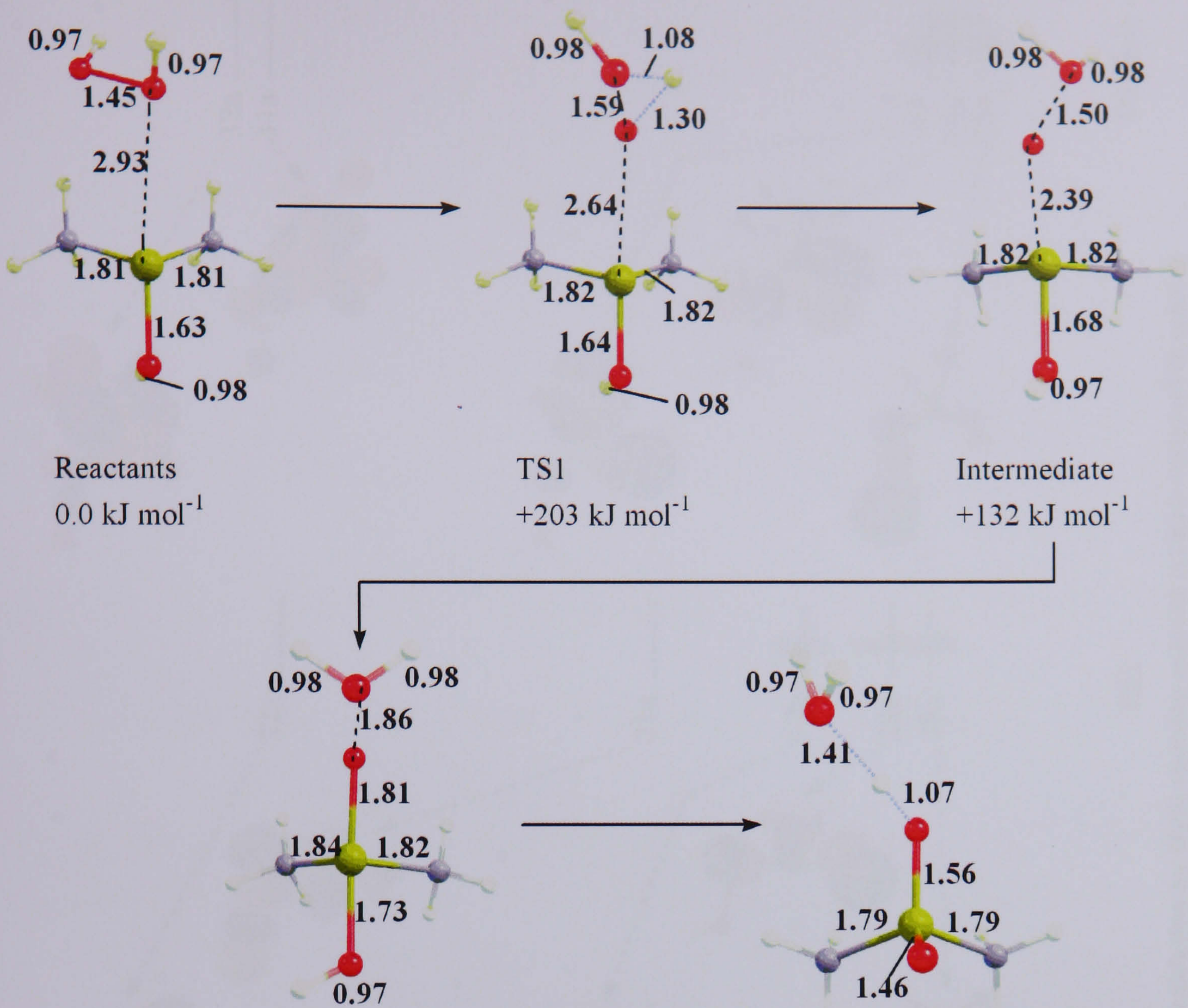

Figure 6-4 – Geometries (bond lengths in Å) and energies for the proton catalysed oxidation of DMSO by H_2O_2 {original in colour}

Following the proton transfer step, the geometry around the sulfur atom (in the intermediate and TS2) is trigonal bipyramidal with a vacant equatorial site, rather than the tetrahedral geometry of the product, and has an O-S-O angle of 176°. As the O-O bond is broken, the sulfur atom becomes more tetrahedral in geometry, until the product has an O-S-O angle of 116°. The reasons for this can be explained by comparing the electronic structures of the different species (Figure 6-5). We see that the HOMO of the intermediate and transition state (30a in both cases) includes a large proportion of the sulfur lone pair, but no such orbital is found in the product.

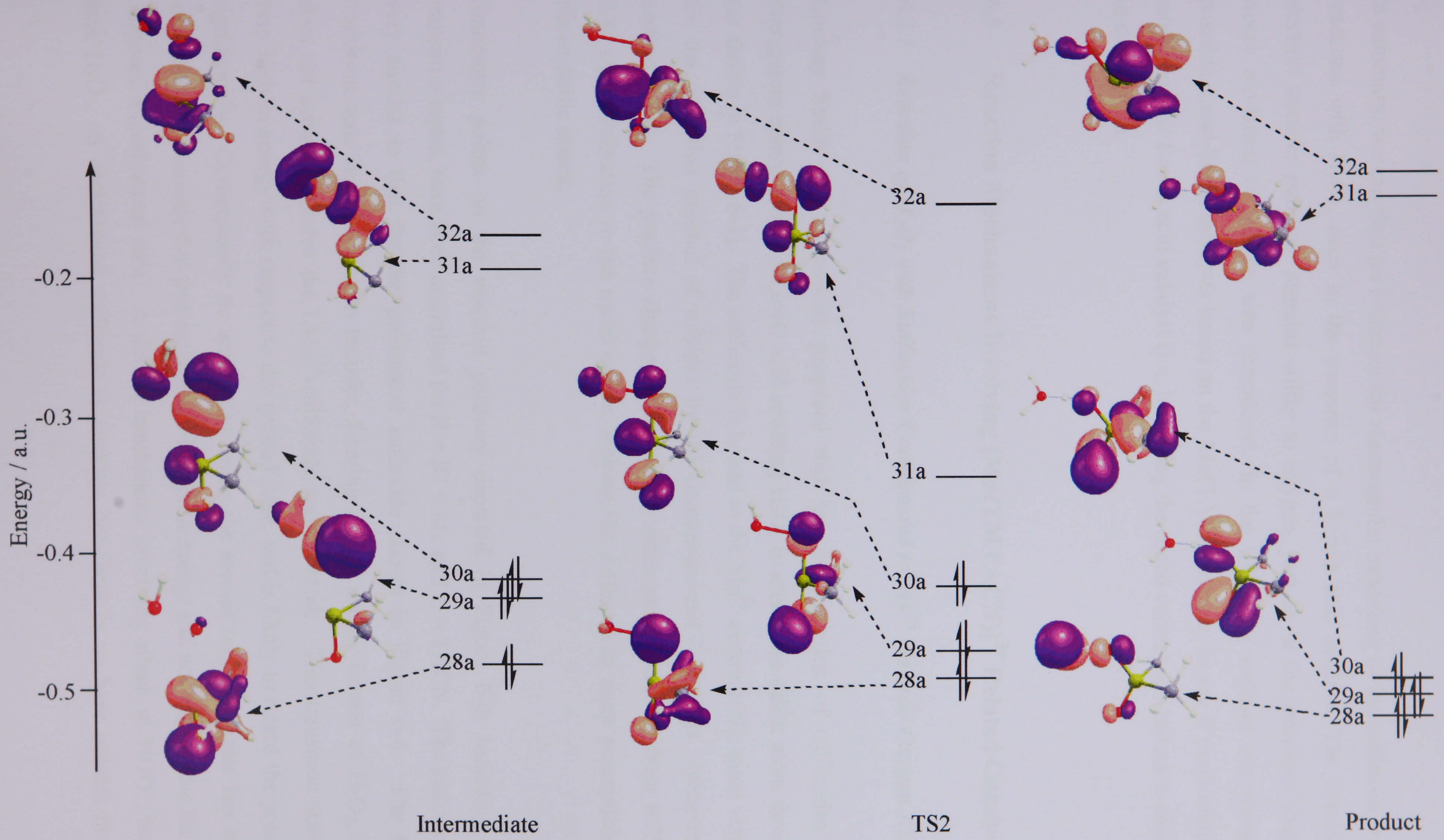

Figure 6-5 - MO diagrams for the intermediate, TS2 and product of DMSO-H oxidation by H_2O_2 showing selected orbitals {original in colour}

In summary, we can find no evidence for electrophilic behaviour of the sulfoxide in its reactions with H_2O_2, even in the presence of a Lewis acid catalyst. The dominant electron transfer pathway remains sulfur to oxygen, just as in the previous chapter where oxidation of sulfide was considered. In the following sections we consider possible metal-based catalysts based on the Mn(TACN) system, to see if more realistic models of the Lewis acid catalyst (i.e. involving the metal centre) can induce a change in mechanism.

6.3 Reaction Mechanisms Involving $[Mn(TMTACN)]^{3+}$ Related Catalysts

6.3.1 Reaction of H_2O_2 with Sulfoxides Coordinated to Mn^{3+} via their Oxygen Atom

Lindsay Smith and co-workers proposed that for the oxidation of sulfoxides the manganese centre acts as a Lewis acid enabling H_2O_2 to attack the sulfur atom directly (as shown in Figure 6-1). The sulfoxide is bound to the Mn^{3+} centre in the same way as for the oxidation product of sulfides by the oxomanganese(V) species (chapter 5, section 5.3.4). The positive charge density at the sulfur atom increases from 0.75 to 0.84 on coordination to the metal centre, making the sulfur atom more susceptible to nucleophilic attack.

Stationary points on the reaction pathway depicted in Figure 6-6, including the transition states, have been optimised for R = R' = Me and L = TACN. The pathway is very similar to that for the protonated sulfoxide shown in Figure 6-4. The first transition state involves proton transfer, forming a high energy isomer of H_2O_2, and does not actually involve the LMn^{3+}-sulfoxide species at all. This transition state is very high in energy with respect to the ground state, and is likely to retard the process significantly. Consequently no attempt to locate the second transition state has been made and we conclude that this mechanism is high in energy and not responsible for the observed experimental data. A similar mechanism involving attack of HOO^-, rather than H_2O_2, on coordinated sulfoxide is possible but there is no base present in the

system to deprotonate the hydrogen peroxide so it is not expected to occur under the reaction conditions used.

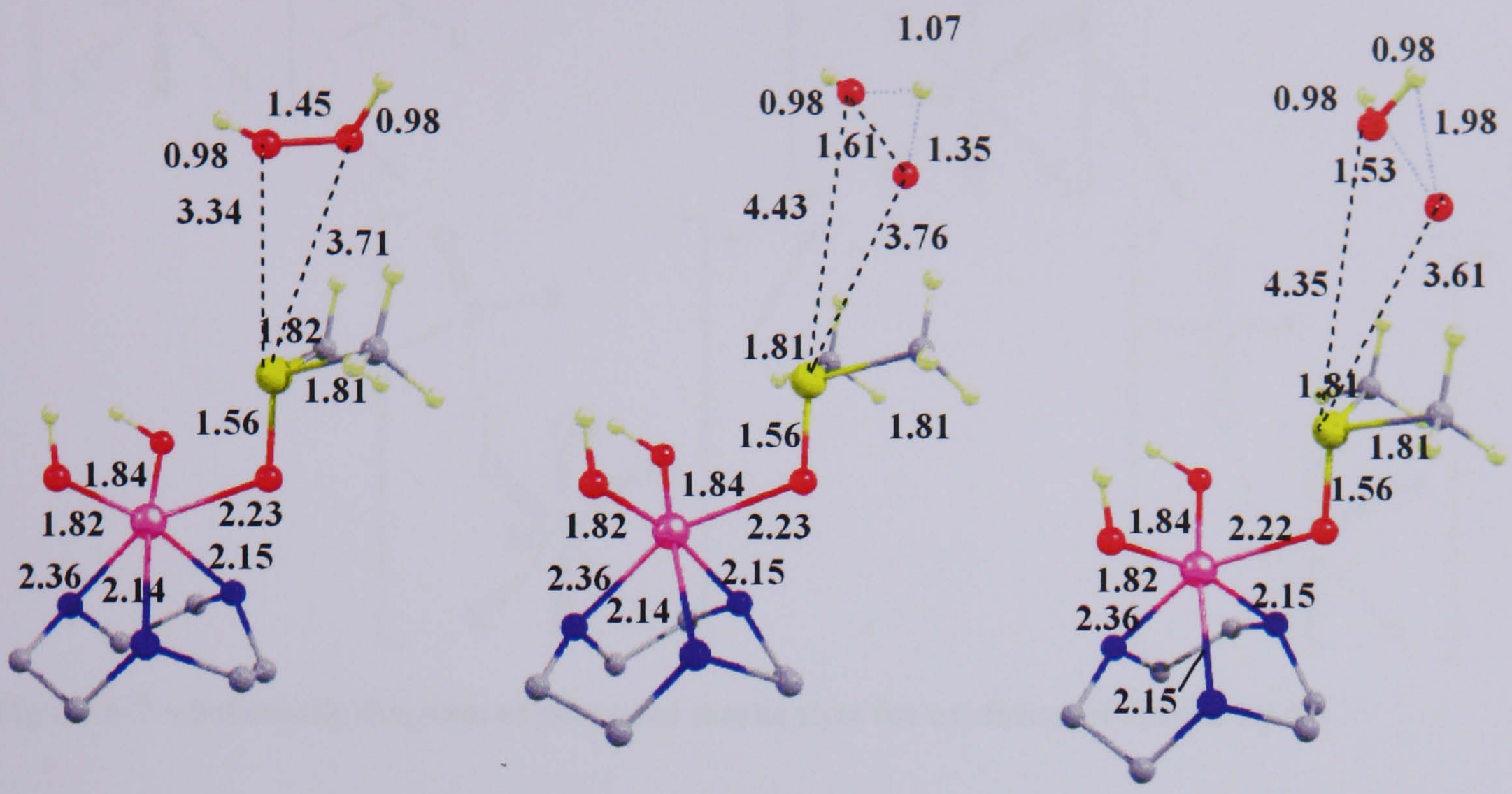

0 kJ mol^{-1} +216 kJ mol^{-1} +175 kJ mol^{-1}

Figure 6-6 – Structures and energies of the reagents, transition state and product for attack of DMSO by H_2O_2 {original in colour}

6.3.2 Oxidation of Sulfoxides by [Mn(TACN)(OH)$_2$(O)]$^+$

In chapter 5, we showed that the oxidation of sulfides could occur via a low energy transition state when the oxidant was the oxomanganese(V) species $[Mn(TACN)(OH)_2(O)]^+$ **(5-6)**. This oxidant is formed in catalytic amounts, and some will still be present (or regenerated) in solution following release of the sulfoxide and so could, in principle, also catalyse the second oxidation step. However, it is worth noting that due to their reduced nucleophilicity, sulfoxides are usually much less reactive than sulfides with the same oxidant.

The reaction pathway calculated for sulfoxide oxidation by $[Mn(TACN)(OH)_2(O)]^+$ was modelled on the mechanism found for sulfide oxidation, and is shown schematically in Figure 6-7. Once again, each stationary point on the PES was optimised and characterised by calculating the vibrational frequencies. After evaluation of the reaction pathway for DMSO, stationary points were reoptimised for *para*-substituted aryl methyl sulfoxides, and the energies for the pathway for each substituent were compared.

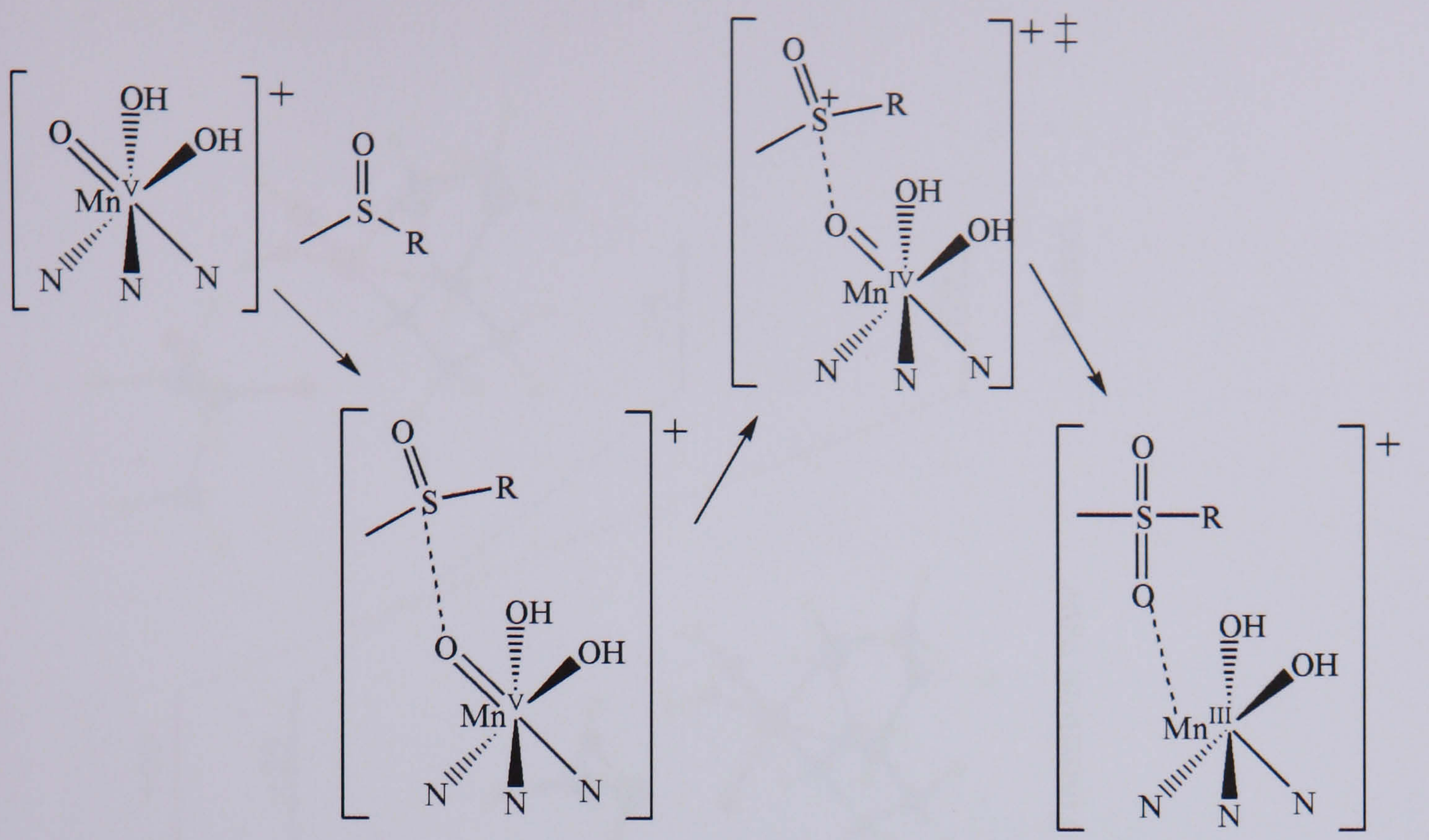

Figure 6-7 – Schematic diagram of proposed mechanism for oxidation of DMSO by 5-6

The reaction pathway for the oxidation of sulfoxides by $[Mn(TACN)(OH)_2O]^+$ mirrors that of sulfide oxidation in that a precursor complex is formed, which reacts via a transition state to give a sulfone product weakly coordinated to $[Mn(TACN)(OH)_2]^+$. The nature of each species is discussed in turn then the overall reaction mechanism is discussed. Finally, the mechanisms for sulfide and sulfoxide oxidation will be compared.

6.3.3 Potential Energy Surface

The potential energy surface for the oxidation of DMSO by **5-6** is shown in Figure 6-8. It follows a similar pattern to the PES of sulfide oxidation although the energetics are slightly different. The triplet surface again lies lowest in energy until after the transition state, and then a change in spin state occurs to yield a quintet product. The barrier for the rate-limiting electron-transfer step is +29 kJ mol^{-1} compared to +17 kJ mol^{-1} for the corresponding sulfide, suggesting a dramatic retardation in rate that is not apparent in the experimental data.

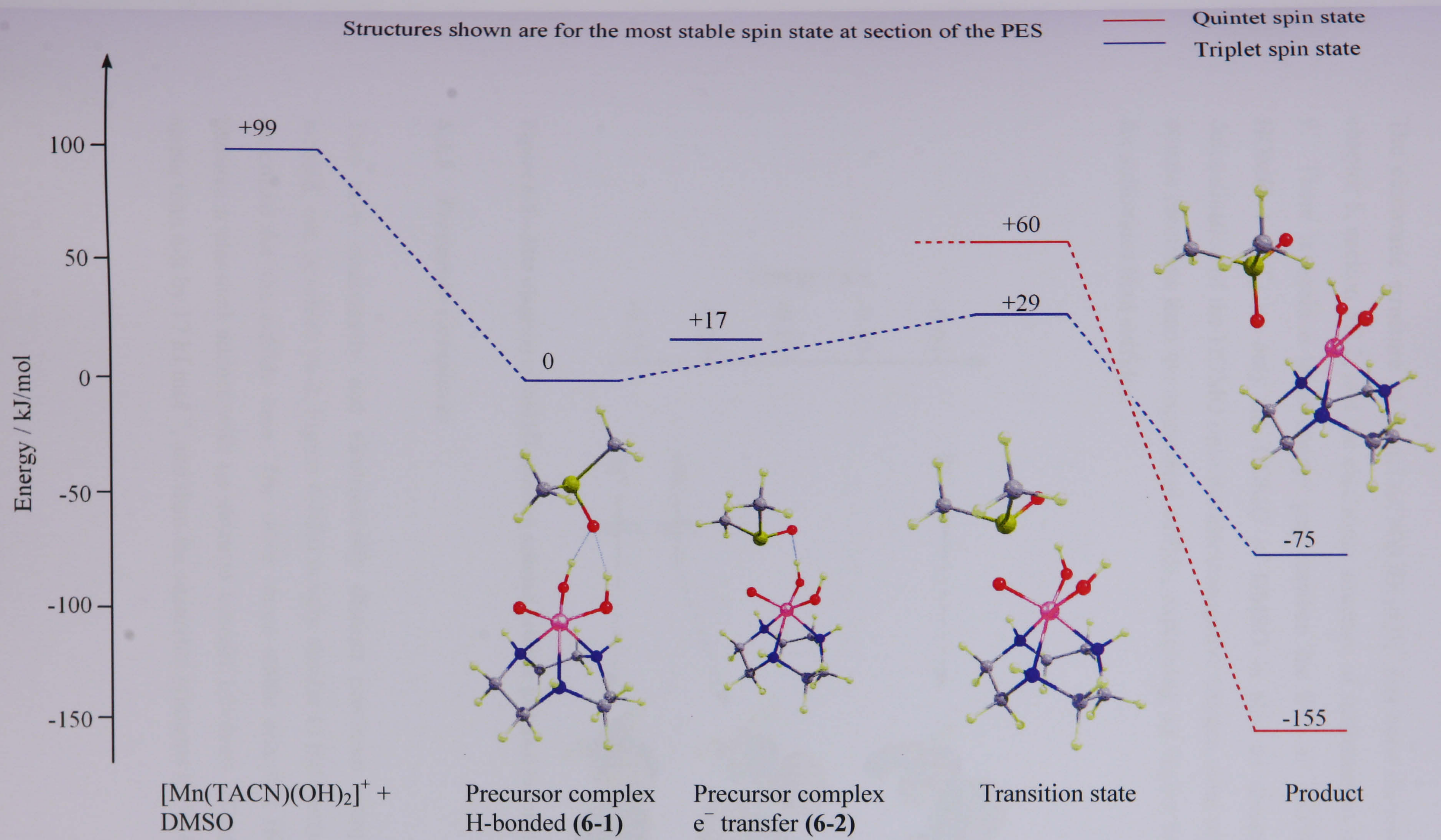

Figure 6-8 – Chart showing the PES for the oxidation of DMSO by (5-6) {original in colour}

6.3.4 Isolated Reactants

The electronic structure of $[Mn(TACN)(OH)_2(O)]^+$ has been discussed extensively in chapter 5, section 5.2.2, and the electronic structure of sulfoxides is shown in Figure 6-9. There is again a large energy gap between the S-O π* HOMO (14a') and the HOMO−1 (7a") so only the HOMO of DMSO is able to donate electrons. The delocalisation of the HOMO onto the electronegative oxygen atom makes it less able to donate electrons than the equivalent sulfide, explaining the higher barrier to oxidation for sulfoxides than sulfides.

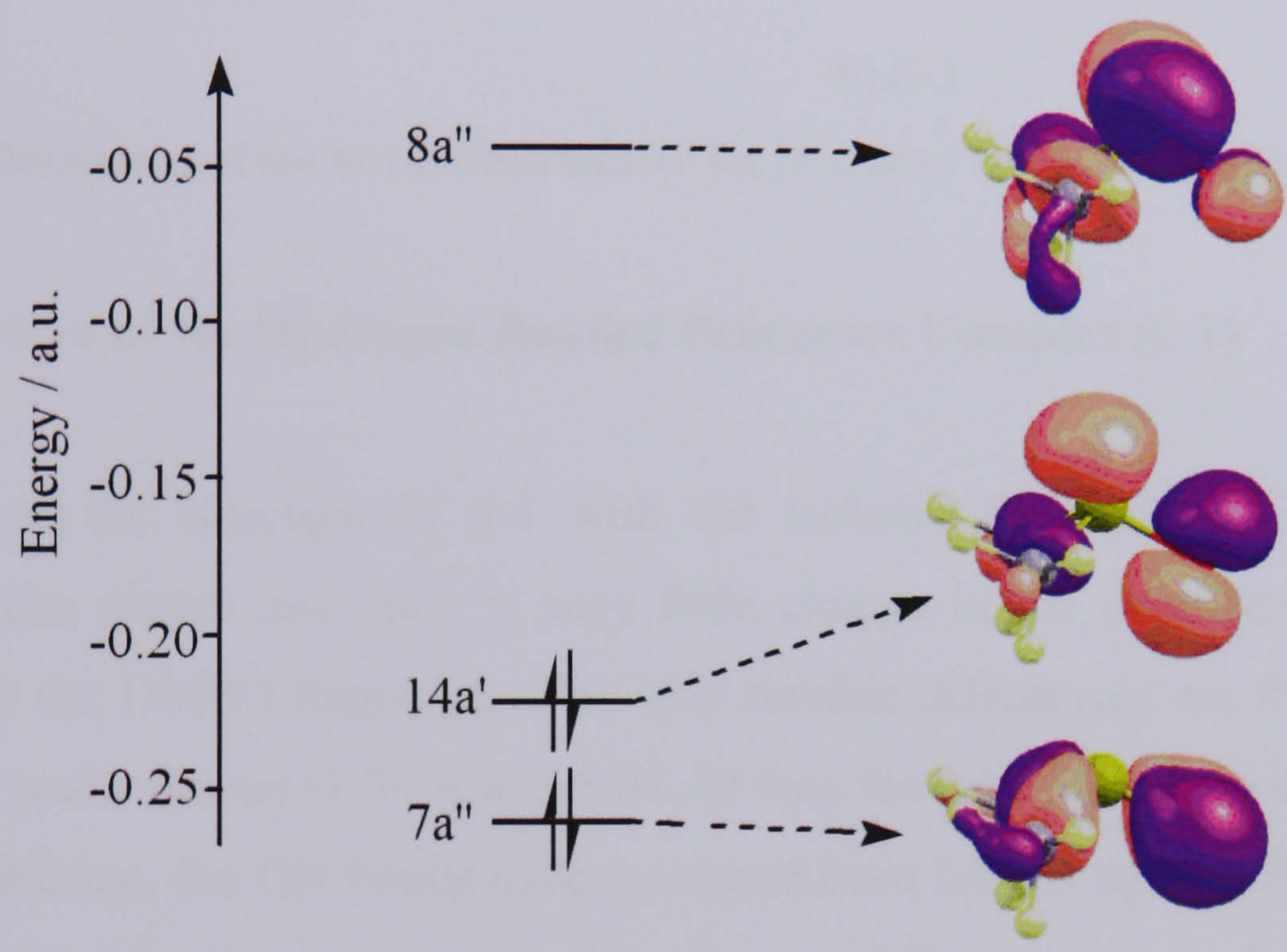

Figure 6-9 – MO diagram of DMSO showing selected orbitals {original in colour}

6.3.5 Precursor Complexes

Two both structurally and electronically distinct precursor complexes have been located, one of which (**6-2**, Figure 6-10b) is very similar to the electron-transfer adduct described for the sulfide case. The other, more stable complex (**6-1**, Figure 6-10a) features a classical adduct with no electron transfer involved Complex **6-1** is more stable than **6-2** by 17 kJ mol^{-1}, and than the separated reactants by 99 kJ mol^{-1}.

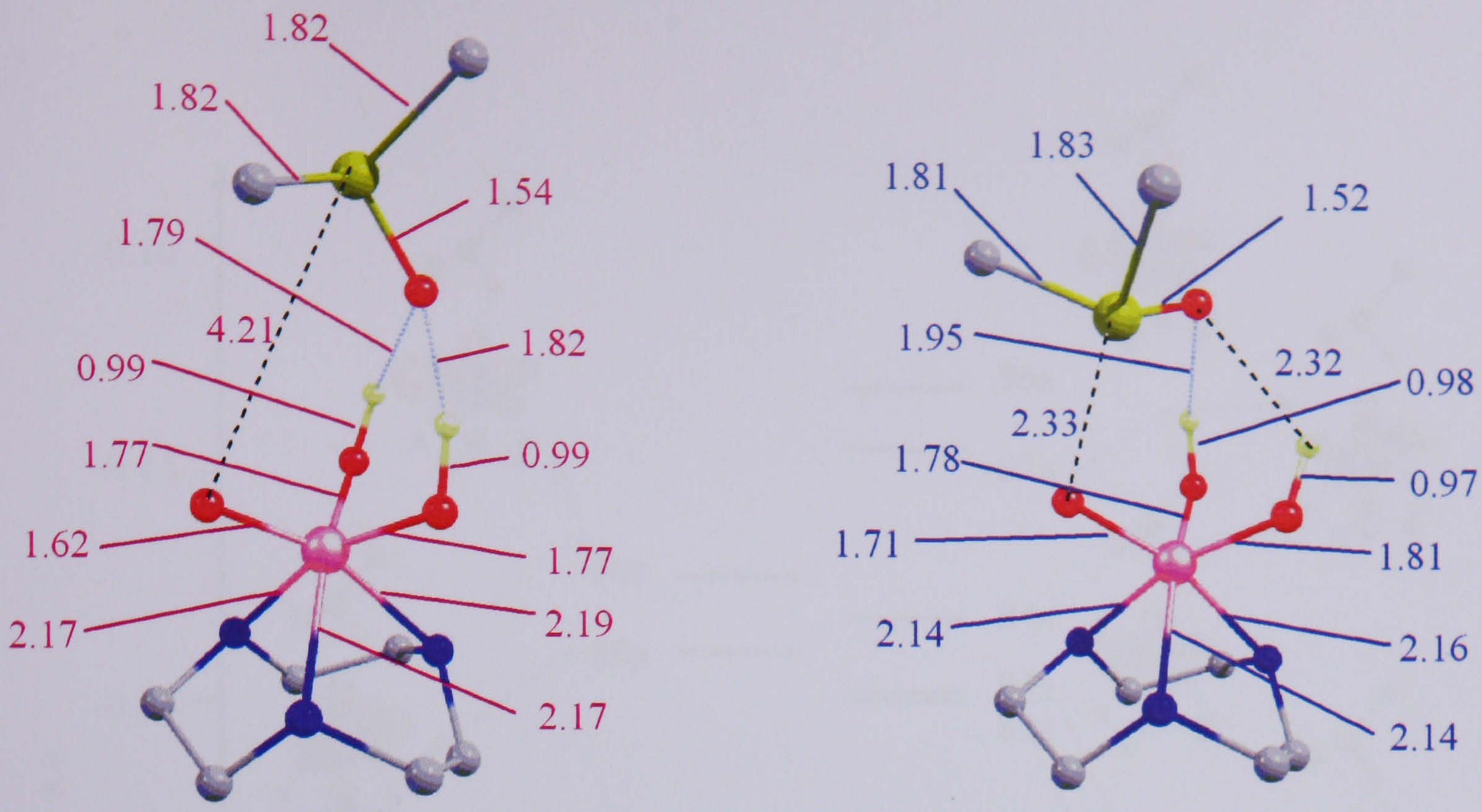

a) **6-1** b) **6-2**

Figure 6-10 – Geometries of the two minima located for precursor complexes {original in colour}

6.3.5.1 Structure of the Hydrogen Bonded Precursor Complex (6-1)

Comparison of the structure of **6-1** with the isolated $[Mn(TACN)(OH)_2(O)]^+$ and DMSO moieties shows that there is very little change in the geometry of either the manganese or the DMSO fragment. The only notable differences are that the SO-HO distances are much shorter (1.79 Å and 1.84 Å) than the sum of the van der Waals radii (2.72).[3] In addition, the OH bonds have increased from 0.97 Å to 0.99 Å, indicative of the hydrogen bonding that is occurring. The large stabilisation energy for **6-1** achieved on forming the precursor complex from the isolated sulfoxide and **5-6** can be largely attributed to the fact that the charge of the manganese complex is +1 and so there will be an electrostatic interaction between the sulfoxide and this complex. In addition, the oxygen atom on the sulfoxide forms strong hydrogen bonds to the hydroxide groups coordinated to Mn. The electronic structure and spin densities of **6-1**, shown in Figures 6-11 and 6-12, confirm that no significant electronic rearrangement has occurred compared to the isolated $[Mn(TACN)(OH)_2(O)]^+$ complex and DMSO.

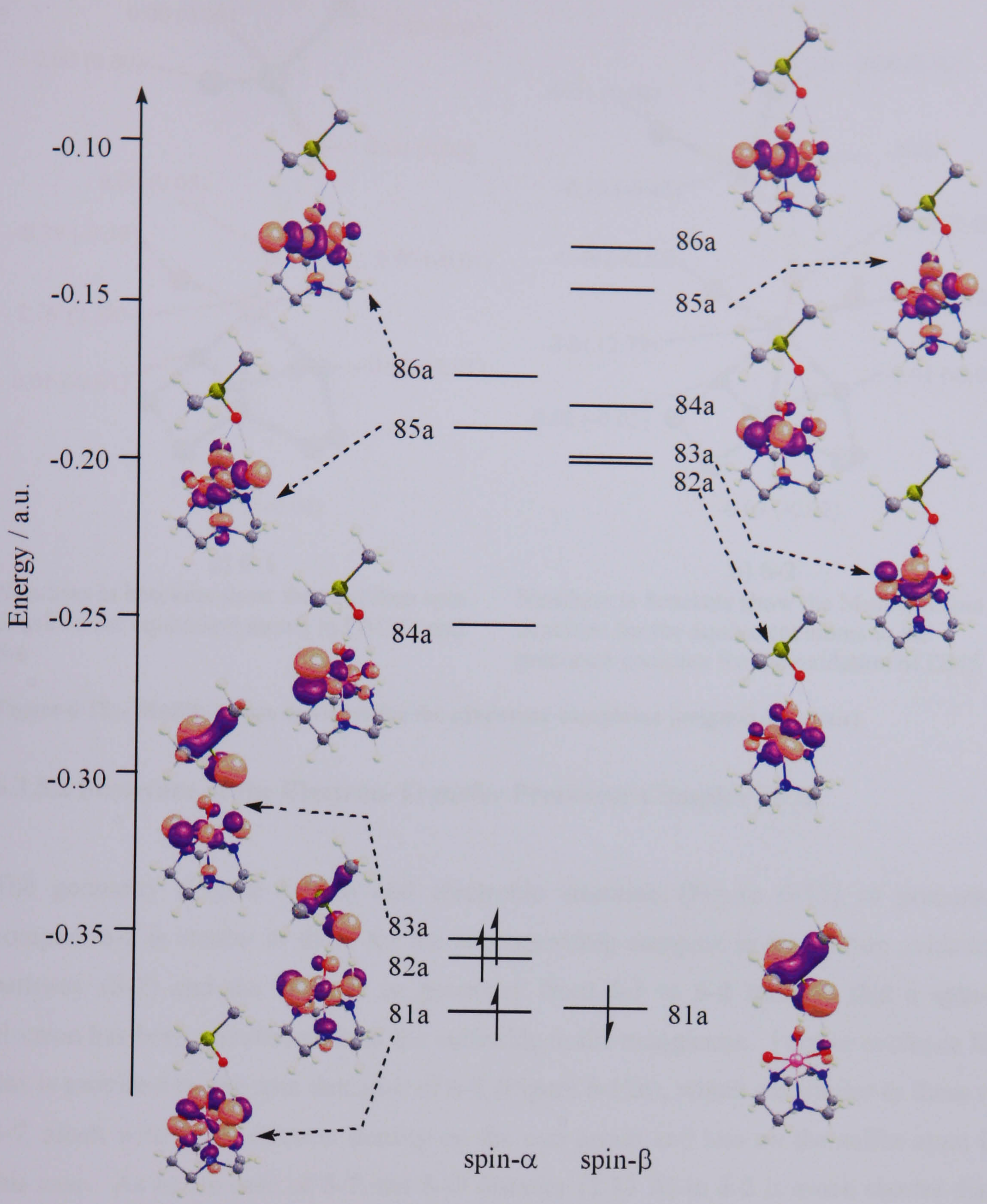

Figure 6-11 – MO diagram of complex 6-1 showing selected orbitals {original in colour}

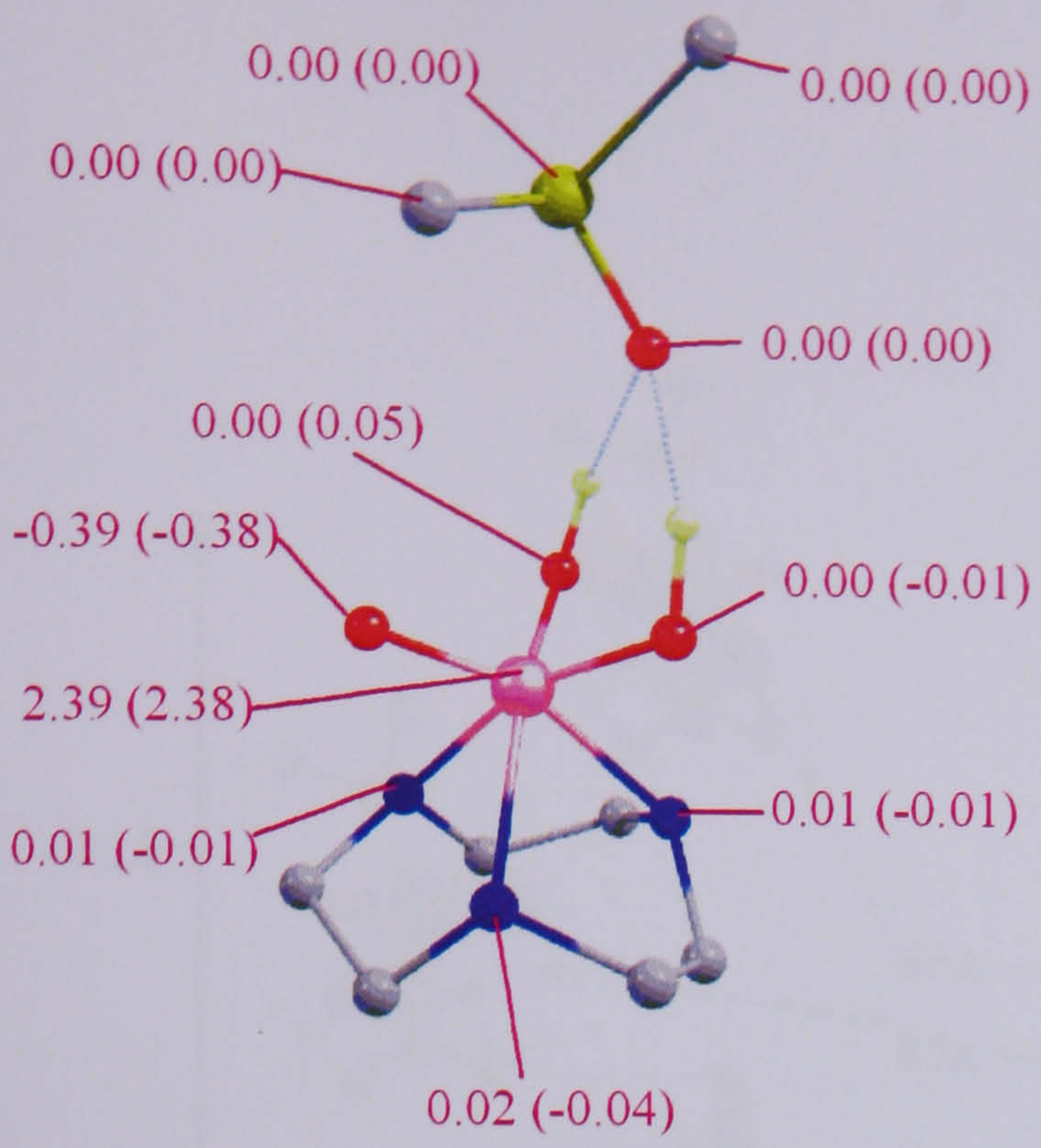

a) **6-1**

Numbers in brackets show the Mulliken spin densities for equivalent atoms in DMSO and **5-6**

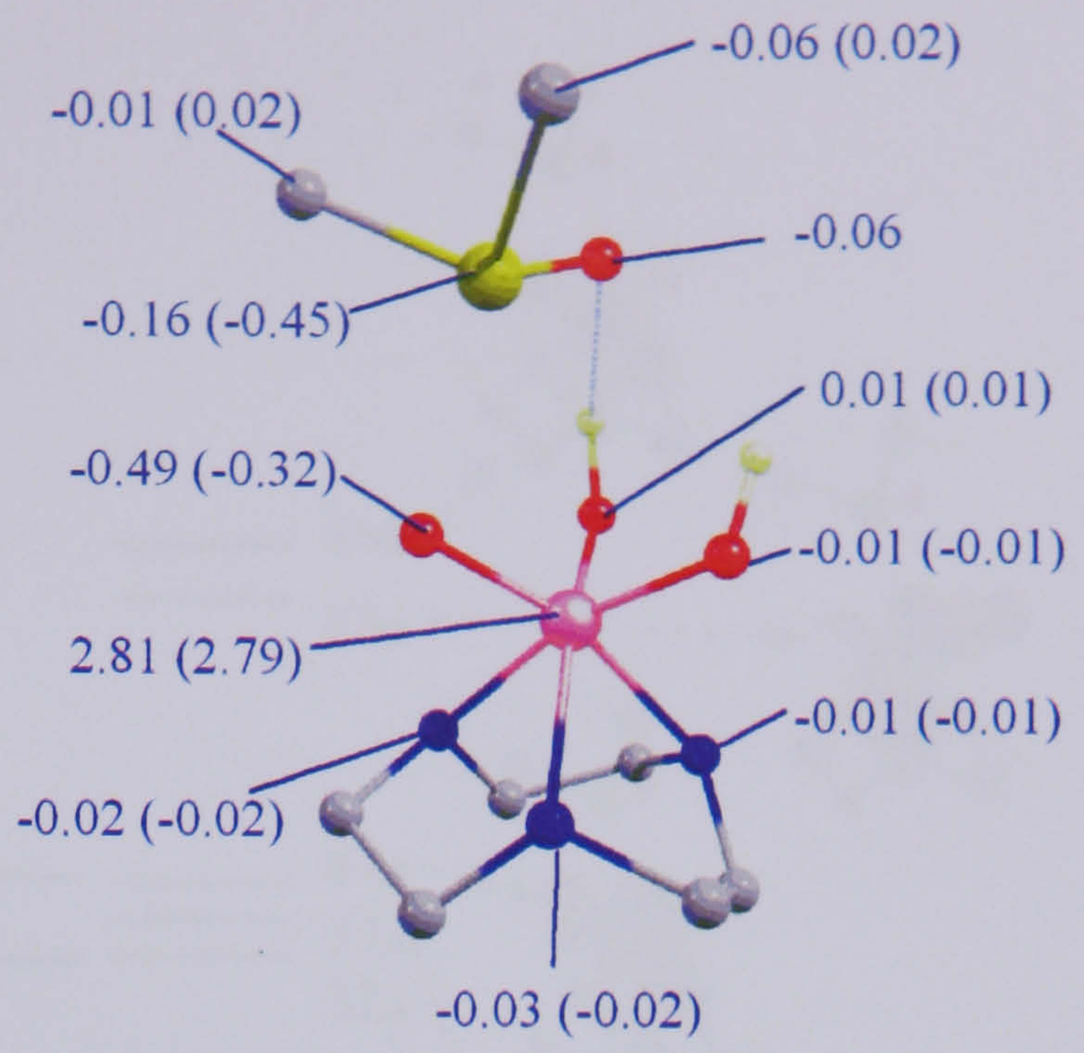

b) **6-2**

Numbers in brackets show the Mulliken spin densities for the equivalent atoms in the precursor complex for the oxidation of DMS

Figure 6-12 – Mulliken spin densities for the precursor complexes {original in colour}

6.3.5.2 Structure of the Electron-Transfer Precursor Complex (6-2)

The geometry (Figure 6-10b) and electronic structure (Figure 6-13) of precursor complex **6-2** is similar to those for the corresponding complex in the sulfide oxidation pathway (**5-7**) and the changes in geometry from **6-1** to **6-2** indicate that a spin-α electron has been transferred from the sulfoxide to the manganese. Further evidence for this is provided by the spin densities of **6-2** (Figure 6-12b), which are similar to those of **5-7**, albeit with more electron density on the oxo group and less on the sulfur atom in this case. As in the case of **5-7**, the S-O distance (2.33 Å) in **6-2** is much shorter than the sum of the van der Waals radii of S and O (3.32 Å),[2] and the Mn-O distance has also increased by 0.09 Å compared to isolated $[Mn(TACN)(OH)_2(O)]^+$ indicating that the occupation of the d-orbital that is anti-bonding to an oxygen based p-orbital (i.e. a Mn-O π* orbital) has increased. This molecular orbital array for **6-2** confirms that this is the case as the 84a α orbital has significant sulfur lone pair character. The S-O and Mn-O bonds in **6-2** are, however, longer (2.33 Å vs 1.94 Å) and shorter (1.71 Å vs 1.75 Å), respectively, than those in the sulfide analogue, **5-7**, presumably due to the reduced nucleophilicity of the sulfoxide ligand. As noted above, this reduced nucleophilicity also results in the overall destabilisation of **6-2** relative to **6-1**.

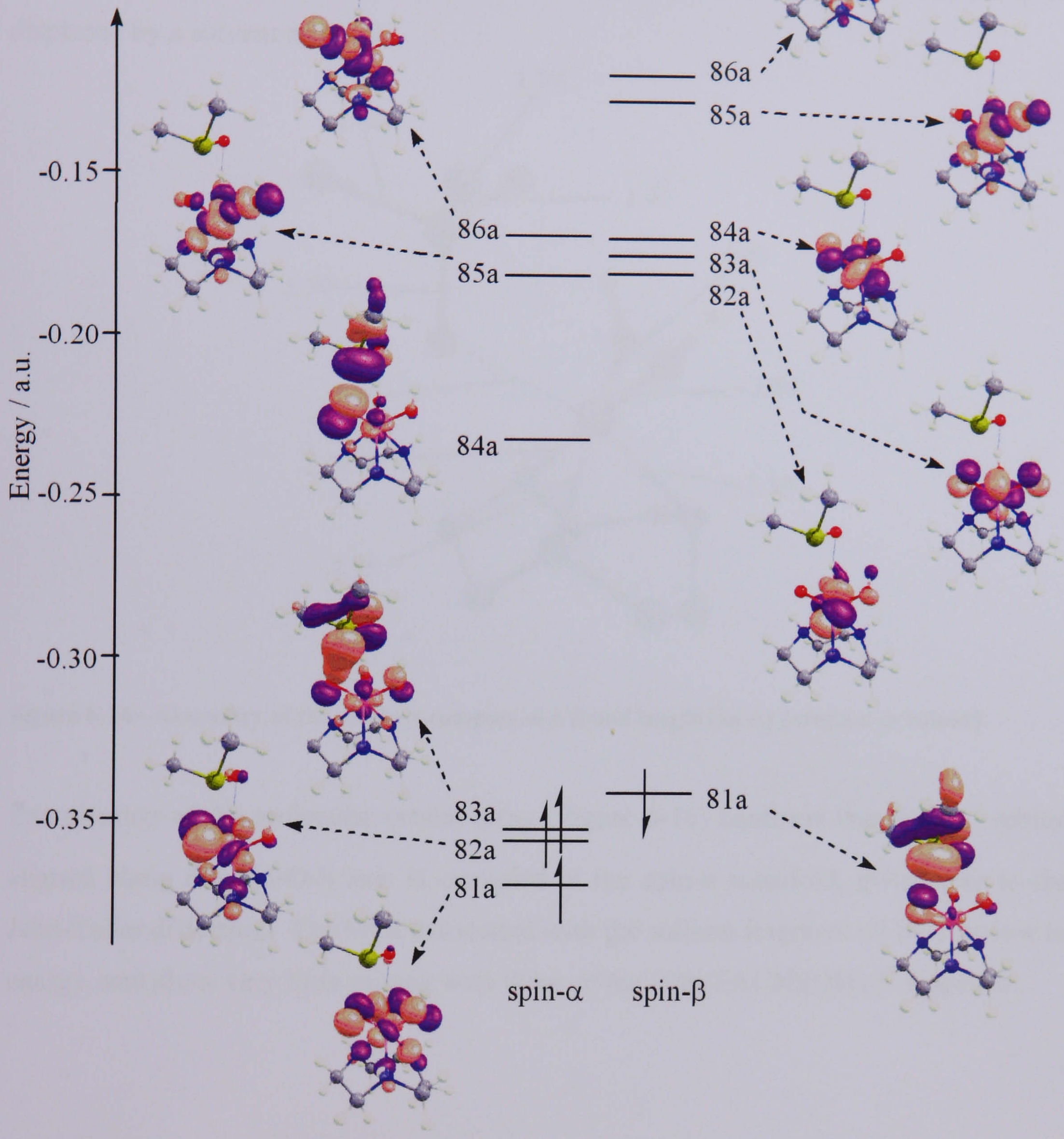

Figure 6-13 – MO diagram showing selected orbitals for complex 6-2 {original in colour}

6.3.6 Product

The product of DMSO oxidation by **5-6** $[Mn(TACN)(OH)_2(O)]^+$ is a quintet where the dimethyl sulfone is weakly coordinated to $[Mn(TACN)(OH)_2]^+$ via the oxygen atom that was donated from the manganese. The manganese is now in the +3 oxidation state,

as indicated by the characteristic Jahn-Teller distortion (Figure 6-14), the Mulliken spin densities (Figure 6-15) and the MO diagram (Figure 6-16). The sulfone is loosely coordinated to the Mn atom via O^1 (that was previously the oxo group), the bond length of 2.46 Å being significantly longer than the Mn-OH bond lengths. This indicates that the coordination of the sulfoxide molecule to the Mn centre is weak, and it will easily be displaced by a solvent molecule.

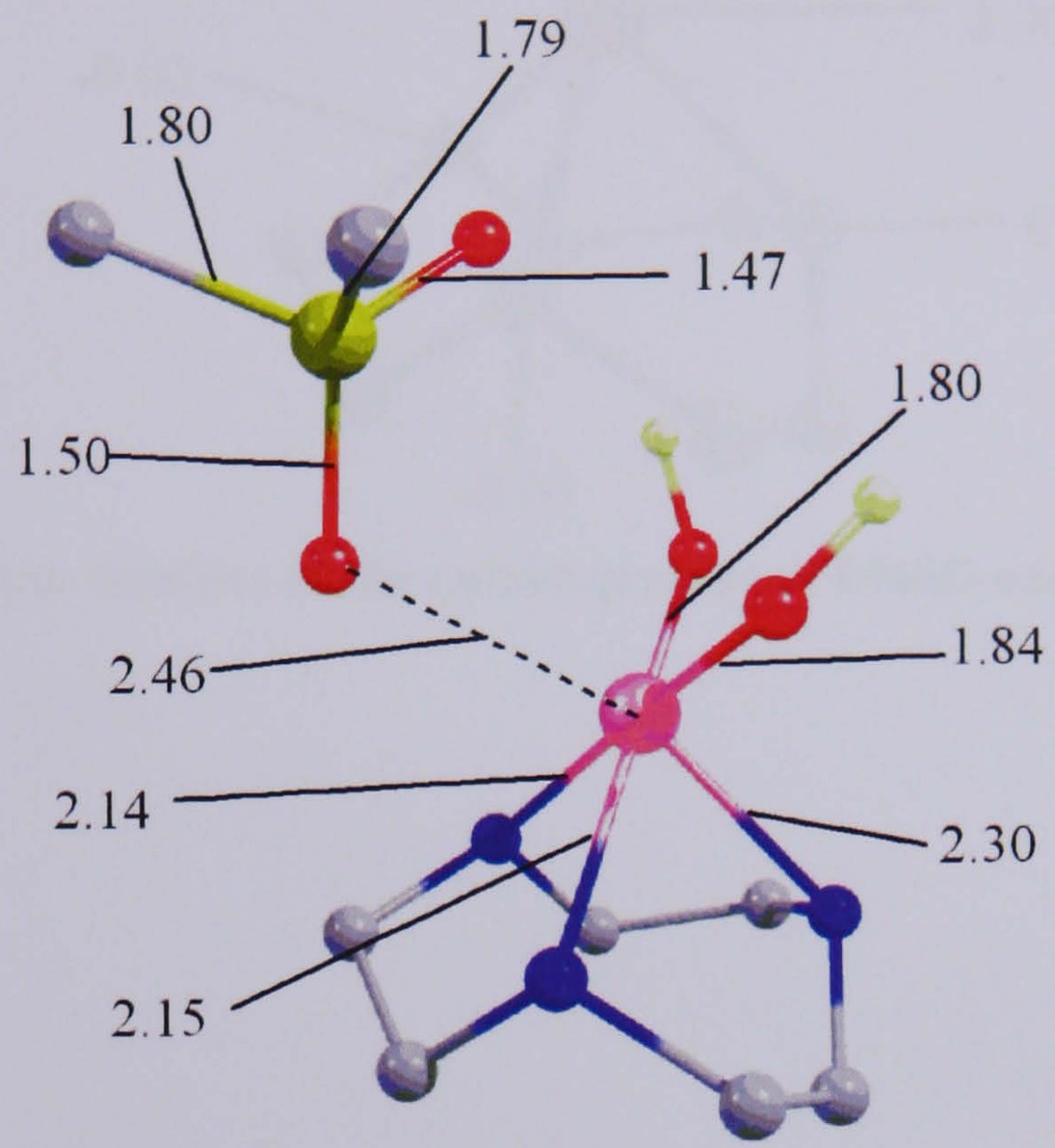

Figure 6-14 – Geometry of the product complex, 6-3 (bond lengths in Å) {original in colour}

Examination of the molecular orbital array (Figure 6-16) confirms that the d_{z^2} orbital aligned along the Mn-O-S axis is occupied in the spin-α manifold, giving rise to the Jahn-Teller distortion. The MOs associated with the sulfone fragment all lie very low in energy, and show very little mixing with those of the $[Mn(TACN)(OH)_2]^+$ fragment.

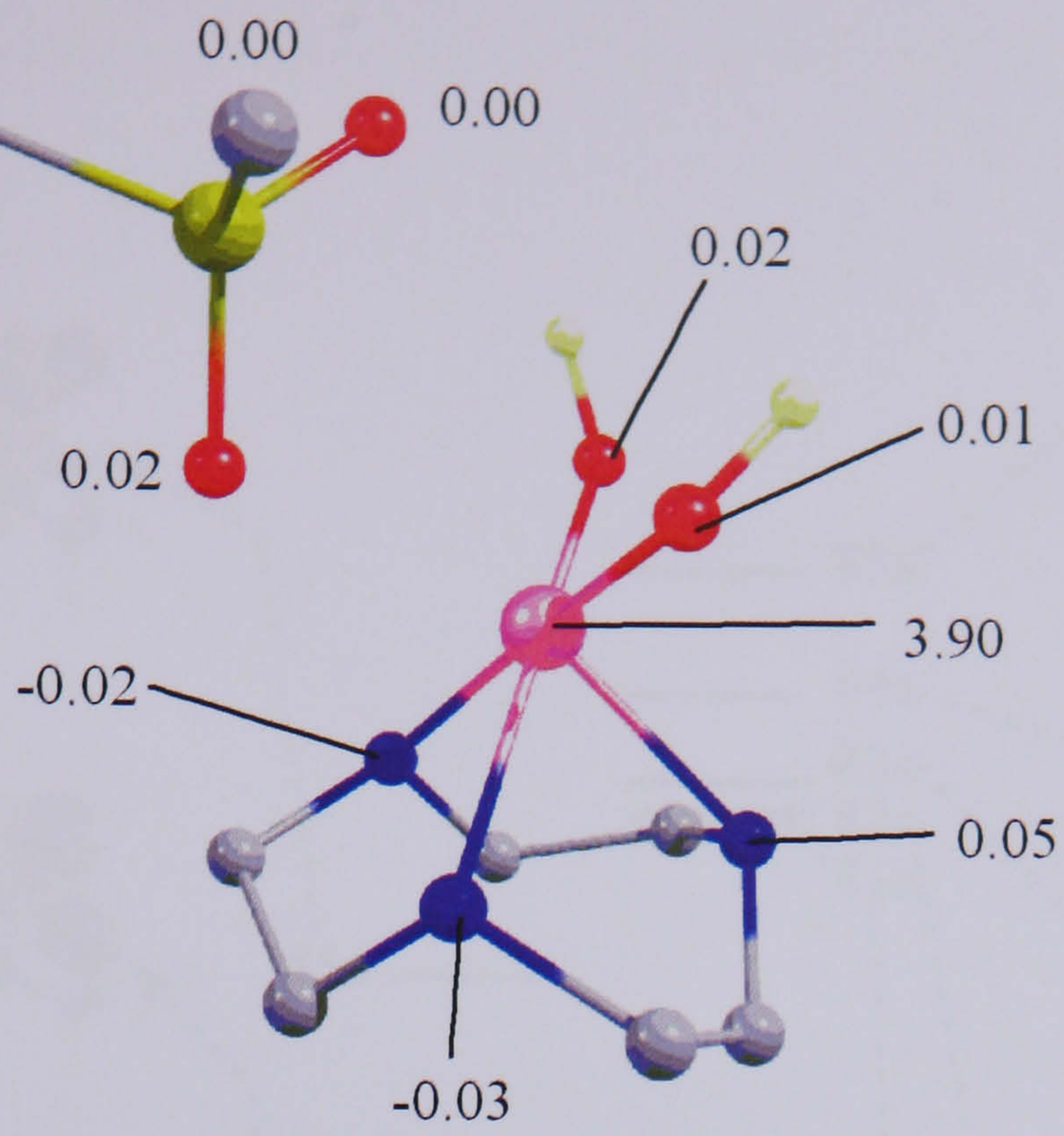

Figure 6-15 – Mulliken spin densities on the quintet product of DMSO oxidation by 5-6 {original in colour}

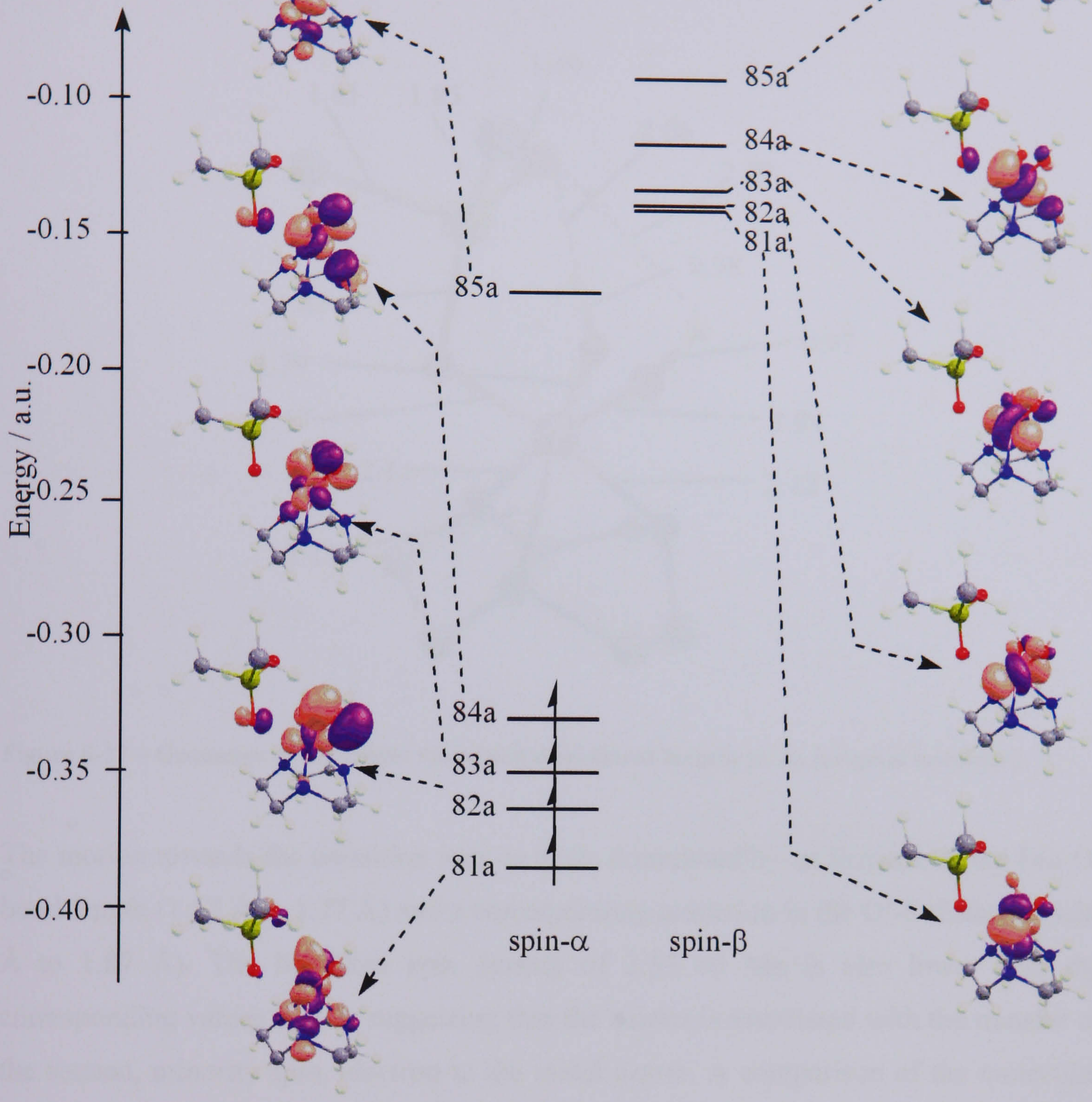

Figure 6-16 – MO diagram of the product showing selected orbitals {original in colour}

6.3.7 Transition state

As noted above, a triplet transition state has been located +29 kJ mol^{-1} above the energy of **6-1**, and characterised by the presence of a single negative frequency (Figure 6-17). All three Mn-N bond lengths are approximately 2.12 Å, and the Mn-O bond lengths are also approximately equal, indicative of the equal occupation of the d-orbitals and consistent with a Mn^{4+} oxidation state. The quintet transition state again lies much

higher in energy, suggesting that the change in spin state does not occur until after the transition state. The transition state actually connects **6-2** and the product, and a transition state connecting **6-1** and **6-2** has not been located. However, we believe that it will be very low in energy.

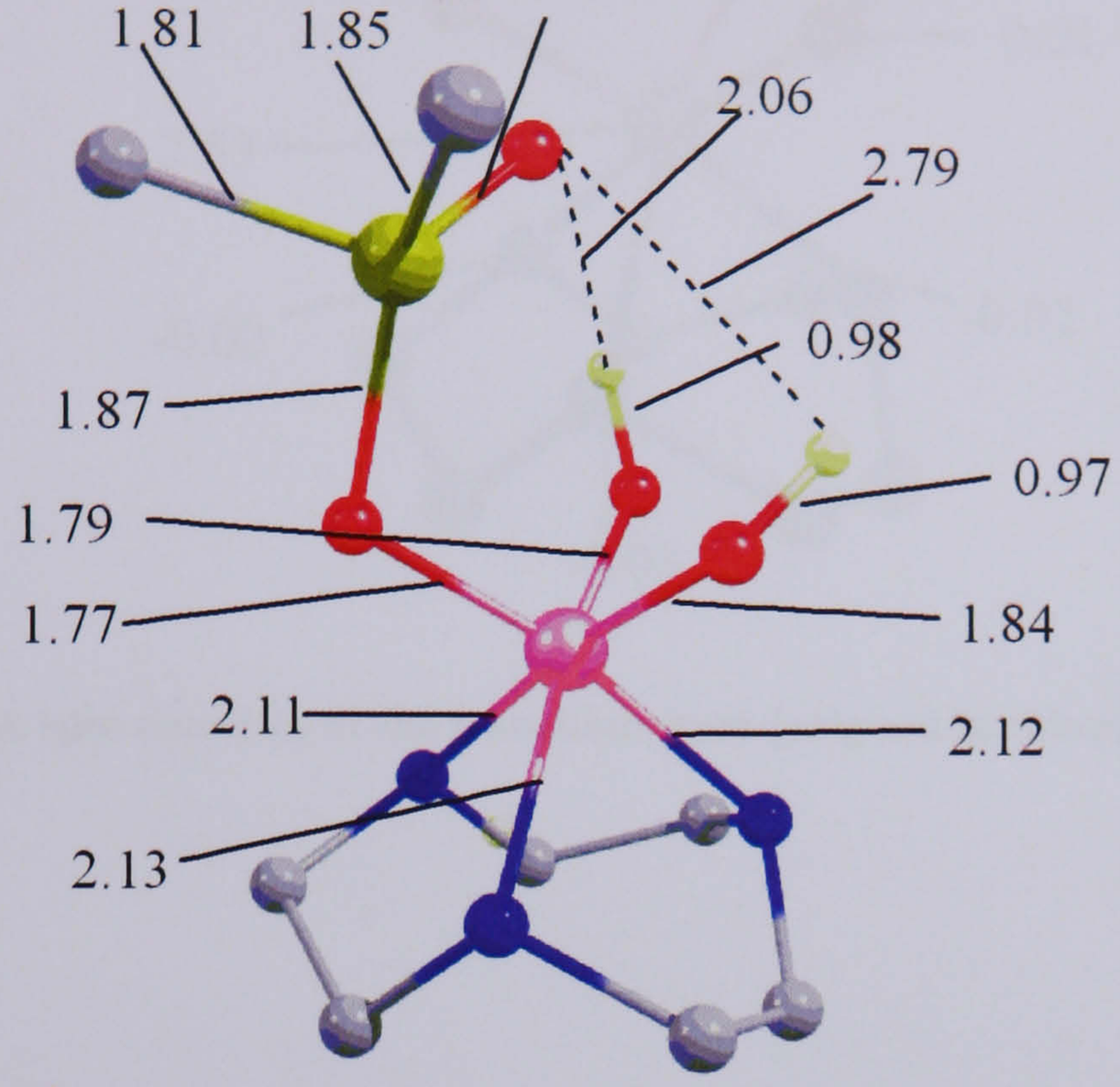

Figure 6-17 – Geometry of the triplet transition state (bond lengths in Å) {original in colour}

The motion towards the transition state is again dominated by an increase in the Mn-O^1 bond length (1.62 Å to 1.77 Å) and a corresponding reduction in the O^1-S distance (4.20 Å to 1.87 Å). The Mulliken spin density of 2.53 on Mn is also lower than the corresponding values in **6-2**, suggesting that the barrier is associated with the transfer of the second, minority spin, electron to the metal centre. A comparison of the molecular orbital arrays for the precursor **6-2** (Figure 6-14) and the transition state (Figure 6-19) is again consistent with this picture: the strong sulfur character in the occupied 81a β orbital in **6-2** is largely transferred to the vacant manifold in the transition state (82a β), implying oxidation of the sulfur centre.

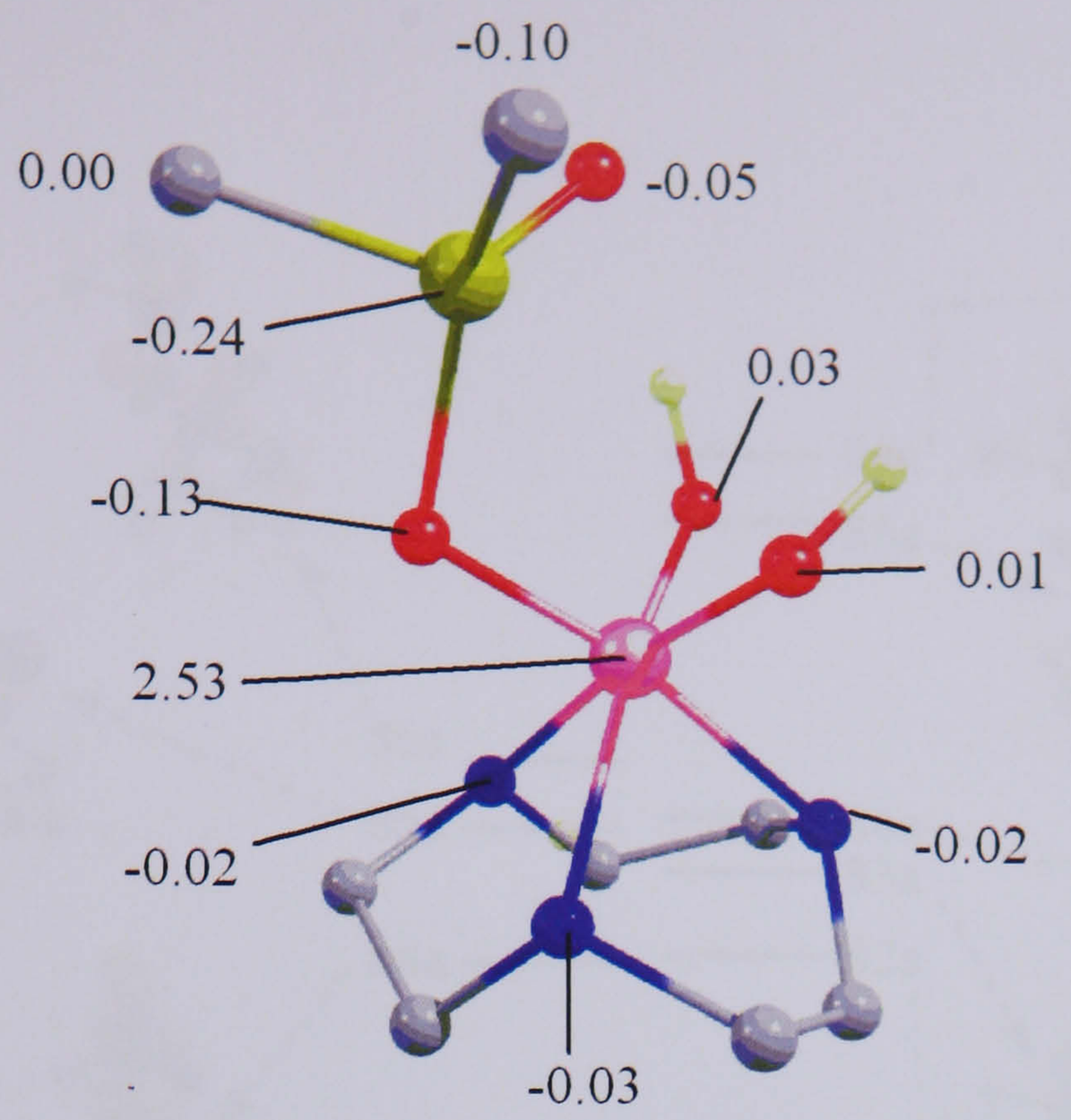

Figure 6-18 – Mulliken spin densities of the transition state {original in colour}

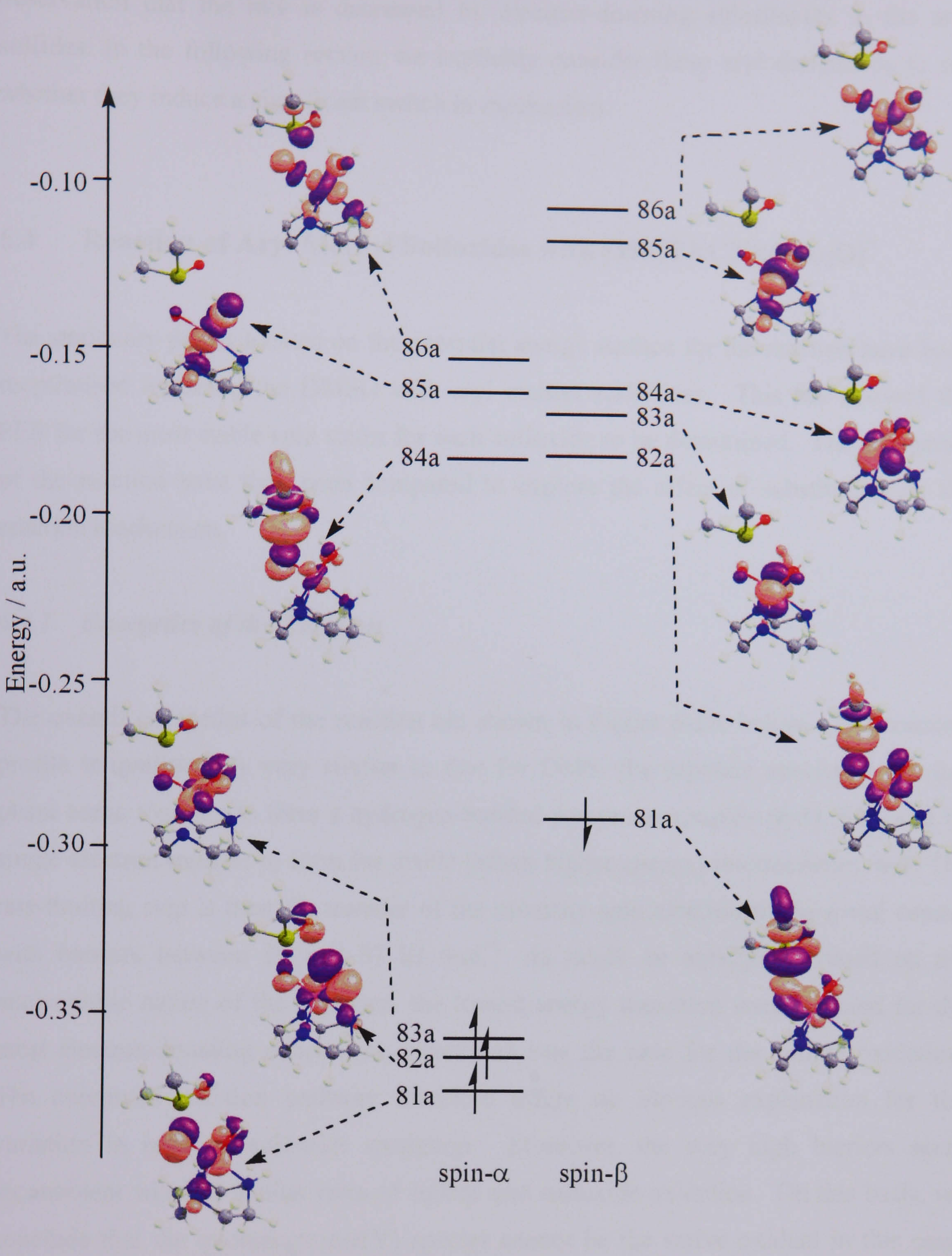

Figure 6-19 – MO diagram for the transition state showing selected orbitals {original in colour}

The oxidation pathway for the sulfoxide by $[Mn(TACN)(OH)_2(O)]^+$ summarised in the previous paragraphs is qualitatively very similar to that for the sulfides, in that it involves sulfur-to-manganese charge transfer in the rate-limiting step. The nucleophilic character of the substrate is, however, apparently inconsistent with the experimental

observation that the rate is decreased by electron-donating substituents in the aryl sulfides. In the following section we explicitly consider these aryl derivatives to see whether they induce a significant switch in mechanism.

6.4 Reaction of Aryl Methyl Sulfoxides with $[Mn(TACN)(OH)_2O]^+$

The stationary points located on the potential energy surface for the reaction have been reoptimised replacing the DMSO with aryl methyl sulfoxides. This has allowed the PES for the most stable spin states for each sulfoxide to be determined. The energetics of the reaction have then been compared to explore the effect of substitution on the reaction mechanism.

6.4.1 Energetics of the Reaction

The overall energetics of the reaction are shown in Figure 6-20, below. The reaction profile is qualitatively very similar to that for DMS: the separate species in the gas phase come together to form a hydrogen-bonded precursor complex **(6-1)**, followed by single electron transfer to form the stable (albeit higher energy) intermediates, **6-2**. The rate-limiting step is then the transfer of the minority-spin electron to the metal centre, with barriers between 29 and 37 kJ mol^{-1}. As might be anticipated based on the nucleophilic nature of the substrate, the lowest energy transition state is found for the most electron-donating substituent, exactly as was the case for the sulfide oxidation. The computed reaction pathway therefore offers no obvious explanation for the variation in rates of sulfoxide oxidation. Moreover, the very high barriers seem inconsistent with the similar rates of sulfide and sulfoxide oxidation. On this basis, we conclude that the oxomanganese(V) species cannot be the active oxidant in this case. We therefore now consider the reaction pathways for alternative metal-based species that could potentially act as oxidants.

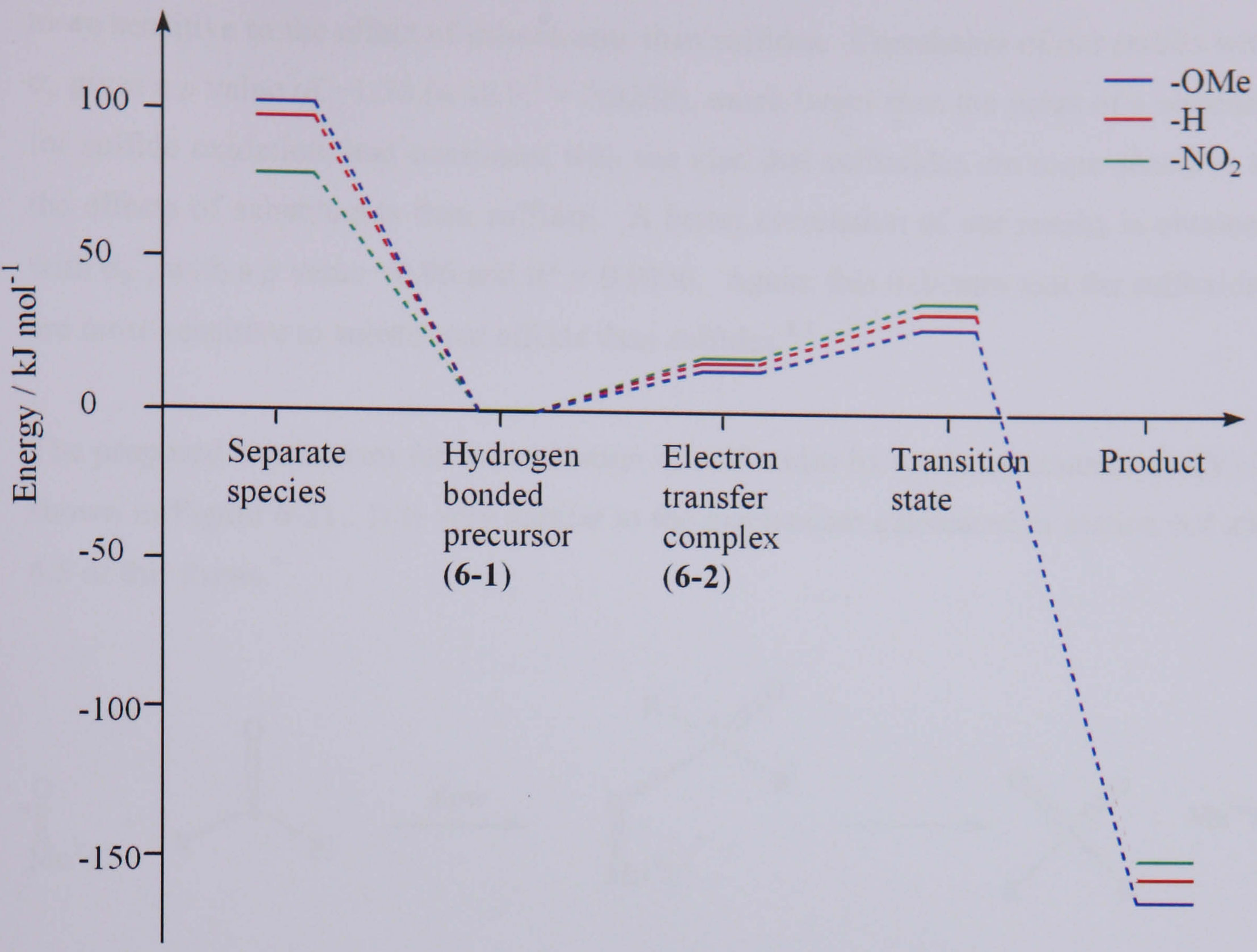

Figure 6-20 – Energetics for the oxidation of *para*-substituted aryl methyl sulfoxides {original in colour}

6.4.2 Comparison of the Mechanism with Oxo(salen)manganese(V)

Rajagopal and co-workers have experimentally studied the reaction of oxo(salen)manganese(V) and substituted aryl methyl sulfoxides to determine the reaction mechanism. A key difference between their study, and the experiments that led to this computational study is that in the case of the salen ligand, the active oxidant was generated from the reaction of (salen)manganese(III) and iodosobenzene, and has been identified spectoscopically as oxo(salen)manganese(V). In contrast the active oxidant here has not been determined experimentally.[4,5]

Rajagopal and co-workers show that in the reaction of oxo(salen)manganese(V) and aryl methyl sulfoxide the oxidant behaves as an electrophile and there is a build up of charge on the sulfur centre in the transition state accompanied by a reduction of charge on the manganese centre. They obtain a ρ value of −2.44 for the oxidation of sulfoxides (correlated against σ_p) compared to −1.86 for sulfides (σ_p), indicating that sulfoxides are

more sensitive to the effect of substituents than sulfides. Correlation of our results with σ_p gives a ρ value of −1.30 (with $R^2 = 0.9208$), much larger than the value of ρ obtained for sulfide oxidation, and consistent with the idea that sulfoxides are more sensitive to the effects of substituents than sulfides. A better correlation of our results is obtained with σ_p^+, with a ρ value −0.96 and $R^2 = 0.9996$. Again, this indicates that the sulfoxides are more sensitive to substituent effects than sulfides.[4,5]

The proposed mechanism for the oxidation of sulfoxides by oxo(salen)manganese(V) is shown in Figure 6-21. It is very similar to the mechanism calculated in section 6.4 and 6.5 of this thesis.[4]

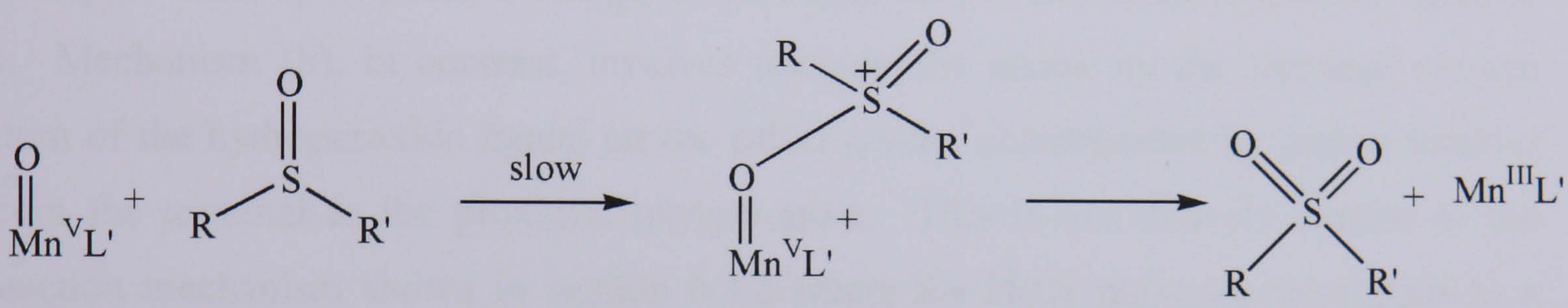

L' = salen

Figure 6-21 – Mechanism proposed for the oxidation of sulfoxides by oxo(salen)manganese(V)

Another observation by the authors about the oxidation of sulfides and sulfoxides by oxo(salen)manganese(V) is that the reaction with sulfoxides is 2-3 times slower than with sulfides due to the reduced nucleophilicity of sulfoxides. This is consistent with our observation that with $[Mn(TACN)(OH)_2(O)]^+$ as the oxidant the activation energy is about 12-17 kJ mol^{-1} higher for sulfoxides than sulfides.

For both sulfide and sulfoxide oxidation an oxomanganese(V) species is potentially an active intermediate and low lying transition states can be located. In the case of sulfide an oxomanganese(V) species seems to be a reasonable intermediate as it explains the electrophilicity of the substrate seen experimentally. In the case of sulfoxide, however, it is in disagreement with the experimental results regarding nucleophilicity and activation energies. The calculations though are in agreement with work done on oxo(salen)manganese(V) complexes lending credibility to our results.

6.5 Oxidation of sulfoxides by $[Mn(TACN)(OH)(OOH)]^+$

Another possible mechanism for sulfoxide oxidation is direct attack by a coordinated HOO^- ligand (Figure 6-22), in which case the role of the metal centre is to act as an anchor holding the sulfoxide and OOH^- together. From the initial geometry there are, in principle, two mechanisms by which the sulfur could be oxidised, both of which are shown in Figure 6-22. Mechanism (a) is qualitatively similar to those discussed for oxomanganese(V) based oxidation – it involves nucleophilic attack by the sulfur lone pair on the oxygen species – in this case OOH rather than O. The electrons are transferred into the O-O σ^* orbital rather than a metal-based orbital, but we would still anticipate build up of positive charge on the sulfur centre, and hence a positive value of ρ. Mechanism (b), in contrast, involves nucleophilic attack by the terminal oxygen atom of the hydroperoxide ligand on the sulfur centre, accompanied by proton transfer from the terminal to the proximal oxygen atom. This is qualitatively similar to the reaction mechanism shown in section 6.3.2 where the H_2O_2 molecule rearranges to a high energy isomer with a negatively charged oxygen atom poised for nucleophilic attack. As was the case in section 6.3.2, we have been unable to locate any intermediates or transition states corresponding to mechanism (b), suggesting that the oxidant again acts as an electrophile rather than a nucleophile.

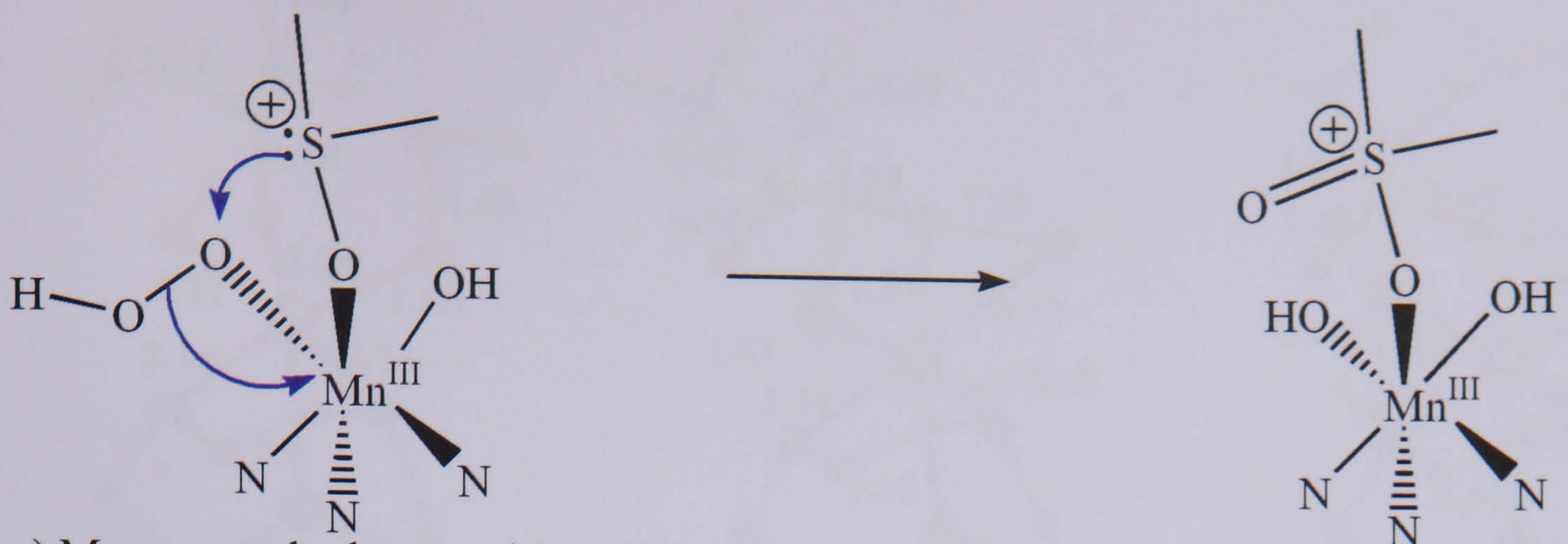

a) Manganese-hydroperoxide species acting as an electrophile

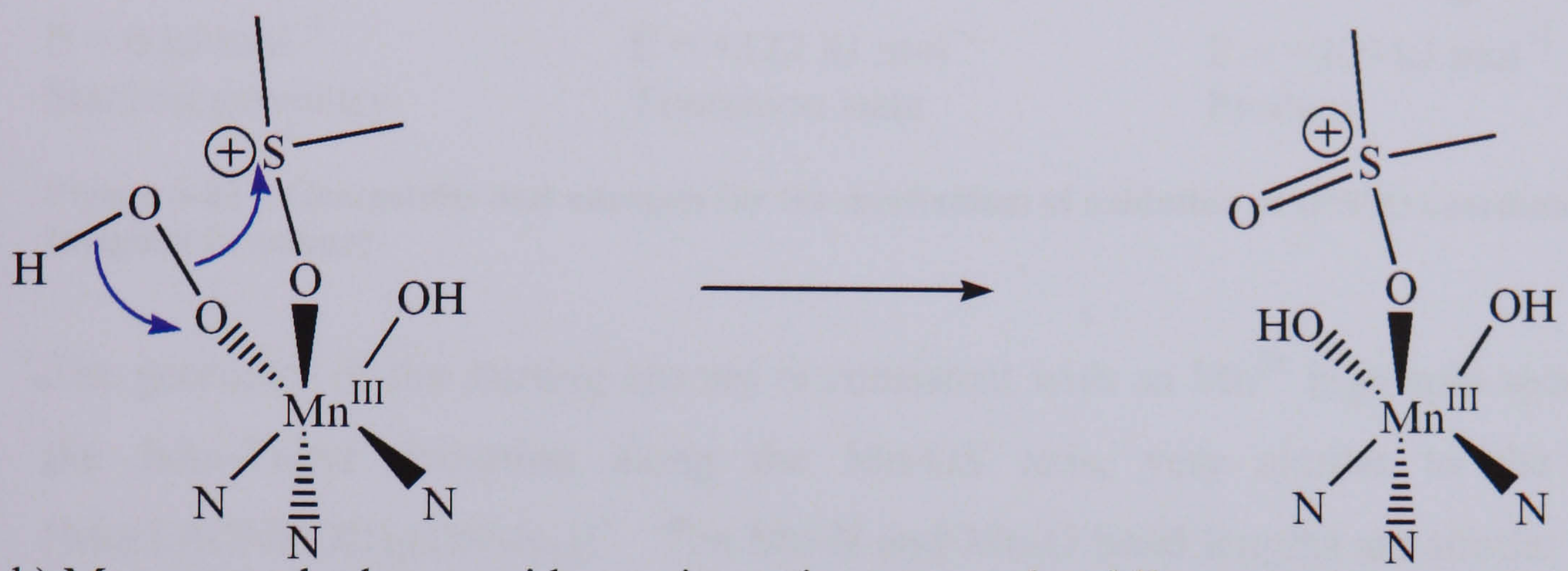

b) Manganese-hydroperoxide species acting as a nucleophile

Figure 6-22 – Different possible mechanisms for oxidation of DMSO by $Mn^{3+}OOH$ {original in colour}

Geometries and energies of the stationary points (all quintets) corresponding to mechanism (a) for the oxidation of DMSO are shown in Figure 6-23. The transition state is high in energy (+122 kJ mol^{-1}) and so a rapid reaction at room temperature is unlikely.

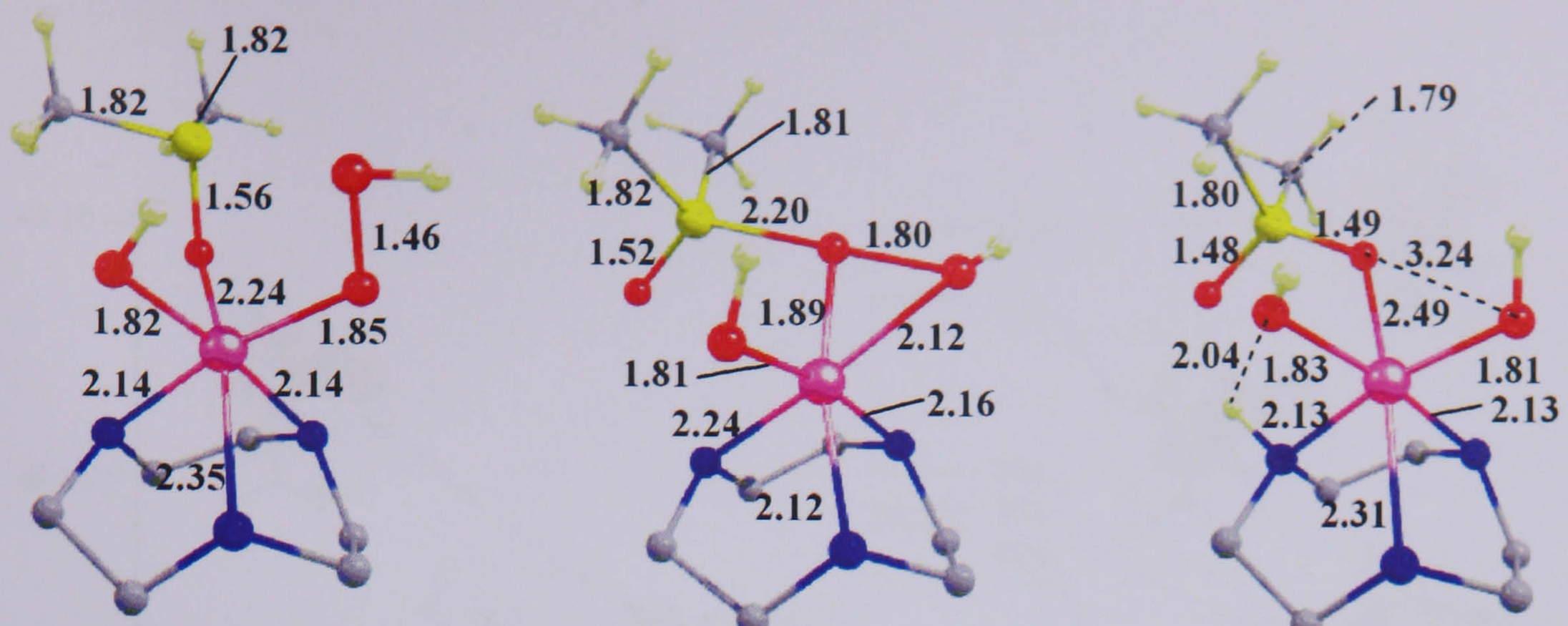

$E = 0$ kJ mol^{-1}	$E = +122$ kJ mol^{-1}	$E = -209$ kJ mol^{-1}
Starting geometry	Transition state	Product

Figure 6-23 – Geometries and energies for the mechanism of oxidation of DMSO coordinated to Mn {original in colour}

The geometry of the starting species is consistent with an Mn^{3+} high spin species with the Jahn-Teller distortion along the Mn-OS axis, very similar to the case of $[Mn(TACN)(OH)_2(OSMe_2)]^+$. The Mn-N and Mn-O bond lengths are similar although the hydroperoxide ligand has a slightly longer Mn-O bond than the hydroxide anion. The hydroperoxide ligand is coordinated to the manganese centre in an η^1 fashion and the other oxygen atom is only 2.07 Å from the H of the hydroxide ligand suggesting that some hydrogen bonding may be occurring. However, the O-H bond is not significantly lengthened compared to $[Mn(TACN)(OH)_2(OSMe_2)]^+$, so this interaction is not very strong.

In the transition state, the hydroperoxide ligand is coordinated to the manganese centre in an η^2 fashion although the Mn-O bond lengths are not identical, and the oxygen centre originally coordinated to Mn still has a shorter Mn-O distance than the terminal oxygen atom. The S-O-O angle is 171°, close to the ideal value of 180° that will allow maximum overlap between the σ^* orbital of the O-O bond and the p-orbital on the sulfur that forms a σ bond (Figure 6-24, α, 83a; β, 80a). The O-O bond is cleaved heterolytically with the oxidant acting as an electrophile, and the mechanism is in fact very similar to that proposed for the epoxidation of olefins by metal-peroxo species,[7,8] with the sulfur lone pair playing the same role as the π electrons on the olefin. It should be emphasised again, however, that the nucleophilic behaviour of the substrate is again contrary to the qualitative conclusion drawn from the experimental results.

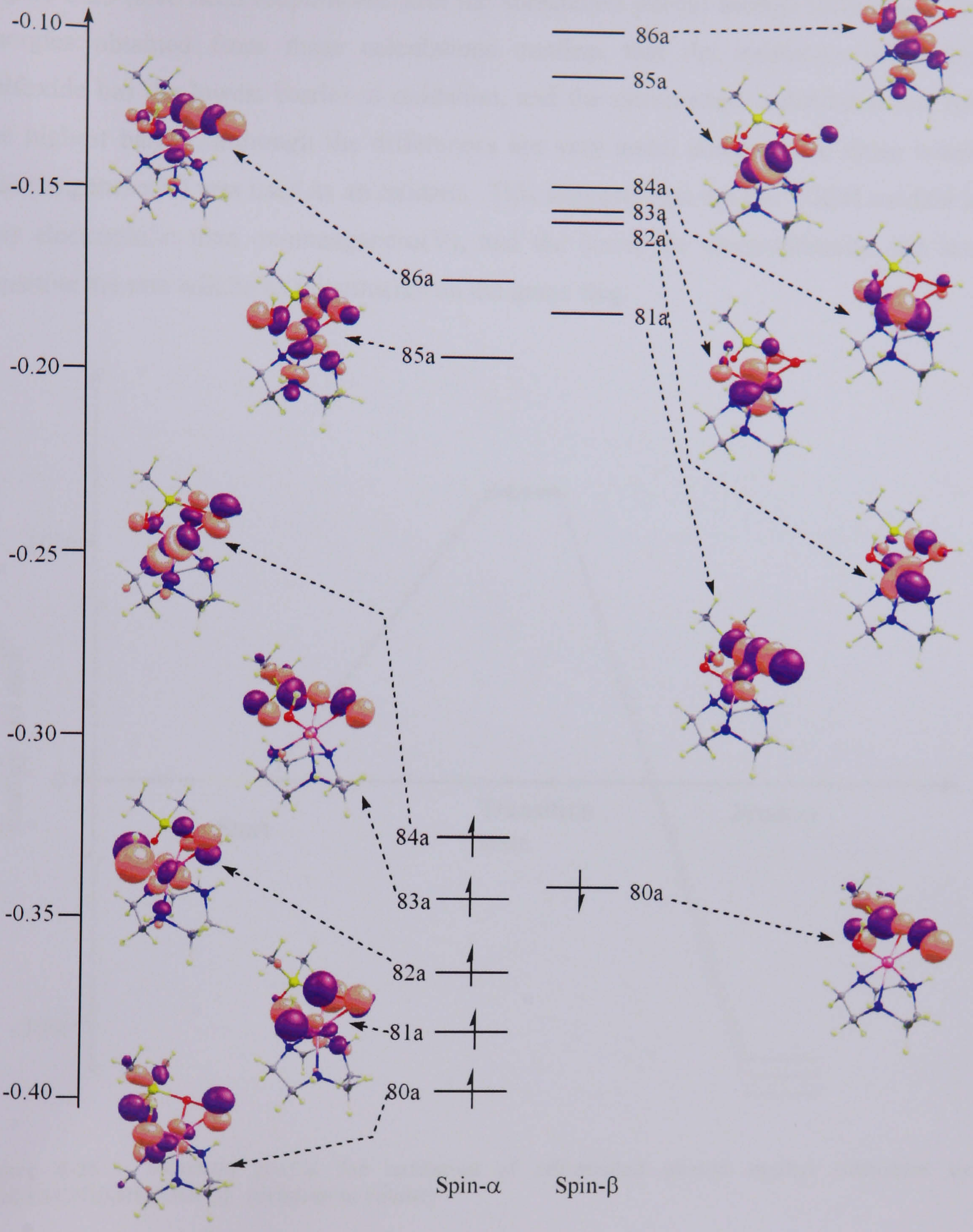

Figure 6-24 – MO diagram (showing selected orbitals) for the transition state of sulfoxide oxidation by $[Mn(TACN)(OH)(OOH)]^+$ {original in colour}

Although the electronic structure of the transition state suggests that sulfoxides with more electron withdrawing substituents will be oxidised more slowly than those with more electron donating substituents due to their reduced ability to donate the lone pair

on the sulfur, the same factor may have some indirect influence on the energy of the σ* orbital of the coordinated HOO^- anion. For this reason, the stationary points shown in Figure 6-23 have been reoptimised with the substituted phenyl methyl sulfoxides. The energies obtained from these calculations confirm that the methoxy- substituted sulfoxide has the lowest barrier to oxidation, and the nitromethyl- substituted one has the highest barrier, although the differences are very small compared to those where oxomanganese(V) was used as an oxidant. This suggests that the $Mn^{3+}OOH$ oxidant is less electrophilic than oxomanganese(V), and the lower the electrophilicity, the less sensitive the rate will be to substituents on the arene ring.

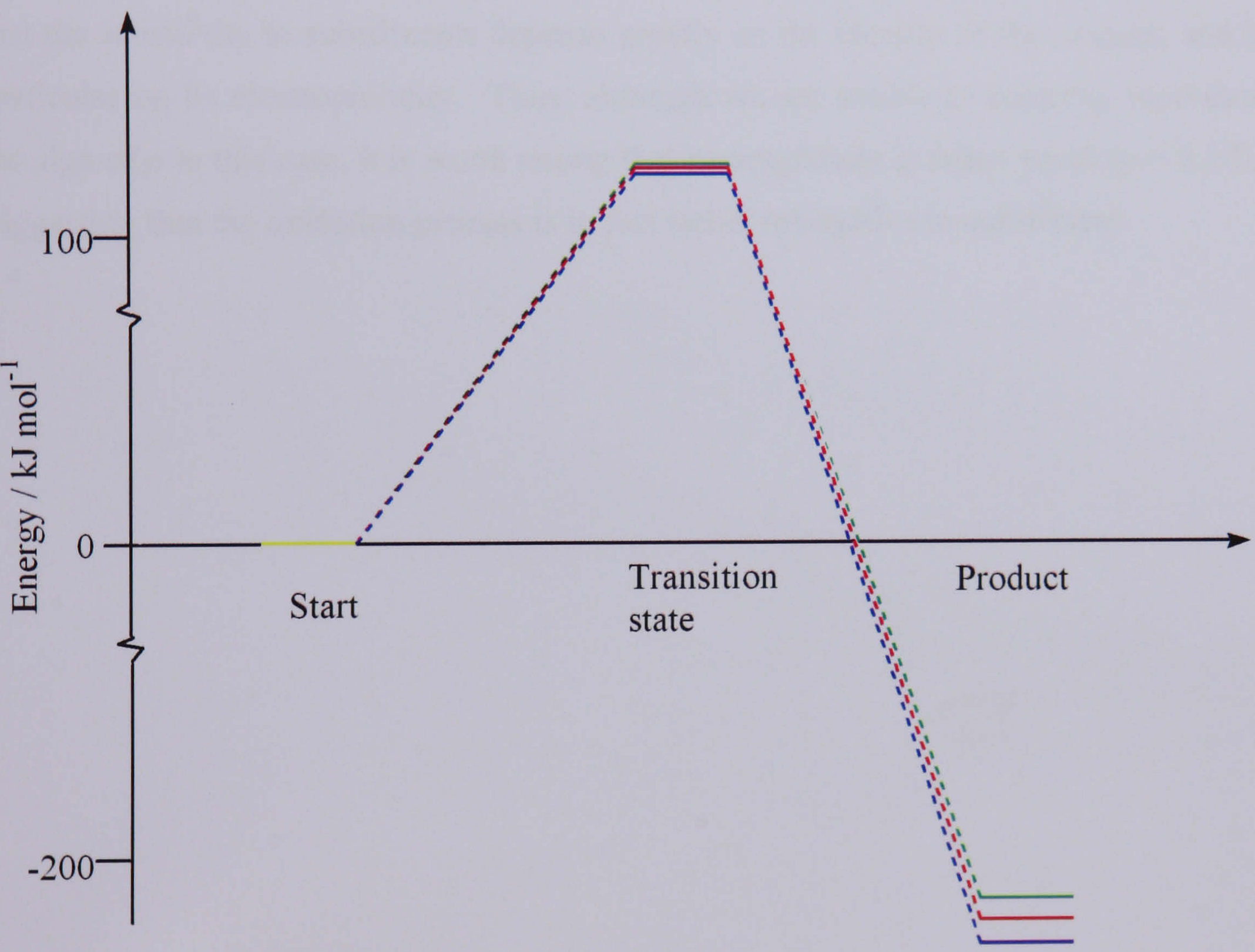

Figure 6-25 – Reaction profile for oxidation of substituted phenyl methyl sulfoxides by $[Mn(TACN)(OH)(OOH)]^+$ {original in colour}

6.6 Conclusions

We have considered a variety of different mechanisms for the oxidation of sulfoxides, where the active oxidant varies from free H_2O_2 through oxomanganese(V) to

$Mn^{3+}OOH$. In no case do we find evidence that the sulfoxide acts as an electrophile, as opposed to a nucleophile: the rate-determining step in each case is the transfer of electrons from the sulfur to the oxidant. In the case of the oxomanganese(V) oxidant this electron transfer occurs in a step-wise manner, the barrier being associated with transfer of the second electron, while for $Mn^{3+}OOH$ the electrons are transferred pairwise. Nevertheless, in each case the rate-limiting step is associated with a build up of positive charge at the sulfur centre, and hence the reaction should be accelerated by electron-donating groups on the sulfur. We are therefore unable to explain the experimental data which suggest that the oxidant is acting as a nucleophile in this case. However, a comparison of the oxidation by oxomanganese(V) and $Mn^{3+}OOH$ suggests that the sensitivity to substituents depends greatly on the identity of the oxidant, and in particular on its electrophilicity. Thus, although we are unable to correctly reproduce the sign of ρ in this case, it is worth noting that its magnitude is rather small ($\rho = 0.20$),[1] suggesting that the oxidation process is in fact rather insensitive to substituent.

References

1) J. R. Lindsay Smith, J. Murray, P. H. Walton, T. R. Lowdon, *Tetrahedron Lett.*. **2006**, *47*, 2005

2) R. Curci, A. Giovine, G. Modena, *Tetrahedron*, **1966**, *22*, 1235

3) A. Bondi, *J. Phys. Chem.*, **1964**, *68*, 441

4) A. Chellamani, P. Kulanthaipandi, S. Rajagopal, *J. Org. Chem.*. **1999**. *64*. 2232

5) A. Chellamani, N. I. Alhaji, S. Rajagopal, *J. Chem. Soc., Perkin Trans. 2*. **1997**. 299

6) A. Chellamani, N. I. Alhaji, S. Rajagopal, R. Sevvel, C. Srinivasan, *Tetrahedron*, **1995**, *51*, 12677

7) C. Di Valentin, P. Gisdakis, I. V. Yudanov, N. Rösch, *J. Org. Chem.*, **2000**, *65*. 2996

8) P. Gisdakis, I. V. Yudanov, N. Rösch, *Inorg. Chem.*, **2001**, *40*, 3755

Appendix

Table A5-1 – Comparison of the Geometries of the S=1 and S=2 transition states (bond lengths in Å)

	S=1	S=2
vibrational frequency	*i*540 cm^{-1}	*i*501 cm^{-1}
$Mn\text{-}N^1$	2.132	2.224
$Mn\text{-}N^2$	2.130	2.136
$Mn\text{-}N^3$	2.122	2.128
$Mn\text{-}O^1$	1.751	1.796
$Mn\text{-}O^2$	1.810	1.812
$Mn\text{-}O^3$	1.845	1.827
$O^2\text{-}H$	0.970	0.971
$O^3\text{-}H$	0.971	0.972
$S\text{-}C^2$	1.813	1.813
$S\text{-}C^1$	1.811	1.813
$S\text{-}O^1$	1.941	2.062

The atom labels in table A5-1and all similar tables, refer to the numbering scheme shown in Figure A5-1. For table A5-1, C^{Me} is equivalent to C^1, and C^{Ar} corresponds to C^2.

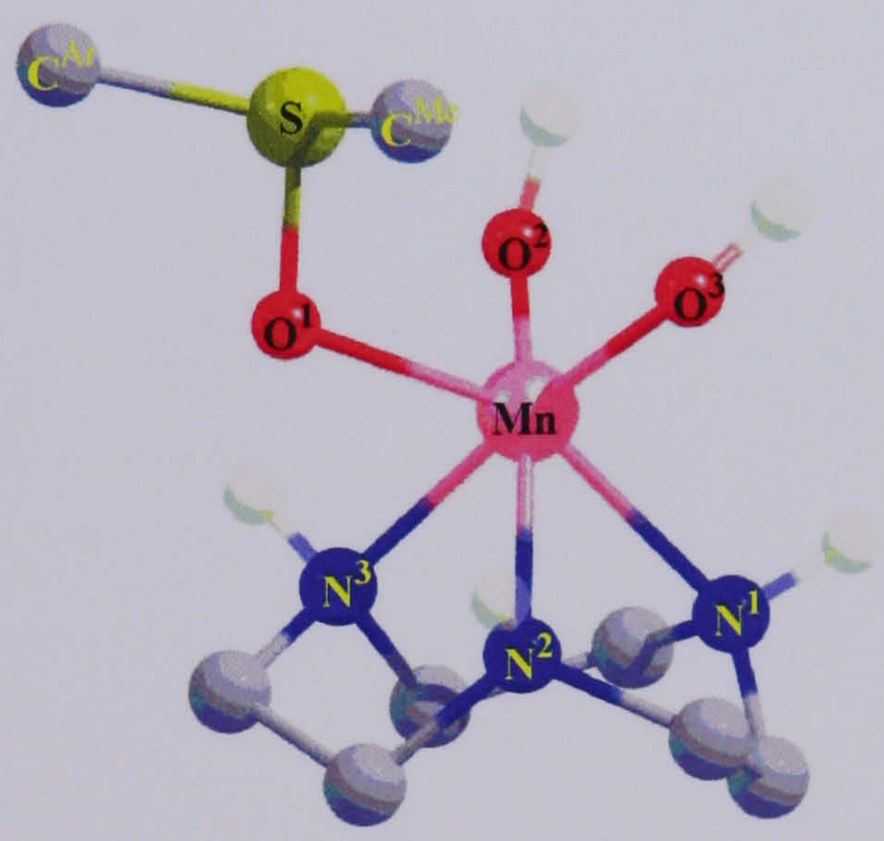

Figure A5-1 – Numbering scheme used in the tables {original in colour}

Table A5-2 – Geometry (bond lengths in Å) and spin densities of the precursor complexes

	5-6	**5-6** + (Ph-NO_2)SMe	**5-6** + PhSMe	**5-6** + (Ph-OMe)SMe
Bond length / Å				
Mn-O^1	1.617	1.691	1.687	1.682
Mn-O^2	1.793	1.803	1.804	1.806
Mn-O^3	1.778	1.820	1.824	1.826
O^2-H	0.973	0.971	0.971	0.971
O^3-H	0.973	0.972	0.972	0.971
Mn-N^1	2.175	2.173	2.180	2.187
Mn-N^2	2.134	2.137	2.139	2.141
Mn-N^3	2.141	2.142	2.145	2.147
S-O^1		2.365	2.366	2.401
O^2H-S		3.237	3.231	3.222
O^3H-S		3.180	3.219	3.166
Mulliken spin densities				
Mn	2.38	2.80	2.79	2.78
O^1	−0.38	−0.34	−0.28	−0.23
O^2	0.05	0.02	0.01	0.01
O^3	−0.01	−0.02	−0.02	−0.02
N^1	−0.01	−0.01	−0.01	−0.01
N^2	−0.01	−0.02	−0.02	−0.02
N^3	−0.04	−0.03	−0.02	−0.02
S		−0.37	−0.40	−0.39

Table A5-3 – Geometries (bond lengths in Å) and spin densities of the transition states

	Ph-NO_2	Ph	Ph-OMe
Imaginary freq	*i*543	*i*533	*i*515
Bond length / Å			
$Mn\text{-}N^1$	2.134	2.130	2.133
$Mn\text{-}N^2$	2.127	2.126	2.126
$Mn\text{-}N^3$	2.123	2.128	2.132
$Mn\text{-}O^1$	1.764	1.755	1.752
$Mn\text{-}O^2$	1.811	1.813	1.814
$Mn\text{-}O^3$	1.842	1.841	1.839
$O^2\text{-}H$	0.971	0.971	0.971
$O^3\text{-}H$	0.971	0.971	0.971
$S\text{-}C^{Ar}$	1.770	1.770	1.762
$S\text{-}C^1$	1.811	1.811	1.813
$S\text{-}O^1$	1.929	1.929	1.944
Mulliken spin densities			
Mn	2.543	2.433	2.441
N^1	−0.021	−0.018	−0.019
N^2	−0.023	−0.021	−0.020
N^3	−0.022	−0.021	−0.019
O^1	−0.103	−0.076	−0.058
O^2	0.022	0.025	0.023
O^3	−0.005	−0.005	−0.006
S	−0.347	−0.356	−0.322
C^{Ar}	0.020	0.020	0.019
C^{Me}	0.050	0.013	0.040

The Metal Oxo Teddy Bear

This is a metal-oxo teddy. It doesn't do catalysis but I like it anyway.